DESIGN, DEVELOPMENT AND VALIDATION OF A NOVEL MECHANICAL OCCLUSION DEVICE FOR TRANSCERVICAL STERILIZATION

By
Muhammad Rehan, M.Sc., M.S.

A Thesis submitted in Fulfilment of the Requirements for the Degree of Doctor of Philosophy

Supervisor
Dr. Abdul-Ghani Olabi

School of Mechanical and Manufacturing Engineering
Dublin City University

August 2010

DECLARATION

I hereby certify that this material, which I now submit for assessment on the programme of study leading to the award of Doctor of Philosophy is entirely my own work, that I have exercised reasonable care to ensure that the work is original, and does not to the best of my knowledge breach any law of copyright, and has not been taken from the work of others save and to the extent that such work has been cited and acknowledged within the text of my work.

Signed: _____ I.D No.: 57103984

Muhammad Rehan

Date: _____

ACKNOWLEDGEMENTS

I would gratefully thank my supervisor, Dr. Abdul Ghani Olabi, for his kind guidance, encouragement, constructive criticism and timely support throughout my research, which made this work possible.

I would like to record my appreciation to Dr. James Coleman whose helpful advices and ideas were of great help in the improvement of this work.

I would like to thank my organization, National Engineering and Scientific Commission (NESCOM), Pakistan for providing me opportunity for PhD studies.

I would also like to acknowledge the Enterprise Ireland, Vasorum and Dublin City University for financing this research.

I thank Ms. Triona McNicholl for her help in proof reading of my papers and thesis.

I would like to thanks Mr. Liam Domican, Mr. Eoin Tuohy and Mr. Keith Hickey and for their support regarding computational and experimental work.

I would also like to show my regards to Dr. Khalid Bin Younis for offering me very useful advices throughout my three years at DCU.

I am thankful to all colleagues in School of Mechanical and Manufacturing Engineering, DCU and Vasorum for providing a friendly environment throughout this duration.

It is very important to mention the support and kind words of my parents that were of great satisfaction for me in times of struggle.

To my wife and children

for their patience, love and support

PUBLICATIONS & PRESENTATIONS

Peer Reviewed Journals

1. **Rehan, M., Coleman, J. E. and Olabi, A. G.**, Novel Implant for Transcervical Sterilization, Journal of Bioscience and Bioengineering, vol. 110, no. 2, pp. 242-249, (2010)
2. **Rehan, M., Coleman, J. E. and Olabi, A. G**., Delivery Actuator for a Transcervical Sterilization Device, Journal of Sensors and Actuators A: Physical, doi: 10.1016/j.sna.2010.07.021, (2010)
3. **Rehan, M. and Olabi, A. G.**, Parametric Design Optimisation By Integrating CAD Systems And Optimisation Tools, V. J. Segui and M. J. Reig (ed.), American Institute of Physics, vol. 6, no. CP1, pp. 681-692, (2009)
4. **Rehan, M. and Olabi, A. G.**, Integration Of CAD Model Topology For Parametric Design Optimisation, Advance Software Engineering, manuscript submitted, (2010)
5. **Rehan, M., Coleman, J. E. and Olabi, A. G**., Transcervical Sterilization: History and Recent Advancements, *In progress.*

Conference Proceedings

1. **Rehan, M., Coleman, J. E. and Olabi, A. G.**, Novel Mechanical Occlusion Device for Transcervical Sterilization, International Congress of Engineering, Imperial College, London, UK (2010)
2. **Rehan, M. and Olabi, A. G.**, Parametric Design Optimisation By Integrating CAD Systems And Optimisation Tools, V. J. Segui and M. J. Reig (ed.), Third Manufacturing Engineering Society International Conference, University of Valencia, Spain, (2009)
3. **Rehan, M. and Olabi, A. G.**, Automated CAD System Based Design Optimisation Methodology, p. 377-385. *In* Simson, R. (ed.), Manufacturing and Design: The Next Generation. Proceeding of the 25th International Manufacturing Conference. Dublin Institute of Technology, Dublin, Ireland, (2008)

ABSTRACT

The use of contemporary medical devices in the human body, such as dilation balloons, closure devices, stents, coils, stent-grafts, etc. are gaining more importance to preclude surgical incisions and general anaesthesia. An analogous procedure for permanent female sterilization is the transcervical approach that does not require either general anaesthesia or surgical incision and uses a normal body passage. However, current methods of transcervical sterilization are unable to provide an instant occlusion of fallopian tubes. This work aims at the design, development and validation of a novel mechanical occlusion device, which achieve both instant and permanent female sterilization via the transcervical approach. The device is designed to provide an instant mechanical occlusion by deploying, under hysteroscopic visualization an implant into the intramural segment of the fallopian tube. The transcervical sterilization devices comprises of three major systems, an occlusion implant, a guiding system and a delivery actuator. All three systems were designed, developed and validated in this research work.

The design of the device has been accomplished through Computer Aided Design (CAD), Finite Element Method (FEM) and experimental testing. Validation of device was performed following a number of successful bench-top *in-air* deployments and *in-vitro* deployments in animal tissue and explanted human uteri. The efficacy of the device and the instant occlusion of the fallopian tubes were proved by hydraulic pressure testing of the implanted uteri using saline and methylene blue solution. Initial results suggest that the device provides a safe, effective and instant method of permanent female sterilization. Further work is ongoing for *in-vivo* clinical trials and, if these are successful, it will be mass-produced and introduced into the market.

TABLE OF CONTENTS

LIST OF FIGURES

LIST OF TABLES

ABREVIATIONS

CAD	Computer Aided Design
FE	Finite Element
FEA	Finite Element Analysis
FEM	Finite Element Method
ANSYS WB	ANSYS Workbench
os	An opening or mouth
UTJ	Uterotubal Junction
AIJ	Ampullary Isthmic Junction
ITD	Intra-Tubal Device
UTS	Ultimate Tensile Strength
σ_y	Yield Strength
v	Poisson Ratio
E	Young Modulus
E_t	Tangent Modulus
ρ	Density
Nd:YAG	Neodymium: Yttrium-Aluminum-Garnet
HSG	Hysterosalpingogram
RF	Radio Frequency
CAE	Computer Aided Engineering
IGES	Initial Graphics Exchange Specifications
STL	Stereo Lithography
IPO	Integrated Parametric Optimisation
DOE	Design of Experiments
ADP	Automatic Design Points
SS	Stainless Steel
par1	Ratio of ellipse y-axis radius to x-axis radius
CNG	Compressed Natural Gas
P	Pressure
F	Force
A	Area
APDL	ANSYS Programming Languages
CADO	Computer Aided Design Optimisation
F	French (0.333 mm)
CCD	Charged Couple Device
CNC	Computer and Numerically Controlled
PTFE	Polytetrafluoroethylene
CW	Clock Wise
CCW	Counter Clock Wise
CNC	Computer Numerical Control
CMM	Coordinate Measuring Machine
F	French
PET	Polyethylene Terephthalate

CHAPTER 1

INTRODUCTION

1.1. INTRODUCTION

Female sterilization involves occlusion of the fallopian tubes and obstructing sperm from inflowing the ampulla of the tube, where fertilization of the ovum occurs [1]. Female sterilization by laparoscopic occlusion of the fallopian tubes is a widely used method for family planning because of its proven safety and effectiveness [2,3]. About 180 million couples per annum are relying on female sterilization to avoid further pregnancies [4]. Regardless of such an apparent demand for sterilization, there have been very few technological developments during the last decade in sterilization methods either via the approach to the fallopian tubes or by tubal occlusion [5]. Conventional and most common surgical procedures are the minilaparotomy and tubal ligation [4]. The advent of fiber-optic laparoscopy opened the path for other techniques such as electrocoagulation, clip or ring application to the tubes [5]. However, such approaches carried risks associated with general anaesthesia and on rare occasions could result in vascular damage, injury to the bowel, bladder, or uterus and associated with postoperative pain [6,7].

The transcervical approach is an alternative to incisional procedures for tubal sterilization as it eliminates the need for surgery and general anaesthesia. Transcervical approaches to sterilization involve gaining access to the fallopian tubes through the cervix. A device or occlusive material is then placed hysteroscopically or blindly to block each tube. The transcervical approach to occlude the fallopian tubes via the uterine cavity is not new and has been studied for more than 150 years [8]. Transcervical sterilization can be categorized in to either destructive or mechanical occlusive methods. In destructive methods, the research has mainly focused on use of chemical caustics, tissue adhesives [9], thermic induction and also the Nd:YAG laser [10,11]. Destructive occlusion results in both a low success rate and higher damage to human organs [6,8]. Contrary to the destructive methods of burning, freezing or fibrosing, the tubal ostia can be occluded by means of mechanical devices. Such intratubal devices are mostly applied by hysteroscopy and occlusion can be achieved either by placing a pre-formed plug or device in the uterotubal orifice or by formed-in-

situ methods. The technological developments in endoscopes, light transmission devices, optical resolution, catheters and tubal cannulation evolved some new technologies such as the Adiana and Essure devices [8]. However, both the Adiana [12,13] and Essure [2,14,15], procedures rely on tissue in-growth from the surrounding tubal walls and are effectual three months after device placement. This is inconvenient for the patient, who has to use an alternate contraception during this time, which means the additional cost of contraception and a hysterosalpingogram (HSG) to confirm tubal occlusion. Therefore, the requirement was to develop a transcervical approach that could provide instant occlusion of the fallopian tubes.

1.2. RESEARCH OBJECTIVE AND METHODOLOGY

The objective of this research was the design, development and validation of a novel mechanical occlusion device, which achieves immediate and permanent female sterilization via the transcervical approach. The transcervical approach to female sterilization is a technique that obviates the need of surgery or anaesthesia, hence eliminating post-operative pain. Under hysteroscopic visualization, the designed device deploys an implant into the intramural segment of the fallopian tube to provide an instant mechanical occlusion.

The development of the following characteristics, which form the design of the device, was the main focus of this research:

1. Deliverable through a small calibre hysteroscope.
2. Provide instant occlusion.
3. Low profiled shape during insertion.
4. Capable of anchor at target location.
5. Minimal invasive, safe and easy to navigate through the tortuous uterine anatomy.
6. Deliverable without perforating the uterus.
7. Quick and simple to deploy and release using an ergonomic actuator.

The mechanical occlusion device comprises of three major systems:

a. An implant for occlusion of fallopian tube;
b. A guiding system for the deliverability of the implant through the cervix;
c. An actuator handle to control the deployment and release of the implant.

Designing a device through trial and error based prototyping and experimentation is both a time consuming and expensive process. Therefore, both Finite Element Analysis (FEA) and optimisation in conjunction with experimental testing were used to achieve the optimum design and prototype of the device.

Starting from various concepts, different designs were evaluated, developed and tested to achieve a final design of the device. FEA simulations and optimisations were performed to investigate the mechanical behaviour of the device during deployments and handling. Validation of the device was performed by bench-top deployments; *in-air*, *in-vitro*, in hysteroscopic diagnostic model and finally in the explanted human uteri.

The physical and mechanical properties of explanted human uteri are dependent on the age of the hysterectomy patient. However, this factor was not considered during testing in the explanted uteri and was not in scope of this research work.

The explanted uteri study was performed by the Midland Regional Hospital, Mullingar and, in accordance with their policy, the Midland Regional Ethics Committee approved the in-vivo study.

1.3. THESIS OUTLINE

Chapter 1 outlines a brief introduction to female sterilization as well as a prologue on transcervical sterilization. This chapter also presents the objective of the current work and summary of procedures adapted.

Chapter 2 reviews the literature related to the anatomy of the uterus and fallopian tubes and conventional and state of the art female sterilization procedures. In addition, it discusses concisely both FEA and design optimisation.

Chapter 3 portrays the approaches to achieve the design of the device. It lays the foundation and comparison of the integrated FEA simulation and optimisation. The design and FEA methodologies are discussed. The equipments, devices and machines used to achieve the research objective are also presented.

Chapter 4 details various challenges faced during the design of the occlusion implant. Starting from the conceptual design, all the design phases in achieving the finalized design were discussed. The development and validation of the occlusion implant are also presented.

Chapter 5 details the various commercially available guiding systems. It also presents the design, development and validation of the finalized guiding system.

Chapter 6 presents the various initial designs of the actuator. The final design, development and validation of the actuator are illustrated here in detail.

Chapter 7 overviews the entire sterilization device and its validation. Results of the validation studies performed in the research are discussed.

Chapter 8 outlines the conclusion of this study and some recommendations for future work.

CHAPTER 2

LITERATURE REVIEW

2.1. INTRODUCTION

The objective of this chapter is to examine and highlight previous research related to this work conducted by various researchers and to develop a basic understanding of the uterus anatomy and female sterilization. This chapter is divided into three sections with the first section providing a brief overview of the anatomy of fallopian tubes. The second section details the various methods of sterilizations. The third section summarizes the optimisation process.

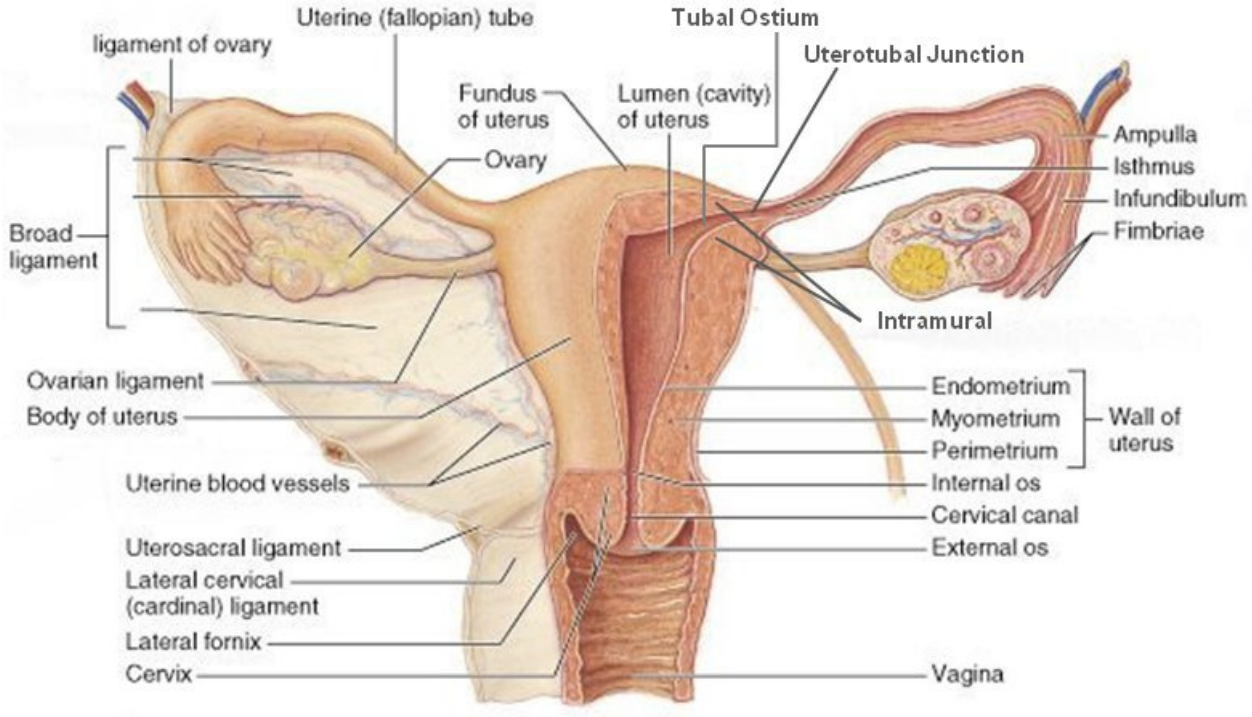

FIGURE 2.1: POSTERIOR VIEW OF THE UTERUS [16]

2.2. ANATOMY OF UTERUS

In order to effectively and safely occlude the fallopian tubes through a transcervical approach, an insight of the *in-vivo* anatomy of the cervical canal, uterine cavity, tubal ostium, intramural, uterotubal junction (UTJ), isthmic and ampullary tube is necessary [17]. It is also obligatory to acquire knowledge of the sizes, shape, behaviour, muscular reflex, and variable epithelial appearances of different parts of the oviductal lumen to achieve an intelligent and successful cannulation procedures [18]. The uterus anatomy is shown in Fig. 2.1. The wall of the uterus is relatively thick and is composed of three layers: endometrium, myometrium, and perimetrium [17]. The oviducts have smooth muscle wall and its thickness reduces as its distance from the uterine horn and as its lumen diameter increases. In addition, the oviduct has a "C" shaped curvature and has a more twisted path in between uterine horn and the ovary [2,19].

The intermural oviduct can accommodate a cannula of between 1 to1.2 mm in diameter without epithelial damage [20,21,22,23]. Understandings of these details are important in performing successful tubal sterilization procedures without causing any complication. After *in-vivo* studies, Corfman et. al. mentioned in a prestigious editorial that the oviduct takes a straight or gently curved course in its intramural segment [24]. Sweeny et. al. concluded in 1961 that passing catheter through the intramural segment is very difficult as they can be damaged easily [25].

2.2.1. FALLOPIAN TUBES

The human fallopian tubes are paired, tubular, seromuscular organs whose course runs medially from the horns of the uterus and laterally toward the ovary. In addition to being the normal site of fertilization, the tubes act as ducts for sperm, oocyte and fertilized ovum transport. The smooth muscle layers become thinner as the tube tracks from the uterus to the ovary with a parallel increase in tube diameter. The length of fallopian tube varies from 70 to 140 mm. It and is divided into four segments, i.e. intramural or interstitial, isthmic, ampullary and infundibulum [25,2].

A. INTRAMURAL SEGMENT

The intramural segment is contained in the wall of the uterus beginning at the tubal ostium and ending at the UTJ. The normal intramural oviduct ranges from 15 to 25 mm in length and takes a straight to slightly curved course to the UTJ. The lumen reaches its

narrowest point at the UTJ and ranges from 0.8 to 1.4 mm in diameter [25]. The intramural oviduct is pale pink in colour and contains between four and six flattened epithelial folds [22]. Visual access of the ostium is feasible only when the ostium is in a state of relaxation.

B. ISTHMIC SEGMENT

The isthmus begins at the UTJ and ends at the ampullary-isthmic junction. Its length ranges from 20 to 30 mm with a diameter of 1 to 2 mm. The isthmic is the narrowest tubal segment and extends from the UTJ to the ampullary-isthmic junction (AIJ). The AIJ has no prescribed boundaries, but it can be characterized by a short segment of about 5 mm, which show a rapid change in lumen diameter [20,18]. The isthmic lumen measures about 20-30 mm in length and l-2 mm in diameter. It is pink in colour and lined by four to six longitudinal folds. The isthmic oviduct has a 40-60º bend as it emerges beyond the UTJ. The layers of the isthmus are muscular and thick even then the UTJ and the initial 20 mm of the curved isthmic can be perforated by transcervical devices [21].

C. AMPULLARRY SEGMENT

The ampullary segment is the longest but varies dimensionally from 50 to 100 mm in length, with a diameter of 1.5 mm at the AIJ to 10 mm at the ampullary-infundibular junction. Beyond the AIJ, there is a rapid increase in lumen diameter from 1.5 to 4 mm over the first l0-20 mm of the ampullary oviduct and a further increase to a diameter of 8-10 mm just proximal to the fimbria [20]. The ampullary oviduct is spacious, thin-walled and flexible, which makes it more prone to perforation.

D. INFUNDIBULUM

A funnel shape cavity or organ is called infundibulum. The end of the fallopian tube closest to the ovary forms an expanded funnel, with numerous fingers like projections that extend into the pelvic cavity. These projections of the infundibulum are called fimbria. The inner surfaces of the infundibulum are lined with cilia that throb towards the middle segment of the uterine tube [17].

2.2.2. UTEROTUBAL GUTTER AND UTEROTUBAL OSTIUM

Tubal Ostia exists in pairs and each ostium is situated at the top of the 'uterotubal gutter' and can be seen visually by hysteroscope. From the hysteroscope, it appears like a ring at the bottom of a deep depression. Its diameter varies from 0.8 to1.2 mm [2]. The ostium is situated in the superior-lateral plane of the uterotubal gutter. The angle to approach ostium through the cervix changes depending on the position of the uterus. Sometimes these larger angles make difficult the approach to the ostium. In such situations, the cervix can be pulled to straighten out the uterine curvatures for easy navigation and cannulation of the fallopian tube [19]. The small calibre hysteroscopes can be aligned axially with the ostium and have eased the tubal cannulation under visual monitoring.

2.2.3. CERVICAL CANAL

The cervix is the lower most part of the uterus and is made up of strong muscles. It also provides support to the uterus due to attachment of muscles to the pelvic bone [17]. The cervix protrudes and opens through a canal into the vagina. The protruding portion of cervix is generally 20-30 mm long. The cervical canal also called endocervical canal is the spindle-shaped, flattened canal of the cervix, the neck of the uterus. The opening of the cervix within the vagina is called external *os* (*an opening or mouth*). Above the external *os* lies the fusiform endocervical canal, approximately 20 mm long and lined with columnar epithelium and endocervical glands. At the upper end of this canal at the junction with the uterine cavity is the internal *os* [20,21].

2.2.4. UTERINE CAVITY

The uterine cavity is roughly triangular in shape and measures approximately 35 mm in length. [26]. The base of the cavity is formed by the internal surface of the fundus between the orifices of the uterine tubes and the apex by the internal orifice of the uterus through which the cavity of the body communicates with the canal of the cervix [17]. The endometrial cavity lies above the internal cervical *os.* Ordinarily, the anterior and posterior walls of the uterus lie in apposition so that little if any actual cavity is present. At each horn of the uterus, the cavity of the uterus becomes continuous with the lumen of a fallopian tube.

2.3. FEMALE STERILIZATION

Sterilization is the preferred and well-established method of termination of fertility, without affecting the hormonal or sexual functions [27,28]. Sterilization has become the most used method of contraception worldwide, involving more than 180 million couples [32]. Sterilization is anticipated for those women who must refrain from having children for medical reasons or who, for non-medical reason decide not to have more children [29]. The latter is applicable when contraception definitely does not provide adequate protection. Initially, female sterilization procedures were completely irreversible because of enormous destruction of tissues or fallopian tubes. In effect, this refrained some couples from opting for these methods for contraception. However, the advancements in procedures have made reversibility of female sterilization possible because of minimal destruction [30]. The number of women accepting sterilization is increasing as the procedures are becoming more sophisticated and refined [5,31].

The first method, which described tubal sterilization, was by Blundell in 1828 when he wrote the "Lectures on the theory and practice of midwifery" [6]. Lundgren et. al. in 1880 reported the first tubal occlusion.

Female sterilization can be categorized into surgical and non-incisional approaches are discussed in the following sections.

2.3.1. SURGICAL TECHNIQUES

In surgical techniques, the fallopian tubes are accessed abdominally by making an incision. The majority of surgical female sterilization procedures are carried out as day cases under general anaesthesia [32]. There are more than 100 different surgical techniques described in the literature. However, the three main approaches used are laparotomy, minilaparotomy and laparoscopy [33]. The two former are being used most often in developed countries but becoming increasingly available in developing areas.

A. LAPAROTOMY

A laparotomy is a surgical procedure involving an incision through the abdominal wall to gain access into the abdominal cavity as shown in Fig. 2.2. Laparotomy may be preferred at Caesarean delivery or in the case of another surgical indication [34]. The procedure adds no risk and induces only a slight prolongation of the operation time. However, sterilization should not be used as an indication for the Caesarean section.

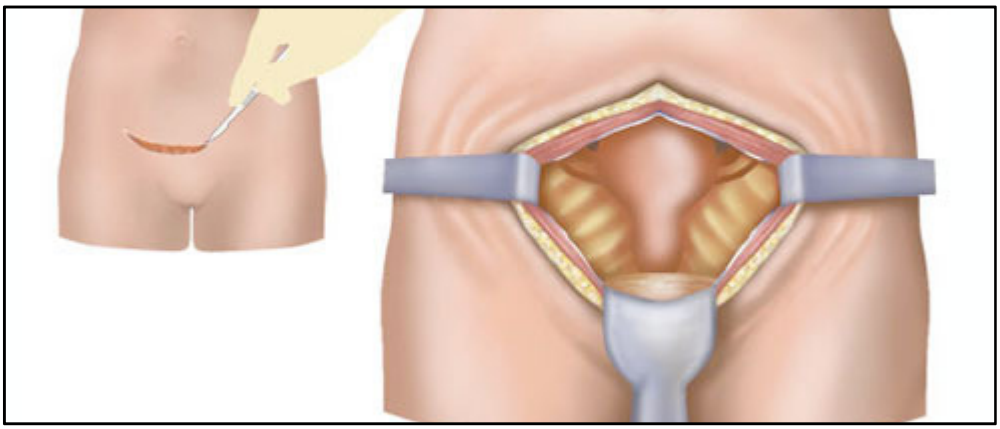

FIGURE 2.2: LAPROTOMY PROCEDURE [35]

B. MINILAPROTOMY

In the early 19th century up to 1930, the minilaparotomy gained universal acceptance because of the requirement of a much smaller incision for approaching the tubes through than that used for laparotomy [4,5]. In this approach of tubal ligation, the doctor closes the tubes through a small incision in the abdomen. The incision used is usually transverse, about 2-3 cm above the symphysis pubis as shown in Fig. 2.3. Access to the tubes was made easier by the development of simple instruments to elevate the uterine fundus into the abdominal wound [34]. The uterus and tubes are elevated just beneath the incision by using a uterine elevating probe. Then the tubes may be tied, cut, burned, or clipped. It can be an outpatient procedure, accomplished under local anaesthesia and conscious sedation [36].

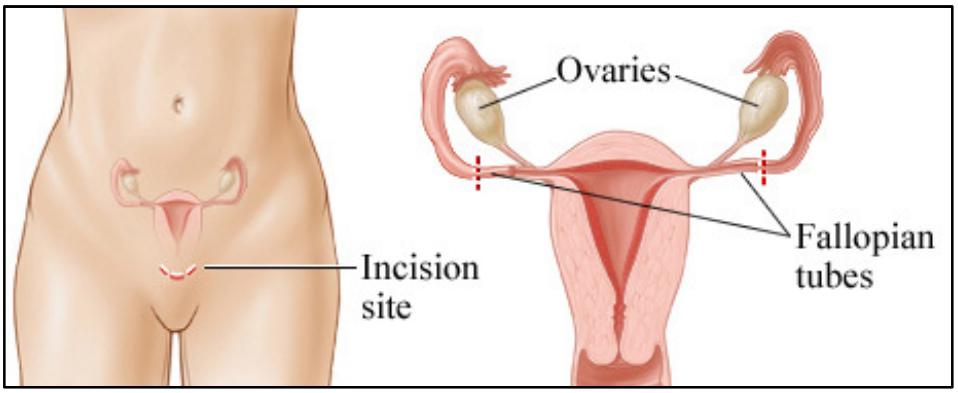

FIGURE 2.3: MINI-LAPAROTOMY [37]

POMEROY TECHNIQUE

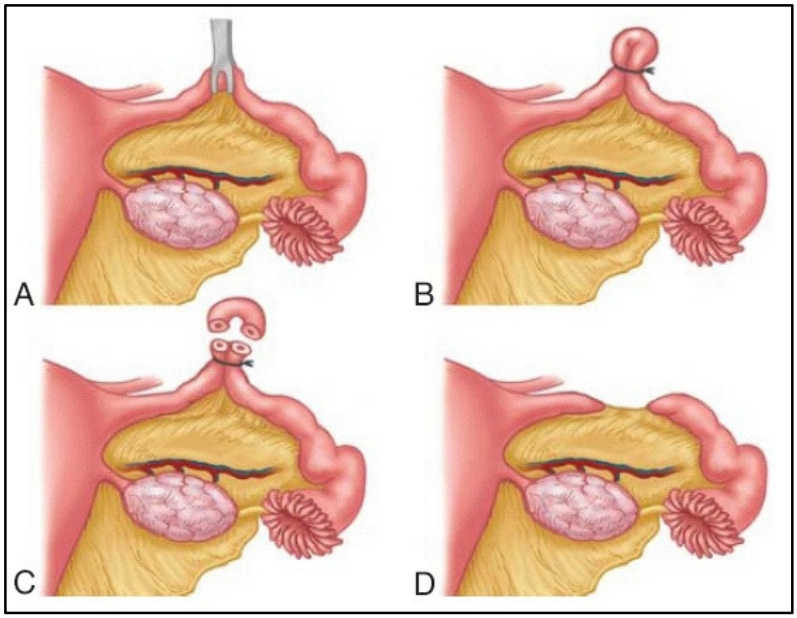

FIGURE 2.4: (A) ELEVATED TUBE WITH FORCEP (B) LIGATED LOOP (C) EXCISED LOOP (D) FIBROSED ENDS OF THE TUBE AFTER FEW MONTHS [38], [39]

The Pomeroy technique is a preferred method for interval surgical female sterilization because of its inherent simplicity and its established effectiveness [40]. The fallopian tube is accessed from the incision and elevated as shown in Fig. 2.4(a). Then about 10mm of the elevated portion is tied around the elevated loop of tube using a single strand of absorbable suture as shown in Fig. 2.4(b). The fallopian tube is excised (Fig. 2.4(c)) and the blood supply is occluded. As seen in Fig. 2.4(d), the excised end of the tube forms a fibrous tissue after few months.

IRVING TECHNIQUE

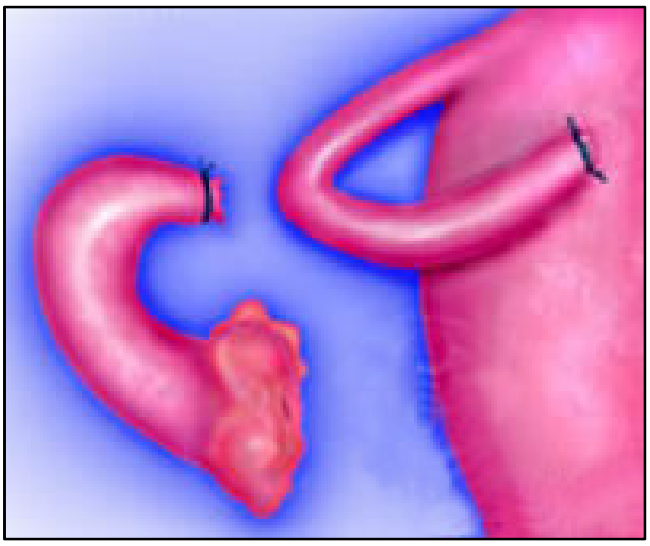

FIGURE 2.5: IRVING TUBAL LIGATION [41]

In Irving technique, the fallopian tube is tied at two places by ligatures or sutures at proximal to mid-segment and the tubal segment between the two ties are excised as shown in Fig. 2.5. Then, the tied end of the segment of fallopian tube attached to the uterus is sutured into the uterus and the other tied end is obscured in the round ligament underlying the fallopian tube [34]. This technique is also very effective with less than 1/1000 pregnancies but the procedure is long and has risk of hemorrhage.

UCHIDA TECHNIQUE

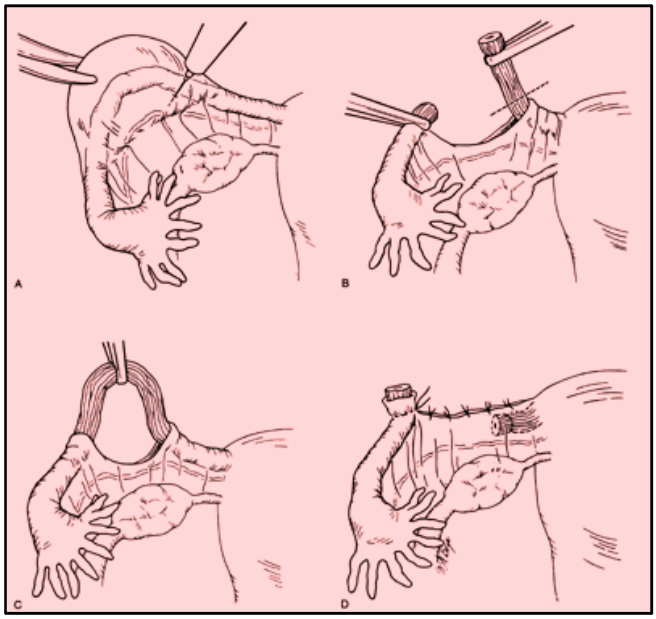

FIGURE 2.6: UCHIDA TECHNIQUE [40]

A Japanese physician, Dr. Uchida, first described this method of sterilization in 1940. As seen in Fig. 2.6(a-d), this method involves removing a large segment of the fallopian tube and suturing the cut end of the fallopian tube into the wall of the uterus [5]. Uchida et. al published information about his method of sterilization after having performed a number of procedures without any pregnancy failures [42]. This is an effective but complicated method of surgical sterilization and success rate is high. A relative disadvantage of the method is the long length of tube need to be excised. However, in modern literature Uchida sterilization technique is no longer in use.

FIMBRIECTOMY TECHNIQUE

This technique was reported in 1935, but not described until 1969. In this technique, a double tubal ligature of silk or catgut was performed on the fallopian tube closest to the ovary. Then about one-third portion of fallopian tube at the fimbrial end is excised and removed as seen in Fig. 2.7. Sometimes, the incised surface is lightly electrocoagulated. Reported failures are quite high from 3-18% [34].

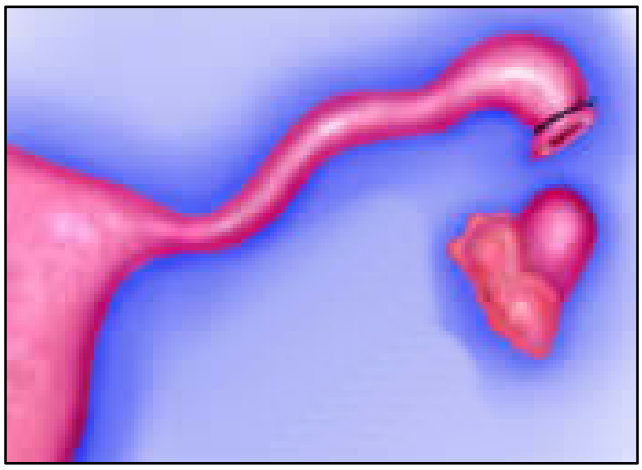

FIGURE 2.7: FIMBRIECTOMY TECHNIQUE [43]

C. LAPROSCOPY

Female sterilization by laparoscopic occlusion of the fallopian tubes is a widely used method for family planning because of its proven safety and effectiveness [17,33]. Laparoscopic surgery is a method to access the abdominal cavity by incision under general anaesthesia in the most of the cases. However, it uses two or more small incisions instead of a single large one. Using optical and electronic visualization equipment high quality images of the surgical anatomy and pathology are obtained from these small incisions as shown in Fig. 2.8. This improved visualisation provides the opportunity of more specific and accurate surgery [44]. Then the tubes can be occluded with a mechanical device such as a clip or silicone rubber band, or may be interrupted using electrocautery or by excision and ligation. It is advantageous for the patient because it is less painful and recovery time is shorter. In addition, the minimal degree of tubal destruction allows for the maximum reversibility [25]. However, these advantages are usually offset by longer operating times and the use of complex and expensive equipment.

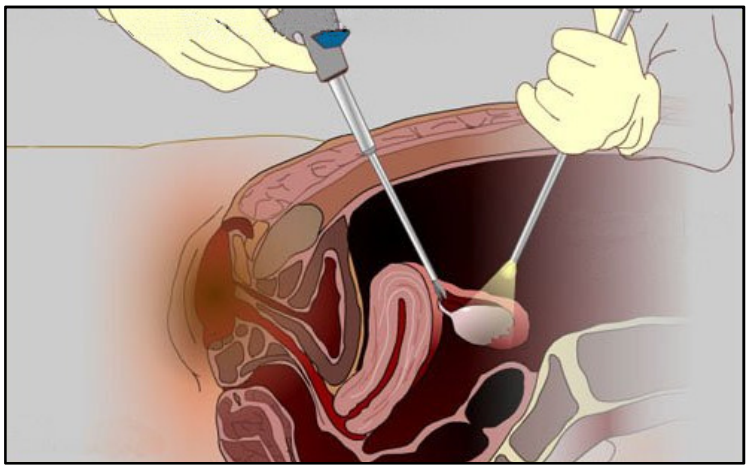

FIGURE 2.8: LAPAROSCOPY SURGERY [45]

ELECTROCOAGULATION

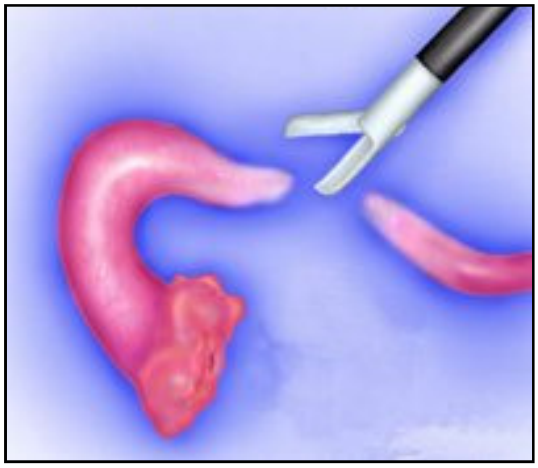

FIGURE 2.9: UNI-POLAR ELECTROCOAGULATION [41]

Palmer described the modern technique of laparoscopic tubal electrocoagulation in 1962 [46,47]. Electrocoagulation can be categorized as uni-polar and bipolar. Uni-polar electrocoagulation is shown in Fig. 2.9. Palmer biopsy forceps was the first instrument used for the uni-polar electrocoagulation [48]. This forceps was used to apply the unipolar electric current from the powerful, grounded, high-voltage generators. Thereby the electrical energy is concentrated on that portion of fallopian tube, which is grasped by the jaws of the forceps. The applied current travels through the patient's body and is collected by a ground plate [49].

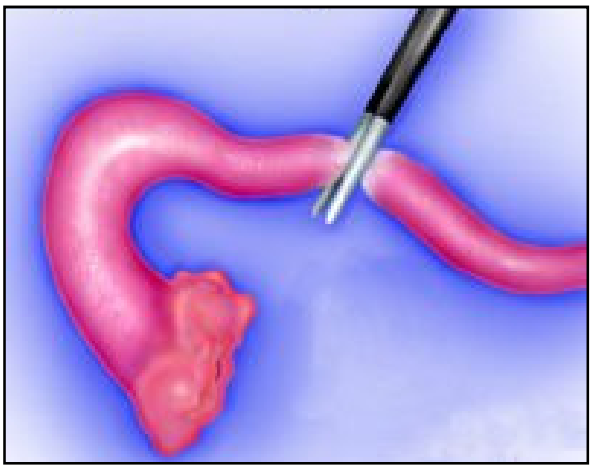

FIGURE 2.10: BI-POLAR ELECTROCOAGULATION [50]

Because of some cases of accidental burns, an alternate bipolar electrocoagulation was introduced in 1973 [49]. In this technique, the two jaws of the forceps are isolated from each other as shown in Fig. 2.10 [51]. High frequency current is passed from one jaw, collected, and grounded from the other. In this way, the current passes through the 1-2 mm of tissue grasped in between the forceps jaws. As the sparking is eliminated during the procedure, the bipolar procedure appears safer than the unipolar system [48]. Another advantage of bipolar electrocoagulation is that the resulting burn is isolated and localized [44].

HULKA CLIP

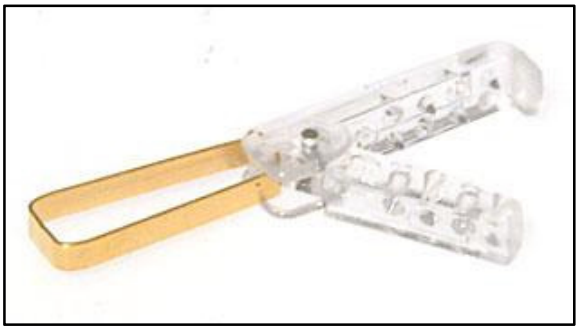

FIGURE 2.11: HULKA CLIP [52]

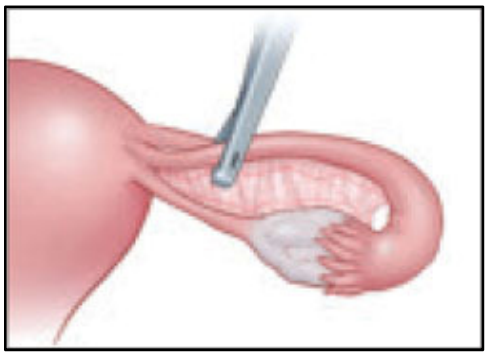

FIGURE 2.12: HULKA CLIP TECHNIQUE [39]

Spring-loaded Hulka clips were developed in as a safe alternative to electrocoagulation to block the fallopian tubes [34]. The Hulka clip was approved for use in the United States in the 1970's and was invented by Dr. Jaroslav Hulka at the University of North Carolina [53]. The Hulka clip is made of plastic and has toothed jaws as seen in Fig. 2.11. It also includes gold plated stainless steel spring loaded clip. The clip is introduced into the abdominal cavity using a clip applicator by laparoscopic

procedure. After placing the clip across the fallopian tube, it is closed and a small spring holds the clip firmly across the tube as depicted in Fig. 2.12. The main advantage is that it produces least damage to the Fallopian tube about 7 mm, therefore, offering the hypothetical advantage of high potential reversibility [54]. A success rate, measured by intrauterine pregnancy, of 87% was reported from a number of centres (Hulka et. Al., 1982).

FILSHIE CLIP

The Filshie Clip System is a small titanium clip lined with thin silicone padding, used to occlude both fallopian tubes as shown in Fig. 2.13. It can be applied through laparoscopic and minilaparotomy procedures. It has been used in Britain and Europe and around the world for the past 20 years [55].

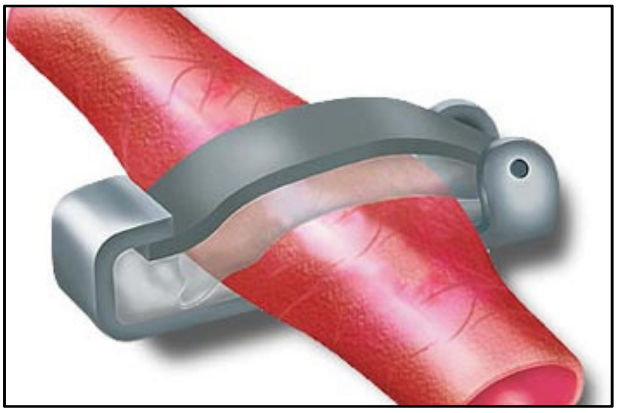

FIGURE 2.13: FILSHIE CLIP OCCLUDING FALLOPIAN TUBE [50]

Locking of the clip is achieved by a pulling down the upper jaw into the lower hooked jaw as shown in Fig. 2.14. After locking the clip, the fallopian tubes are squashed in between the jaws, thus achieving complete tubal occlusion. As compared to the Hulka clip, the Filshie clip is easier to position and deploy. Filshie clip can be used on almost any fallopian tube, regardless of thickness or shape, including postpartum tubes. One of the advantages of the clip is that it only damages a very small portion around 4 mm of the fallopian tube [53,54,56,57,58,59].

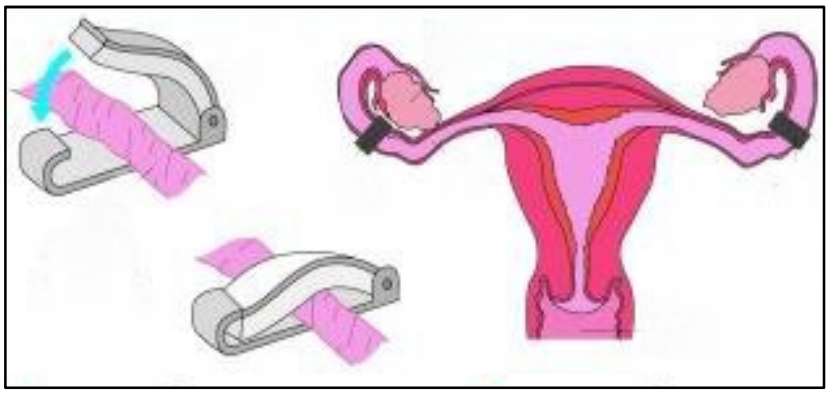

FIGURE 2.14: FILSHIE CLIP TECHNIQUE [60]

FALOPE (YOON) RING [6]

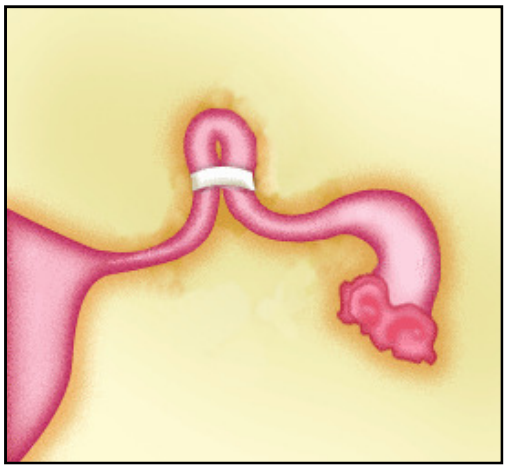

FIGURE 2.15: FALOPE RING LOOPED AROUND FALLOPIAN TUBE [61]

Falope ring is also called the Yoon ring was first reported in 1974 [55]. It is a small silastic band placed around a loop of the fallopian tube as shown in Fig. 2.15 [62,63]. The ring, with the assistance of a special applicator, is designed to enclose a loop of the isthmic portion of the fallopian tube [64,65,66]. An applicator is used to draw about 20-30 mm segment of the isthmic portion inside.

The loaded Silastic band is then released onto the tubal loop by the forward action of an outer cylinder by a squeezing of the applicator handle. This results in the release of band from the applicator. Because of the elasticity, the ring contracts and tightens the base of the loop and blocks the fallopian tube. The pregnancy rate is 70% following reversal of tubal rings procedures [46,61].

All the surgical approaches to female sterilization, carry risks associated with general anaesthesia and on rare occasions can result in vascular damage, injury to the bowel, bladder or uterus and may be associated with postoperative pain [5].

2.3.2. HYSTEROSCOPY

Hysteroscopy [67] is an outpatient non-surgical procedure to access the inside of the uterus and fallopian tubes through the cervix as shown in Fig. 2.16.

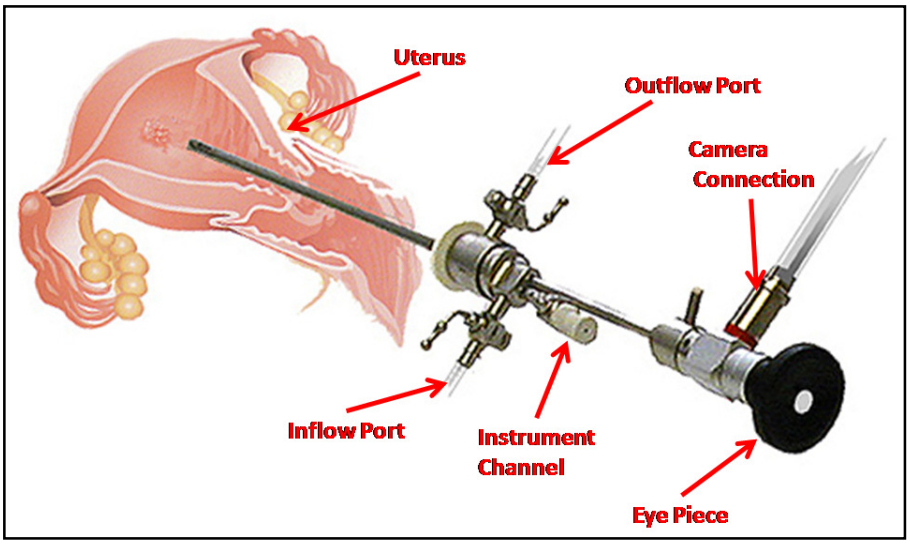

FIGURE 2.16: HYSTEROSCOPE INTRODUCED INTO UTERUS [68]

The following steps are followed during a normal hysteroscopic procedure [69]:

- The first step involves cervical dilatation. The cervical opening must be enlarged to allow passage of the hysteroscope. Thus during hysteroscopy either fluid (saline, sorbitol, or a dextrane solution) or CO_2 gas is introduced to expand the cavity.
- After cervical dilation, the hysteroscope is guided into the uterine cavity and UTJ openings are located.
- The uterine walls, openings of the fallopian tube, and overall architecture of the uterus can now be visualized and examined.

The hysteroscopic view of the UTJ and openings of the fallopian tubes (tubal Ostia) are shown in Fig. 2.17.

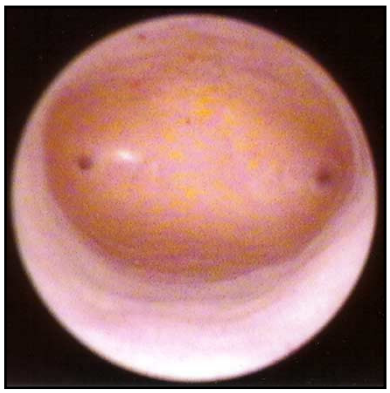

FIGURE 2.17: HYSTEROSCOPIC VIEW OF TUBAL OSTIA

2.3.3. TRANSCERVICAL METHODS

The transcervical approach is an alternative to incisional procedures for interval tubal sterilization as it eliminates the need for surgery and general anaesthesia [70]. The word 'transcervical' means "through the cervix." Sterilization is another term used for permanent contraception [71]. In transcervical sterilization, the fallopian tubes are accessed through the cervical opening of the uterus as shown in Fig. 2.18. After that, the tubes are occluded to block the passage of sperm, preventing it from reaching the egg.

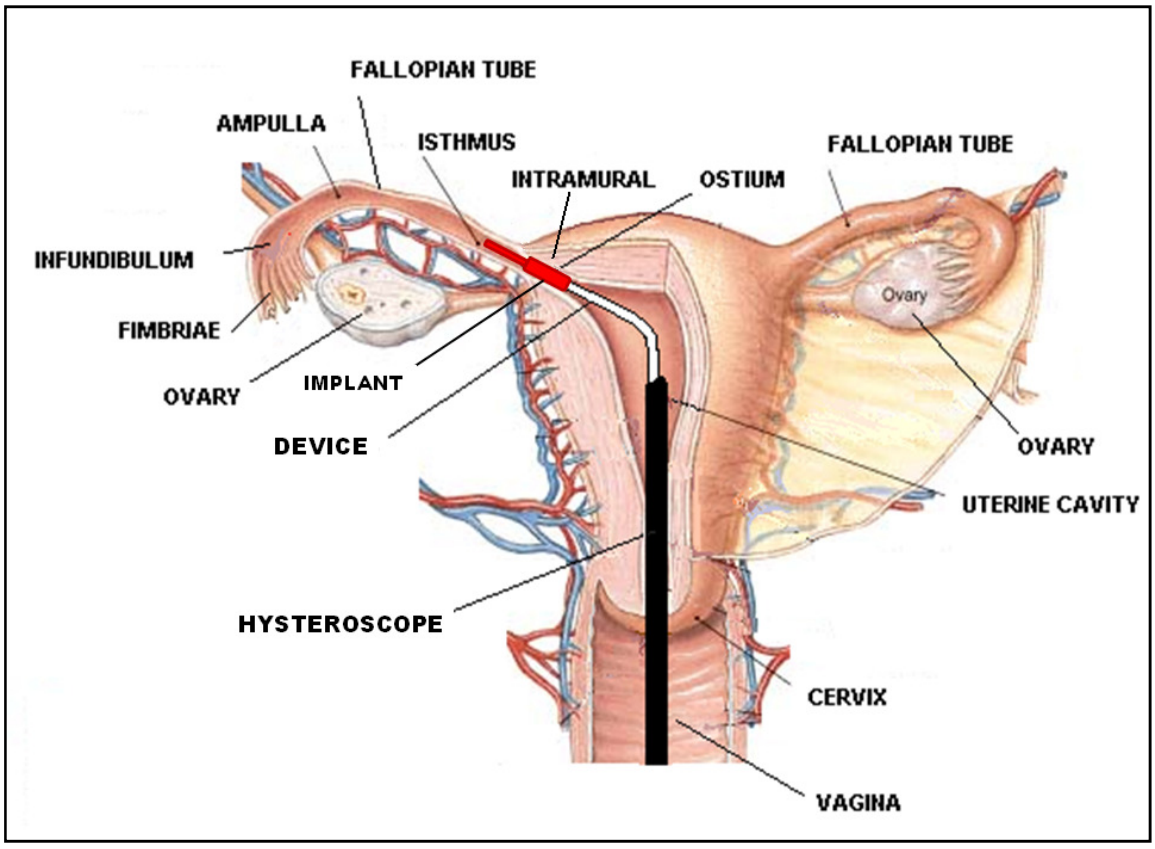

FIGURE 2.18: CROSS-SECTION VIEW OF UTERUS SHOWING TRANSCERVICAL STERILIZATION (ORIGINAL PICTURE [17])

Transcervical sterilization is gaining more attraction because of its expediency and various advantages over tubal-ligation method [72]. Transcervical sterilization is also a comparatively less risky and more cost effective method [73] and generally performed in a clinical setup. In addition, it takes only half an hour to be completed, while the surgical methods take almost two days of hospital stay followed by some days of bed rest at home.

Transcervical approaches to occlude the fallopian tubes via the uterine cavity are not new and have been studied for more than 150 years [8]. Numerous approaches and attempts have been made during the 1970s and 1980s but an acceptable transcervical method of sterilization was not developed that time [74]. Up to 1995, no scientifically validated transcervical method was available and this potential approach was the most challenging for development [5]. However, the development of the modem hysteroscope, made possible through fibre-optic technology opened a range of possibilities for transcervical sterilization [15]. Since then various methods have been evaluated and tested but very few achieved success [75]. The first successful attempts at transcervical tubal catheterization were published in 1985 [76].

Transcervical sterilization can be categorized into destructive and mechanical occlusive methods:

A. DESTRUCTIVE METHODS

In destructive methods of female sterilization, the intramural segment of the fallopian tube is destroyed using various techniques. This blocks the passage of the sperm to reach ovary. The research has mainly focused on chemical caustics, tissue adhesives, electrocoagulation and thermic induction.

ELECTROCOAGULATION

In 1878, Knocks reported the first electrocauterization of the cornual portion of the uterus by means of a specially developed galvanocaustic uterine probe [77] and in 1934 Hyams reported the same procedure using a specially-designed unipolar electrode [78]. However, failure rates were high, and there were several interstitial or cornual pregnancies [34]. In the early 1970s, transcervical electrocoagulation was attempted using insulated electrodes guided by hysteroscopy in order to coagulate the intramural portion of the fallopian tubes as shown in Fig. 2.19. Afterwards different investigators

evaluated this technique and the coagulation of tubal area varied among every investigator. This was due to the variations in wattage and applied time. However, the preliminary results were satisfactory with 75% to 80% bilateral tubal occlusion with one application and roughly 85% to 90% occlusion with a second application.

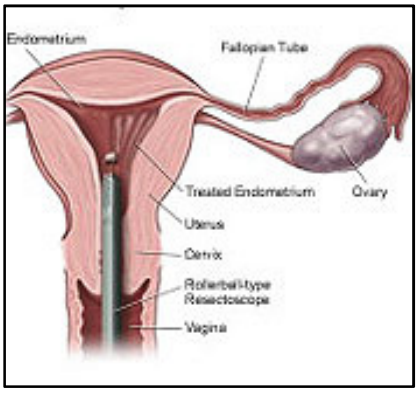

FIGURE 2.19: TRANSCERVICAL ELECTROCOAGULATION [50]

CRYOCOAGULATION

In 1970, Droegemueller et al discussed the cryocoagulation technique for occlusion of the fallopian tubes under visual hysteroscopy [79]. This technique used subfreezing temperatures to coagulate the fallopian tube followed by fibrosis. No long-term follow up of this technique was available [6].

THERMAL METHODS

Thermal damage to the tubes by laser heating has been extensively tested. The Nd:YAG laser has been investigated for occlusion of human and rabbit fallopian tubes to induce sterilization [10,11]. Kukreja et. Al. also performed an in vitro study on the coagulation of fallopian tube tissue using continuous wave Nd:YAG laser [80]. More recently, other methods to damage tubal openings that relied on direct heating and electrocautery thermal reaction have been attempted. However, the further development in use of thermal methods have not been reported. Most probable because of the technical issues or unreliability [10,11].

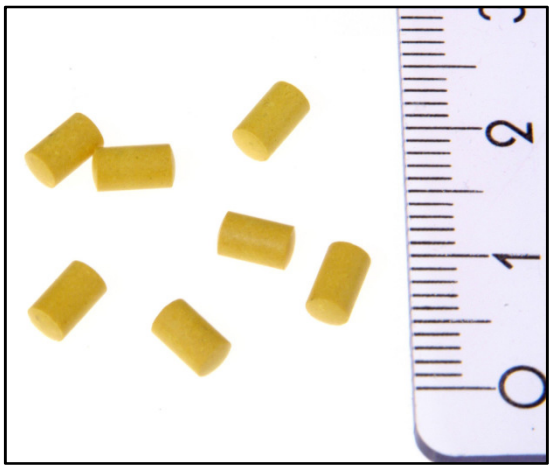

FIGURE 2.20: QUINACRINE PELLETS

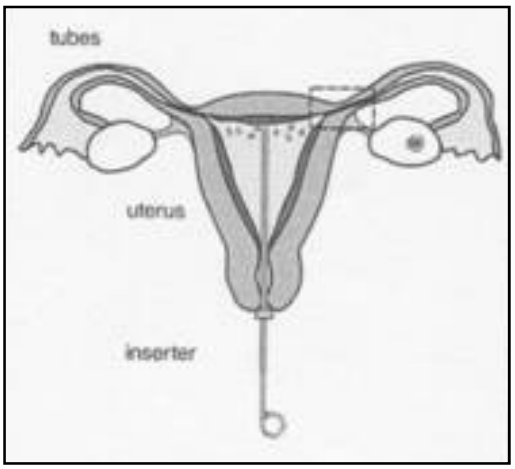

FIGURE 2.21. PELLET PLACEMENT INTO UTERUS

The chemical occlusion of the fallopian tubes was first investigated by Zipper, who performed intrauterine installation of quinacrine pellets [81,82]. Various studies have been done on the quinacrine procedure after this initial investigation [83,84]. This procedure can be performed both blindly and hysteroscopically. It involves placement of 7 small pellets (Fig. 2.20) of quinacrine into the uterus using a small plastic tube. The quinacrine pallets, their applicator and placement are shown in Fig. 2.21. These pellets dissolve in half hour allowing the liquid quinacrine to flows in the fallopian tubes. This liquid quinacrine causes inflammation of the tubal lining. Over the next 3 months, scar tissue is formed and the tubes are occluded. Quinacrine is a cheap and effective way of permanent female sterilization, and has been widely used in developing countries in the past [85,86]. However, because of possibility of transformation of scar tissue in to malignant cells, its use was warned in 1991. However, the direct evidence of quinacrine carcinogenicity in humans or animals has never been established [6].

B. MECHANICAL METHODS

Contrary to the destructive methods of burning, freezing or fibrosing, the tubal Ostia can be occluded by mean of mechanical devices. Such occlusive intratubal devices are mostly applied by hysteroscopy and occlusion can be achieved either by placing a pre-formed plug or device in the uterotubal orifice or by formed-in-situ methods. The cornual area and the tubal orifice can be approached blindly by specially designed instruments or under visual control by hysteroscopy.

PREFORMED PLUGS

Preformed materials that have been tested with devices or plugs are made from materials including ceramic, nylon, and polyethylene [87]. Hefnawi, Fuchs, and Laurence reported the pioneering experimental trials in animals in 1967 [88]. Their investigation proved that this method is effective, non-tissue damaging and reversible [88]. Rakshit reported the first investigation in humans in 1967 who had introduced a liquid plastic into the uterine cavity and fallopian tubes [89]. Two types of plugs, which were investigated more extensively, were the Hossenian plug and the Brundin plug. The Hossenian Plug was cone shaped; 1 mm to 2 mm tip to base diameter, with length varies from 7 to 9 mm. It was made of silicone rubber with four anchoring spines made of Elgiloy that served to fix and keep the device in place. A special assembly screw of stainless steel attaches the anchoring spines to the plug and provides a grasping base for the device carrier [90]. The P-Block Tubal Plug was the Brundin plug made of hydrogel. The body of plug, 4 mm long and 1.2 mm wide has 2-mm-wide nylon wings to prevent expulsion from the tube before hydration. It is fixed on a nylon skeleton in its dry state and swells by moisture absorption in 30 minutes, and this swelling maintains the plug in position. Because of the number of failures caused by faulty placement or expulsion of the device, the clinical studies were discontinued [91].

INTRATUBAL DEVICE (OVABLOC®)

The concept to create an ‘intra-tubal device’ (ITD) formed in situ was first applied in 1966 [6,92]. In 1988 hysteroscopic tubal occlusion with intratubal siloxane device (Ovabloc®) was introduced which uses siloxane rubber solution for occlusion [77,93]. In this technique, the catalyzed liquid siloxane is injectedinto both fallopian tubes, under hysteroscopic visualization, which is then cured into fallopian tube. Consequently, it takes its shape in the fallopian tube as a flexible plug, which remains stable and operational as shown in Fig. 2.22. The plug weighs about 0.2 grams and its hysteroscopic view is shown in Fig. 2.23. Ovabloc retains its flexibility and elasticity for years. The procedure was introduced by Advanced Medical Grade Silicones BV, Reeuwijk, The Netherlands [93].

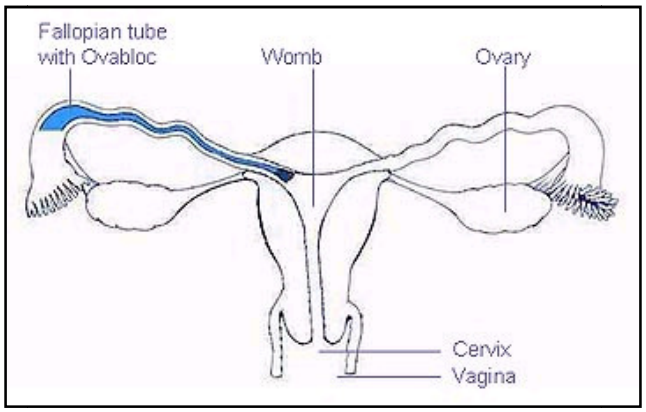

FIGURE 2.22: A SET OVABLOCK SOLUTION IN LEFT FALLOPIAN TUBE [94]

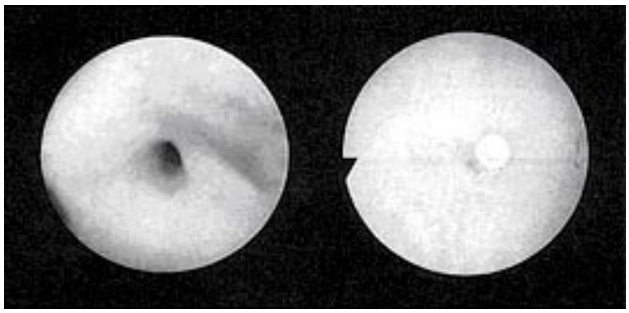

FIGURE 2.23: A TUBE WITH AND WITHOUT THE OVABLOCK PLUG [94]

TUBAL SCREW

This tubal screw (Fig. 2.24) that can be inserted hysteroscopically is made out of polytetrafluoroethylene, which is self-lubricating material. It is also sono-opaque and can be visualized with ultrasonography. It has a maximum diameter of 3 mm to ensure the occlusion of uterotubal junctions. It has a 15 mm length in which only 10 mm is the effective length [8]. Magos and Chapman reported 97% insertion rate of the tubal screws, however the retention rate was only 60% [6].

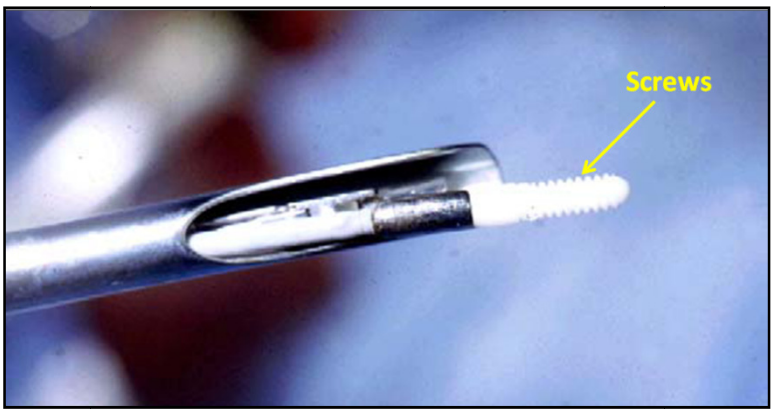

FIGURE 2.24: TUBAL SCREW AT THE DISTAL END OF HYSTEROSCOPE [6]

ADIANA

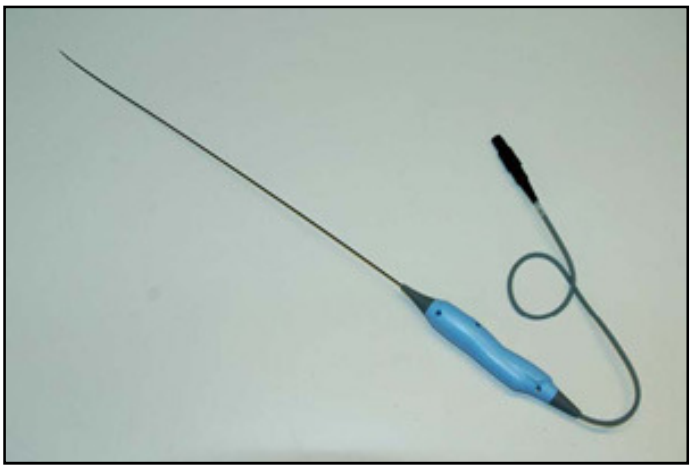

FIGURE 2.25: ADIANA STERILIZATION SYSTEM [95]

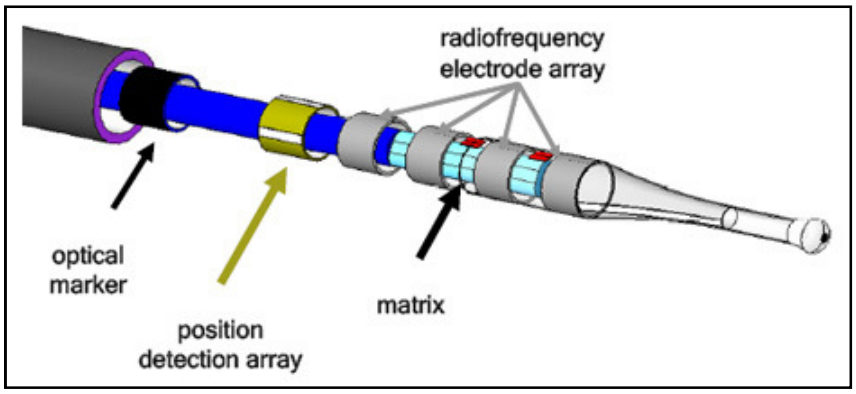

FIGURE 2.26: ADIANA IMPLANT [95]

The Adiana transcervical sterilization system (Fig. 2.25) involves placement of a silicone implant (Fig. 2.26), called a matrix, into each fallopian tube of the female patient to effect tubal occlusion and permanent sterilization as shown in Fig. 2.27 [96]. The implant is delivered using catheter through the working channel of a hysteroscope. An optical mark on the catheter, proximal to the electrode array and matrix, is visualized to confirm correct catheter placement prior to silicone matrix delivery [12,13,97]. After placement in to the intramural section of the fallopian tube, the distal tip of the catheter delivers Radio Frequency (RF) energy to the electrode array. This creates a lesion at the applied area of the fallopian tube. Occlusion of the lumen is achieved by tissue in-growth into the matrix in place as shown in Fig 2.28. The average treatment time of the procedure is 15 minutes [12], [13]. The occlusion of the fallopian tube results after 12 weeks of the procedure [96]. The physician conducts a

hysterosalpingogram (HSG) three months after matrix placement to confirm the occlusion of the tubes.

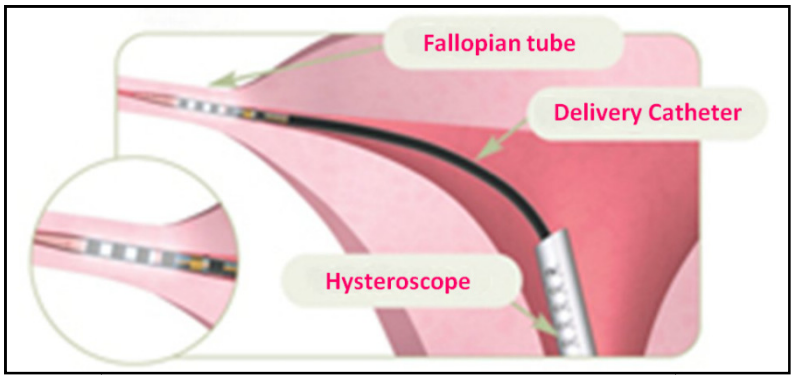

FIGURE 2.27: ADIANA IMPLANT PLACEMENT IN LEFT FALLOPIAN TUBE [98]

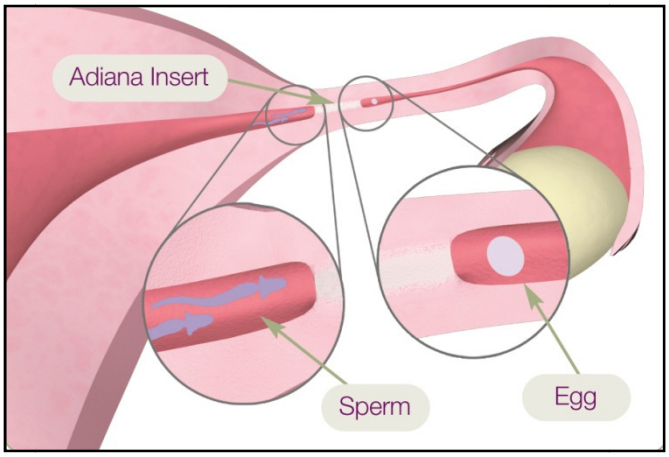

FIGURE 2.28: TISSUE IN-GROWTH AROUND ADIANA IMPLANT [98]

ESSURE®

In November 2001 the European Health Office approved a method of hysteroscopic sterilization; the Essure® System (Conceptus) which was launched on the Dutch market in 2003 [5]. It is the most recent and successful hysteroscope sterilization device available in the market [99,100]. The Essure® micro-insert, initially called STOP, is a dynamically expanding micro-coil which is placed in the proximal section of the fallopian tube using the hysteroscopic approach for cannulating the fallopian tube [101] as shown in Fig. 2.29.

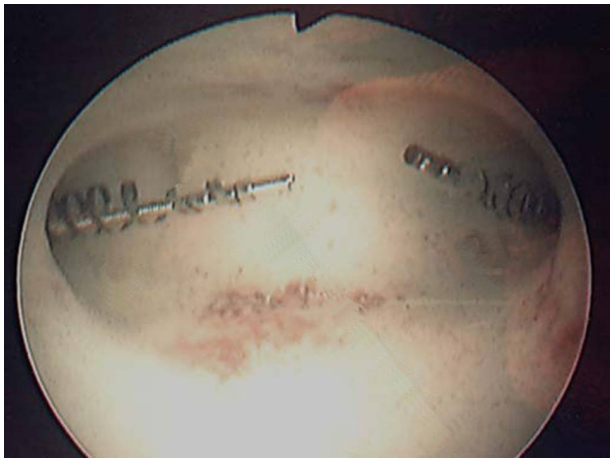

FIGURE 2.29: ESSURE MICRO-INSERT PLACED AT BOTH FALLOPIAN TUBES [102]

The micro-insert shown in Fig. 2.30 is comprised of a stainless steel inner coil, an outer coil made from nitinol and polyethylene terephthalate (PET), and Dacron fibres. The initial diameter of insert is 0.8 mm, deployed diameter ranges from 1.5-2.0 mm and length is 40 mm [103]. The inner coil attaches the device to the guide wire used in its placement. The outer coil anchors the device in the fallopian tube on deployment [14,74,91].

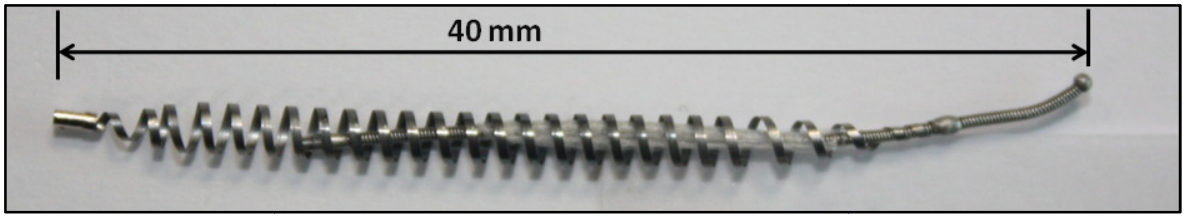

FIGURE 2.30: ESSURE MICRO-INSERT

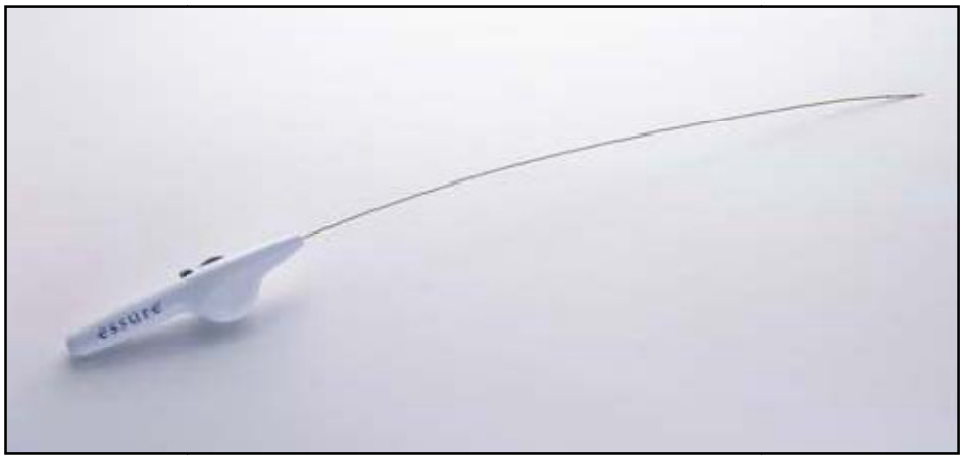

FIGURE 2.31: ESSURE COMPLETE DEVICE

The entire system is attached to an actuator handle, aligned for single-handed release of the device as shown in Fig. 2.31. The micro-insert achieves tubal sterilization through mechanical occlusion of the fallopian tube by inducing a local fibrous tissue in-growth from the surrounding tubal walls [4,14,74,104,105]. The Essure [14,19,74] procedure requires about 3 months for complete tubal occlusion after device placement. Therefore, the patients are instructed to use alternative contraception during this duration. After 3 months the tubal occlusion needs to be confirmed by performing HSG before discontinuing alternative contraception [102,106,107,108].

2.3.4. CONCLUDING REMARKS

Various techniques of female sterilization have been discussed and it was concluded after the literature review that:

1. Transcervical sterilization devices that can provide an instant occlusion are not in use as those devices have the inherent problem of expulsion due to uterus spasm.
2. At present, two mechanical occlusion devices are in use but their implants are relatively large in size and take 3 months (minimum) for complete occlusion of the fallopian tubes.

These findings indicate that a novel transcervical sterilization device is required, which can provide an instant occlusion of the fallopian tube to achieve permanent female sterilization.

2.4. ENGINEERING DESIGN OPTIMISATION APPROACHES

Currently, several design optimisation techniques from human knowledge-based engineering to intelligent (adaptive) algorithms are used to meet the technological challenges in the field of design optimisation. Roy et. al. [109] complied the various design optimisation approaches in research from 1997to 2006 as shown in Fig. 2.32. The two major classifications of engineering design optimisation are manual and parametric optimisation, which are discussed below:

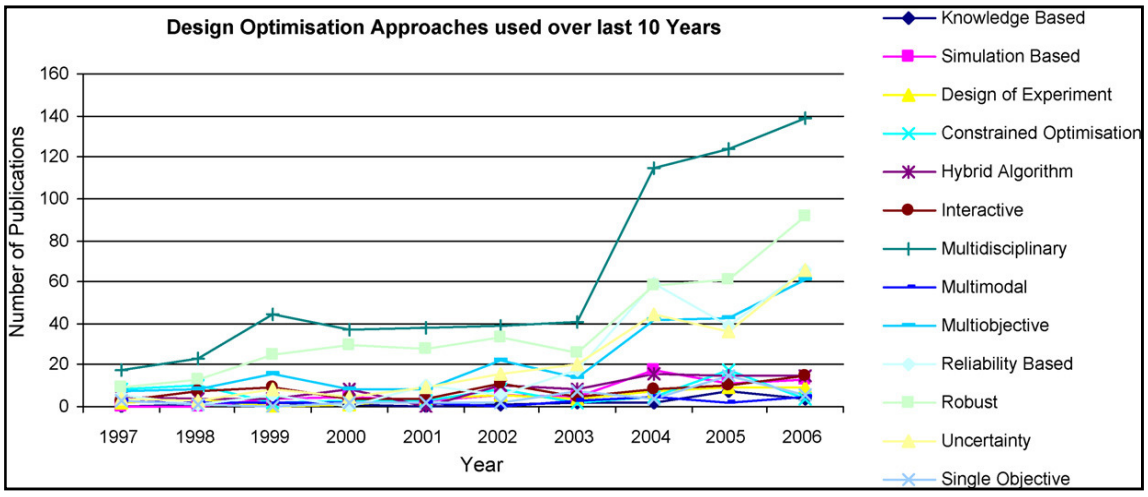

FIGURE 2.32: DESIGN OPTIMISATION APPROACHES (1997–2006) [109]

2.4.1. EXPERT-BASED OPTIMISATION (MANUAL)

Design optimisation of real life problems is often done by designers using their experience. Engineering designs are still optimised mostly through a manual iterative process where the designer compares a few designs based on a defined criterion (such as maximum stress and weight) and then selects the best design. The designs are initially checked against any constraints such as maximum cost, and only feasible designs are considered for optimisation. This manual process is often limited to selecting designs, which are recognised by the designers, and it fails to identify any unknown but potentially significantly better designs. This experienced based design optimisation is normally phrased as expert based optimisation [109]. This expert-based optimisation approach often uses expert judgement or simulation techniques such as FEA or CFD analysis for the design optimisation. The major advantage of this approach is that designers do not need to define optimisation study, it may take less time to select a better design, and it gives incremental improvement. On the other hand, the major

challenges are in the form of dependency on a few experts who could evaluate the designs and find truly novel and significantly better designs.

Zirn et al. developed a design optimisation method using on a nonlinear stability analysis [110]. This optimisation was based on experimental results that were limited and did not explore the complete design space. A trial and error approach to develop advanced materials for net shape sintering of graded laminated powder compact is also presented by Mori and Osakada [111]. A 'what-if' analysis based decision support system for design optimisation was developed by Lutters et al. and Vaneker et al. This approach provides better insight about the design space and reduces workload of expert designers. However, this approach was also limited by the quantity of search one can perform to achieve an optimum solution [109].

An expert based optimisation approach can be based on rapid prototyping to verify the design and to achieve an optimum solution. A methodology to link CAD and rapid prototyping key areas in a design to support the product development process was presented by Krause et al. [112]. It was discussed that rapid prototyping is useful in the fast production of physical prototypes and therefore constitutes a key element in the optimisation and abbreviation of product development processes.

An approach to optimise designs manually based on value-oriented life cycle cost analysis was also developed by Janz et al. This approach considered the perception of a designer to improve product performance over the whole life-cycle though simultaneously optimising the cost [113]. In another approach to expert based design optimisation, a computer based system can be used that employ knowledge educed from experts and can automate the design. These knowledge-based systems are computer programs embodying knowledge about a narrow domain for solving and/ or searching for the optimal solution to problems related to that domain [109,114]. Yang et al. also described an intelligent design system by integrating a FEA and a CAD system for forging tool design. In this integrated approach, it was tried to reduce the design optimisation time through automated link, but the final selection is still driven by the designers [115].

In addition, to the above mentioned expert based or manual design optimisation techniques the design of experiment (DOE) technique is employed. This technique empirically comprehend the impacts of design variables on the design performance and

therefore aid in identifying optimum variable values [116]. This experimental method of optimisation is based on a fractional factorial experiment, which allows an experiment to be conducted with only a fraction of all the possible experimental combinations of design variable or design factor values. Standard orthogonal arrays are used to design the experiments [109].

2.4.2. PARAMETRIC DESIGN OPTIMISATION

The conventional design process depends on the designer's instinct and expertise [117]. Thus, an inexperienced designer can lead to invalid results in the designing of the complicated system. In this contemporary world, the requirement of cost-effective and efficient designs has lead to evince great interest in cost-effective and improved designs. The CAD optimisation process is playing a great role to achieve this goal. During the system design and evolution, both the expert based and integrated optimization techniques can be used at different stages. The main advantage of the conventional design process is that the designer's experience and intuition can be used in making conceptual changes in the system or to make additional specifications in the procedure. However, during the detailed design, the conventional design process has some disadvantages. Therefore, the combination of conventional and optimum design process can lead to better designs according to customer requirement.

In addition to customer requirement the product must be cost optimised and introduced onto the market quickly [118]. In order to achieve this goal, design tools are being implemented by companies. In some new design procedures, the engineering calculations are already integrated into the concept phase of the design process to reduce design cycle time [119]. The demand to reduce optimisation time can only be met if structural optimisation tools are intelligently used in conjunction with established Computer Aided Engineering (CAE) and CAD systems [120,121]. However, generation of FEA analysis from a CAD model is a challenging task [122]. Kosaka et. al. [123] linked the GENESIS optimiser and SDRC-IDEAS (CAD system) to optimise the material reinforcement of an automobile body for rigidity improvement. They used topology and sizing optimisation to acquire an optimal feasible design. The FE model was created in IDEAS after manual interpretation of results from topology optimisation. In another example [120], a CAD system was integrated with a FE-based design optimisation system to obtain the optimum design of multi-physics problems. Cristello et. [124] has used the FEA package ANSYS and MATLAB for design optimisation of

an automotive universal joint in which part modelling and analysis were conducted in ANSYS and optimisation was implemented using MATLAB. Nima et. al. [119] integrated CAOSS (Computer Aided Optimisation System Sauter) and MSC/NASTRAN to perform sizing, shape and topology optimisation. In some earlier works standard formats such as Initial Graphics Exchange Specifications (IGES) or Surface Tessellation (STL) were used to import CAD model into the optimisation tools and vice versa. One notable shortcoming of these methodologies is that STL data cannot be directly converted into FE data. In another example, a mesh model was imported to CAD systems using the IGES format during multi-objective optimisation of an auto panel die face design using mesh morphing techniques [125]. In the above-mentioned examples, the designer has to manually update the CAD model after the optimisation process followed by a FE analysis that is based on the solid model. Therefore, any modification in the design parameters results in modification of the model or sometimes complete remodelling [120]. Bayandor et. al. has detailed the parametric design optimisation of the configuration and composite structure of a Krueger flap [126].

A. PARAMETRIC OPTIMISATION PROCEDURE

The design of a system can be varied by varying its different parameters [127]. The parameters that can be changed to achieve an optimal design are called design variables. The optimisation process can be defined as the process of finding the minimum or maximum value of some characteristics, which may be called the objective function. A good design must satisfy certain requirements called design constraints or state function. Hence, the optimisation changes the design variable to achieve the maximum or minimum of objective function, which would satisfy all the required design constraints [128].

Optimisation can be formulated as follows

$$d = \begin{Bmatrix} d1 \\ d2 \end{Bmatrix} \qquad \text{(design variables)}$$

Minimize/Maximize: $x = f(d1, d2)$ (objective)

Subject to: $F_1 = f_1(d1, d2) \leq 0$ (constraints)

$$F_2 = f_2(d1, d2) \leq 0$$

Structural optimisation techniques are mainly classified into two types of optimisation processes namely topology optimisation and size/shape optimisation [129].

TOPOLOGY OPTIMISATION:

Topology optimisation is the concepttual design phase of an optimal design [130]. It is used to find a preliminary structural configuration that meets a predefined criterion. This type of optimisation sometimes gives a design that can be completely new and innovative. Thus, starting from a specified design space, it is used to generate conceptual designs for specified loads and boundary conditions [120]. It removes material from the defined design space to find the optimal distribution of material in a given design region. The suggested design gives an indication of the optimal strain energy distribution [131].

SIZING / SHAPE OPTIMISATION

Sizing / shape optimisation involves the modification of "sizing / shape variable" to achieve an optimum objective variable (minimum or maximum) while satisfying state variables. During this optimisation, the structural elements are modified on the FE level [132]. Due to its inherent non-linear behaviour, shape optimisation has gained more importance among other structural optimisation problems. A review paper has stated that the first research on optimisation of structures was by Zienkiewicz and Campbell [133]. They discussed the problem of finding the optimum shape of two-dimensional structures. Since then many other authors have modified and improved the approach of using nodal coordinates of finite element model as design variables [134,135,136,137,138]. Petchsasithon et. al. incorporated fully automated mesh generation scheme and analytical sensitivity analysis into integrated shape and thickness optimisation of shell structures [139].

Sizing / shape optimisation can be categorized into integrated and non-integrated techniques. In integrated shape optimisation, Computer Aided Design (CAD) model and FEA model are fully integrated and have complete associativity. This allows parameters of solid model to be used as a shape optimisation design variables. The main benefit of this approach is that at the end of the design cycle, the designer can get the final dimensions of the solid model. This enables the designer to use the geometry directly for manufacturing drawings and process planning. Non-integrated shape optimisation uses a FE model in which shape variables are defined using FE nodes and specifying the changes in nodal coordinates to take place [140].

CHAPTER 3

GENERAL APPROACHES FOR DESIGN, DEVELOPMENT AND VALIDATION OF STERILIZATION SYSTEM

3.1. INTRODUCTION

The design of a medical device can be a fairly complex process because of the involvement of human factors. A number of conceptual designs must be made initially to develop models that can be subjected to analysis. These analyzed models are prototyped and must be verified by experimentation. This chapter will describe briefly the mechanical occlusion device for female sterilization and its subsystems. It will also explain the approaches followed in the design and development process. In addition, the verification techniques and the testing approaches followed during the design and development are discussed.

3.2. SYSTEM EVOLUTION MODEL

The design process should be a well organized activity. Design is an iterative process. Iterative implies analyzing several trial designs one after another until an acceptable design is obtained. The process begins with the identification of need, which may be conceived by engineers. The design evolution model used for the design and development of sterilization system is shown in Fig. 3.1.

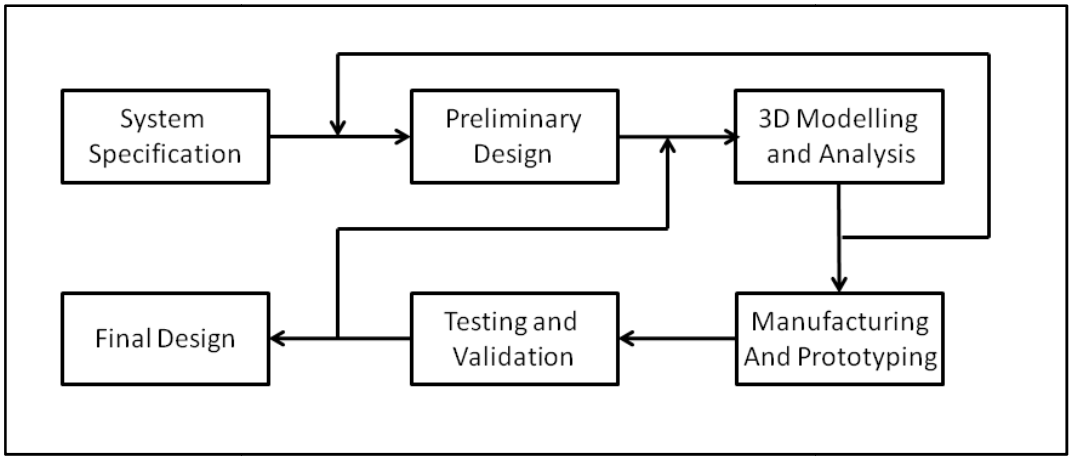

FIGURE 3.1: DESIGN EVOLUTION CYCLE

The first step in the evolutionary process was to define precisely the specification for the system. The second step was to develop a preliminary design of the system. The third step was to carry out a detailed design for all the subsystems using an iterative process. The fourth step involved the manufacturing and prototyping of the system. The final step was the testing and clinical evaluation of the system. All these steps were followed in the design finalization and this thesis is structured according to these design evolution steps.

For this thesis, both conventional and optimum design process were used at different stages of the system evaluation. The optimisation of component design was achieved using optimisation tools. However, the optimisation of the occlusion device was achieved from experimentation and testing i.e. in explant studies and *in-vivo* clinical trials.

The design cycle followed throughout the research to achieve a novel mechanical occlusion device was as follows:

1. Conceptual design.
2. 3D modelling.
3. FEA analysis and optimisation.
4. Manufacturing and prototyping.
5. Testing and Validation.
    a) Bench Testing.
    b) Explant Studies.
    c) Clinical Trials.

3.3. SYSTEM SPECIFICATION

The objective of this research work was the design, development and verification of a novel mechanical occlusion device, which achieve both instant and permanent female sterilization via a transcervical approach. Therefore, system specification was the first step in the design evolution of the sterilization system. The following characteristics were identified as forming part of the design of an ideal occlusion device:

1. Deliverable through a small calibre hysteroscope.
2. Provide an instant occlusion.
3. Have a low profiled occlusion implant during insertion.
4. Capable of anchoring at the target location.
5. Quick, easy and safe to both locate and deploy.

In this research, an innovative design was envisioned based on the ideal device characteristics; experienced physicians' feedback and the study of uterine anatomy. All the subsystems and their components were identified during device specification. The identified mechanical occlusion device comprised of three major systems:

1. An occlusion implant for blocking of the fallopian tubes.
2. A guiding system for guiding and placing the implant.
3. A delivery actuator for deployment and release of the implant.

The block diagram of the system is shown in Fig. 3.2. This mechanical device for female sterilization includes an implant for occlusion of fallopian tubes, a guiding system comprising of both guide tube and wire for guidance of implant through the cervix and an actuator handle to deliver and deploy the implant into the fallopian tube.

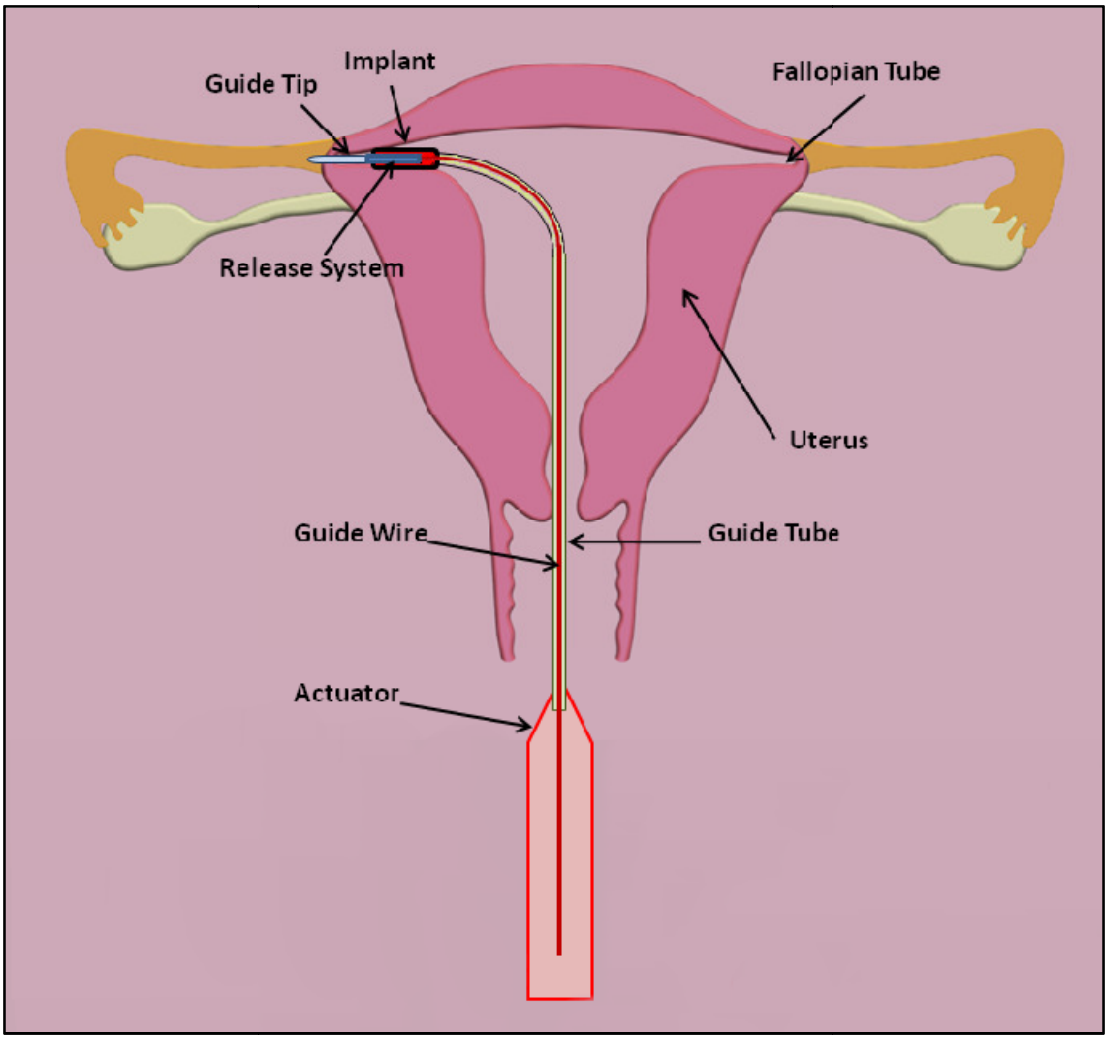

FIGURE 3.2: BLOCK DIAGRAM OF THE MECHANICAL OCCLUSION DEVICE

3.4. FEA AND OPTIMIZATION METHODOLOGIES

In this research work, the CAD software was used for the visualization of conceptual design and generation of 3D model. In order to arrive at the final design in a minimum time was a challenging task. To meet this challenge, the requirement of integrated FE simulations and optimisation become an imperative focus. In traditional FE techniques, the designer has had to go back to Computer Aided Design (CAD) system for remodelling. These back and forth modifications in the CAD and FE models are a time consuming process. Therefore, the requirement was to use a methodology, which can integrate the 3D CAD model with FEA tools for simulations and optimisation. This study was performed to devise a method that could be used throughout the research process for FEA simulation and optimisation of the device. This section gives an insight of integrated FEA and parametric design optimisation process using existing capabilities of various FE tools and their validation against standard non-integrated methods.

3.4.1. INTEGRATED FEA AND PARAMETRIC OPTIMISATION METHODOLOGIES

In integrated FEA and parametric optimisation (IFPO), the transfer of parametric model among different software carried out by manual work is eliminated by using the FEA tools in integrated mode with CAD system. Initially the emphasis was to integrate Pro/E with ANSYS and to use parametric modelling of Pro/E as an input for ANSYS optimiser. The interface between Pro/E and ANSYS was established successfully by installing module ANSYS connection for Pro/E. The model generated in Pro/E was imported successfully into the ANSYS environment. However, it was found that the parameters defined in Pro/E could not be transferred directly into ANSYS. Therefore, a parametric model of Pro/E could not be used by ANSYS for optimisation purpose. Consequently, the approach to use FEA tools in integrated mode for FE simulations and parametric optimisation were implemented. Therefore, two different FEA software were opted for that could be used in integrated mode with Pro/E Wildfire 2.0 to create an integrated environment [141]. Both the FEA software ANSYS WB ver. 11.0 and Pro/Mechanica Wildfire 2.0 were chosen for this study as both have already developed optimisation modules and they can be used in integrated mode with Pro/E.

A. INTEGRATED FEA AND PARAMETRIC OPTIMISATION USING ANSYS WB

ANSYS WB provides a module called DesignXplorer for design optimisation and understanding the analysis response of parts and assemblies [116]. Therefore, in the first methodology, DesignXplorer was used for IFPO. The idea behind using DesignXplorer was to use its powerful capabilities of importing a model from Pro/E and implementing a chosen design change back into the original model. Using this methodology the designer can generate the parametric model in Pro/E, which can be integrated, with ANSYS WB by linking the geometry file (Pro/E model) from ANSYS WB environment. This linking process transfers the design parameters of Pro/E geometry into the parameter manager of ANSYS WB design modeller. Once there, these integrated design parameters can be used anywhere in the other modules of ANSYS WB. Material properties and boundary conditions can be defined from the simulation module within ANSYS WB environment. DesignXplorer can be launched after defining the analysis in the simulation module. It uses statistical methods for optimisation which allows the designer to reach the optimised design in a very short time thereby reducing the design cycle time and increasing the productivity of analysts and designers. Therefore, a deterministic approach can be used to study the sensitivity of the design variables. This approach is based on Design of Experiments (DOE) and uses input, response and derived parameters for optimization [19]. In the next step, upper and lower limiting values can be assigned to parameters leading to the generation of Automatic Design Points (ADP). Based on ADP, the response of maximum von-Mises stress with respect to design variables can be plotted and reviewed to narrow the limits of design variables. After reviewing the ADP, the best feasible design point can be selected. Goal driven optimisation can be performed based on ADP study that uses a calculated set of sample design points [116]. A candidate design based on current goals can be generated and the best candidate design can be selected and inserted as a soft (preliminary) design. The best candidate design can be used to generate the hard reference design and by performing FEA analysis in ANSYS WB environment. Finally, the reference design point can be rated and the current (optimum) parameter values for the best design can be automatically updated from the DesignXplorer into the parameter manager, consequently updating Pro/E model. A final analysis can be performed in the WB environment to verify the results obtained from the design optimisation.

B. INTEGRATED FEA AND PARAMETRIC OPTIMISATION USING PRO/MECHANICA

In this methodology, Pro/Mechanica is used in integrated mode with Pro/E to achieve an optimal solution. Pro/Mechanica is a simulation tool that can be used to simulate the physical behaviour of a part or assembly to improve the mechanical performance of a design [142]. In this methodology, the simulation functionality of Pro/Mechanica is combined with the parametric solid modelling of Pro/E to automatically optimise the design that meets the specific performance criteria and goal. The parametric model can be generated in Pro/E as defined earlier, after which Pro/Mechanica can be launched from within the Pro/E environment so that it can be used in integrated mode. Material properties and boundary conditions can be assigned from Pro/Mechanica environment. A base line analysis can be performed to define the optimisation and sensitivity study. The design parameters are created and their limits are defined in the Pro/Mechanica design controls in order to make them available for optimisation. Multi-pass adaptive method with increasing polynomial order can be used for convergence. Global sensitivity analysis can be performed to study the behaviour of design parameters and in this study, the design variables can actually be swept through their full range in a specified number of steps. The results can be analyzed by plotting the variation of design parameters against von-Mises stresses that depicts the sensitivity of the variables on the design. Finally, the optimisation study is defined by applying constraints on state variable, defining initial and limiting values of design parameters and objective of the study. After launching the optimisation process, the optimal configuration can be accepted and all the values of optimum design parameters can be automatically updated in the Pro/E model resulting in optimised geometry and associated deliverables. A final analysis of the optimised geometry may be performed and the results can be reviewed.

3.4.2. NON-INTEGRATED FEA METHODOLOGIES FOR VALIDATION

Two different non-integrated optimisation techniques were performed to validate the results obtained from IFPO methodologies. Already established optimisation techniques were used for validation purpose. In the first validation technique, parametric modelling and optimisation was performed using the FEA software, ANSYS ver. 11.0. The optimisation capability in ANSYS is a powerful tool that is used to determine the optimum design variables without compromising the performance of a product

[143,144]. Fig. 3.3 outlines the standard optimisation cycle used by ANSYS for evaluating an optimum design.

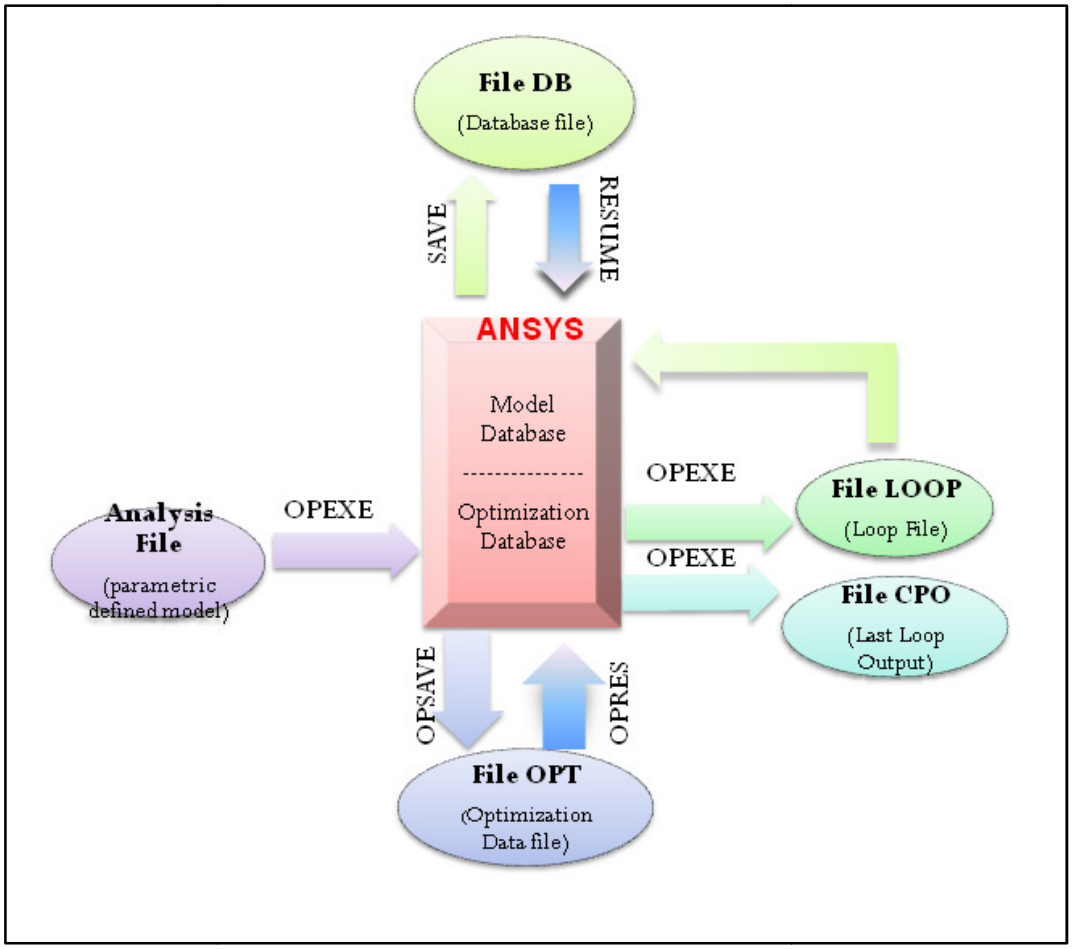

FIGURE 3.3: ANSYS OPTIMISATION CYCLE

The second validation technique was also conducted using ANSYS ver. 11.0. In this case, optimisation was performed manually through various iterations using the ANSYS solver. Since optimisation requires systematic modification of part geometry, a robust and parametric model needs to be constructed using a "bottom-up" modelling approach. The keypoints, lines, areas and volumes can be constructed using parameters and can be entered through ANSYS command-line. The usage of command-line can be helpful to build a clean log file that can be used during iterations for modifications of 3D geometry. The results obtained after every step are interpreted manually and changes are made in the design variables to prepare the geometry for the next iteration.

3.4.3. FINALIZED METHODOLOGY FOR FEA AND OPTIMISATION

The benefit of integrated parametric optimisation has been presented in this work by demonstrating the use of ANSYS WB and Pro/Mechanica in integrated mode. The main advantage therefore of using IFPO is that it eliminates all the protracted work of manual modifications in a 3D model and its associated deliverables thereby ultimately leading to a reduction in design cycle time. Secondly, the design cycle time can be further reduced as the manufacturing data pack can be generated in parallel with optimisation process.

Two case studies were solved to demonstrate the IFPO (detailed in Appendix A). In these case studies, two different methodologies for IFPO were used in which two FEA tools were used in integrated mode with a CAD system. In the first methodology, ANSYS WB was used in integrated mode with Pro/E and for the second methodology Pro/Mechanica was integrated with Pro/E. Proposed optimisation techniques were assessed against established techniques of optimisation using ANSYS optimiser and optimisation by manual iterations. The results obtained from IFPO were comparable with validation methodologies. In both case studies optimisation variables were successfully transferred between Pro/E and the optimisation tools (ANSYS WB and Pro/Mechanica) leading to an automated optimisation. After optimisation in both case studies, the max von-Mises stresses were within limits and the geometry of the model was within desired values. However, it was observed from the results that ANSYS WB achieved more mass reduction even though it uses statistical techniques for optimisation.

It was observed during this study that ANSYS WB produces comparative results for both FEA simulations and optimisation. In addition, the ANSYS WB optimisation is based on design of experiment, which minimizes the optimisation time. Therefore, it was reasonably assumed that ANSYS WB could be used for both FEA and design optimisation of device components generated in Pro/E software, without compromising the results by a reduction in design cycle time. Throughout this research work, it was decided to use the ANSYS WB for both FEA and design optimisation of the device.

3.5. HYSTEROSCOPIC EQUIPMENT

The hysteroscope is one of the major components of the equipment used in hysteroscopy. The hysteroscope is a small telescopic type apparatus, which has an optical system connected to a video camera, a light bearing system with fiberoptics, and a channel for delivery of the device. The video hysteroscopy system used in this research is shown in Fig. 3.4.

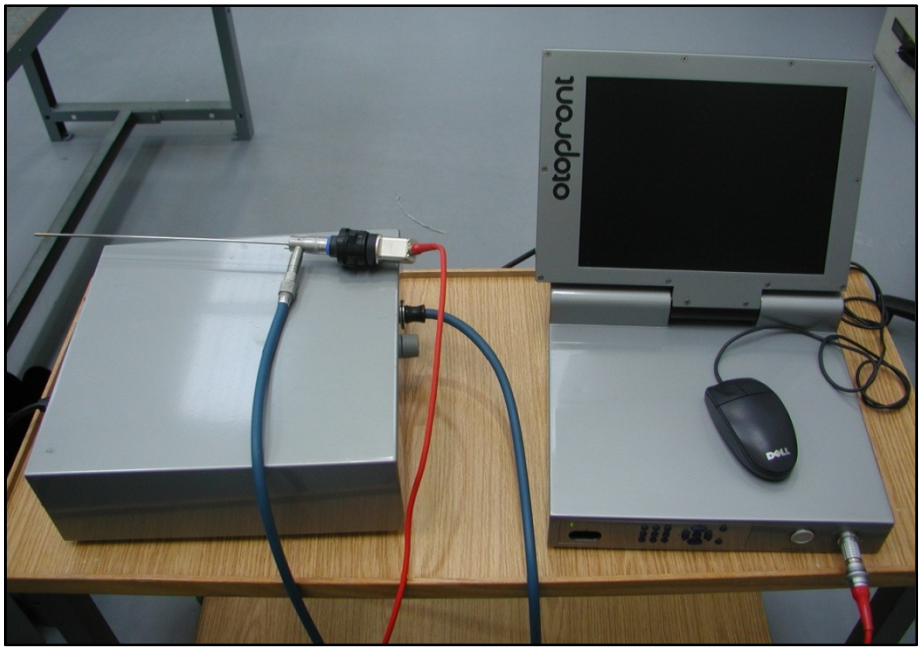

FIGURE 3.4: VIDEO HYSTEROSCOPY SYSTEM

3.5.1. HYSTEROSCOPY DESIGN CONSTRAINTS

The first step to begin the design of the occlusion device was to investigate the type of hysteroscopes being used in transcervical occlusion systems. For this purpose, following gynaecologists were consulted:

- Dr. Micheal Gannon and Dr. Nina Adran of Midland Regional Hospital, Mullingar
- Dr. Rona Gleeson of Rotunda Hospital, Dublin
- Dr. Andreas L. Thurkow and Dr. John Dowson of St Lucan Andreas Hospital, Amsterdam

It was found from these discussions and literature surveys that 5 French (F) hysteroscopes are the preferred choice for such procedures

[12,14,90,100,103,106,145,146,147,148]. Two of the most common types of hysteroscopes in use were dimensionally and geometrically analysed. The working channel of these hysteroscope was one of the constraints in designing and sizing the occlusion implant and its delivery system. The hysteroscopes used in this research for designing the device and performing explanted uterus studies are discussed below:

a) OLYMPUS A4674A 30^{o} (Germany)

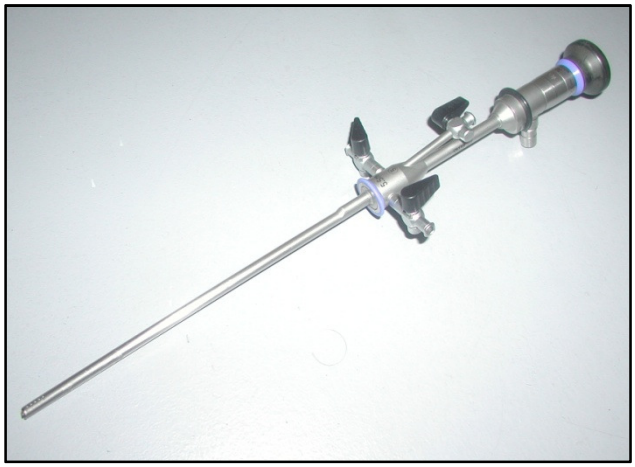

FIGURE 3.5: OLYMPUS A4674A HYSTEROSCOPE

This Olympus A4674A hysteroscope shown in Fig. 3.5 is the most popular hysteroscope used for hysteroscopy and delivering of various occlusion devices including the ESSURE® device. This hysteroscope has a diameter of 5.5 mm, a 5 F (1.63 mm) operative channel and a 186 mm length for delivery of devices.

b) KARL STORZ 26161 BN (Germany)

The Karl Storz 26161hysteroscope shown in Fig. 3.6 has a 3.7x5 mm sheath, a 5 F (1.665 mm) instrument channel and a 178 mm length for delivery of devices.

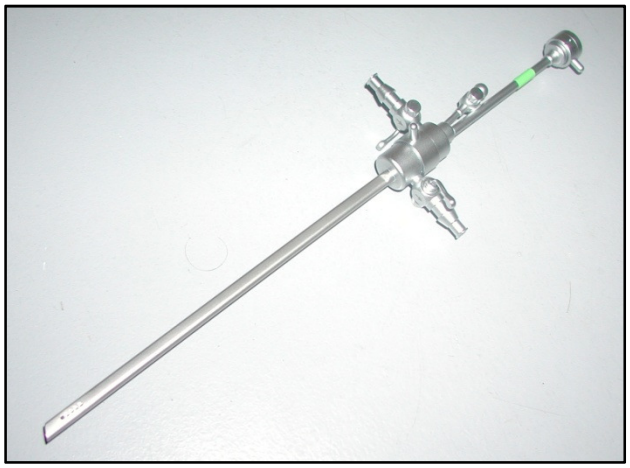

FIGURE 3.6. KARL STORZ 26161 HYSTEROSCOPE

3.6. DEVELOPMENT AND TESTING APPROACHES

In order to finalize the design of a medical device vigorous testing as a part of design verification and validation is required. Therefore, experimental testing in conjunction FEA simulation was used to achieve the optimum design and first prototype of the device. Various state of the art fabrication, testing and inspection techniques were used during this research work to evaluate and finalize the design of the occlusion device.

3.6.1. LASER CUTTING

Due to the miniature size of some of the device components which included features having dimensions at the µm level, the manufacturing was impossible with standard mechanical manufacturing techniques. They proved also intricate to machine because of the softness of the light walled SS-316LVM tubing. In view of this, a laser (light amplification by stimulated emission of radiation) cutting system provided a fabrication alternative down to µm level. A specialized laser-cutting machine (LPL Stent Cutter) was employed for cutting all the intricate components. The LPL Stent Cutter used in this research work shown in Fig. 3.7, was available at Vasorum Ltd., and was accessible throughout the research duration. This machine is equipped with a power supply, a computer control panel, a coolant pump and system, an oxygen supply and charged coupled (CC) vision system. The cutting specifications used on this machine are detailed in Table 3.1. This machine uses a pulsed Nd: YAG (neodymium: yttrium aluminium) beam source for precision cutting. It has longer focal length lens for excellent beam quality, which minimizes taper in the cut (LPL Systems, Inc.). This assures a high cutting quality, which is characterized by narrow cuts and near parallel gap edges. The other advantage of this fabrication method is that it was gentle on the extremely small wall thickness fragile tube of annealed SS-316LVM. As a result, the components fabricated on this machine, were extremely precise within a linear accuracy of 2.54 µm and angular accuracy of 0.028^{o}.

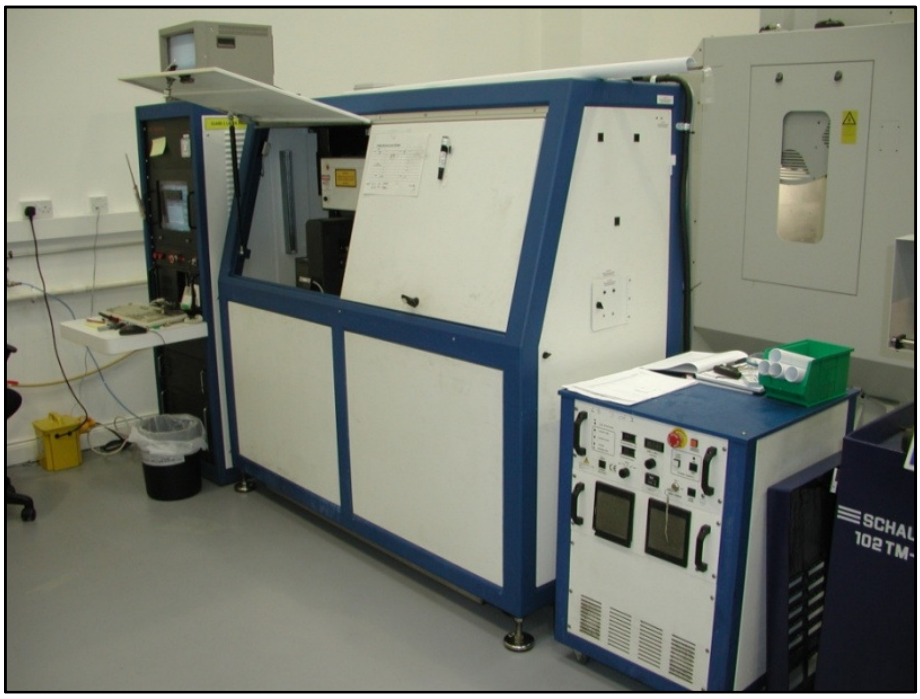

FIGURE 3.7: LPL STENT CUTTER

TABLE 3.1: SPECIFICATIONS FOR LPL STENT CUTTER

Voltage (V)	220
Frequency (Hz)	50
Current (A)	15
Average power (W)	50
Pulse energy (mJ)	130
Pulse frequency (Hz)	1000
Pulse interval (ms)	11
Pulse width (ms)	0.1
Spot size of beam (µm)	6

LASER CUTTING PROCEDURE

Prior to the laser cutting process, CAD data of the component with the desired configuration is generated. In order to generate the CNC program for laser cutting, the coordinate points of the component profile are imported from Pro/E. For the cutting process, the desired SS tubing with specified OD and thickness is prepared and installed into the tube. To grip the tube in the laser machine the respective size of collet and bush insert is assembled in to the machine. The tube is then gripped with this single collet and supported by a bush insert as shown in Fig. 3.8. The width of the laser is adjusted according to the width of the required slot i.e. 0.06 mm for the implant's slots. The focal point of the beam is centred on the tube and verified by a charged coupled device (CCD) attached to the laser head. Straightness of the tube is also ensured using this CCD vision system by gradually turning and linearly moving the tube. Optimised parameters used for the laser cutting process of the SS tubes are illustrated in Table 3.2. The CNC program for the implant is loaded into the software of the laser-cutting machine. During operation of the machine, the laser power and the chiller (cooling system for laser lamp) are switched on. The oxygen gas with a pressure of 6–8 bars is pumped in from a cylinder to assist laser-cutting process. The CNC program is run and the component is cut with an interpolation of rotary and linear movement of the tubing relative to the laser.

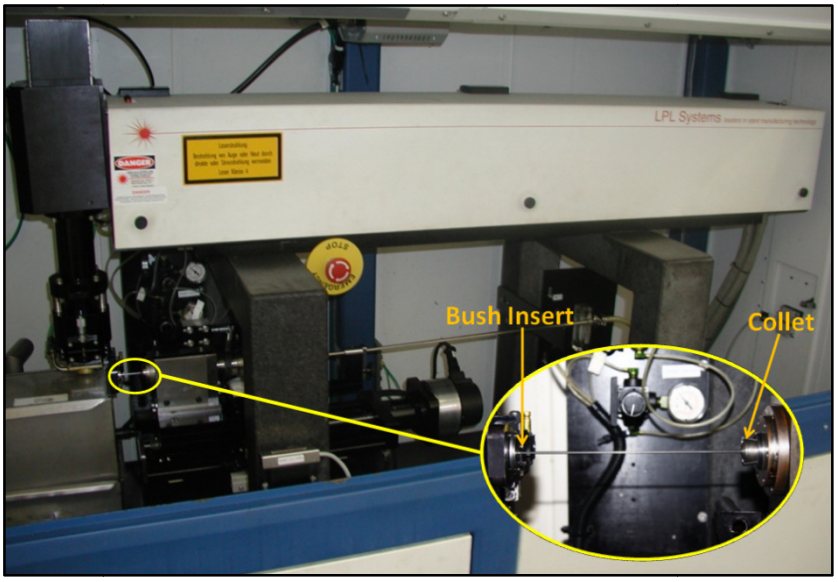

FIGURE 3.8: ASSEMBLED TUBE IN LASER CUTTING MACHINE

TABLE 3.2: CUTTING PARAMETERS FOR VARIOUS SS TUBINGS

Parameters	Thickness	
	0.1 mm	**0.125 mm**
Frequency (Hz)	50	50
Pulse Interval (ms)	11	11
Pulse width (ms)	0.1	0.1
Pulse energy (V)	180	192

3.6.2. LASER WELDING

In order to join miniature components with µm level accuracy there was no other choice other than to use laser welding. Therefore, a Rofin SWMP/B2432 micro welding machine (Fig. 3.9) available at Vasorum Ltd. was used during this research work to weld the device components. This machine is able to produce the finest welding, with diameters from 100 µm up to 2.5 mm. The specification of this machine is detailed in Table 3.3. The welding specifications used for welding various components are described in Table 3.4.

FIGURE 3.9: ROFIN SWMP/B2432 LASER WELDER

TABLE 3.3: ROFIN WELDING MACHINE SPECIFICATIONS

Parameters	Value
Type	Nd:YAG
Wavelength	1064 nm
Power	60 W
Energy	110 J
Voltage	230 V
Frequency	50/60 Hz

TABLE 3.4: MACHINE SETTINGS FOR WELDING

Thickness (mm)	Voltage (V)	Pulse Duration (mS)	Frequency (Hz)	Power (J)	Power Density (J/ cm^2)
0.1	225	1.7	2.1	0.87	481.8
0.125	230	2.0	2.1	1.15	611.6

3.6.3. CNC MACHINING

In order to fabricate highly accurate device components a combination of CNC lathes and CNC milling machines were used. The accuracy and repeatability in the device components were required in order to achieve the accurate displacements for implant deployment.

A. MICRO CNC LATHE

A Schaublin 102 TM-CNC was used for fabrication of the miniature implant core shaft and the actuator components including pawl pin, grub screws and assembly pins. This machining facility is shown in Fig. 3.10.

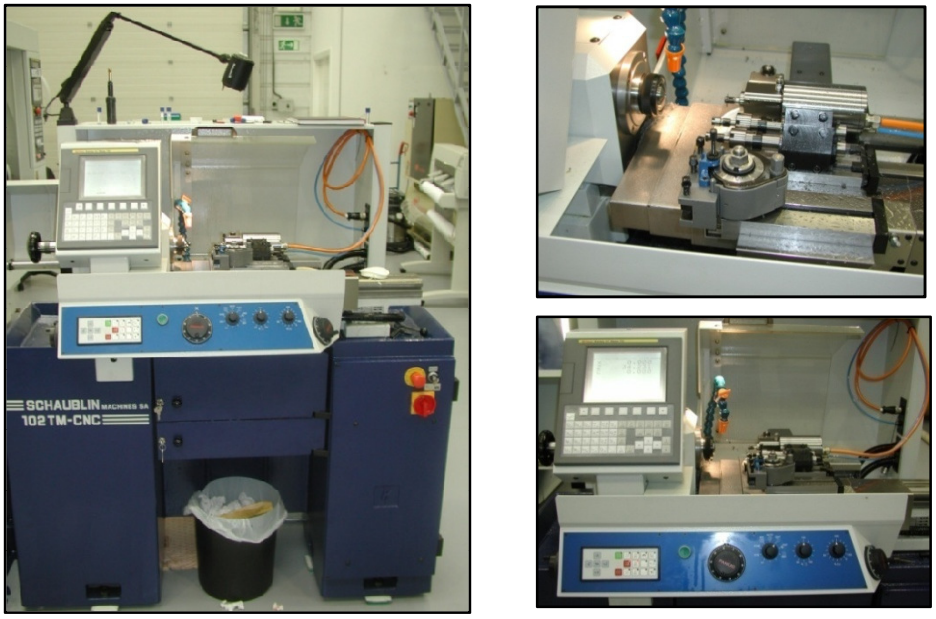

FIGURE 3.10: SCHAUBLIN 102 TM-CNC

B. CNC LATHE

Most of the actuator components were machined on a high precision Schaublin 140-CNC lathe. This machine with an accuracy of 0.001 mm is shown in Fig. 3.11.

FIGURE 3.11: SCHAUBLIN 140-CNC LATHE

C. CNC MILLING

A Schaublin 48 V vertical milling machine (Fig. 3.12) was used for performing milling operations on some of the actuator components.

FIGURE 3.12: SCHAUBLIN 48 V

D. ELECTRICAL DISCHARGE MACHINING

Electrical Discharge Machining (EDM) uses spark erosion to machine or remove material with an electrode from any electrically conductive work piece. If a travelling wire electrode is used for EDM machining it is called Wire EDM. The wire electrode usually consists of brass or zinc-coated brass material. The *ONA PRIMA E250* wire EDM shown in Fig. 3.13 was used in this research work is available at the school of mechanical and manufacturing engineering workshop. This EDM was used for the machining of the ratchet and release wheels used in the actuator handle.

Alternately, when a machined electrode is used to produce sparks along the surface of the electrode to sink or plunge the cavity, a Sinker EDM machine is employed. It is used to machine blind cavities which are difficult or impossible to mill. This machining technique was used to machine cavities in some of the actuator components. The EDM machining was performed at the DCU mechanical engineering workshop using *ard Pulse P50* shown in Fig. 3.14.

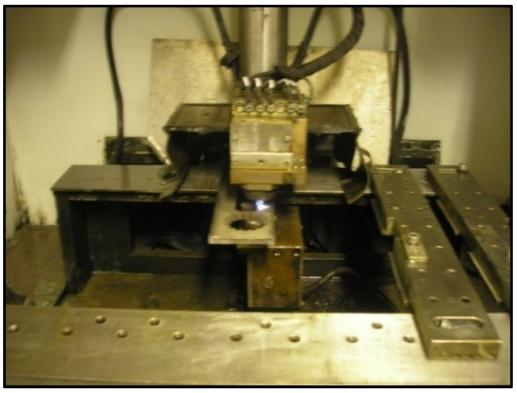

FIGURE 3.13: ONA PRIMA E250

FIGURE 3.14: ARD PULSE P50

3.6.4. LABORATORY OVEN / FURNACE

A Gallenkamp laboratory oven was used to recover heat shrink on the delivery tube. The 500ºC oven can be used in programmed or manual mode. The oven shown in Fig. 3.15 was used to provide the required recovery temperature of 340ºC to the PTFE heat shrink.

FIGURE 3.15. LABORATORY OVEN

3.7. TESTING AND VALIDATION

Numerous tests were performed to validate the design of the sterilization device. The various testing equipment used during this validation process are discussed briefly below:

3.7.1. TENSILE, COMPRESSION AND SPRING TESTING

In this work, tensile, compression and spring testing were carried out on various device components at room temperature. For this purpose a universal testing machine by Lloyd Instrument Ltd. shown in Fig. 3.16 was used. This machine can work under complete computer control and is loaded with NEXYGEN™ MT software that provides virtual testing and data analysis. The software offers a full complement of testing categories with multiple test types within each category complying with industry and international testing standards. The NEXYGEN software presents test results in both tabular and graphical formats.

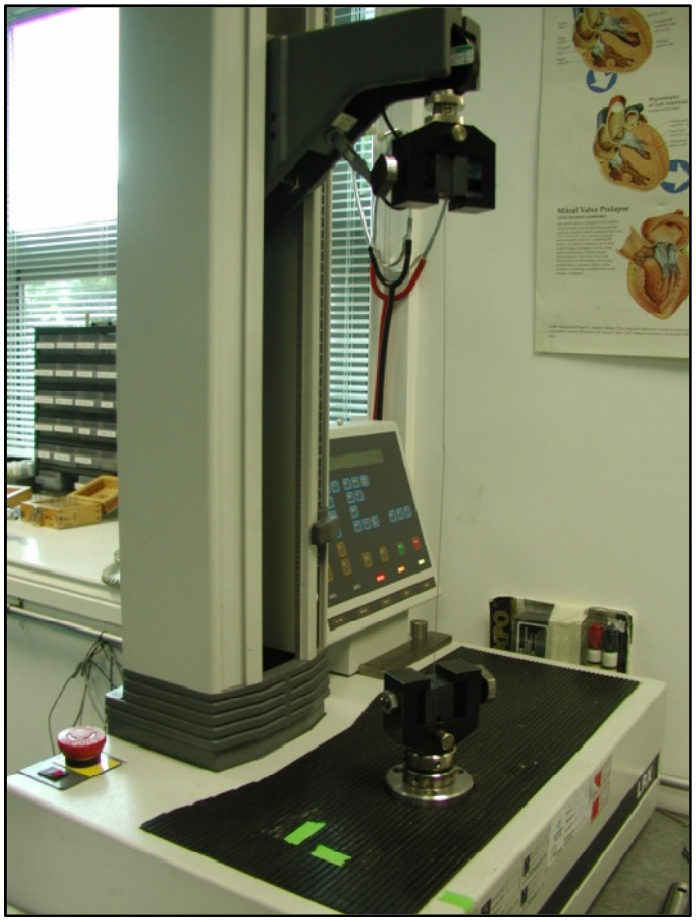

FIGURE 3.16. LLYOD UNIVERSAL TESTING MACHINE

3.7.2. TORQUE MEASURING EQUIPMENT

As a part of the research, torque measurements and validations were required at various stages. An IMADA portable torque measuring equipment shown in Fig. 3.17 was used for this purpose. It has a capacity of 200 N-cm with an accuracy of ±0.5%. It is equipped with a digital display that includes peak-hold function, comparator function and a memory function.

FIGURE 3.17: TORQUE MEASURING EQUIPMENT

3.7.3. VIDEO INSPECTION

Because of the delicacy of the device especially the occlusion implant, the inspection of the device was performed using a video inspection system by Deltronic, DVC-110 shown in Fig. 3.18. The DVC-110 provides precise, non-contact three-axis measurement capability with a 50mm x 50mm x 100mm (X x Y x Z) travel stage. It is equipped with a geometric digital readout and CCD display. The DVC-110 combines a wide variety of quality features and options from standard visual optical comparators to the high magnification of a toolmaker's microscope while providing X-Y-Z readout capability of 0.001 mm. All the dimensional inspections and profile measurements were performed on this video inspection system.

FIGURE 3.18: VIDEO INSPECTION PROBE, DELTRONICS

3.7.4. OPTICAL STEREO MICROSCOPE

Visual inspections of the miniature components for µm level accuracy were inspected using a Leica stereo microscope shown in Fig. 3.19. It is equipped with a modular camera system for the professional displaying and recording of digitized images and a high end software with easy-to-use functions for inserting and editing images as well as image management software for archiving, processing and analysis. Images can be transferred to and from Adobe PhotoShop, PaintShop Pro, Leica Image Manager or analysis systems.

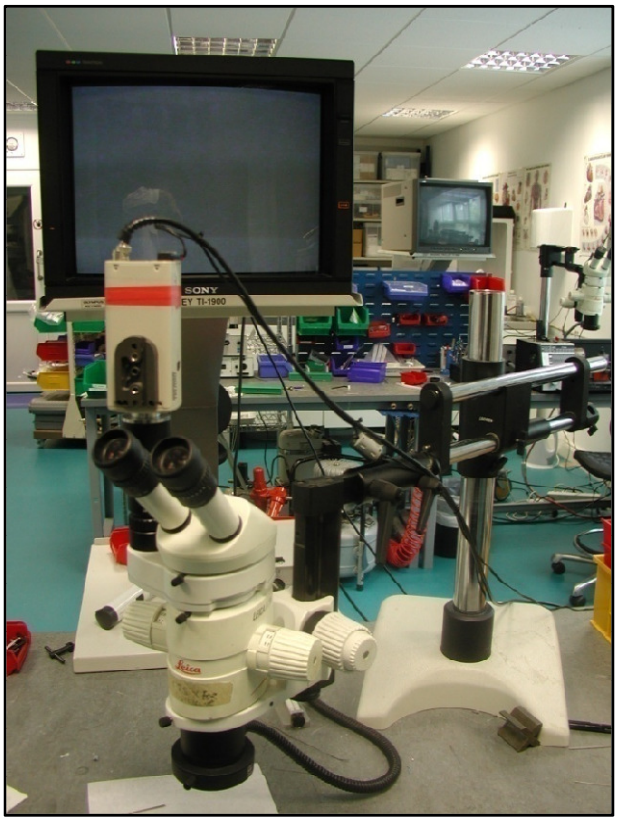

FIGURE 3.19. STEREO MICROSCOPE WITH MODULAR CAMERA

CHAPTER 4

DESIGN, DEVELOPMENT AND VALIDATION OF OCCLUSION IMPLANT

4.1. INTRODUCTION

Occlusion implant [149] is the implantable part of the device, which is designed to be deployed into the tubal ostium to block the fallopian tubes as shown in Fig. 4.1. The implant is permanent for the lifetime of the patient [150]. The occlusion implant consists of an implant body, a flexible guide tip, a core shaft and a release mechanism. This chapter presents the design, development and validation of the implant and the individual components.

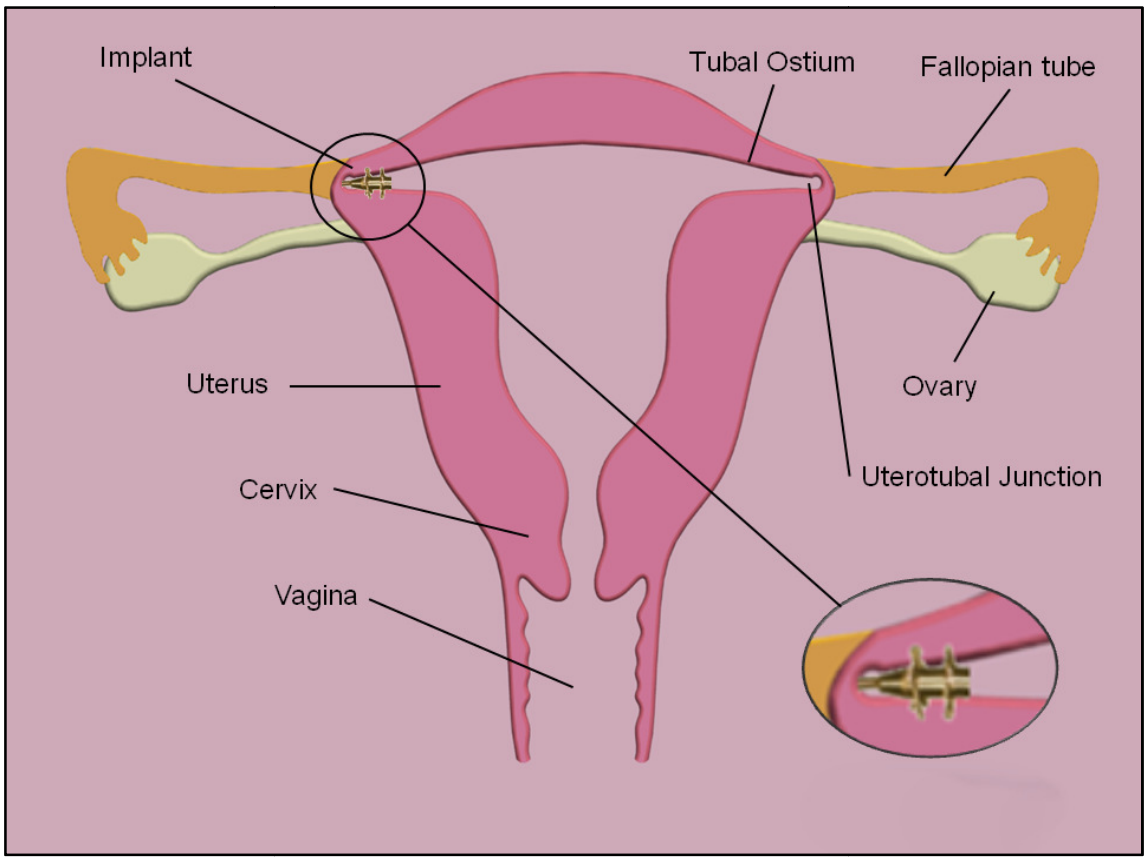

FIGURE 4.1: DEPLOYED IMPLANT AT THE LEFT TUBAL OSTIUM

4.2. CONFIGURATION OF OCCLUSION IMPLANT

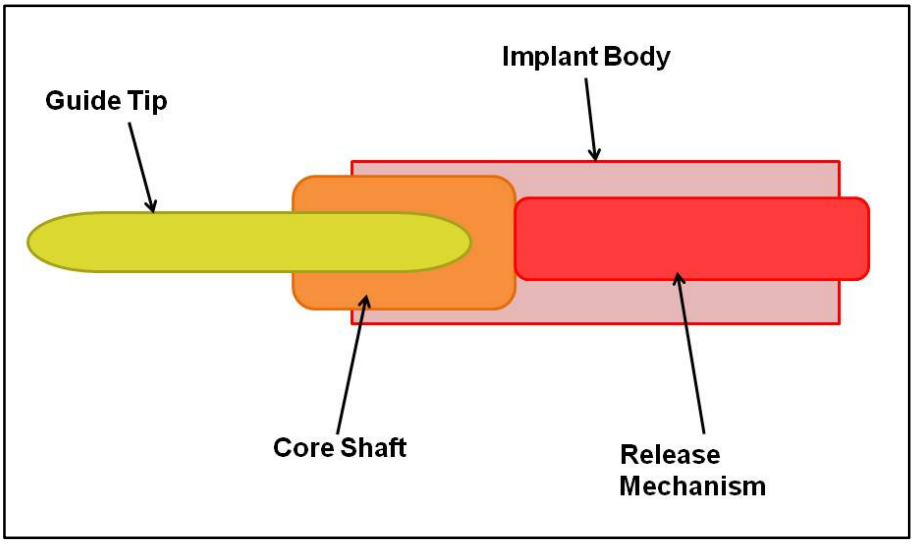

FIGURE 4.2: BLOCK DIAGRAM OF OCCLUSION IMPLANT

As shown in Fig. 4.2 the occlusion implant comprises of following components

a) An implant body that actually occlude the fallopian tubes
b) A guide tip to guide the implant through the tortuous paths of uterus
c) A release mechanism to release the implant from the delivery system following deployment
d) A core shaft to interface the implant with both the guide tip and the release mechanism.

All of the above mentioned components of the occlusion system were individually designed, developed and validated.

4.3. DESIGN, DEVELOPMENT AND VALIDATION OF IMPLANT

Starting from the conceptual design, this section details the complete design, development phase and validation of the implant.

4.3.1. IMPLANT'S CONCEPTUAL DESIGN

In order to achieve the ideal implant attributes, the following concepts were envisioned based on both feedback from experienced gynaecologists' and physicians' and the study of uterus anatomy and existing devices:

1. A cylindrical shape would be the best possible low profile shape that could be introduced through the instrument channel of a hysteroscope.

2. A diameter less than 1.665 mm that could be delivered through a 5F hysteroscope.
3. Prongs on the surface of the cylindrical body that could provide anchoring at the target location.
4. Sandwiching of tubal ostium tissue in between two set of prongs to provide an instant occlusion.
5. Can be safely and efficiently deployed through a hysteroscope using an actuator.

It is detailed in literature that most of the transcervical sterilization devices failed because of device expulsion due to uterine spasm [77]. Therefore, an innovative design based on a cylindrical metallic implant with two set of wings or prongs on its surface presented itself as the most feasible solution. The most challenging task however was to design a device that could transform the cylindrical body into an implant capable of anchoring into the tubal ostium and thereby providing an instant occlusion of the fallopian tube.

It is known from the dynamics of thin cylindrical shells, that a cylinder body can be deformed into another shape by application of axial compressive force. Such buckling of the cylinder shell however was not desirable [151,152,153]. It is also recognized that controlled buckling in a cylindrical shell with known imperfections can be achieved under axial loadings [154]. These imperfections could be the out-of-plane displacements or slots at preferred portion of cylindrical shell. Such a common example in everyday life is of rawl plugs.

Pre-generated out-of-plane displacement in the cylindrical implant can however increase the implant's effective diameter. This makes it difficult to be inserted from a small calibre 5 F hysteroscope. Therefore, the requirement was to generate an out-of-plane displacement in the implant body at the target location.

Hence, an out-of-plane displacement followed by compression was required for the cylindrical shell implant to achieve the desired shape. It was obvious from engineering intuition that torsion creates an out-of-plane displacement in thin cylindrical shells. Such deformation in cylindrical shell has been described by various researchers [155,156,157,158]. Kumosa et. al. has mentioned that an out-of-plane deformation is observed near the cracks of a cylindrical shell under torsion [159].

In this research, it was envisaged from previous experience of mechanical design that a cylindrical body with pre-defined cracks can be deformed in to a desired shape. Therefore, a thin cylindrical shell having pre-defined slots could be deformed into the shape of the desired implant by application of both torsion and compression loadings. The next step was to establish the shape of the slots, which under torsion could produce an out-of-plane displacement and after compression, deform into desired wing shape. It was also thought that two set of wings on the implant body would provide better design. The first set of wing would provide anchoring and the second set of wing would entrap tissue in between the wings.

The outcomes of the conceptual design phase of the implant were:

1. The implant should be a thin cylindrical shell with a diameter of less than 1.665 mm.
2. It would contain slots on its body, which would displace outwards by application of torque.
3. The outward displaced slots would be compressed under axial loads to form a set of wings.
4. Two set of wings would be designed on the implant's body to anchor and entrap the tissue of the tubal ostium.
5. The wings would be individually deployed to get better deployment control.

4.3.2. IMPLANT MATERIAL

The implant is implanted into the human body and has to remain there throughout the patient life. Therefore, it was necessary to use a biocompatible material for this purpose. The term 'biocompatibility' may be simply defined as the ability of a material to be accepted by the body. Since all materials potentially generate a 'foreign body reaction' when introduced into the body, the degree of biocompatibility is related to the extent of this exposure. Therefore, biocompatibility is directly related to the corrosion behaviour of the material in a specified solution and the tendency for the alloy to release potential toxic ions. The most suitable material to fabricate biomedical implants is Stainless Steel 316LVM. The chemical composition of this material is detailed in Table 4.1. The deployment of the implant is a complex phenomenon. During implant deployment, the implant must undergo plastic deformation to ensure that it remains in its deployed configuration and occlude the fallopian tube. The most suitable material condition for

such type of deformations is an annealed form, which is a softer and more ductile material as compared to normalized SS-316LVM. It was described as an isotropic material, which follows a straight line in the elastic region. When the stress reaches the yield stress, the material no longer exhibits elastic behaviour and the stress-strain behaviour becomes non-linear. A bilinear isotropic hardening rule was adapted to describe the mechanical properties of the material. The tangent modulus defines the work-hardening slope, which relates the incremental stress to incremental plastic strain in the inelastic region and dictates the conditions of subsequent yielding. The stress-strain curve of the material was described by mechanical properties detailed in Table 4.2.

TABLE 4.1: CHEMICAL COMPOSITION OF SS-316LVM [165]

Elements	**Symbol**	**Percentage**
Carbon	C	0.030 %
Chromium	Cr	17.0 %
Iron	Fe	65.0 %
Manganese	Mn	2.0 %
Molybdenum	Mo	2.50 %
Nickel	Ni	12.0 %
Phosphorous	P	0.045 %
Silicon	Si	1.0 %
Sulphur	S	0.030 %

TABLE 4.2: MECHANICAL PROPERTIESOF SS-316LVM [160]

Material	**Young Modulus *E* *(GPa)***	**Poisson Ratio *v***	**Yield Strength σ_y *(MPa)***	**Tensile Strength *UTS (MPa)***	**Tangential Modulus E_t *(GPa)***
SS 316-LVM (Annealed)	193	0.3	286	560	2.5
SS 316-LVM (Hardened)	193	0.3	690	860	8.9

4.3.3. DESIGN EVOLUATION OF IMPLANT'S SLOTS

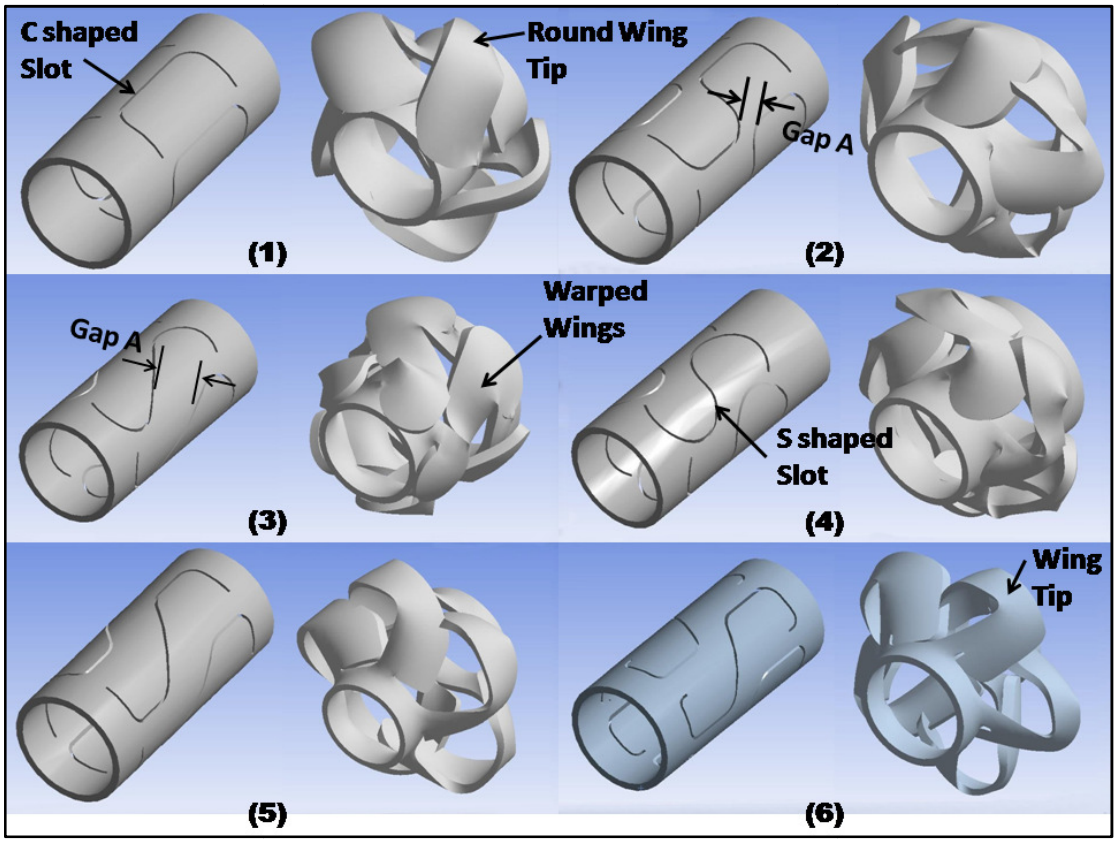

FIGURE 4.3. DEVELOPMENT OF SLOT PROFILES TOWARDS FEASIBLE WING FORMATION USING SIMULATION

Designing an implant described in the conceptual design section through prototyping and experimental testing is time consuming and expensive. Therefore, FEA simulation in conjunction with experimental testing was used to achieve the preliminary design of the implant. First, the conceptual 3D model of the implant was generated using CAD software, Pro/E. Then the implant deployed shape was predicted using integrated FEA simulations. FEA simulations were performed to evaluate the shape of slots, transformable into flat wings, capable to anchor, able to penetrate and trap the tissue in between. Based on the diameter of the implant, five slots were incorporated in the conceptual design to create a five wing shapes. Fig. 4.3 shows six sequential iterations of the shape of the slots that were analysed for this conceptual design phase. As there was no pre-defined design of the slots or implant, a primitive geometry ("C" shaped slot) was selected as a starting point for slot design as shown in Fig. 4.3 (1). After performing FEA simulation it was observed that the formed wings on the implant surface were warped and had rounded wing tips. After animating the simulation results of the C shape slots and closely examining the implant's deformed shape, it was

inferred that a “S” shape could be a better profile for this purpose. Two different S shape profiles were simulated shown as iteration 2 and 3 in Fig. 4.3. After comparing results of both these simulations it was found that the inter slots gap determines the shape of wings tip and the force to deploy the wings. This gap is mentioned as “Gap A” in Fig. 4.3. The smaller the Gap A was kept, the more pointed the tip became. Therefore, different variants of “S” shape were tried to reduce this gap as shown in Fig. 4.3 (4-6). After simulating these profiles by keeping the slot shape and “Gap A” as design variables, a first feasible slot design was achieved. The shape of this feasible slot allowed adding another slot onto the implant. An additional slot (sixth) was added into the design in order to further reduce the Gap A. The first feasible design of the slots that determine the desired implant shape following deployment by formation of six wings is shown in Fig. 4.4. While analysing this slot shape it was found that pointed wings would form by application of torque in one direction and application of torque in the reverse direction reduces the slot gaps. Consequently the slots lock themselves at the zero gap position.

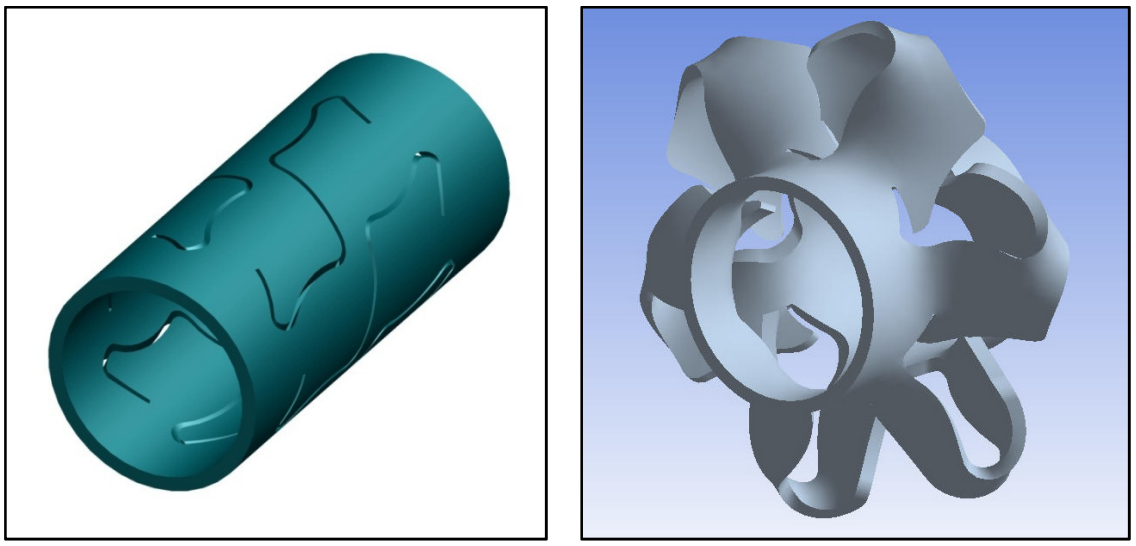

FIGURE 4.4. FIRST FEASIBLE SLOT SHAPE PRE AND POST DEPLOYMENT

4.3.4. IMPLANT’S PRELIMINARY DESIGN

As discussed in Section 4.3 (Conceptual design), two set of wings were required to entrap the ostium tissue in between thus occluding the entrance of the fallopian tube. It was also desired that each set of wings deploy individually. Therefore, two set of slots were introduced in the implant such that one set of slots was a mirror image of the other.

The preliminary design of the implant consisted of a thin cylindrical shell featuring two sets of six slots at both the distal and proximal segments of the implant (Fig. 4.5). These slots determine the implant's final shape following deployment by formation of two sets of six wings. A complete depiction of a deployed implant is shown in Fig. 4.6. The size of implant is chosen such that it can be delivered transcervically through a 5-Fr (1.665 mm) operative channel of a standard hysteroscope. The implant is designed to be positioned optimally in the intramural section of the fallopian tube. The implant is inserted in low profiled cylindrical form, through the working channel of the hysteroscope by mean of a flexible guide tube and inner guide wire. As the implant requires both torque and compression for deployment, the guide tube and wire therefore also serve the purpose of torque transmission and compression to the implant. Implant deployment is achieved in three phases. In the first phase, a counter-clockwise torque followed by a compressive force transforms the distal slots into six fully formed wings. The second phase comprises of a clockwise torque and compression to achieve deployment of the second set of six proximal wings. Finally, the third phase completes the deployment process by dispensing the implant from the guide wire and consequently the delivery tube.

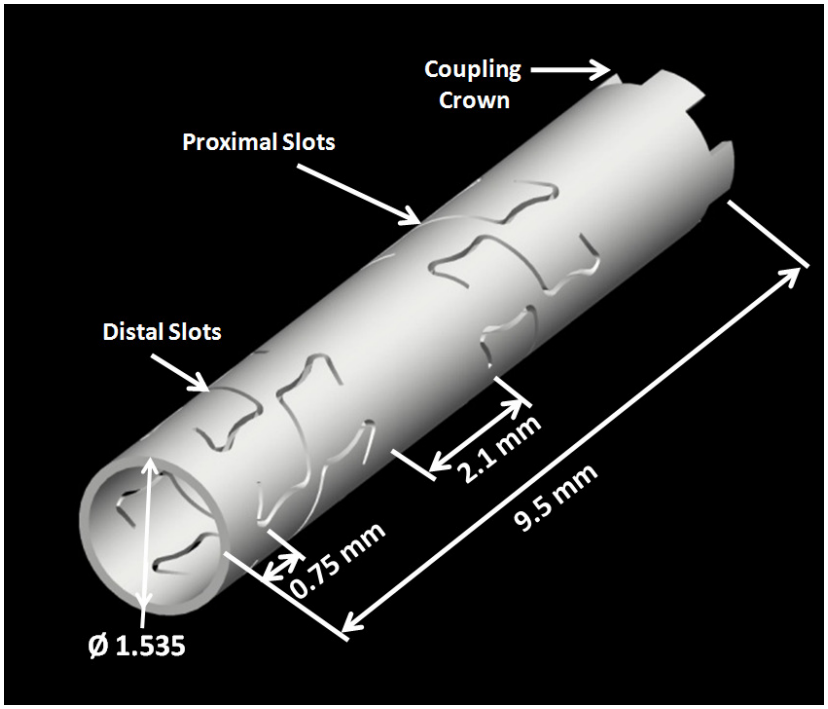

FIGURE: 4.5: PRELIMINARY IMPLANT PRE-DEPLOYMENT

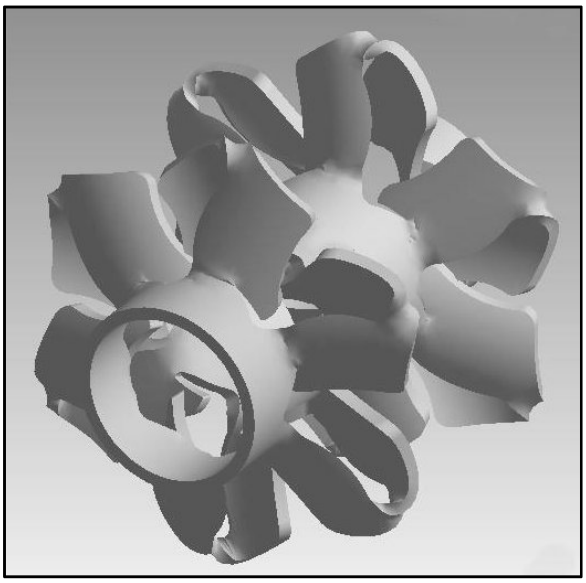

FIGURE: 4.6: PRELIMINARY IMPLANT POST-DEPLOYMENT

A. MODEL GEOMETRY

The 3D parametric model of the implant generated using Pro/E is shown in Fig. 4.5. The implant consists of an annealed SS-316LVM tube having an outer diameter of 1.535 mm and a thickness of 0.1 mm. It includes an inner release system, which includes a core shaft and release tube. The core shaft is a hardened SS-316LVM solid shaft, whose one end is laser welded to the distal end of the implant, and the other end attached to the guide wire. The hollow cylindrical shaped implant has two sets of slots at the distal and proximal segments and axial straight splines on the proximal end as shown in Fig. 4.5. The gap between the proximal and distal slots was 2.1 mm. Each set of slots comprises of six slots and both set of slots have a bilateral symmetry (mirror symmetry). The transformation from these slots into wings occurs via a two-step procedure; first torque followed by compression. Torque and compression are transmitted to the implant by a delivery actuator through a combination of a flexible guide tube and wire. The details of the guiding system and delivery actuator are discussed in chapters 5 and 6 respectively. The flexible guide tube is coupled with the implant through the straight splines and the guide wire is connected to the inner tube. Hence, the distal end of the implant is held by the guide wire and the proximal end by the flexible guide tube. Application of torque initiates the formation of wings by radially expanding the slots and compression concludes their formation by plastically deforming them to a final shape as shown in Fig. 4.6. As both sets of slots have bilateral symmetry, only one set of wings can be formed by applying torque in one direction. To deploy the second set of wings a torque applied in the opposite direction followed by compression

is required. The axial straight splines at the proximal end of the implant are used to couple the implant with the flexible guide tube and consequently to the delivery system. This 3D model of the implant was further used for FEA simulation and generating Computer and Numerically Controlled (CNC) program for laser cutting machine.

B. FEA SIMULATIONS

FEA simulations were performed to evaluate the shape of slots, transformable into flat wings, capable to anchor, able to penetrate and trap the tissue in between. In addition, the mechanical behaviour of complete implant with these finalized slots was simulated and analyzed.

ANSYS WB was used for FE simulations and analysis. The parametric model generated in Pro/E was integrated with ANSYS WB for FEA simulations [141,161,162]. The first objective of these simulations was to predict and investigate the slot profile. Therefore, to predict the slots profile the simulation of the whole implant was not required. Due to bilateral symmetry considerations, half of the whole model having one set of six slots was considered for simulations. Non-linear static analysis was performed in ANSYS WB in order to cope with large deflections and plastic deformations in the implant during its deployment. To simulate implant deployment, a bilinear isotropic hardening rule was adapted to describe the mechanical properties of the material. Material properties of annealed SS-316LVM were assigned in the ANSYS WB environment. Young's modulus E used for this material was 193 GPa, Poisson ratio υ was 0.3, yield strength σ_y was 286 MPa and the tangentional modulus E_t for the plastic hardening phase was 2.5 GPa. As mentioned in the "model geometry" section, the implant houses a core shaft and a release tube. The core shaft serves two purposes; firstly, it is an interface between the implant, release system and guide tip. Secondly, it provides a sliding surface to the implant during deployment and only permits the translation and rotation along and about the X-axis, which prevents the implant from buckling. Boundary conditions were applied to simulate the actual conditions in which a fixed displacement was applied at the proximal end of the implant. As the implant can only slide and rotate about the core pin, the translational and rotational displacement of UY, UZ, RY and RZ were constrained at the proximal end. The load was applied in two load sets at the distal end. First, clockwise torque was applied in six load steps. Second, a compression force was applied in fifteen load steps to deal with the maximum plastic strain and solution convergence during each step. Mesh density was tested and the

default mesh was refined based on mesh convergence analysis. The volume of the implant was meshed with hexahedral elements and there were 114374 nodes and 31143 elements in the model as shown in Fig. 4.7. The von-Mises stress distributions at the conclusion of each load step and deformation along y-axis at the final step are shown respectively in Fig. 4.8, Fig. 4.9 and Fig. 4.10.

The outer profile of the deployed implant wings was generated in ANSYS. In order to generate the outer profile of the implant's wings, the nodal coordinates of deformed shape were exported from ANSYS WB using the UPCOORD command. Following the UPCOORD command, CDWRITE was executed from the pre-processor to write out a node file with the deformed nodal coordinates. These nodal coordinates were imported into Pro/E to generate the outer profile of the wings.

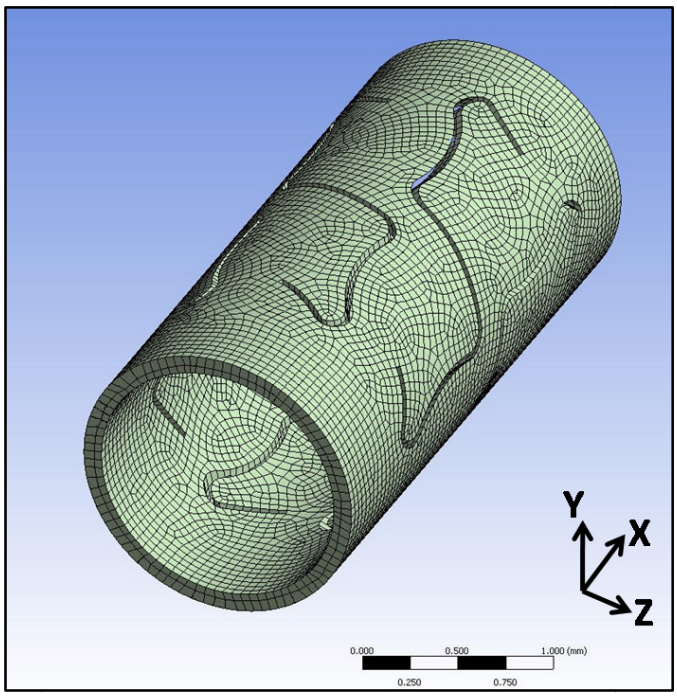

FIGURE 4.7: FE MESH OF HALF IMPLANT FOR EVALUATION OF SLOT PROFILE

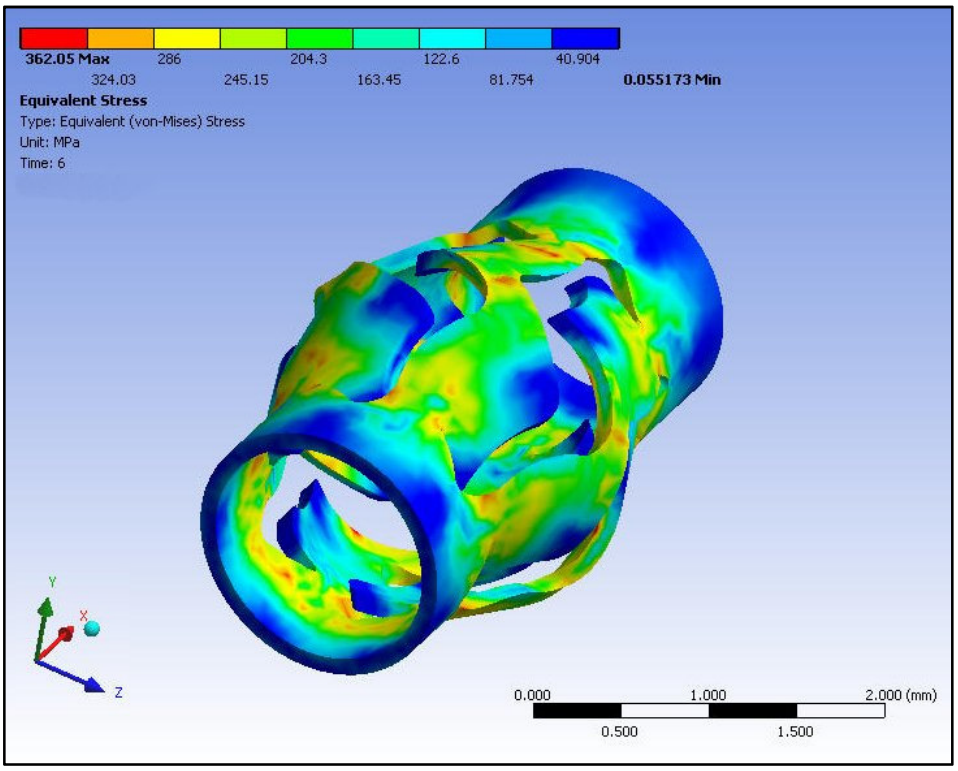

FIGURE 4.8: VON-MISES STRESS DISTRIBUTION IN HALF MODEL AT END OF LOAD STEP 1

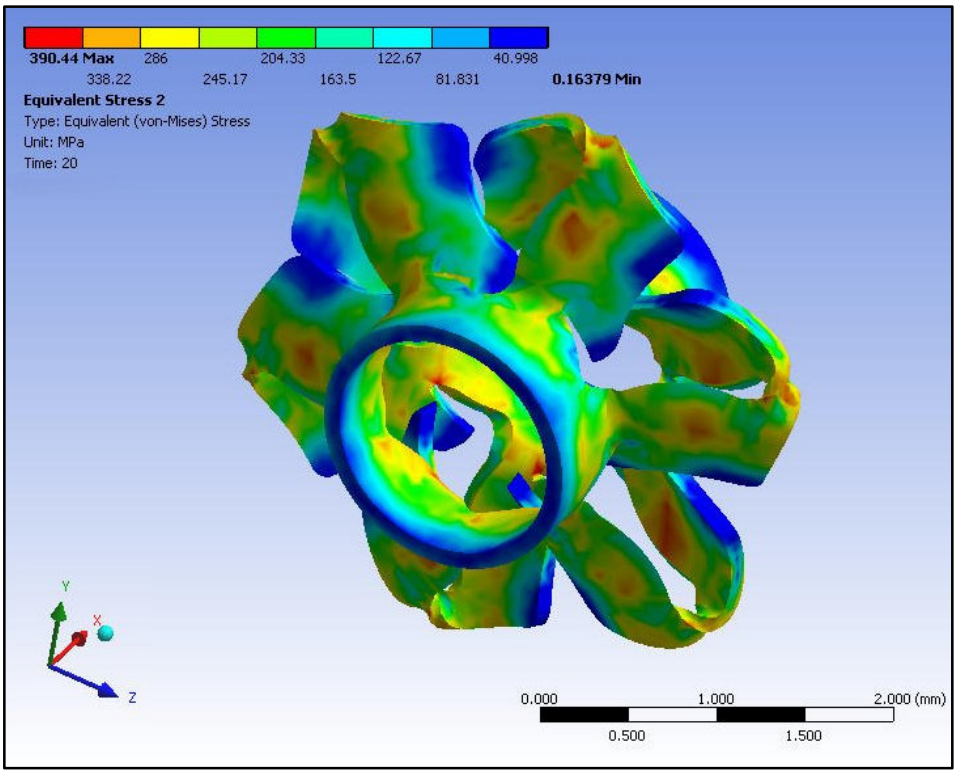

FIGURE 4.9: VON-MISES STRESS DISTRIBUTION IN HALF MODEL AT THE END OF LOAD STEP 2

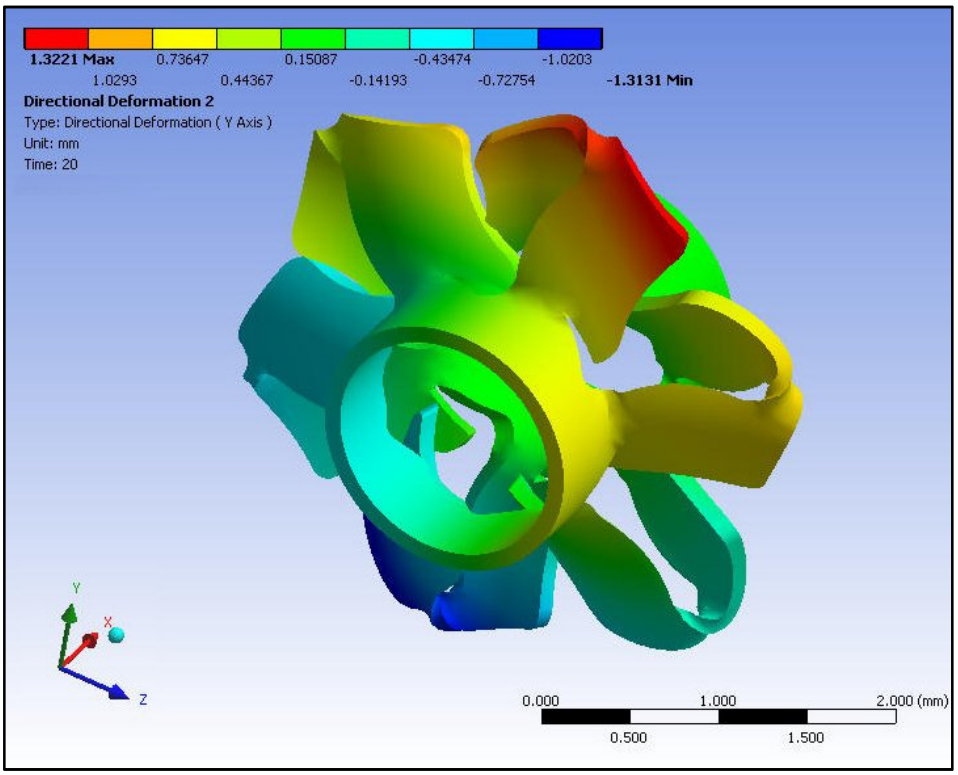

FIGURE 4.10: DEFORMATION ALONG Y-AXIS AT END OF FINAL LOAD STEP

In order to simulate the deployment of the whole implant and to investigate its mechanical behaviour, the complete model of the implant, including two sets of six slots was used. A sequence comprising of four load sets was adopted to simulate the deployment phases:

Load Set 1: Counter-clockwise moment to achieve an out-of-plane displacement in the distal slots.

Load Set 2: Compression to transform the displaced slots into fully deployed distal wings.

Load Set 3: Clockwise moment to achieve an out-of-plane displacement in the proximal slots.

Load Set 4: Compression to transform the displaced slots into fully deployed distal wings.

These load sets were applied in 42 load steps at the distal end of the implant. The model was constrained in the same way as described previously for the half model. However, surface-to-surface frictional contacts were defined in between the slot surfaces to prevent model penetration. A coefficient of friction 0.74 for SS316 was used for these contacts [163]. Mesh density was tested and the default mesh was refined

based on mesh convergence analysis. The volume of the implant as shown in Fig. 4.11 was meshed with hexahedron elements and there were 231292 nodes and 64322 elements in the model. The von-Mises stress distributions at the end of each load step are shown in Fig. 4.12, Fig. 4.13, Fig. 4.14 and Fig. 4.15.

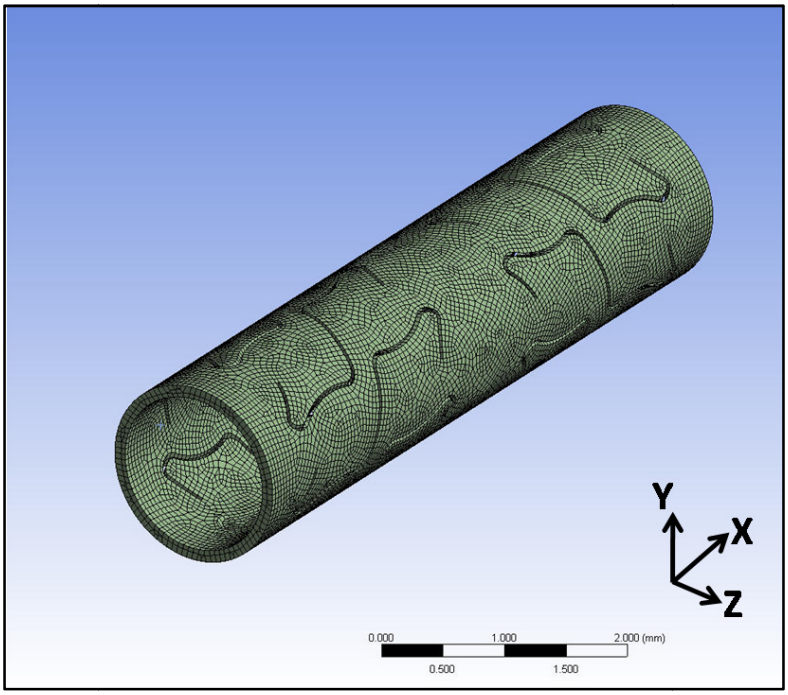

FIGURE 4.11: FE MESH OF WHOLE IMPLANT

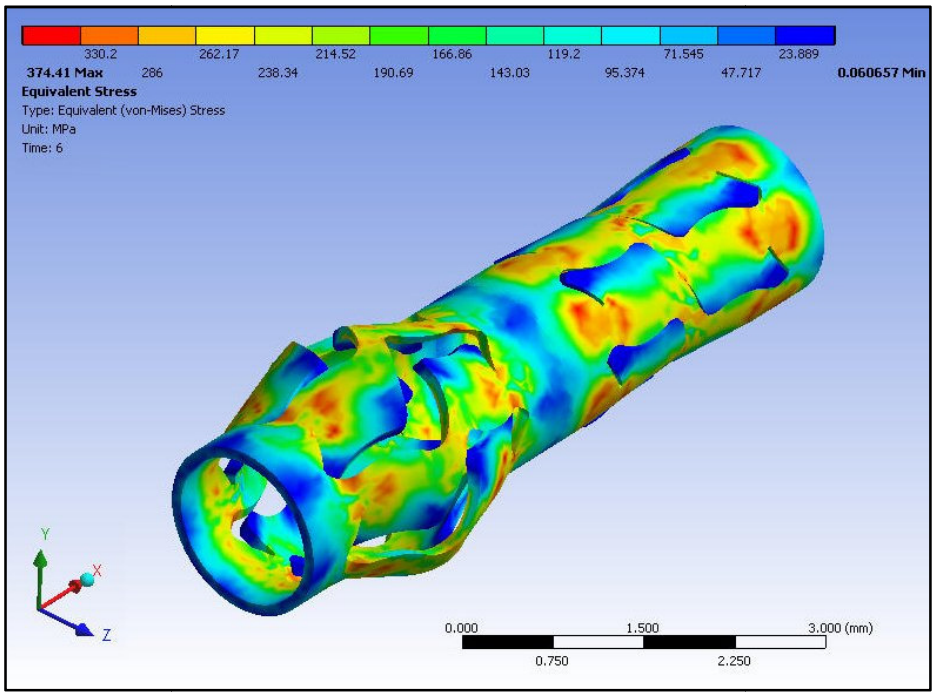

FIGURE 4.12: VON-MISES STRESS DISTRIBUTION IN WHOLE IMPLANT AT THE END OF LOAD STEP 1

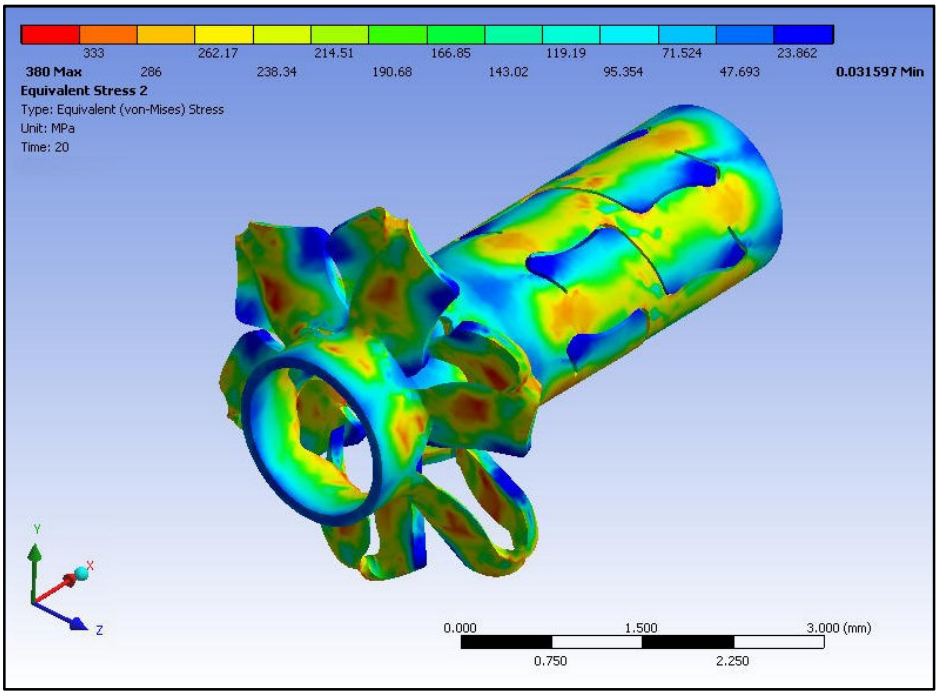

FIGURE 4.13: VON-MISES STRESS DISTRIBUTION IN WHOLE IMPLANT AT THE END OF LOAD STEP 2

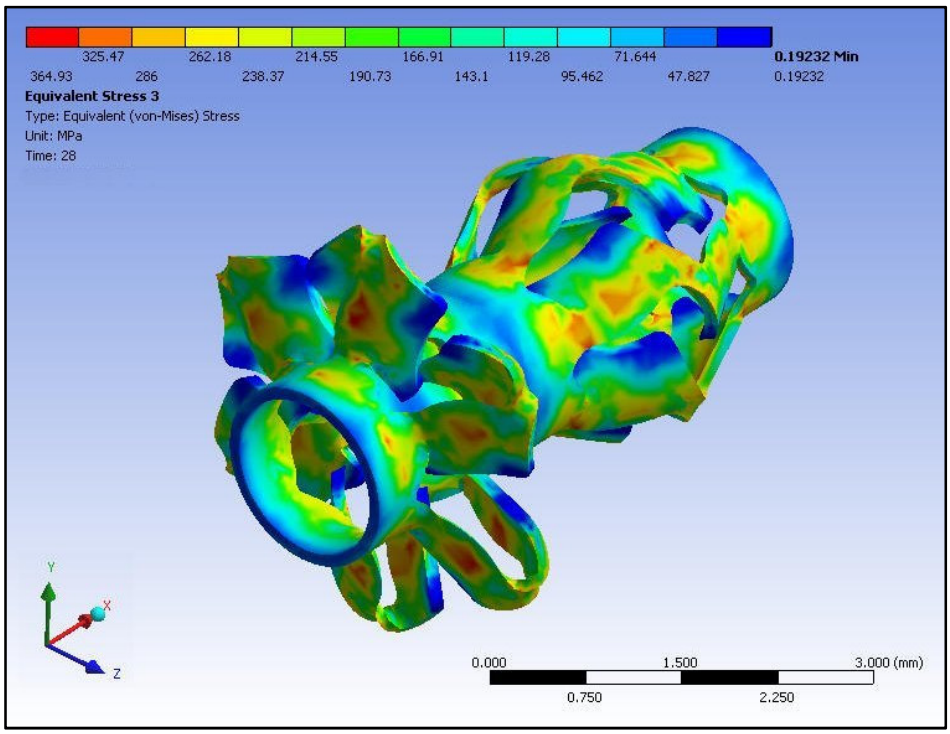

FIGURE 4.14: VON-MISES STRESS DISTRIBUTION IN WHOLE IMPLANT AT THE END OF LOAD STEP 3

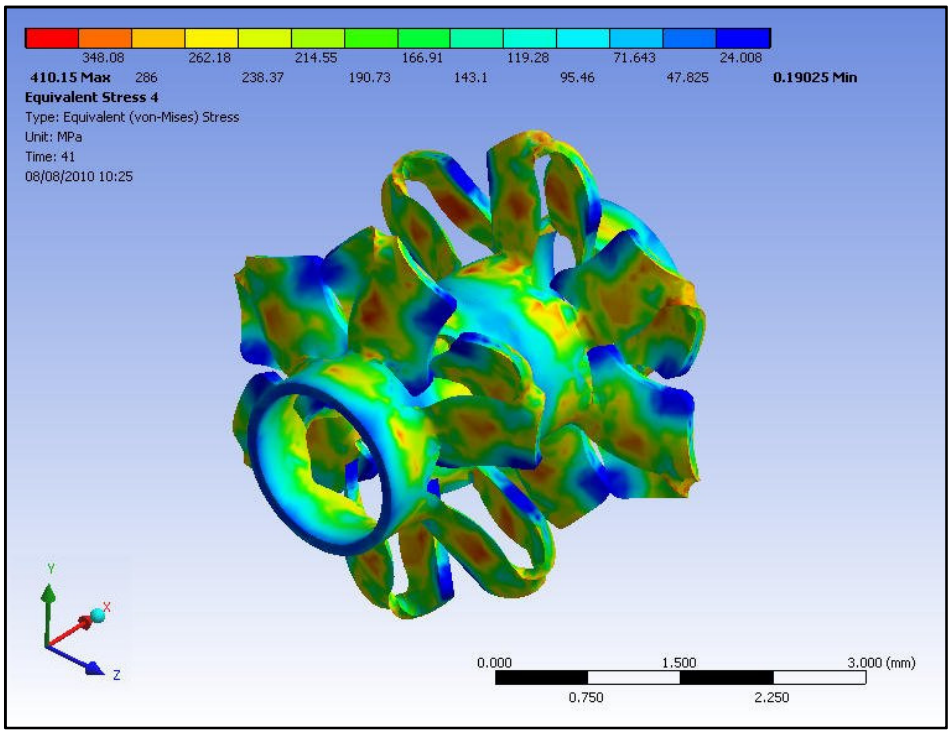

FIGURE 4.15: VON-MISES STRESS DISTRIBUTION IN WHOLE IMPLANT AT THE END OF FINAL LOAD STEP

The axial straight splines at the proximal end were analyzed independently to both simplify the analysis and reduce computation time. The parametric models of the implant splines and corresponding splines of the guide tube were generated in Pro/E. The whole coupling assembly was integrated with ANSYS WB for linear contact analysis. Frictional contact was defined between implant and guide tube splines. As both components were of SS-316, a coefficient of friction 0.74 was used for this contact. Fixed displacement was applied on the opposite end of the implant's splines. A cylindrical support boundary condition was applied at the inner surface of the guide tube and a moment of 16 N-mm was applied on the opposite end of the guide tube splines. Fig. 4.16 shows the von-Mises stress distribution in splines of implant after linear contact analysis.

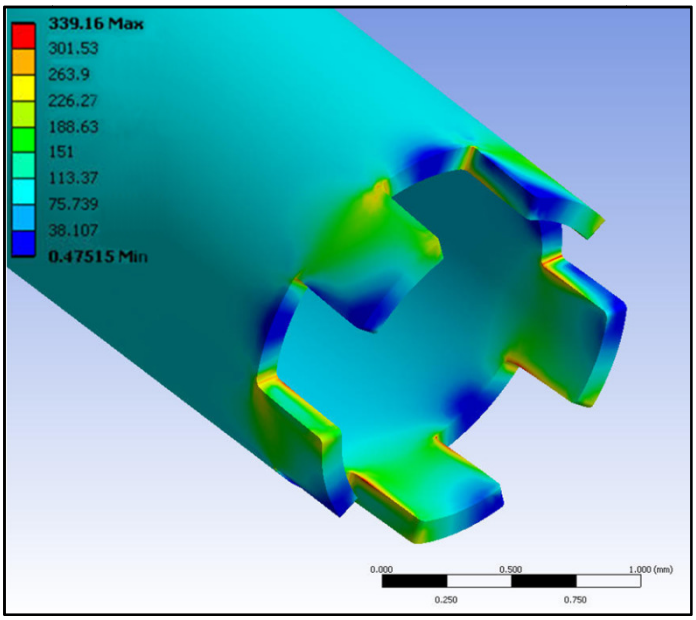

FIGURE 4.16: VON-MISES STRESS DISTRIBUTION IN SPLINES

C. DEVELOPMENT AND TESTING

The implant was manufactured with light walled annealed SS-316LVM tubing using LPL Stent Cutter. Prior to processing, CAD data of the implant with the desired configuration was generated. In order to generate the CNC program for laser cutting, the coordinate points of the profile of the implant and its slots were imported from Pro/E. The minimum possible width of laser beam on the available laser cutting machine was 0.06 mm, therefore this value was used for the width of implant's slots.

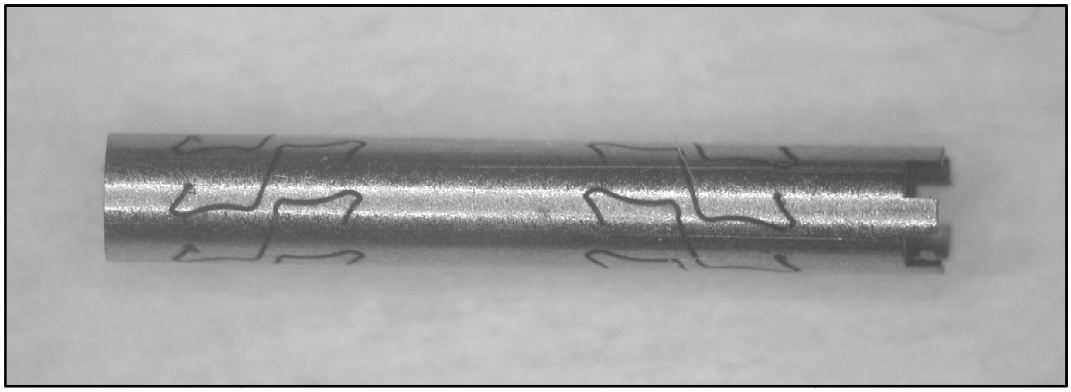

FIGURE 4.17: PRELIMINARY IMPLANT FABRICATED ON LASER CUTTING MACHINE

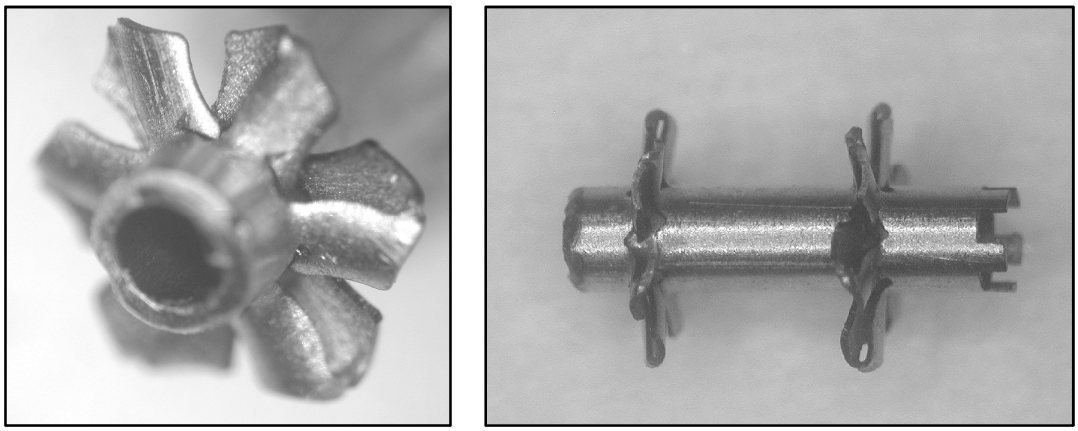

FIGURE 4.18: IN-AIR DEPLOYED WINGS

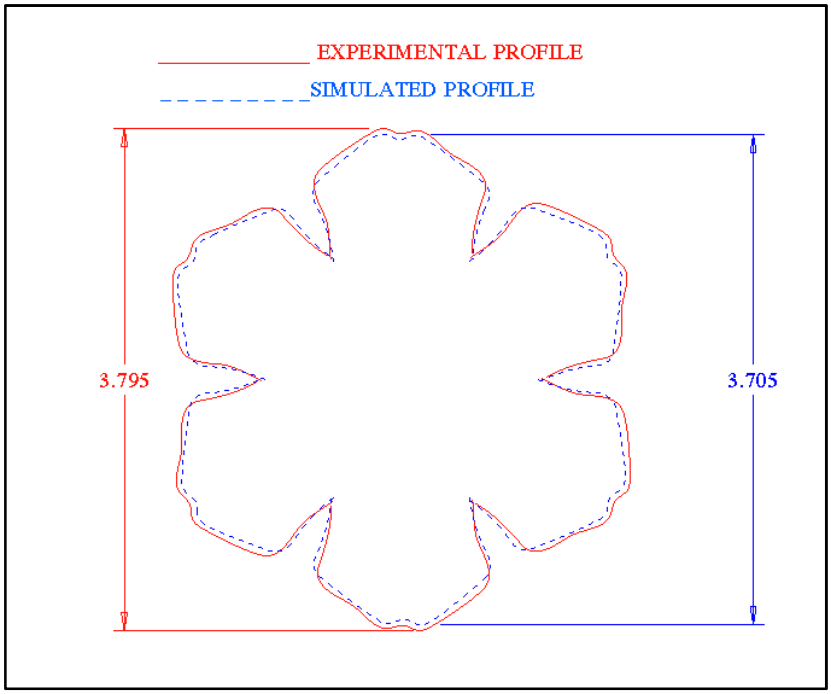

FIGURE 4.19: COMPARISON OF FEA SIMULATED AND EXPERIMENTALLY MEASURED WINGS PROFILE

Fig. 4.17 illustrates the fabricated implant on the laser cutting machine. The implant was inspected using video inspection probe and critical dimensions showed that the fabricated implant was an exact representative of the CAD model having an error of less than 2.6 µm. The fabricated implant was deployed under microscope and its mechanical behaviour was studied. Fig. 4.18 shows the shape of the implant wings deployed *in-air* on test bench. The wing profile of these deployed implants was measured using a video inspection probe. The coordinates obtained from the video inspection probe were imported into Pro/E and plotted. Using Pro/E, this experimentally measured profile of

the wings was superimposed on the profile obtained from FEA simulations as shown in Fig. 4.19. It was observed with this comparison that the FEA results are comparable with experimentation. The standard error of mean of the difference of experimental and simulated profile was 0.003543 and the maximum percent error was 3.129%.

4.3.5. DESIGN IMPROVEMENT

In house *in-vitro* and *in-air* deployments were performed to validate the mechanical behaviour and functionality aspect of the preliminary implant design. This design was also investigated in explanted human uteri. The details of these tests are discussed in Chapter 7. It was observed in these studies that the wing profile and shape were exactly as required and provided the instant occlusion of the fallopian tubes. However, it was construed from testing that the implant size could be reduced and that a reduction of gap between the implant slots could provide a better tissue entrapment. As a result, two design modifications were made to the initial design.

a) Modification 1

The gap between the implant slots was reduced from 2.1 mm to 1.0 mm. In addition, the distance between the distal end of implant and distal slots was reduced from 0.75 mm to 0.40 mm as shown in Fig. 4.20. The modified implant design was fabricated and bench-top in porcine tissue tested. More tissue entrapment was observed after this modification. The results were appealing and this change has been incorporated in to the design. The fabricated and in-air deployed implant is shown in Fig. 4.21.

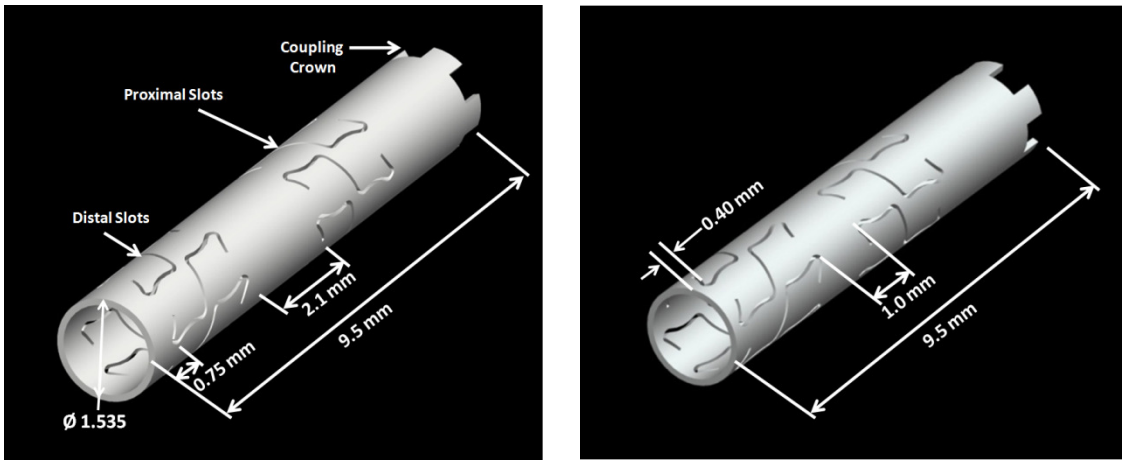

FIGURE 4.20: GAP REDUCTION (RIGHT) IN PRELIMINARY DESIGN (LEFT)

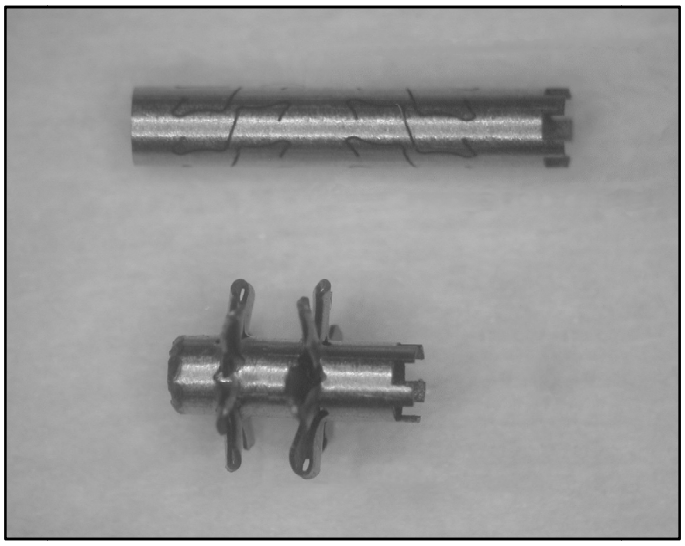

FIGURE 4.21: PRE AND POST DEPLOYED IMPLANT AFTER FIRST MODIFICATION

b) Modification 2

The second modification was to reduce the length of the implant. The distance between the coupling crown and proximal wing was designed to incorporate the elongation of the release tube before breaking. Therefore, the diameter of the release tube was reduced in order to accommodate it into the guide tube, which made the reduction of the implant length possible. Hence, the implant length was reduced from 9.5 mm to 6.5 mm. The 3D model of the reduced length implant is shown in Fig. 4.22. This fabricated design shown in Fig 4.23 was tested *in-air* and *in-vitro* on bench-top.

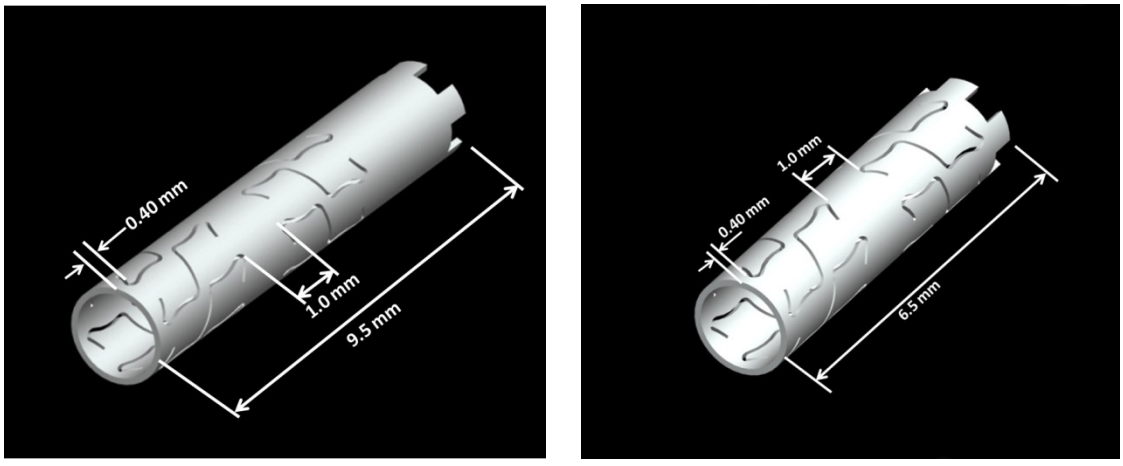

FIGURE 4.22: COMAPRISON OF MODIFICATION1 (LEFT) AND MODIFICATION 2 (RIGHT)

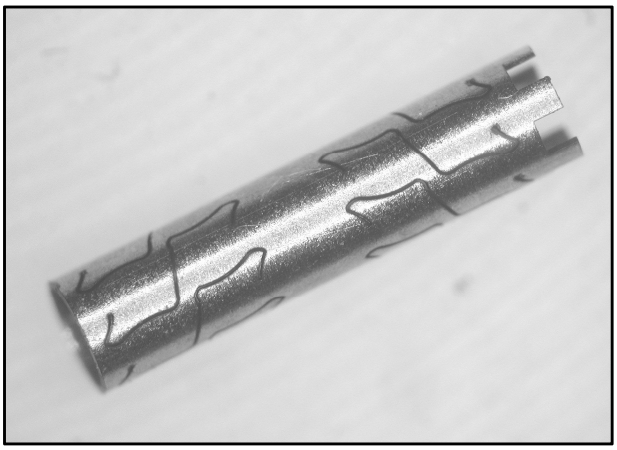

FIGURE 4.23: FABRICATED MODIFIED DESIGN

4.3.6. FINAL DESIGN

As mentioned earlier that most of the transcervical sterilization devices in research failed because of device expulsion. However, in this research work no such problem was observed. Instead, it was found that the implant wings completely entrap the ostium tissue resulting in perfect anchoring. Even during dissection of tissue, it was very hard to free the tissue from the implant wings. To provide additional safety, an innovative design was introduced. In this design, pair of incisors at the implant proximal slot profile was included. The 3D model of the implant with incisors in place is shown in Fig. 4.24. This provided a better anchoring of the implant and more grabbing of ostium tissue. The idea behind these incisors was that the proximal wings open at the end of deployment and during formation; they apply an axial compression on the tissue. Therefore, during this compression the incisors could grab additional tissue and provide greater reliability. These incisors were only introduced on the proximal wings of the implant.

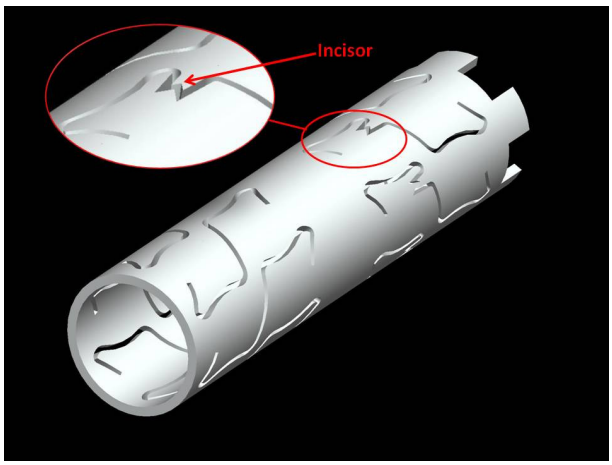

FIGURE 4.24: 3D MODEL OF IMPLANT WITH INCISORS

A. FEA SIMULATIONS

The challenging task was to evaluate the shape and location of the incisors. In order to meet this challenge, FEA simulations were performed. Various profiles and locations of the incisors were modelled in Pro/E and simulated in ANSYS to arrive at the desired geometry. The procedure for FEA simulation described in section 4.3.5.2 was used for this model. However, section 4.3.5.2 simulations deals with the distal slots whereas in this case, simulation of proximal slots was required. Therefore, a few modifications were required in the loadings. As the incisors are on proximal slots, a rotational displacement in the opposite direction is required. Therefore, the direction of the moment was reversed in this case. As discussed earlier, half of the model was used for simulating slot profile. The additional incisor profile increased the density of mesh to 285856 nodes and 117548 elements in the model volume as shown in Fig. 4.25. The von-Mises stress distribution at the end of load step 1 and 2 is shown in Fig. 4.26. The deployed shape and position of the incisors can be seen from Fig. 4.26. The deformation of the model in y-axis at the end of load steps is represented in Fig. 4.27.

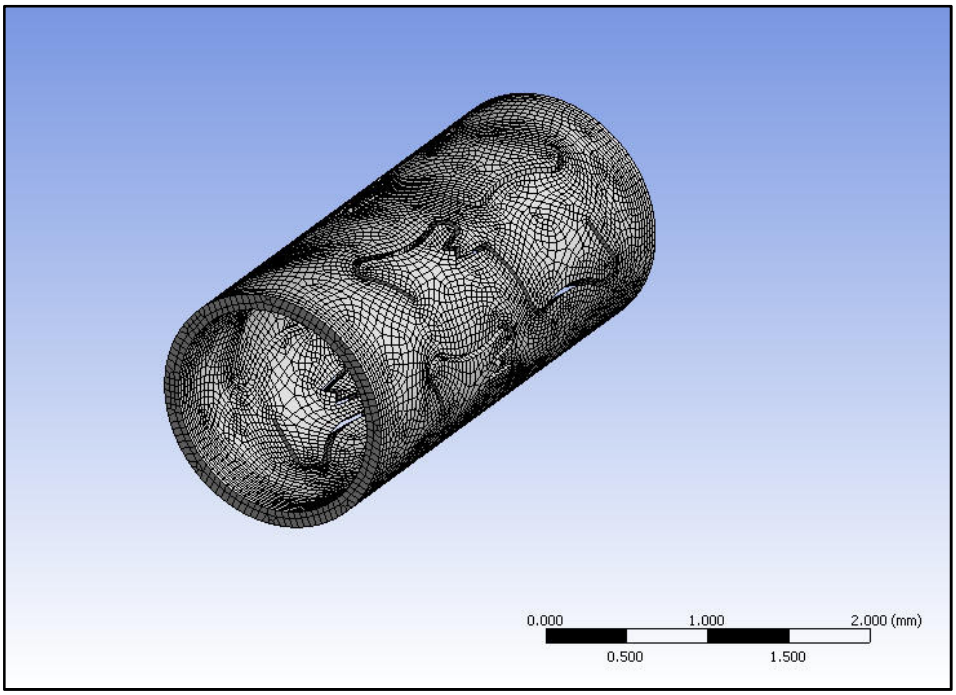

FIGURE 4.25: FE MESH FOR EVALUATION OF FINAL SLOT PROFILE

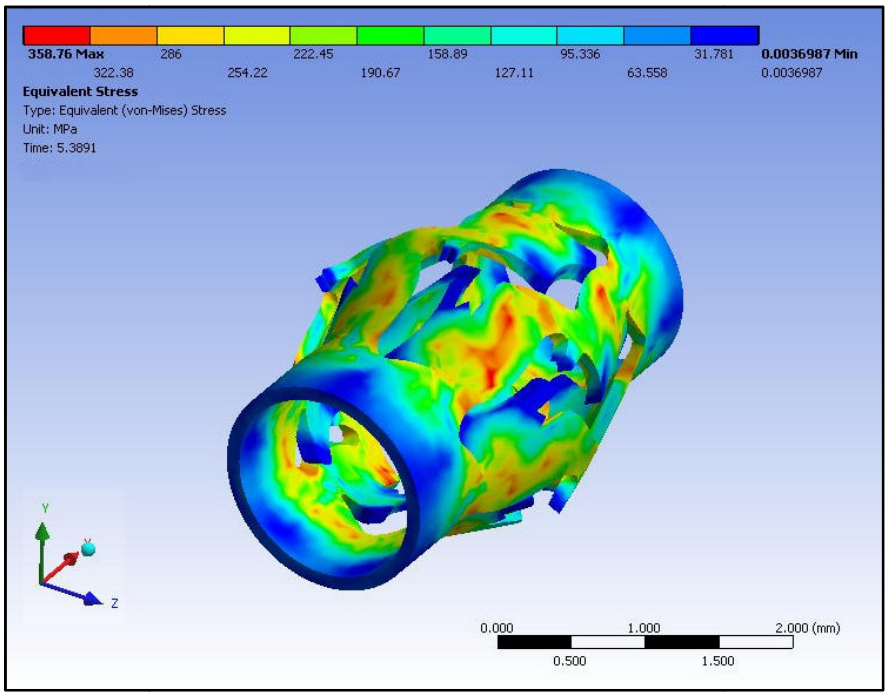

(a)

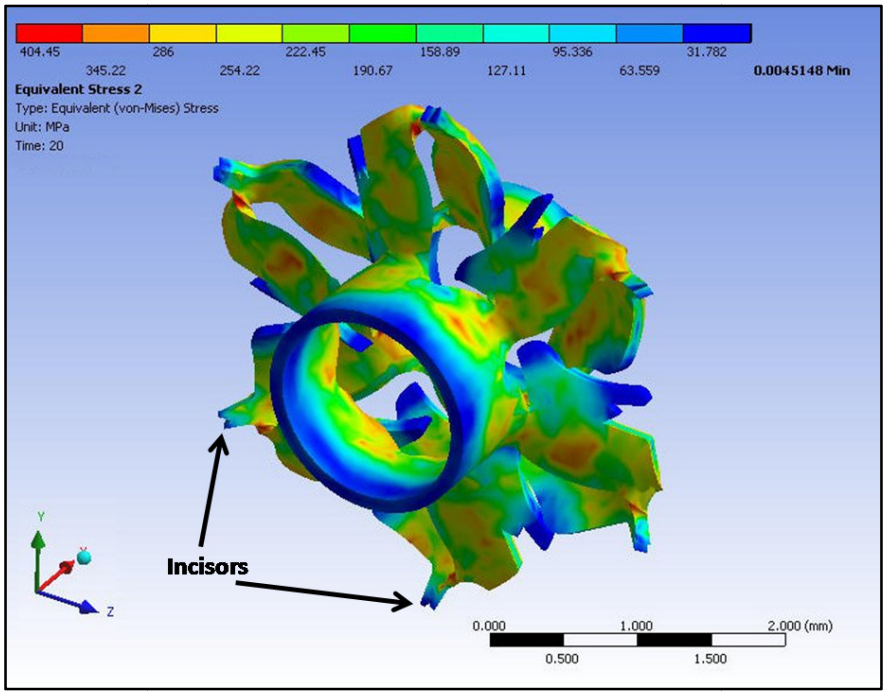

(b)

FIGURE 4.26: VON-MISES STRESS DESTRIBUTION AT END OF (a) LOAD STEP 1 (b) LOAD STEP 2

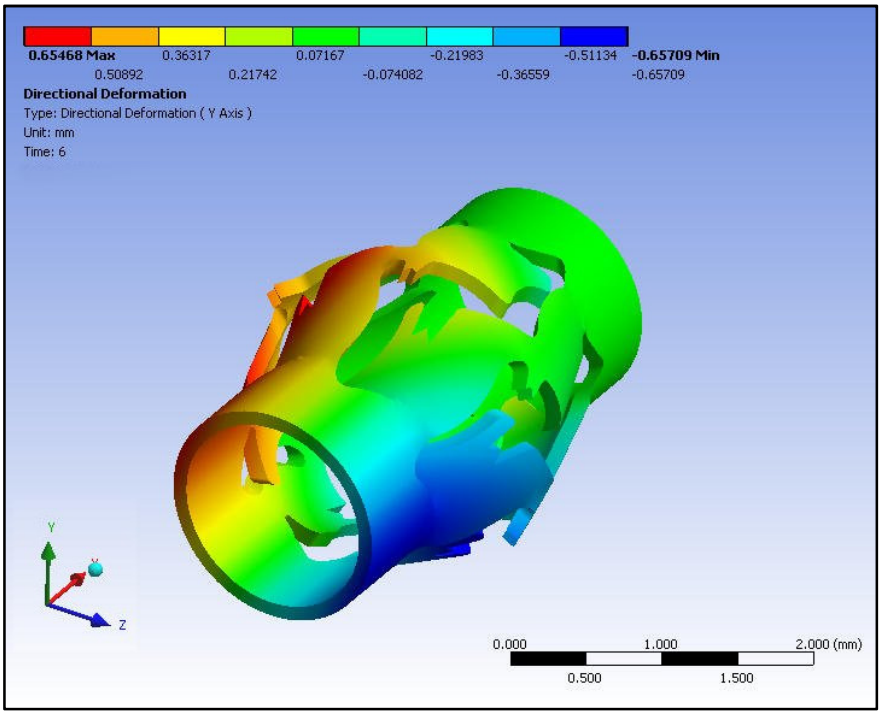

(a)

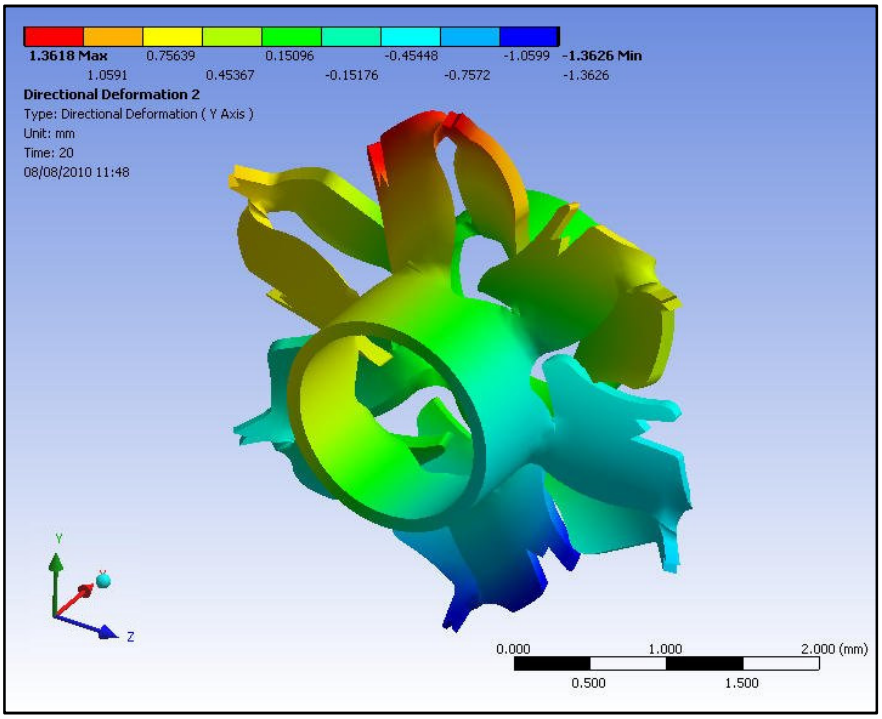

(b)

FIGURE 4.27: DEFORMATION (Y-AXIS) AT THE END OF (a) LOAD STEP 1 (b) LOAD STEP 2

B. DEVELOPMENT AND TESTING

Fig. 4.28 shows the implant including incisors, fabricated using the laser cutting machine. The point coordinate data of the incisors was exported from the Pro/E model and used to modify the CNC program for the laser-cutting machine. The implant was inspected via video inspection probe and critical dimensions showed that the fabricated implant was an exact representative of the CAD model, having an accuracy of less than 2.6 µm. The fabricated implant was deployed under microscope and its mechanical behaviour was studied. Fig. 4.29 shows the shape of the implant wings deployed in air on test bench. As seen in Fig. 4.29 the incisors make an angle of 45° with the longitudinal axis. This incisor's angle helps to anchor the implant both axially and radially.

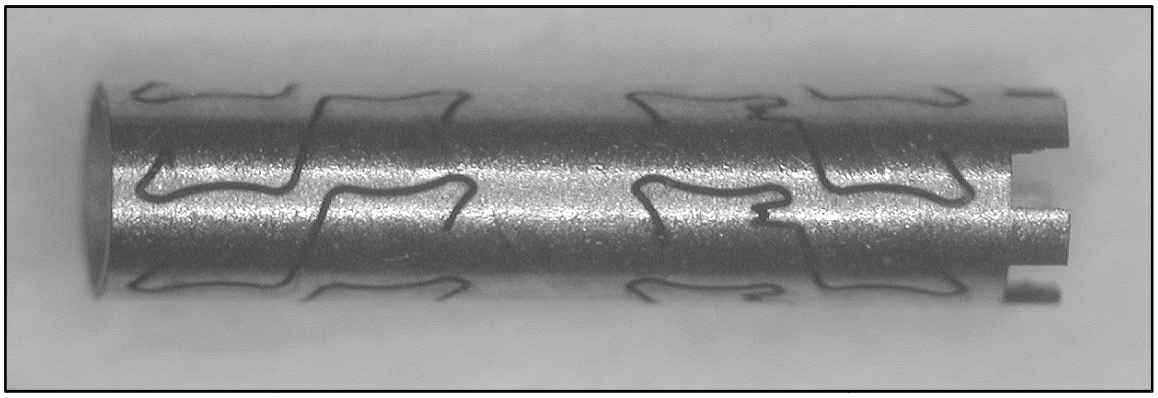

FIGURE 4.28: IMPLANT INCISORS PRE-DEPLOYMENT

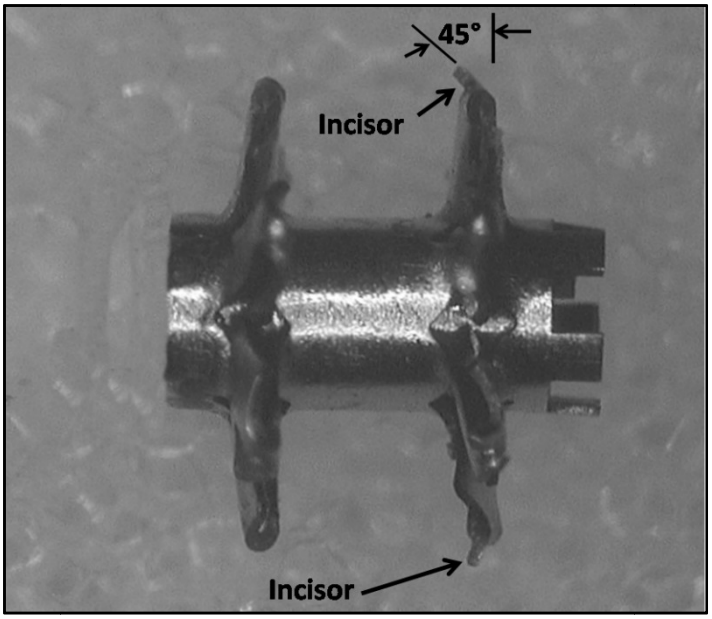

FIGURE 4.29: IMPLANT INCISORS POST-DEPLOYMENT

4.3.7. TORQUE TESTING

The torque required to displace slots out-of-plane was validated experimentally using torque testing equipment. In this setup shown in Fig. 4.30, the torque meter was held in a vise. In a second vise, a handle was held, which was capable of applying torque on the implant using a guide tube and coupling crown. The apparatus was set to measure peak torque values and the torque was applied.

It was found from ANSYS WB at the end of load set 1 that a moment of 16.0 N-mm moment is required before compression of the implant. This moment produces a 0.353 mm out-of-plane displacement in implant slots. This torque value was measured experimentally and Table 4.3 summarizes the force measured on five samples during these testing. From this torque testing, a comparable mean value 15.4 N-mm was measured from torque meter when same amount of radial expansion (from Ø1.535mm to Ø2.241mm) in implant slots was achieved.

TABLE 4.3: TORQUE TESTING OF WING SLOTS

Samples	Torque Value (N-mm)
1	15.3
2	15.6
3	15.4
4	15.3
5	15.5
Mean	15.42
Standard Deviation	0.1304
Standard Error of Mean	0.0583

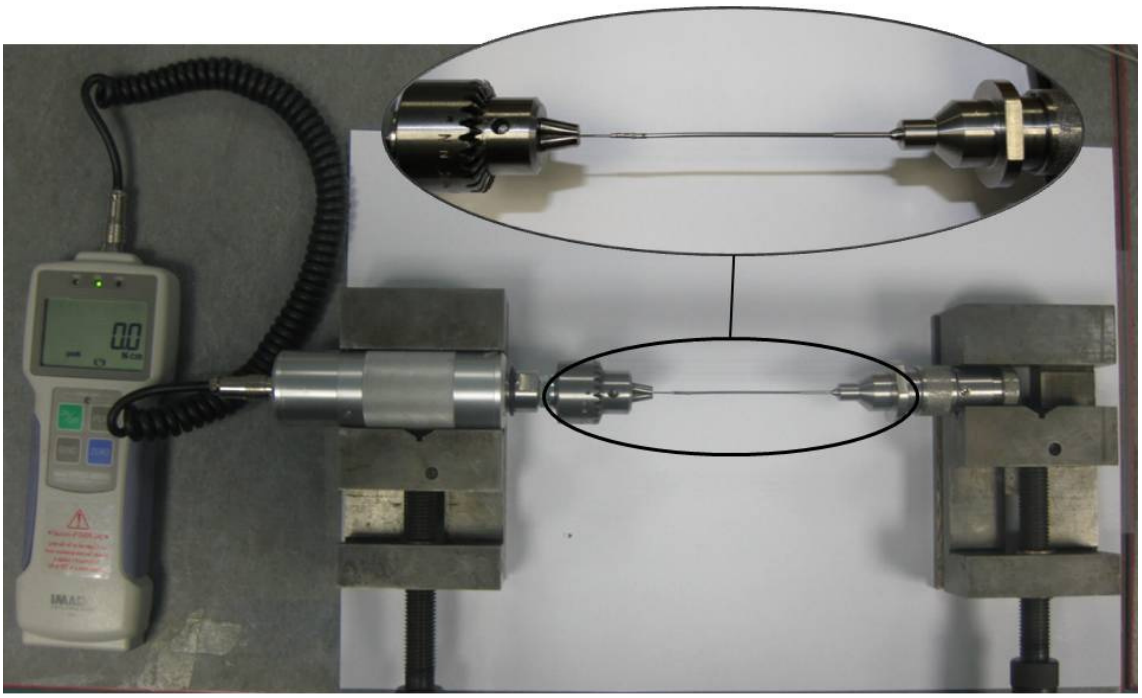

FIGURE 4.30: TORQUE TESTING SETUP OF IMPLANT

4.3.8. COMPRESSION TESTING

In order to plastically deform the expanded implant slots obtained from torque testing, a fixture was fabricated to hold the implant during compression. The fixture comprises of SS-304 tubing with a laser cut crown shape at the top end. This matching crown shape was to couple with the implant crown. This tube was laser welded on the top of a solid cylinder that can be mounted on the lower grip of the Lloyd tensile testing machine as shown in Fig. 4.31. A truly flat cylindrical was block mounted at the top grip of the machine through the load cell. The machine was programmed to perform a compression test with a limiting force of 40 N at a speed of 100 N/min.

Five implant samples of radially displaced distal slots were prepared and mounted on the holding fixture for the compression testing of distal slots as shown in Fig. 4.32(a). Similarly, five implant samples having distal wings deployed and radially displaced proximal slots were mounted for the compression testing of proximal slots as shown in Fig. 4.32(b). After placement of the implant on the fixture, the test was performed and the graph of load versus extension was obtained for both distal and proximal wings. Fig. 4.33 shows a representative graph for the proximal wings. The first peak marked as “A” in the graph indicates the maximum compressive force require to overcome the internal

resistance of the material and to plastically deform the slots into wings. This was the value of compressive force required from the testing. The second smaller peak “B” in the graph represents the disengagement of the incisors from their respective slot. The third peak “C” appeared when the opposite edges of wing came in contact with each other. The last peak “D” only indicates the limiting value of this test. Fig. 4.34 shows a representative graph for the distal wings. The only difference in this graph is the smaller peak “B” of the Fig. 4.33, which is not present because of missing incisors. Compressive force values (peak “A”) ranging from 24.9 N to 25.8 N were recorded from these tests. Table 4.4 summarizes the forces measured during these testing and their statistics. Thus, an average value of 25.4 N and 25.3 N is required to plastically deform the proximal and distal out-of-plane displaced wing slots respectively.

FIGURE 4.31: SETUP FOR WING SLOTS COMPRESSION TEST

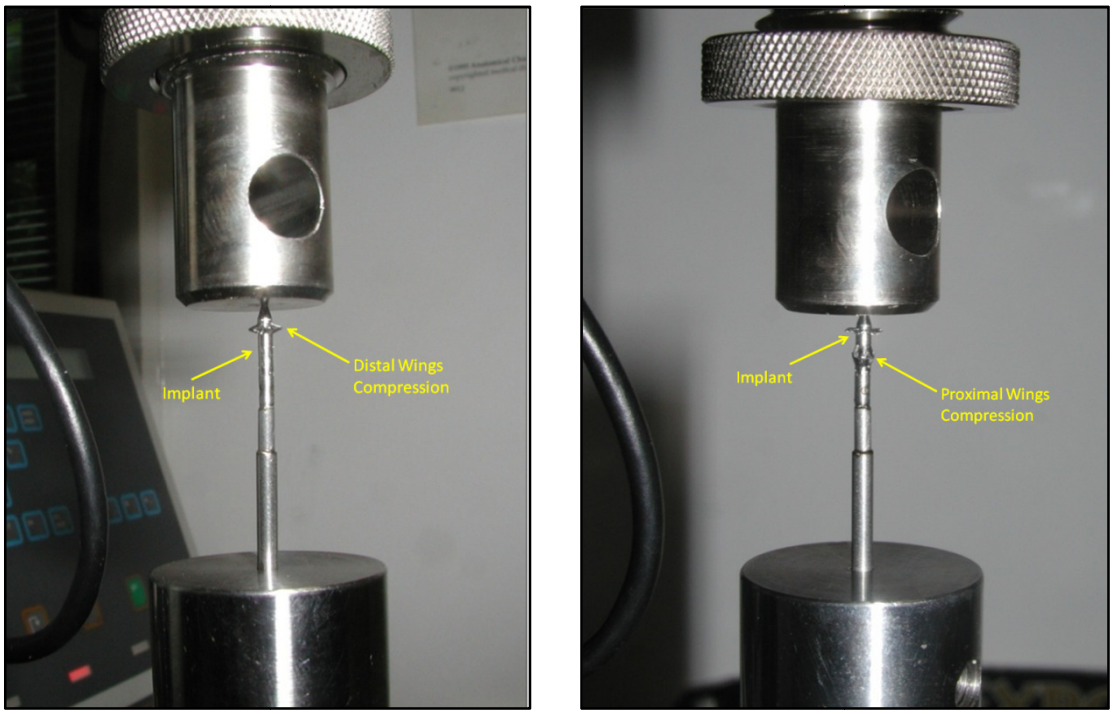

FIGURE 4.32: COMPRESSION TEST (A) DISTAL WINGS (B) PROXIMAL WINGS

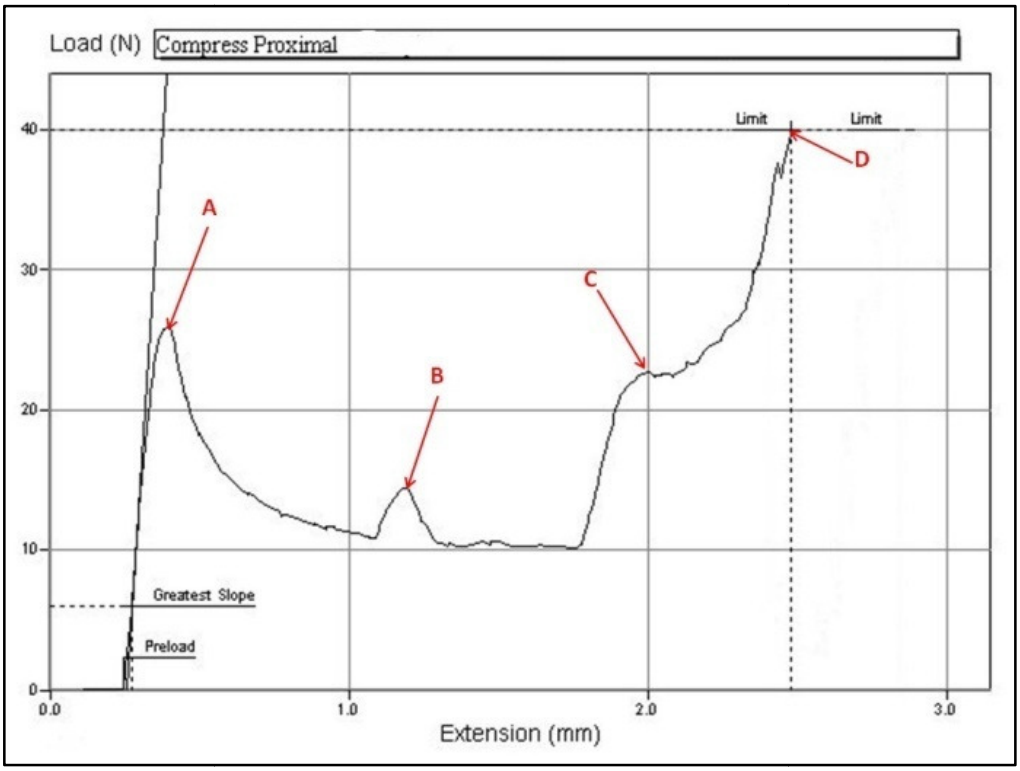

FIGURE 4.33: COMPRESSIVE FORCE MEASUREMENT FOR PROXIMAL WING

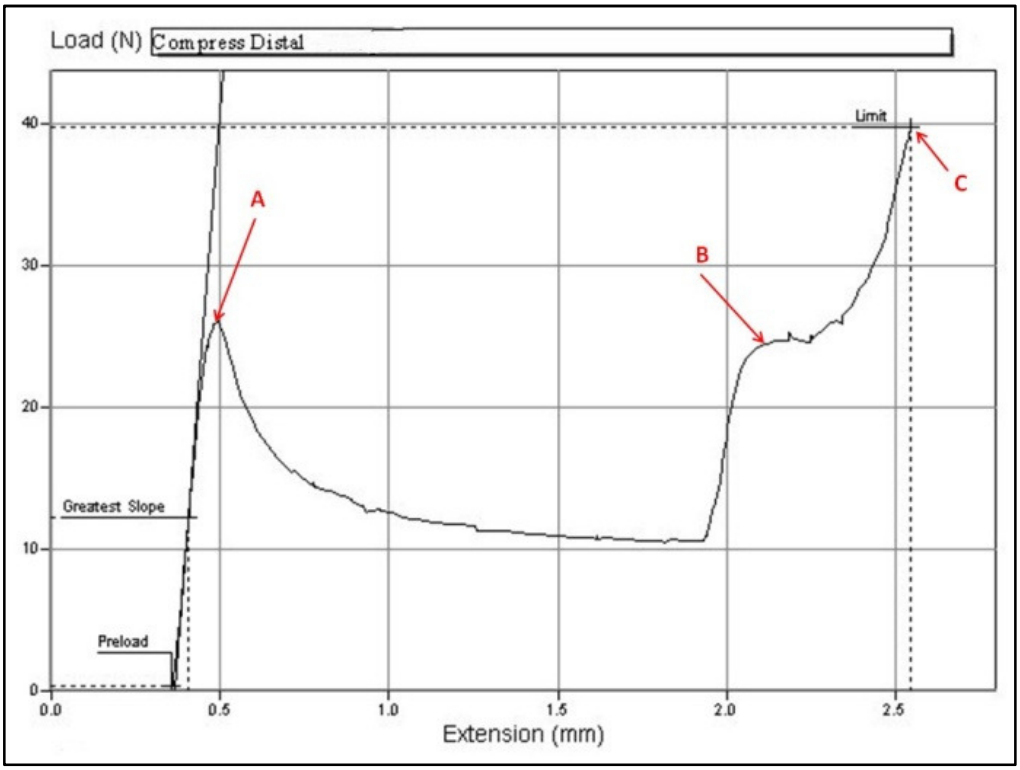

FIGURE 4.34: COMPRESSIVE FORCE MEASUREMENT FOR DISTAL WING

TABLE 4.4: COMPRESSION TESTING OF WING SLOTS

	Compressive Force (N)	
Samples	**Proximal Wings**	**Distal Wings**
1	25.8	25.5
2	25.6	25.7
3	24.9	24.9
4	25.4	25.4
5	25.2	25.1
Mean	25.38	25.32
Standard Deviation	0.34928	0.14283
Standard Error of Mean	0.15620	0.31937
Confidence level (95%)	0.43369	0.39656

4.4. DESIGN, DEVELOPMENT AND VALIDATION OF GUIDE TIP AND CORE SHAFT

The guide tip is designed to guide the implant through the uterus into the fallopian tube. Hence, a fine balance between column strength (for push-ability and forward progression) and flexibility (to negotiate the curvatures of the uterus and fallopian tube) was required.

4.4.1. DESIGN EVALUATION OF GUIDE TIP

Guide tips are most commonly categorized by their flexibility. Three different types of guide tips are commonly used in the medical industry: floppy, intermediate and standard.

(a) Floppy Guide Tip:

The floppy guide tip was provided by COOK® Ireland Ltd., Limerick Ireland. It is a nitinol core guide tip encased in polyurethane with hydrophilic coating. The OD of the guide tip was 0.69 mm.

(b) Intermediate Guide Tip:

Lake Region Manufacturing Co. Ltd., Co. Wexford, Ireland provided this type of guide tip. It is full-length spring coil, with an OD of 0.7 mm and is wound over an inner core wire. It is made of SS-316 and has a rounded tip.

(c) Standard Guide Tip:

This type of guide tip was provided by TFX Medical, Co. Armagh, Northern Ireland. It is spring coil wound over three inner core wires and has a smooth rounded tip. It is made of SS-316 with an OD of 1.0 mm.

The guide tips investigated in this research work are shown in Fig. 4.35.

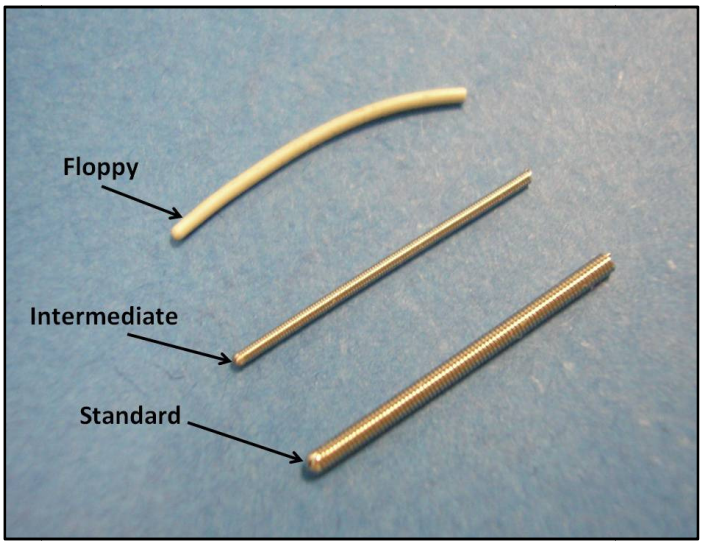

FIGURE 4.35: THREE TYPES OF GUIDE TIPS

4.4.2. DESIGN AND DEVELOPMENT OF CORE SHAFT

The core shaft is a cylindrical shaft laser welded to the distal end of the implant. Initially, it was incorporated into the implant design to serve two purposes. Firstly, to provide internal support to the implant during deployment and prevents buckling. Secondly, to provide an interface in between the implant body, the release mechanism and guide tip. The CAD model initial configuration is shown in Fig. 4.36 and the deployed implant with cylindrical core shaft is shown in Fig. 4.37.

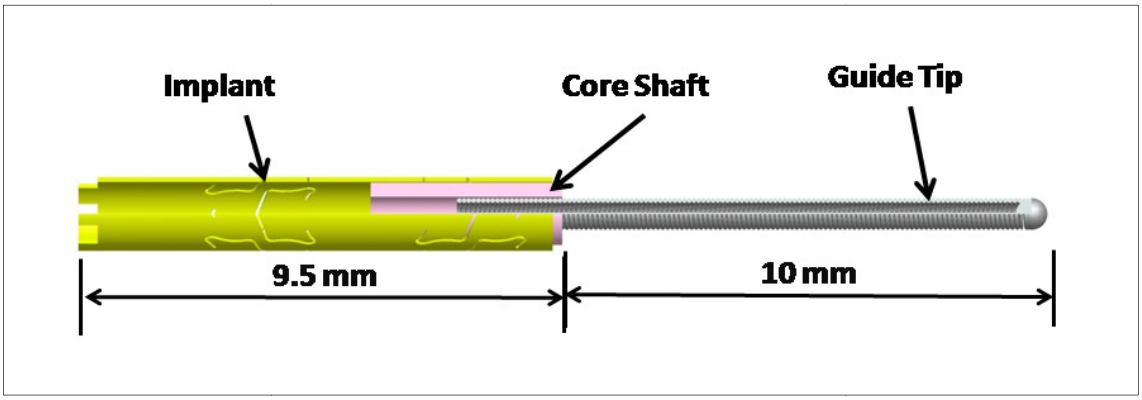

FIGURE 4.36: INITIAL CONFIGURATION OF CORE SHAFT

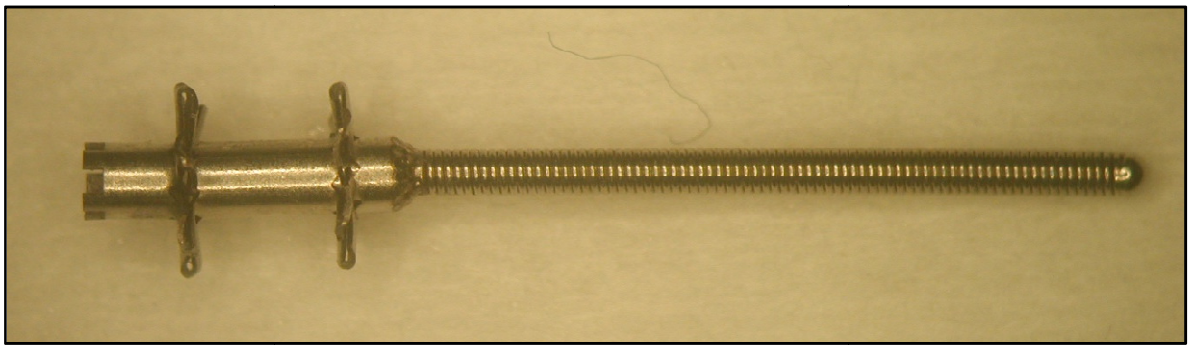

FIGURE 4.37: CYLINDRICAL CORE SHAFT

After the first explants' study in human uterus, it was observed that the step in between the guide tip and the implant body impeded the delivery and placement of the implant. Therefore, the core shaft was modified to serve the third purpose, to provide transition in between the guide tip and implant body as shown in Fig. 4.38. Finally, the distal end of the core shaft was transformed into a conical shape, which made the transition from the Ø 0.5 mm guide tip to the 1.535 mm implant achievable. The core shaft was machined on the high precision micro CNC lathe, Schaublin 102 TM-CNC. The initial fabricated design of conical core shaft is shown in Fig. 4.39.

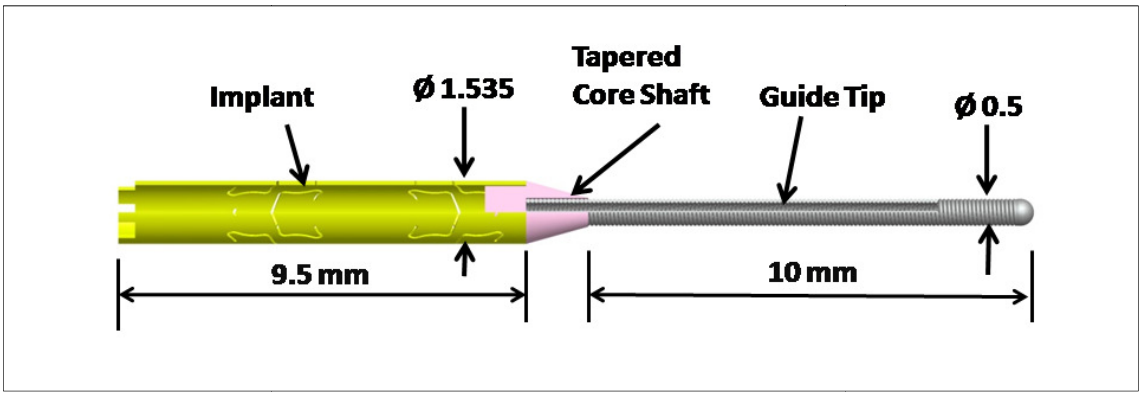

FIGURE 4.38: IMPLANT WITH CONICAL CORE SHAFT

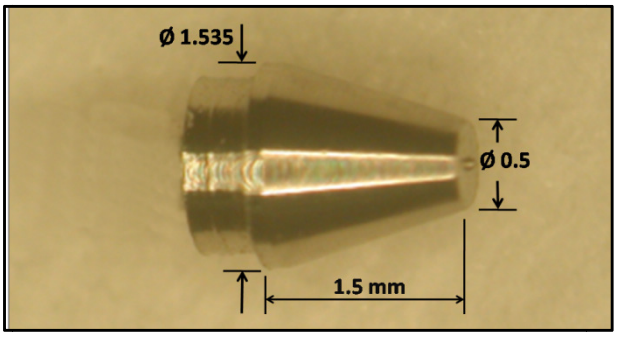

FIGURE 4.39: FIRST CONICAL CORE SHAFT

4.4.3. TESTING AND EVALUATION OF GUIDE TIP AND CORE SHAFT

In this study, all three types of guide tips were tested for flexibility and functionality. For the flexibility testing, guide tips with length of 10 mm were assembled on the implant through the core shaft as shown in Fig. 4.40 and Fig. 4.41. The setup for flexibility testing of the guide tips is shown in Fig. 4.42. In this setup, the implant assembly including guide tip and core-shaft was held in the upper grip attached to a miniature, low force load cell of the Lloyd universal testing machine. A cylindrical stand was mounted at the lower grip location. A rubber patch was placed on the stand to prevent slippage of the guide tips on the cylindrical surface. The Lloyd machine was programmed to apply a 5 mm of longitudinal displacement and measure the deflection load of the guide tips. The measured deflection load for the floppy, intermediate and standard guide tips was 0.085 N, 0.44 N and 0.81 N respectively.

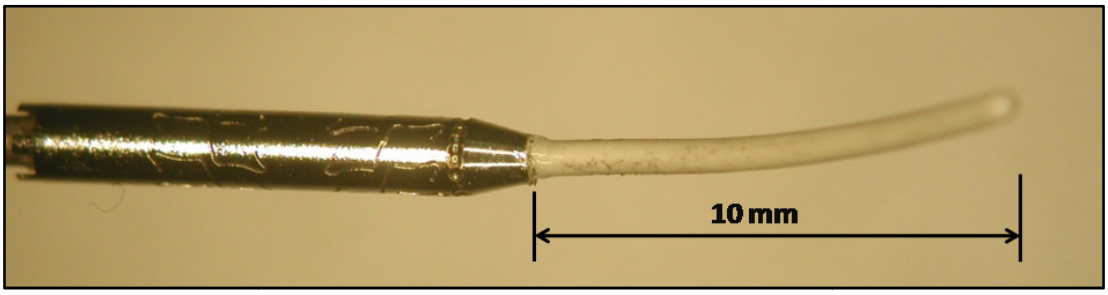

FIGURE 4.40: FLOPPY GUIDE TIP ASSEMBLED WITH CONICAL SHAFT

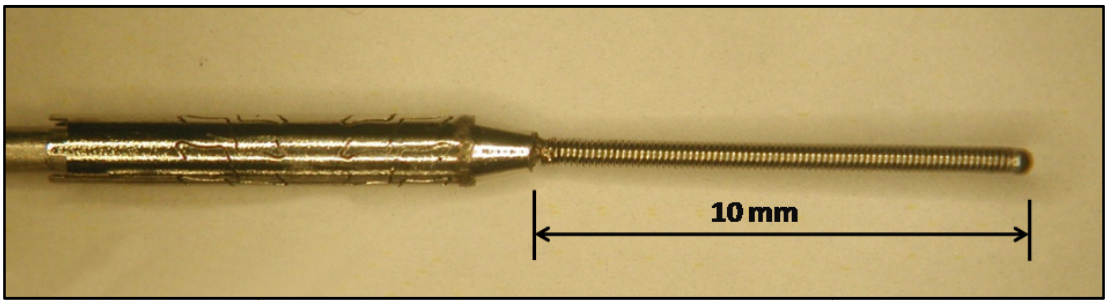

FIGURE 4.41: INTERMEDIATE GUIDE TIP ASSEMBLED WITH CONICAL SHAFT

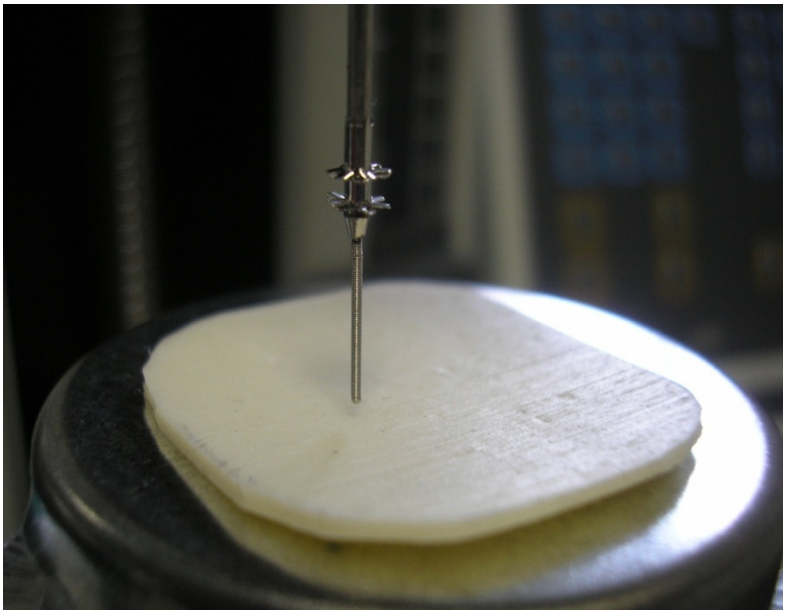

FIGURE 4.42: FLEXIBILITY TESTING OF THE GUIDE TIP

4.4.4. FUNCTIONALITY TEST

The guide tip is the leading member of the guiding system and it is the only part of the device, which enters the delicate portion of the fallopian tubes. Therefore, it was essential to evaluate the guide tips in the situation that is most representative of actual scenario. This functionality test involved the guidance of the implant through the hysteroscope into the fallopian tube of human explanted uterus. The objective of this test was to evaluate the overall ability of the guide tips to navigate through the anatomy of the uterus and fallopian tube. Dr. Michael Gannon at the Midland University Hospital, Mullingar, Ireland, performed the hysteroscopy and placement of the implant. In this test, all the three guide tips were assembled on the implant. Then the implant's assemblies were attached with the guide tube and wire assembly. These assemblies were introduced one by one into the hysteroscope to approach the fallopian tubes as shown in Fig 4.43 (a), (b) and (c).

It was observed during test and confirmed by Dr. Michael Gannon that the floppy tip provided the best transition of flexibility from guide tip to the guide tube and wire. This system with the floppy guide tip was most convenient for delivery and placement. Therefore, the floppy guide tip was found to be the most feasible solution in the designing of the guide tip.

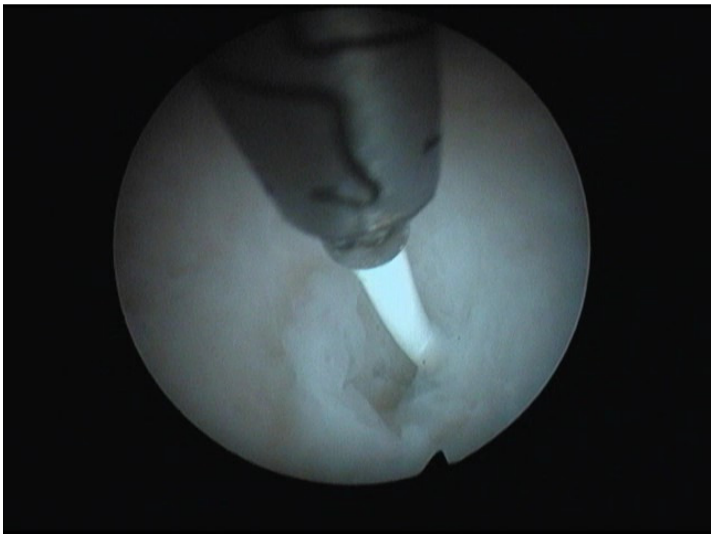

(a) Floppy Guide Tip

(b) Intermediate Guide Tip

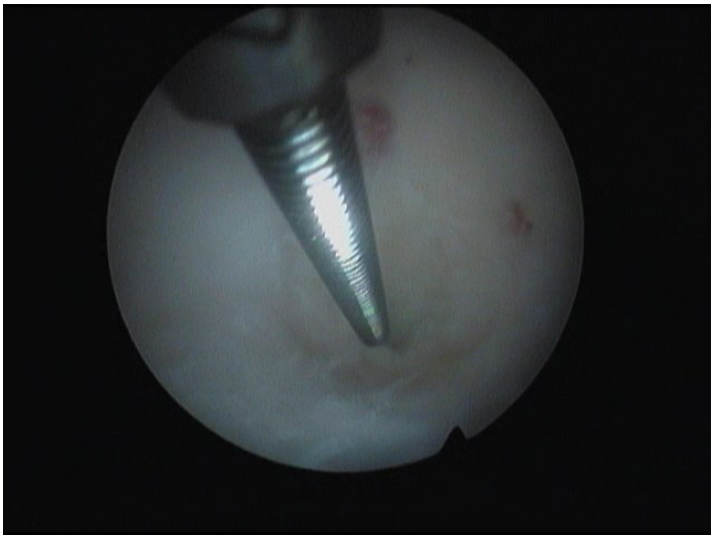

(c) Standard Guide Tip

FIGURE 4.43: HYSTEROSCOPIC VIEWS OF THE GUIDE TIPS

4.4.5. FINAL DESIGN OF GUIDE TIP AND CORE SHAFT

After functionality testing of the guide tip and feedback from Dr. Gannon, the flexibility of floppy guide tip was incorporated in the guide tip design. The floppy guide tip investigated was glued to the implant during testing. However, for *in-vivo* testing it is not recommended to leave glue inside the human body. In this research work, the requirement was to design a SS-316LVM guide tip that could be laser welded with the implant. Therefore, the task was to design a SS-316LVM guide tip having flexibility equivalent to the "nitinol core encased in polyurethane" guide tip. In order to achieve this flexibility, various SS-316LVM multi-filament cables were obtained from Fort Wayne Metals. The flexibility of these cables was measured using the Lloyd machine as discussed section 4.4.3. From these testing, it was found that a multi-filament (7x7x7) cable, with Ø 0.5 mm possessed flexibility comparable to the floppy guide tip. The cross sectional view of this cable is shown in Fig. 4.44.

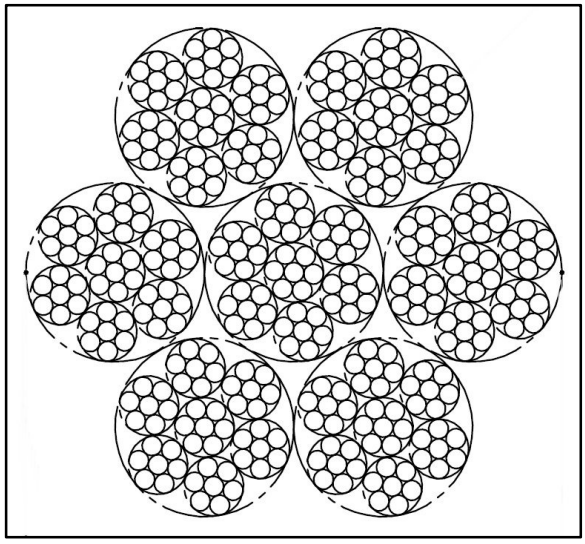

FIGURE 4.44: SECTIONAL VIEW OF 7x7x7 MULI-FILAMENT CABLE

As the diameter of the cable was only 0.5 mm, it was envisaged that a spherical ball shape at the distal end cable could provide a larger projected area, which would make it improbable to perforate the fallopian tube. Therefore, the final design of the guide tip includes a Ø 0.5 mm, multi-filament (7x7x7) cable with a Ø 1.0 mm spherical ball shape at the distal end as shown in Fig. 4.45. Fort Wayne Metals, Mayo, Ireland, fabricated the final design of the guide tip shown in Fig. 4.46.

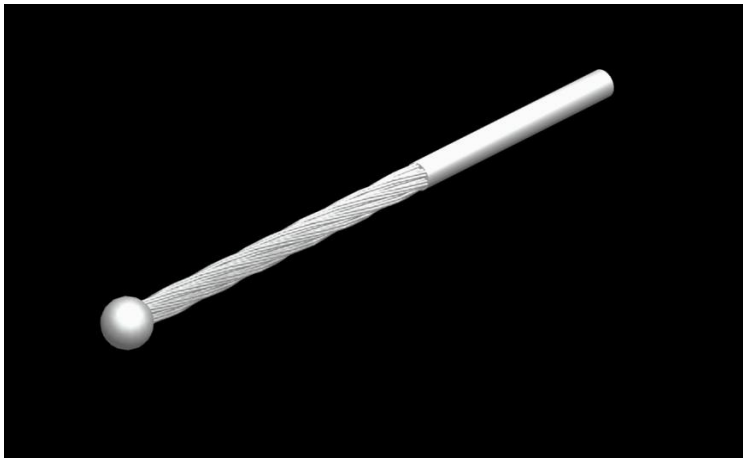

FIGURE 4.45: 3D CAD MODEL OF GUIDE TIP

FIGURE 4.46: FINAL DESIGN OF GUIDE TIP

The Core shaft was modified according to the final design of the guide tip as shown in Fig. 4.47. The centre hole is to assemble the guide tip. The first step is to locate the implant for laser welding and to provide a sliding surface to the implant during deployment. The second step at the proximal end aligns the release tube axially before laser welding. The final design of the guide tip and core shaft can be seen in Fig. 4.48.

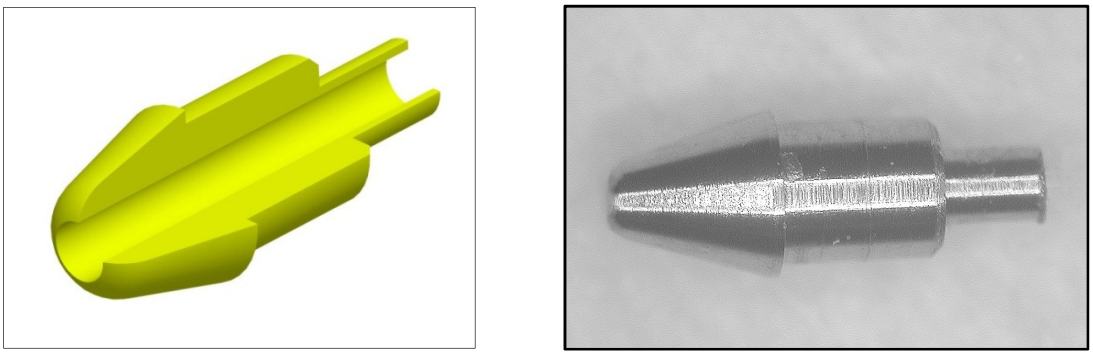

FIGURE 4.47: FINALIZED CORE SHAFT

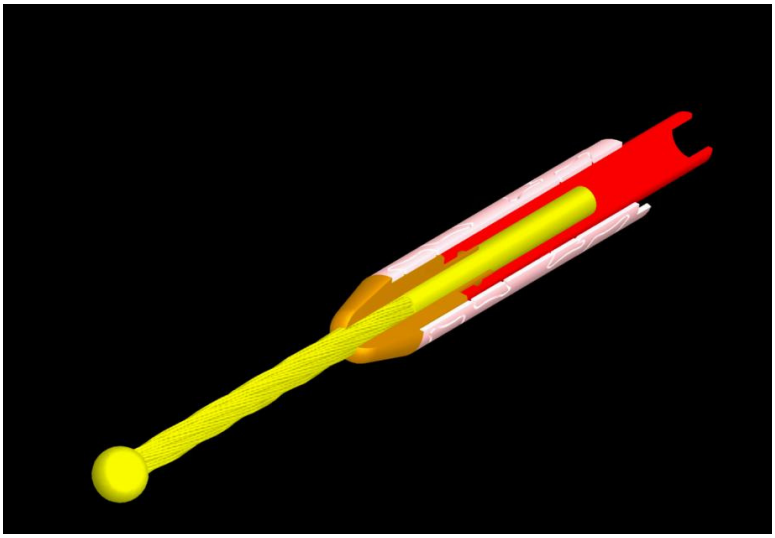

FIGURE 4.48: FINALIZED GUIDE TIP AND CORE SHAFT

The flexibility testing of the finalized guide tip of length 10 mm was performed in same manner as discussed earlier. The testing setup is shown in Fig. 4.49 and Fig. 4.50 Table 4.5 summarizes the deflection forces measured during these testing. It was found that the mean deflection force of the finalized guide tip is 0.09 N. Finally, the guide tip was evaluated in the explanted uterus for functionality and deliverability. The hysteroscopic view of the guide tip and core shaft approaching tubal ostium is shown in Fig. 4.51.

The functionality tests proved that the designed guide tip provided the ease of navigation through the anatomy of the fallopian tube. It was also observed that this guide tip has a fine balance between column strength (for push-ability and forward progression) and flexibility (to negotiate the curvatures of the uterus and fallopian tube).

TABLE 4.5: FLEXIBILITY TESTING OF FINALIZED GUIDE TIP

Test	**Deflection Force (N)**
1	0.090
2	0.089
3	0.091
4	0.091
5	0.090
Mean	0.090
Standard Deviation	0.00084
Standard Error of Mean	0.00037

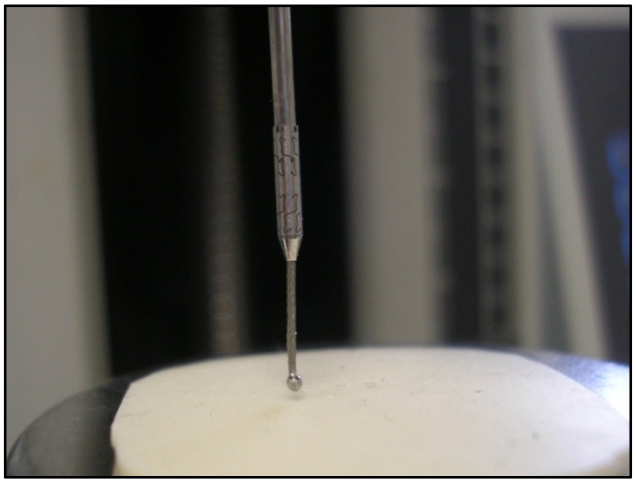

FIGURE 4.49: FLEXIBILITY TESTING OF GUIDE TIP

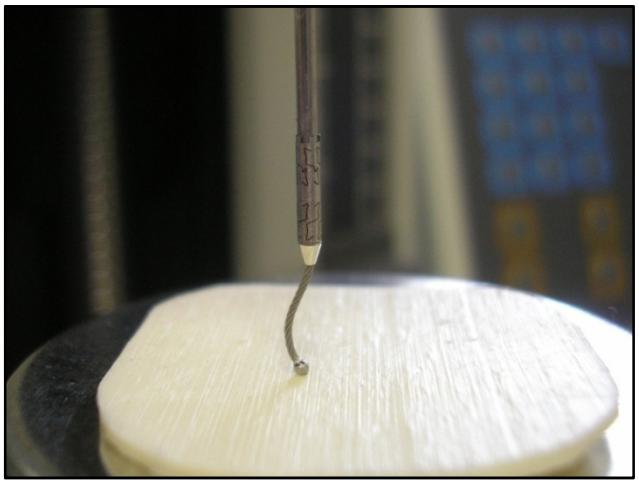

FIGURE 4.50: DEFLECTED GUIDE TIP IN FLEXIBILITY TESTING

FIGURE 4.51: HYSTEROSCOPIC VIEW OF GUIDE TIP DURING FUNCTIONAL TESTING

4.5. DESIGN, DEVELOPMENT AND VALIDATION OF RELEASE MECHANISM

Designing the release mechanism is the most important part of any medical device because of its risk factor. If the device is deployed and unable to release then there is no other way other than surgery to remove it. Most of the transcervical sterilization devices use an unscrew mechanism to release like ESSURE® and Adiana [91,95,98,100].

4.5.1. INITIAL CONCEPT

The initial concept of the release mechanism worked out on the super-elastic properties of nitinol wire. This mechanism involved the forced insertion of nitinol wire into the hole of the core shaft. In order to achieve this, a hole was drilled with an interference fit tolerance at the centre of the core shaft. The nitinol wire was inserted in the hole under a controlled axial force of 300 N using Lloyd machine. In order to release the wire, an opposing force was exerted on the nitinol wire. It was observed that with an insertion force of 300 N the range of release force was from 60 N to 90 N. The 3D model of this mechanism is shown in Fig. 4.52. The fabricated mechanism with nitinol wire before and after insertion into the core shaft is shown in Fig. 4.53.

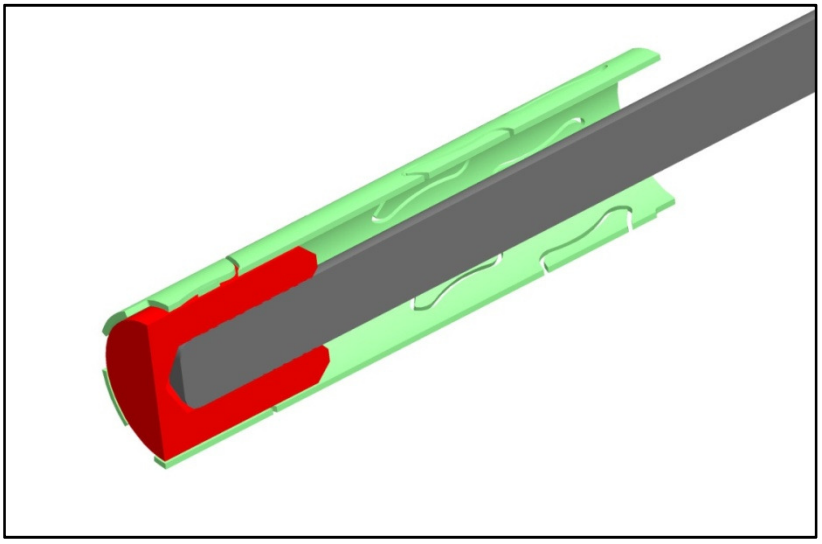

FIGURE 4.52: CAD MODEL OF INTERFERENCE FIT RELEASE MECHANISM

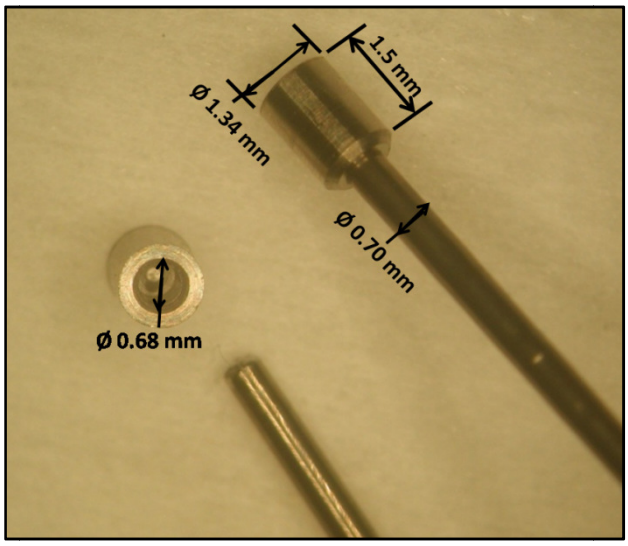

FIGURE 4.53: CORE SHAFT AND NITINOL WIRE IN INTERFERENCE FIT RELEASE MECHANISM

This simple mechanism was appealing and applicable but after a number of bench top tests the following limitations of this mechanism were observed:

1. No consistency in release force, ranges from 60 N to 90 N.
2. No physical or visual technique to inspect the insertion distance of nitinol wire in to the hole.
3. Requirement for very stringent tolerances in between the hole and wire diameter. If the tolerances are tight then it became difficult to release and if they are, loose then the implant releases before achieving 70 N force.
4. Dependent on the mechanical properties of the nitinol and core shaft material. The ductile material of core shaft allows to release under required force and stiff material increases the release force.

Therefore, an improved release mechanism was required for this research work.

4.5.2. FINAL DESIGN OF RELEASE MECHANISM

Based on the previous experience of mechanical designing of quick release systems and ejection mechanism, an innovative design was envisioned. The new mechanism was based on the tensile strength of the material in-use. It is well documented and proven that the tensile test specimen breaks at the neck region. The same concept of breaking of a dumbbell shape tensile specimen was applied in this mechanism. Due to the requirement of biocompatible material, SS-316LVM tubing was used in this design. The challenging task was to design a mechanism that can withstand the bi-directional torque

involved in the deployment of the implant. Therefore, a rectangular profile pattern was introduced to protect the neck region from the torque loading. The envisioned profile for the release mechanism for a tube of OD 1.3 mm is shown in Fig. 4.54. Because of the availability of high-end laser cutting machine, the profile cutting was not an issue. In order to design and optimise the profile for the required breaking load, a CAD model was generated and integrated optimisation was performed in ANSYS WB environment. The finalized design was extensively tested by performing tensile tests.

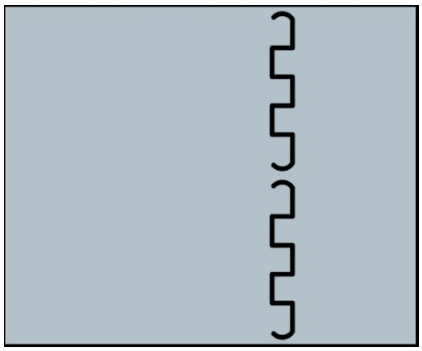

FIGURE 4.54: FLAT FORM OF DIAMETER 1.3 MM RELEASE PROFILE

A. DESIGN AND MODELING

As the ID of the implant is 1.34 mm, an initial thought was to use a tube with an OD 1.3 mm in the design of the release tube. However, a Ø 1.3 mm tube cannot be accommodated in the ID of the guide tube. Therefore, the only possibility was to accommodate the whole length of the release tube inside the implant body. In addition, the elongation of the release tube under breaking load also needed to be accommodated along the entire length of the implant. All these requirements of axial lengths were additions in the implant length. The Ø 1.3 mm release tube was fabricated and successfully tested. However, as mentioned in Section 4.3.6, it was decided to reduce the length of the implant. In order to achieve this goal, it was mandatory to reduce the diameter of the release tube from Ø 1.3 mm. Finally, the design of the release tube was modified to Ø 1.0 mm tubing to minimize the length of the implant.

The final design of release tube, with a length of 7 mm, an OD of 1.0 mm and a thickness of 0.125 mm is made of hardened SS-316LVM tube and includes a pair of slots. This symmetric pair of laser cut slots forms an arc shape at both ends and a rectangular pattern in between as shown in Fig. 4.55. The gap in between this pair of slots forms a neck region, which determines the breaking load of the tube. This gap is

designed to break at a specified tensile load. Once the implant is deployed into the intramural segment of the fallopian tube, the weak link designed on the release tube is broken by application of tensile force, releasing the implant from the guide system and consequently from the delivery actuator.

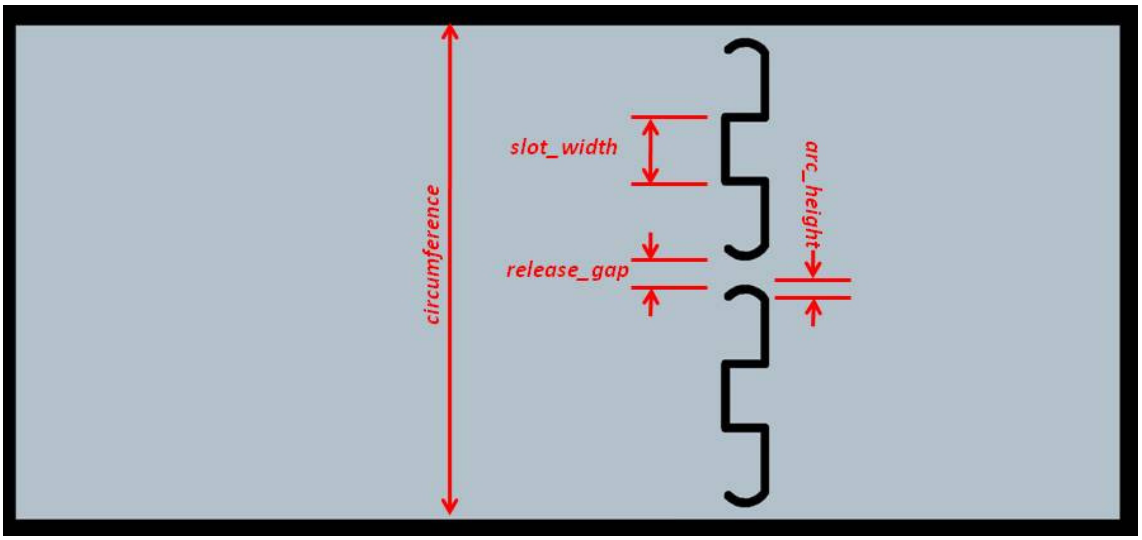

FIGURE 4.55: PROFILE ON RELEASE TUBE FOR BREAKING

FIGURE 4.56: 3D MODEL OF RELEASE TUBE

B. FEA AND OPTIMISATION

The parametric model of the release tube was generated in Pro/E as shown in Fig. 4.56. The design variable *release_gap* was defined for the half width of the neck region. This width of the neck region determines the breaking load of the tube. The variables *circumference, arc_height and slot_width* effecting profile of the release pattern were defined (Fig. 4.56). The relations in between this variable *release_gap* and rest of the profile dimensions were written, so that the complete profile of the release pattern could be varied during optimisation study as in Eq. 5.1.

$$release\_gap = (circumference - 4 \times arc\_height - 6 \times slot\_width)/2 \qquad \text{Eq. 5.1}$$

This equation allowed the width of neck region to vary by varying design parameter without affecting the rest of the profile shape.

The procedure described in Chapter 3 was followed for the optimisation process. The 3D parametric model was integrated with the ANSYS WB for the design optimisation. Due to mirror symmetry, half of the model was generated. Non-linear analysis was defined in ANSYS WB in order to cope with plastic deformation and elongation before break. A bilinear isotropic hardening rule was adapted to describe the mechanical properties of the material. Material properties of annealed SS-316LVM were assigned in the ANSYS WB environment. The boundary conditions were applied by applying symmetry on the longitudinal plane and fixed displacement at the distal end of the release tube. The tensile load of 70 N in the form of pressure was applied in 7 load steps at the proximal end. Mesh dependency was tested by meshing and analyzing the model with tetrahedron and hexahedron elements. After analyzing the results the volume of the implant was meshed with the tetrahedron elements and there were 5657 nodes and 2812 elements in the model as shown in Fig. 4.57. The default mesh size was refined at the necking region. The model was meshed and initial analysis was performed. The design variable *release_gap* was varied from 0.15 mm to 0.25 mm for the optimisation study. The response of von-Mises stress with respect to the design variable was plotted as shown in Fig. 4.58. After achieving the optimum release gap at a breaking load of 70 N, the parameters were simultaneously updated in the Pro/E environment hence updating the 3D model. A final analysis was performed on the optimum geometry to verify the results of optimisation study as shown in Fig. 4.59.

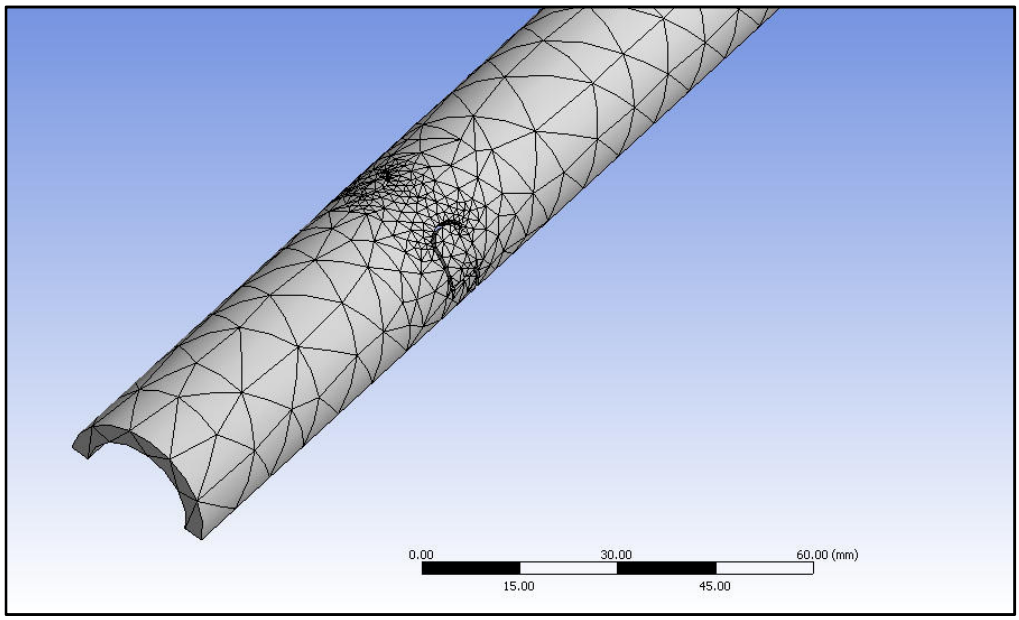

FIGURE 4.57: FE MESH OF RELEASE TUBE

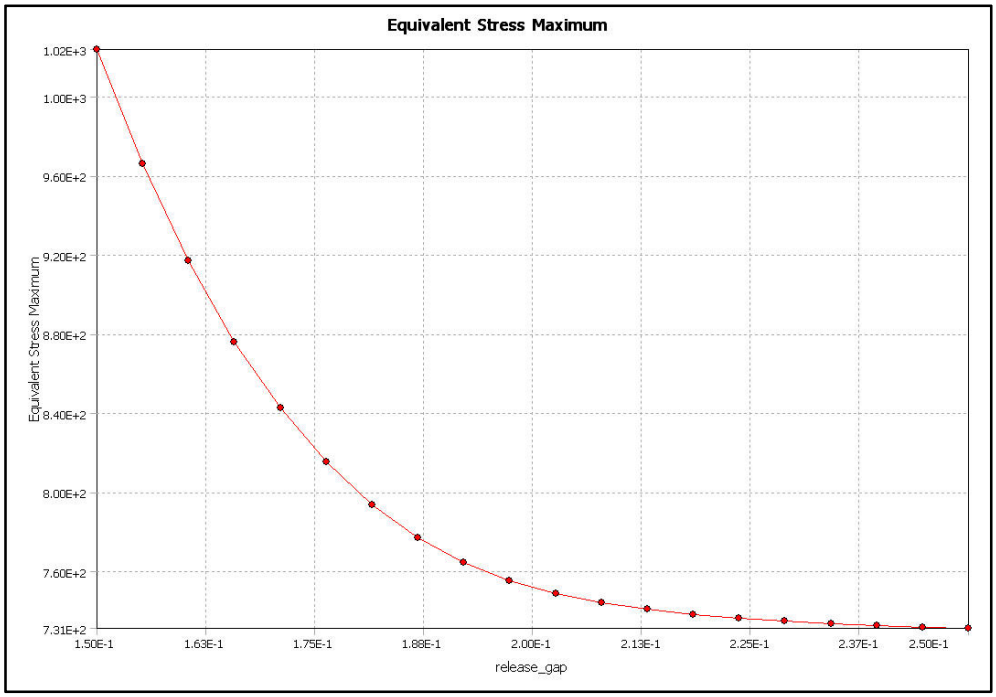

FIGURE 4.58: RESPONSE OF VON-MISES STRESSES VS. DESIGN VARIABLE

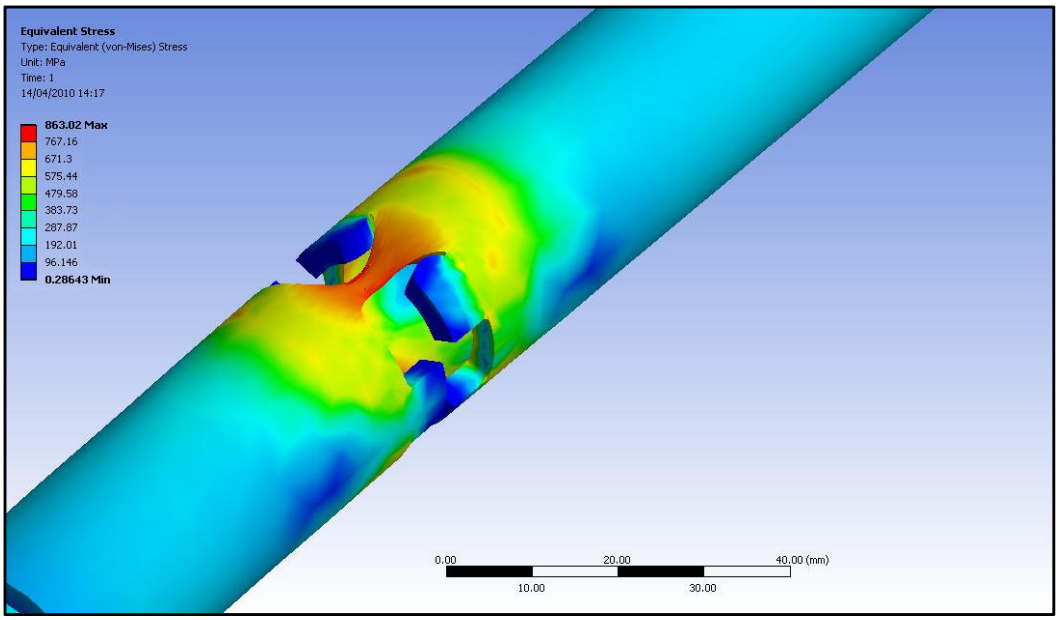

FIGURE 4.59: VON-MISES STRESS DISTRIBUTION AT FINAL ANALYSIS

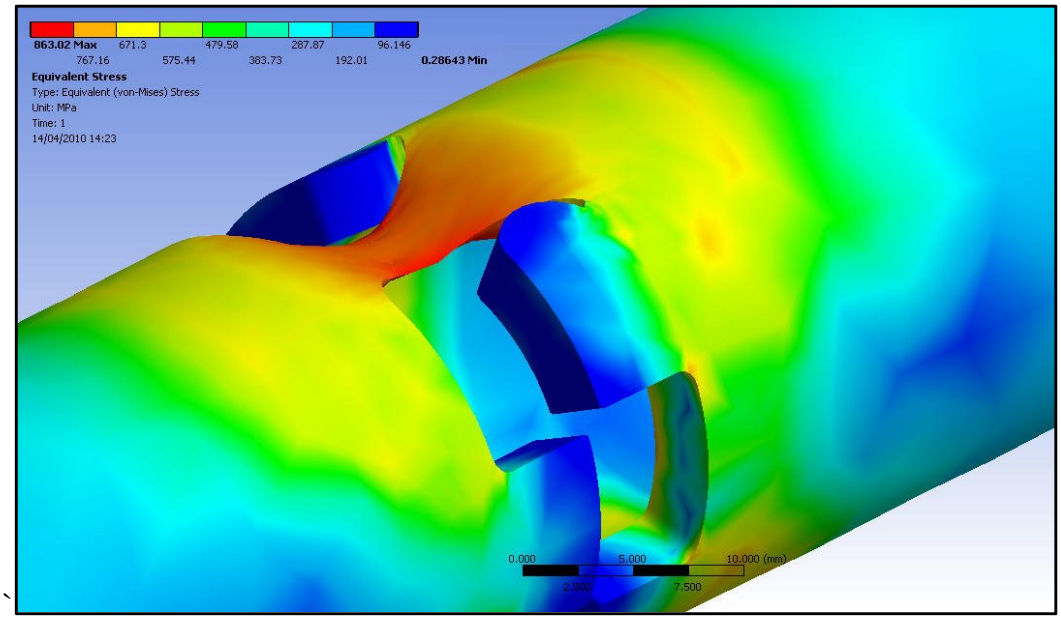

FIGURE 4.60: NECKING AT THE RELEASE GAP

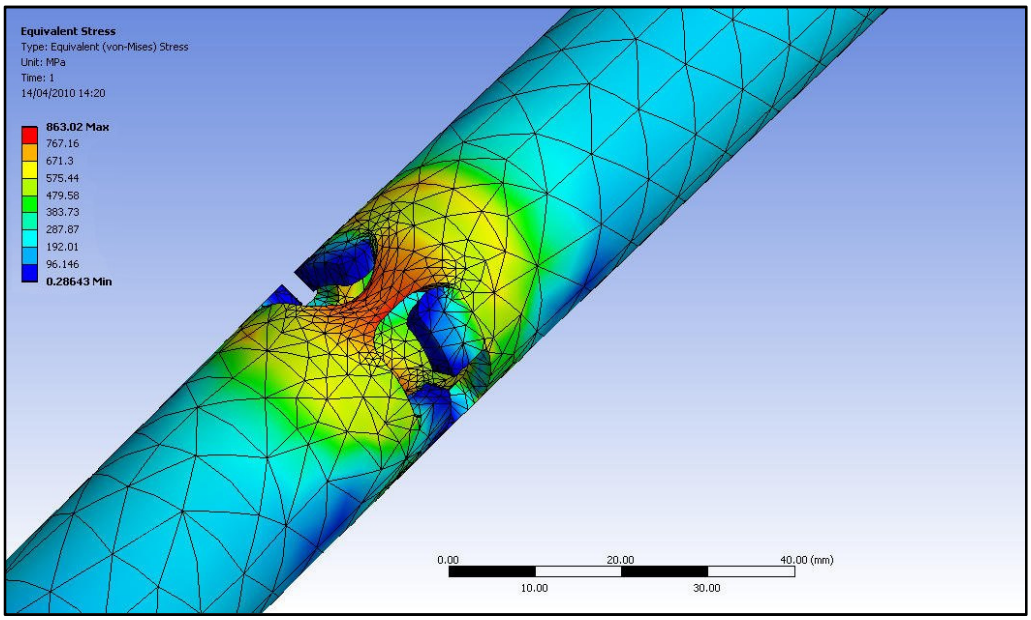

FIGURE 4.61: FE ELEMENTS AT FINAL LOAD STEP

It can be observed from Fig. 4.59 that the von-Mises stresses exceed the UTS of the material at a release gap of 0.34 mm (*release_gap* = 0.17 mm x 2) under loading of 70 N. Therefore, release gap of 0.34 mm is the optimised value at which the release tube would break under a load of 70 N. Therefore, the design was finalized using this value for a breaking load of 70 N. The FEA simulation also showed the necking of the release gap before break as seen in Fig. 4.60. The FE mesh at the final load step can be seen in Fig. 4.61.

C. DEVELOPMENT AND VALIDATION

The optimum design achieved from the optimisation study was fabricated on the LPL stent cutter. The fabricated release tube is shown in Fig. 4.62. The design was further validated by performing tensile break testing on Lloyd machine. The sample for testing was prepared by laser welding two SS-316 hardened wires at both ends of the release tube as shown in Fig. 4.63. These wires were gripped in the chucks of the Lloyd machine as shown in Fig. 4.64. Pull to break test was defined on the machine and the test was performed on eight samples. Table 4.6 summarizes the breaking load measured on these samples during testing. This table shows that the breaking load of the samples was in between 68 N to 71 N The representative graph of load versus extension is shown in Fig. 4.65. The mean of the test was 70 N with a standard deviation of 1.301 and percent error of mean 0.45998.

FIGURE 4.62: FABRICATED RELEASE TUBE ON LPL STENT CUTTER

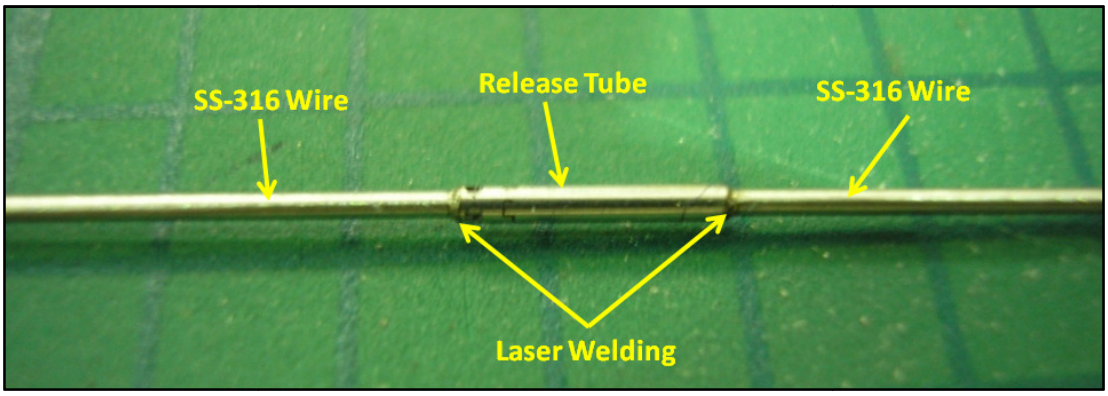

FIGURE 4.63: SS-316 WIRES LASER WELDED AT BOTH ENDS OF RELEASE TUBE

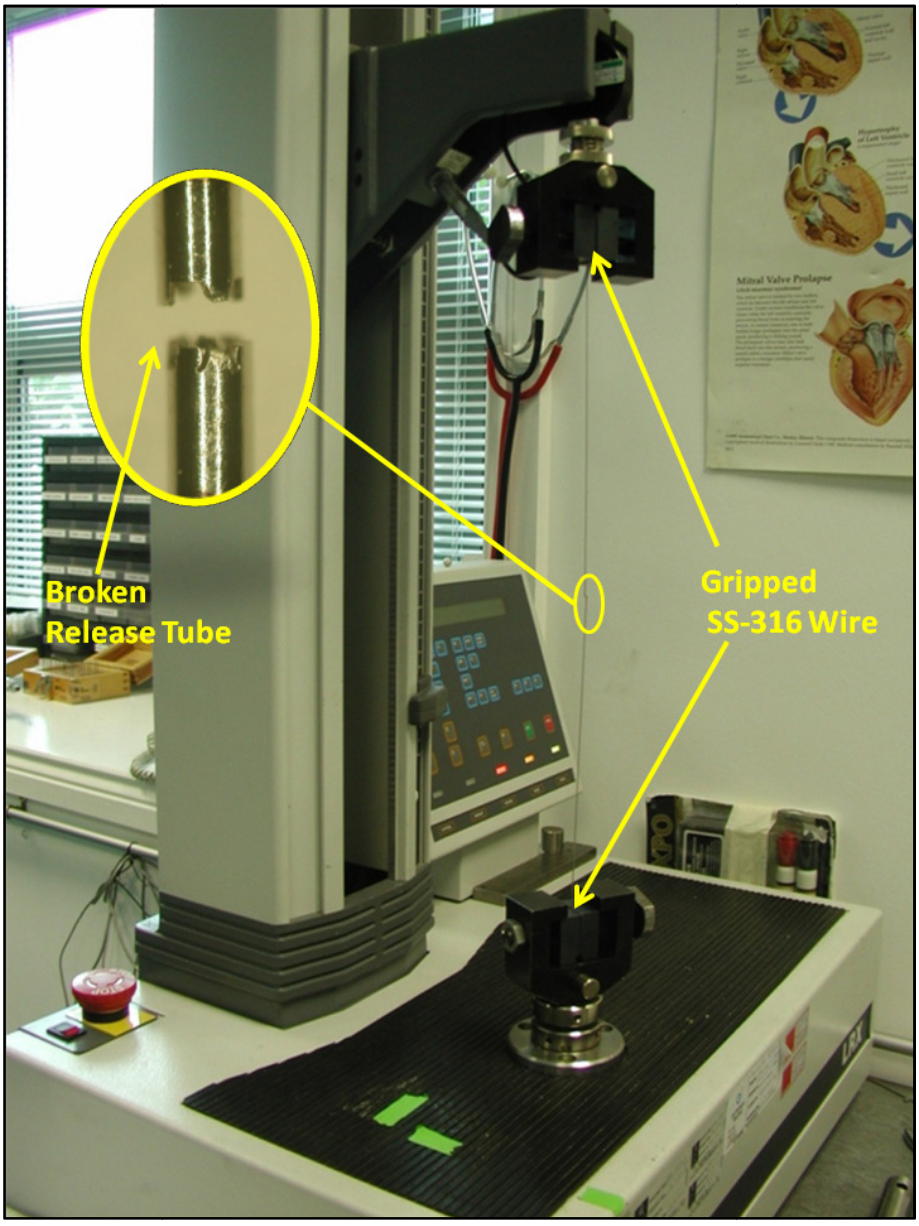

FIGURE 4.64: BROKEN RELEASE TUBE IN TENSILE TESTING

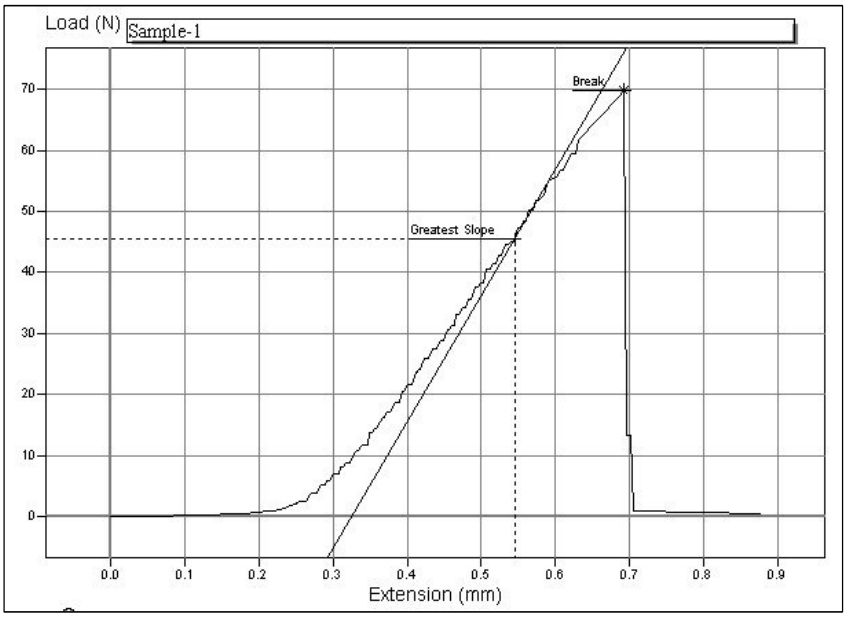

Figure 4.65: Tensile testing of Release tubes

TABLE 4.6: TENSILE TESTING OF RELEASE TUBE

Sample	Release Force (N)
1	70.101
2	71.216
3	70.051
4	67.510
5	71.024
6	71.421
7	68.793
8	69.125
Mean	70.005
Standard Deviation	1.30104
Standard Error of Mean	0.45998

4.6. FINALIZED COMPLETE OCCLUSION IMPLANT

The finalized design possessing all the characteristics an ideal occlusion implant is shown in Fig. 4.66.

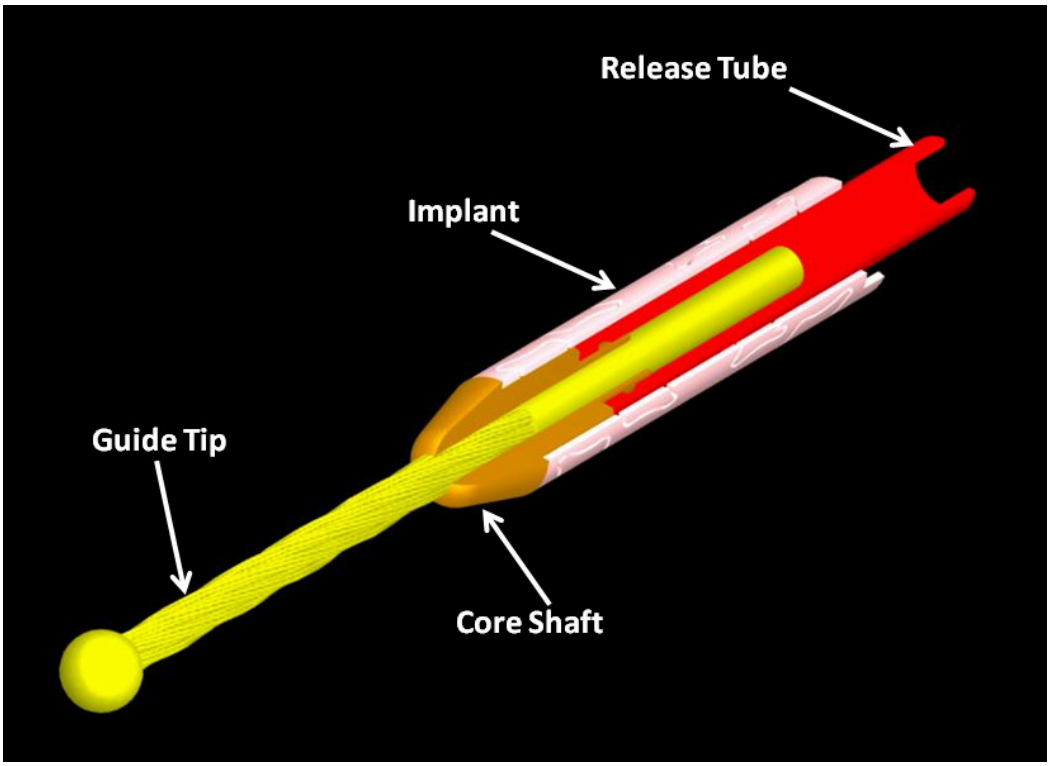

FIGURE 4.66: OCCLUSION IMPLANT ASSEMBLY

It is obvious from the size of the implant (Fig. 4.67) that it has a low profiled shape and can be easily inserted through a small calibre hysteroscope. The finalized implant post-deployment is shown in Fig. 4.68.

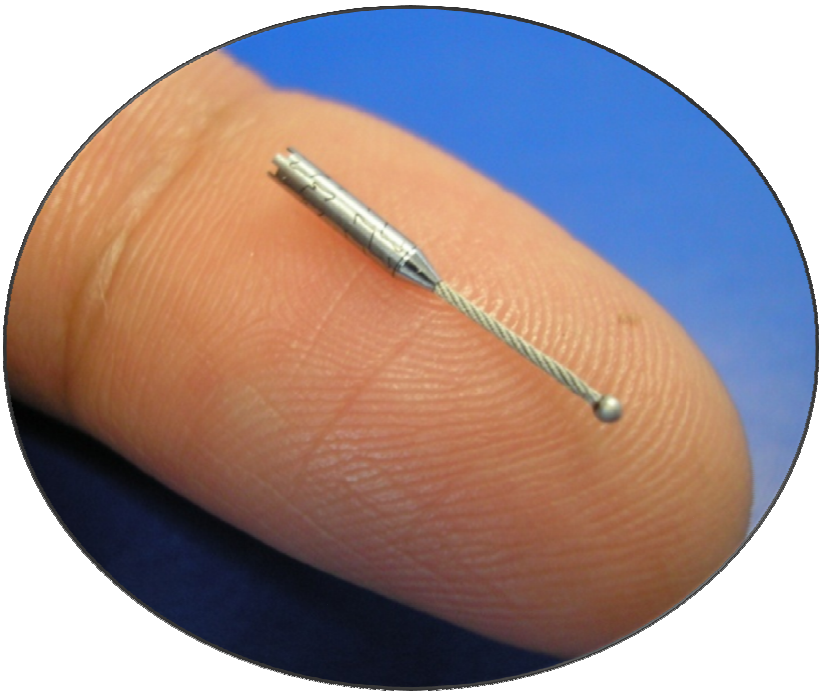

FIGURE 4.67: IMPLANT PRE-DEPLOYMENT

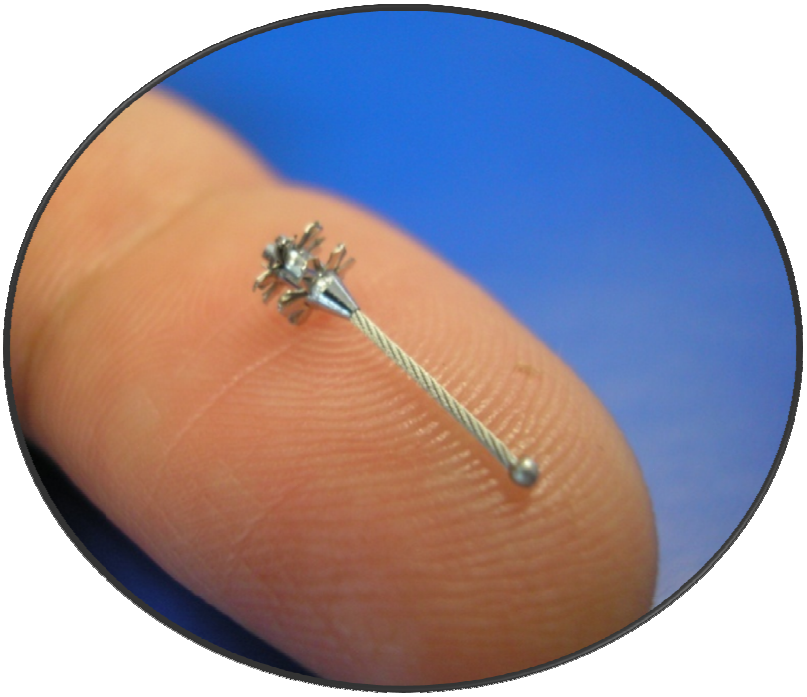

FIGURE 4.68: FINALIZED IMPLANT POST-DEPLOYMENT

CHAPTER 5

DESIGN, DEVELOPMENT AND VALIDATION OF GUIDING SYSTEM

5.1. INTRODUCTION

Internationally, the access to the internal organs of the human body using a normal body passage is not possible without a reliable guiding system. Such a system should not either cause damage or perforation of internal organs. A guiding system therefore is a key element in the overall design of a medical device. The following chapter outlines the design and development of the guiding system including a guide wire and guide tube.

5.2. DESIGN APPROACH FOR THE GUIDING SYSTEM

Initially it was decided to use the commercially available guiding system for this research work. Therefore, various guide tubes and guide wires were sourced and tested. However, it was observed after the testing that the commercially available guide tubes and wires were unable to meet the required criterion. Hence, it was decided to design a customized guiding system for this research work. Fig. 5.1 shows the design approach followed in the designing of the guiding system.

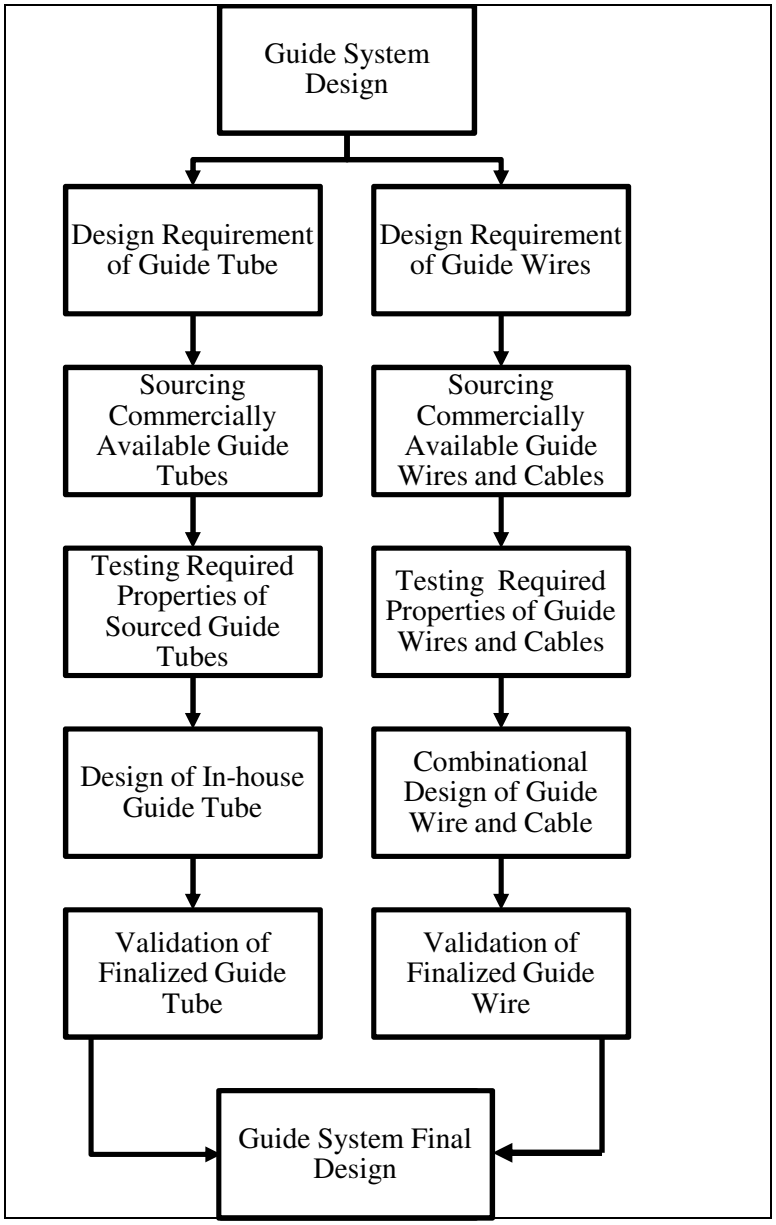

FIGURE 5.1: DESIGN APPROACH FOR THE GUIDING SYSTEM

5.3. DESIGN REQUIREMENT OF THE GUIDING SYSTEM

The demand for specialized guiding system has been brought about by the increase in the number of medical interventions performed percutaneously. The following properties are the basic requirements of a guiding system.

a) Column strength

Column strength is the ability of the guiding system to transmit a longitudinal force applied at the proximal end to the distal end of a device. It can be defined as the ratio of input force at the proximal end to output force at the distal end.

Ideally, when a pushing movement or force is applied on the proximal end of a shaft, an equal movement and force should be transmitted to the distal end. Therefore, adequate column strength was one of the basic requirements for pushability and forward progression of the guiding system. This feature allows the physician to easily navigate the device to approach the desired target.

b) Flexibility

Flexibility is required to negotiate the anatomy of the uterus tortuous paths. In addition, a fine balance between excessive column strength to avoid perforation and too much flexibility to avoid bunching was essential. Flexibility can be measured by either the amount of deflection in the guiding system under a certain load or the bending radius achieved by the system.

c) Torqueability

Torqueability is the ability of the guiding system to transmit a moment or a rotational displacement along the length of the device. In order to steer the device through the uterus and to deliver a high-level tactile feedback to the physician, a certain amount of torsional manipulation is required. A device, which responds well distally to proximal rotational manipulation, makes navigation effortless.

d) Kink Resistance

Kink resistance is the ability to retain the original cross-section of the guiding system under compressive loading. If a guiding system is bent around a small enough radius, a permanent kink can result, which can compromise both the internal lumen and the mechanical properties. A severe kink could lead to a device breakage, which may cause complete failure.

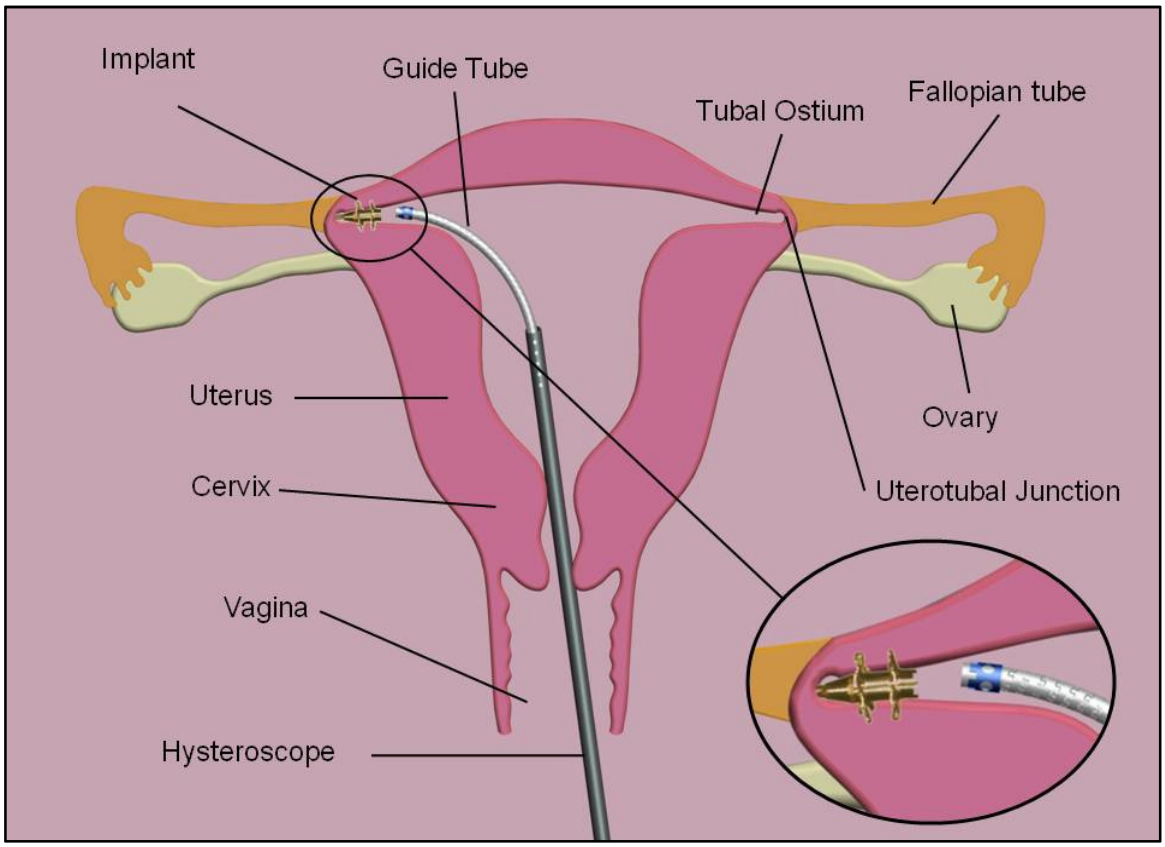

FIGURE 5.2: DELIVERED IMPLANT AT THE LEFT FALLOPIAN TUBE

In this research work, the implant needs to be delivered into the tubal ostium through the cervix using the normal body passage as shown in Fig. 5.2. The tubal ostium is approached via the guiding system, which comprises of an outer guide tube and an inner guide wire. This combination of guide wire and guide tube is also used to transmit the required forces to the implant. The requirement was to transfer a clockwise and counter-clockwise torque followed by compression and tension from the delivery actuator to the implant. Therefore, designing such a guide system was a challenging task when compared to a standard system. In addition to the properties mentioned earlier, the following were also required from the guiding system:

a) Trackability

Trackability can be defined as the capability of the guiding system to track through the desired body passage to its target destination. The friction between the device and its surrounding environment influences trackability. As the device is designed to deliver through a hysteroscope having a metallic instrument channel, a low friction between the device and the hysteroscope was required. The lower the tracking forces, the easier it would be to handle and position the device.

b) Stretch Resistance

This property describes the ability of the guiding system to transfer a tensile force. As noted previously, a compressive force is required for the deployment of the implant and a tensile force for its release mechanism. Therefore, the guide wire should be able to withstand the required tensile force with minimum elongation.

5.3.1. UTERUS PERFORATION FORCE (FLEXIBILTY REQUIREMENT)

An important factor in the design process of the guiding system was to quantify the flexibility requirement. Flexibility is required to negotiate the curvature of the uterine anatomy and to prevent perforation. This complication (uterus perforation) can occur with the use of a stiffer guiding system during hysteroscopy [164]. Despite of this importance, no effort has been made by researchers to measure the uterus perforation force. However, some literature is available on perforation of the uterus with intrauterine devices (IUD) [164,165]. The IUD devices are *T* or *U* shaped, with greater surface area. Therefore, perforation forces of these devices could not be used in this research. It was therefore, decided to measure human uterus perforation force in the laboratory setup. The perforation force was measured on tissues of two different explanted human uteri removed at hysterectomy for various benign indications. Small portions of the uterus were dissected longitudinally and placed on a perforated plate having a small diameter holes. Perpendicular perforation with the blunt end of a hardened SS-316 wire, with a 0.7 mm diameter was measured using the Llyod universal testing machine. As compared to the diameter of the implant, a Ø 0.7 mm wire was selected to measure the perforation force as a worst-case scenario. The setup for the measurement of the perforation force is shown in Fig. 5.3. The wire approaching and penetrating tissue is shown in Fig. 5.4 and Fig. 5.5 respectively. The perforated uterus tissue is shown in Fig. 5.6.

Test was repeated four times at different locations of the uterus tissue. Fig. 5.7 shows the representative graph of the perforation force against penetration of SS-316 wire. The three peaks in the graph represent the three layers of the uterus walls, which were perforated one after another. The first peak indicates the perforation of outer layer, which was the value of concern. Among four tests, the recorded values were 8.62 N, 8.78 N, 8.502 N and 8.69 N. The minimum 8.5 N of these perforation forces was considered for additional safety.

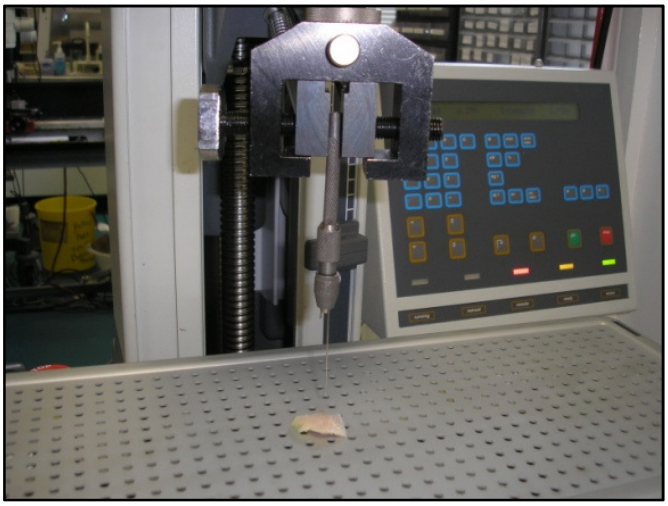

FIGURE 5.3: UTERUS PERFORATION FORCE MEASURING SETUP

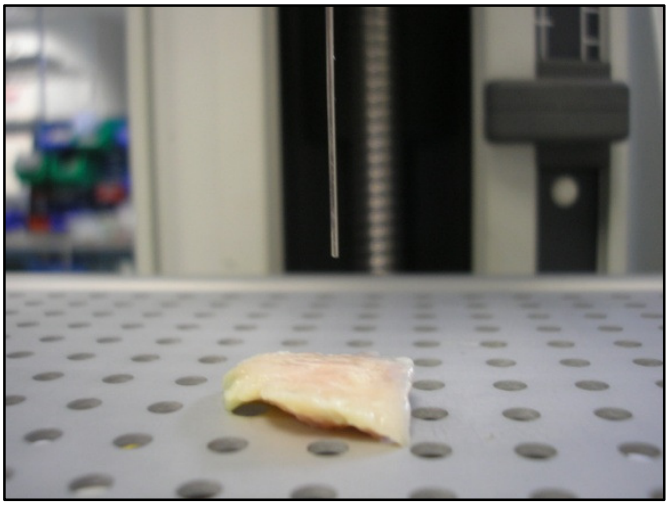

FIGURE 5.4: CLOSE-UP OF SS-316 WIRE AND UTERUS TISSUE

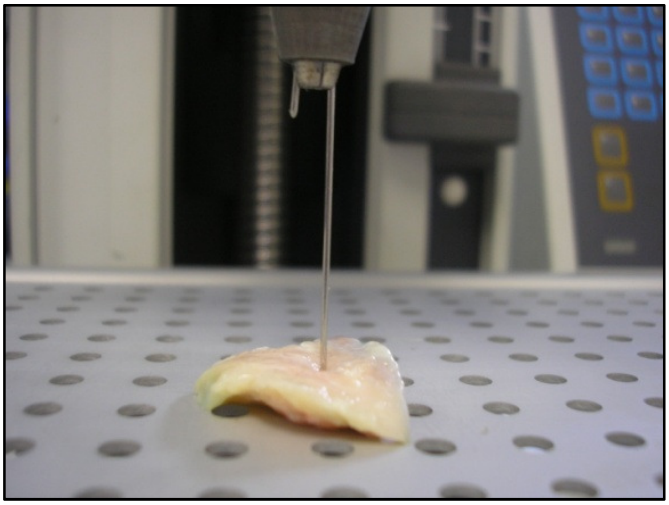

FIGURE 5.5: WIRE PUSHING THROUGH TISSUE

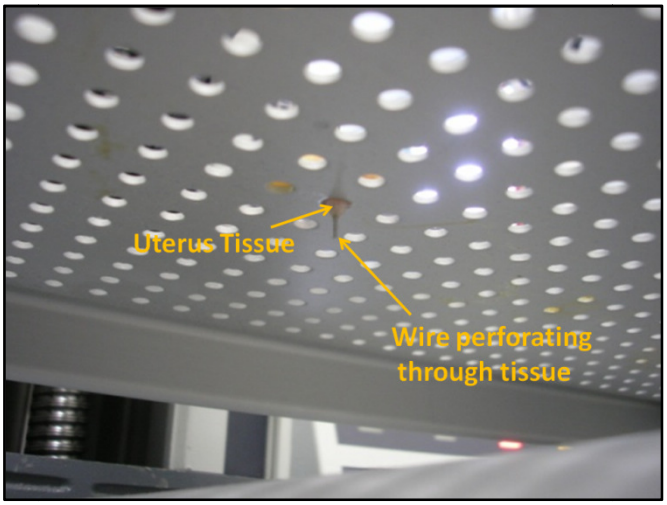

FIGURE 5.6: WIRE PROTUDING OUT OF PERFORATED TISSUE

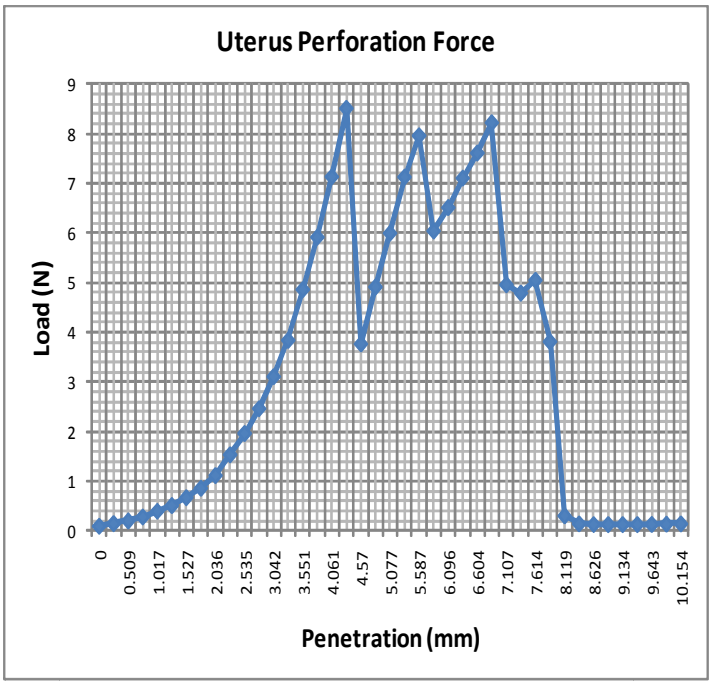

FIGURE 5.7: UTERUS PERFORATION FORCE AGAINST WIRE PENETRATION

5.4. DESIGN, DEVELOPMENT AND VALIDATION OF THE GUIDE TUBE

In order to attain an optimum guide tube for this research work, a measure of the performance characteristics; column strength, flexibility, torqueability, kink resistance and trackability were required. Acquiring such a guide tube possessing all the characteristics was not an easy task. Therefore, a number of commercially available hypotubes were tested for their physical and mechanical properties to arrive at an effective solution and to investigate the desired properties of a guide tube.

5.4.1. SIZING AND DIMENSIONS

The guide tube has to couple with the implant's crown in order to transfer forces. Therefore, the diameter of the guide tube needed to be comparable with the implant. There was no possibility to fabricate the coupling crown at the distal end of the tubing. Therefore, the only possibility was to separately fabricate the crown from SS-316 tubing and then welding it onto the guide tube as shown in Fig. 5.8. In this configuration, the required diameter of the crown was 1.535 mm. To achieve this configuration, the maximum possible diameter of the guide tube was 1.30 mm.

The length of the guide tube was dependent on both the working length of instrument channel of the hysteroscope and the anatomy of the uterus. Therefore, the necessary length of the guide tube required to approach the fallopian tube beyond the distal end of hysteroscope was obtained using uterus diagnostics models and from available literature. It was found that the total length of the guide tube require to reach the fallopian tubes irrelevant of the size of the uterus is 350 mm. This length measures in between the implant's proximal end and the actuator distal end.

FIGURE 5.8: A COUPLING CROWN WELDED ON GUIDE TUBE

5.4.2. ACTONE® HYPOTUBE

Two different types of flexible metallic ACTONE® hypotubes consisting of multifilar wires were investigated for their properties. The first type was a simple hollow rope hypotube and the second was with a grounded smooth surface as shown in Fig. 5.9. These ACTONE® tubes, with an OD of 1.3 mm were provided by ASAHI INTECC USA. Ltd. The multifilar cable tubes features high torque transmission, pushability, low elongation, and kink resistance [166]. They also offer a degree of flexibility between that of a conventional stainless-steel hypotube and that of a conventional stainless steel coil [166]. The torque performance comparison of these tubes provided by ASAHI INTECC is shown in Fig. 5.10. However, after torque testing it was found that the hypotubes follow these curves in one torque direction only.

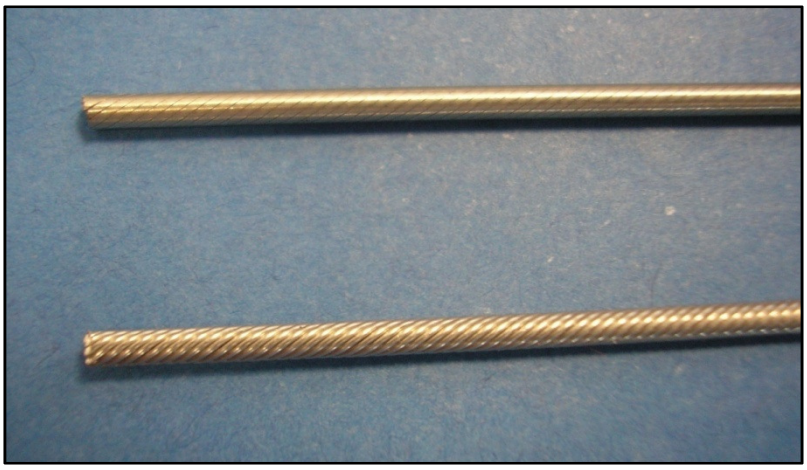

FIGURE 5.9: ACTONE HYPOTUBES

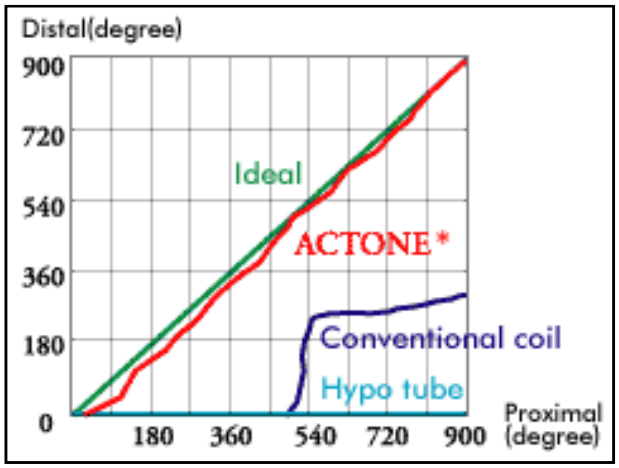

FIGURE 5.10: TORQUE PERFORMANCE COMPARISON [166]

5.4.3. CREGANNA HYPOTUBE

This specially designed laser cut hypotube shown in Fig. 5.11 was provided by Creganna, Tactx Medical, Ireland. This tube, with an OD 1.3 mm and thickness 0.2 mm is made of SS-316. It features a series of intermittent 1080° spiral laser slots with slot width 0.15 mm to incorporate flexibility into the SS-316 tubing.

FIGURE 5.11: CREGANNA HYPOTUBE

5.4.4. SPIRAL CUT HYPOTUBE

This hypotube was in-house developed to improve the torqability and the flexibility properties of the Creganna hypotube. The intermittent spiral cut pattern of Creganna tube was modified by reducing both the width of laser cuts and intermittent gap as shown in Fig. 5.12. This tube was fabricated with Ø 1.3 mm and thickness 0.125 mm tube, made of SS-316LVM. The spiral cutting was performed using laser cutting machine, LPL Stent cutter.

FIGURE 5.12: SPIRAL LASER CUT TUBE

5.4.5. COMPARITIVE ANALYSIS OF HYPOTUBES

As part of the research work, the mechanical properties of all four types of hypo tubes were investigated to determine their effectiveness. The investigation included flexibility and torqability testing.

A. FLEXIBILITY TESTING

During hysteroscopy, it was observed that in both human uterus, diagnostic model, only a small length of guide tube emerges out of the hysteroscope, and the remainder stays inside the instrument channel. This “emerged” portion of the guide tube flexes to navigate through the uterus, tubal ostium and into the fallopian tube. The maximum required length of this flexible portion was determined as 60 mm. To conduct the testing, 80 mm length samples were prepared from each type of hypotubes. Out of this 80 mm, 20 mm was required to grip the tubes in the chuck of Lloyd tensile testing machine.

The setup for the test is shown in Fig. 5.13, in which 20 mm of the hypotube is held in the upper grip of the machine through a miniature load cell. Gauge pins were introduced inside the tube ends to prevent squashing. A rubber padded cylindrical stand was mounted at the lower grip location to prevent tube slippage during testing. The machine was programmed to apply a 5 mm longitudinal displacement on the hypotubes and to measure the deflection load. The graphs of the displacement versus deflection load for each type of hypotube were obtained. The peak load was observed just before deflection when the hypotube made its initial contact with the rubber lining of the cylindrical stand. The deflected hypotube under applied displacement is shown in Fig. 5.14.

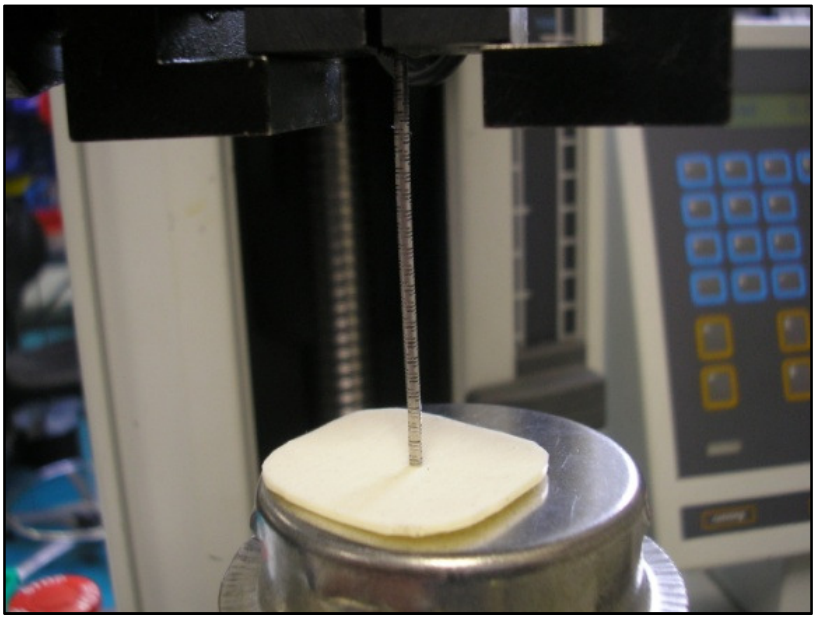

FIGURE 5.13: CREGANNA HYPOTUBE GRIPPED IN TENSILE TESTING MACHINE FOR FLEXIBILITY TESTING

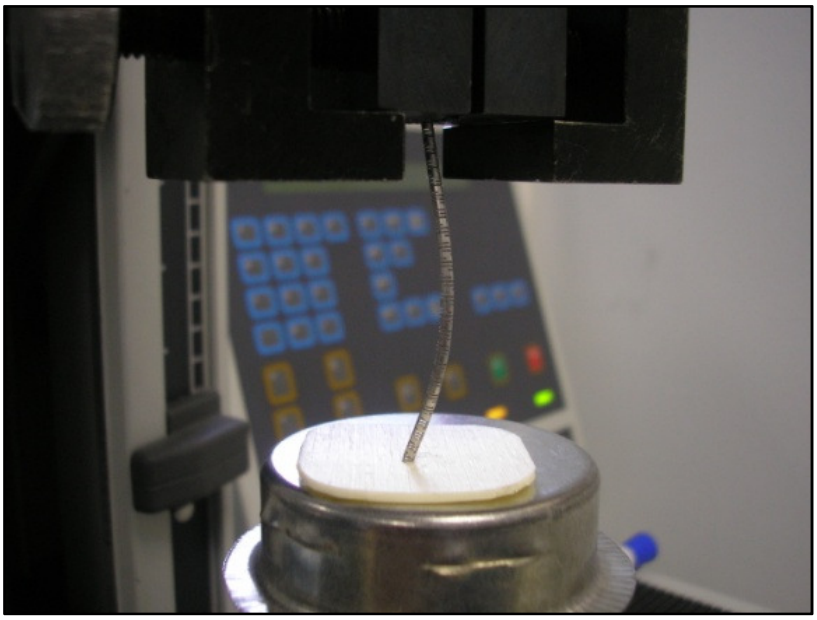

FIGURE 5.14: FLEXED HYPOTUBE UNDER LONGITUDNAL LOAD

B. TORQABILITY TESTING

As discussed in Chapter 4, to deploy the implant the hypotubes are required to transmit a torque of 16 N-mm in both directions. Therefore, torque testing of the tubes was performed using IMADA portable torque testing equipment. Samples of hypotubes with a length of 200 mm were prepared for this testing. One end of the hypotube was clamped inside the chuck of the torque meter and the opposite end was gripped in a handle specially fabricated for this test, as shown in Fig. 5.15. A measured torque of 16 N-mm was applied from the handle and the rotational angle was measured using a bevel protector. The effect of the applied torque on the hypotubes was also visually inspected under the microscope. It was observed in this testing that both the Creganna and spiral cut hypotubes failed to transmit the required torque of 16 N-mm. The Creganna and spiral cut hypotubes after torque testing are shown in Fig. 5.16 and Fig. 5.17 respectively.

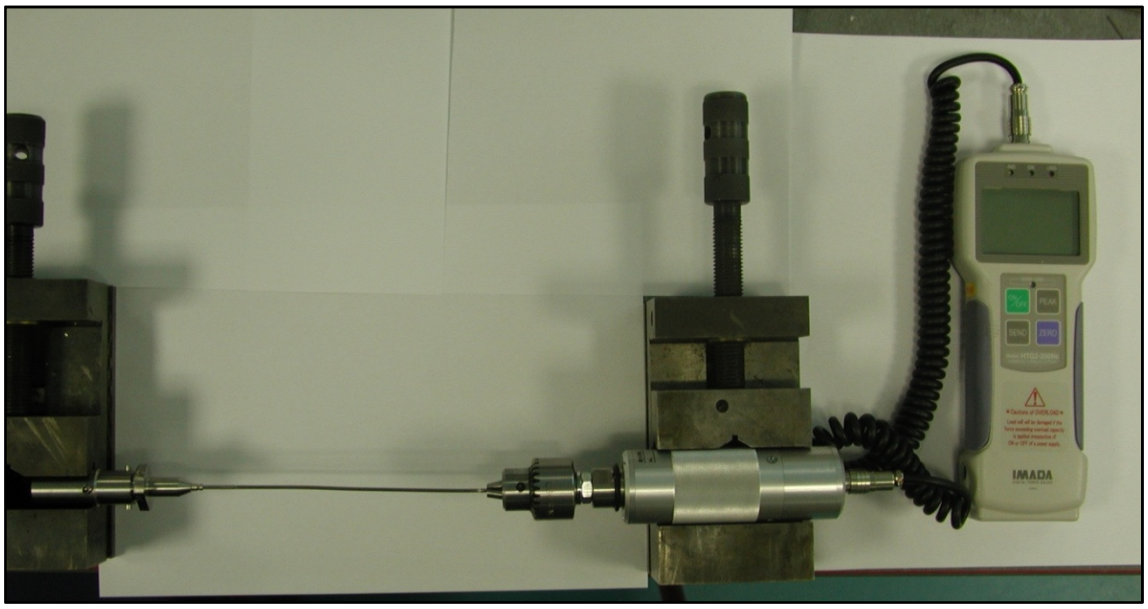

FIGURE 5.15: TORQUE TESTING OF HYPOTUBES

FIGURE 5.16: CREGANNA TUBE UNDER TORQUE

FIGURE 5.17: SPIRAL CUT TUBE UNDER TORQUE

The flexibility and torqability tests were performed on all four hypotubes mentioned earlier. Table 5.1 presents the summary analysis:

TABLE 5.1: COMPARATIVE ANALYSIS OF HYPOTUBES

Hypotube	Diameter (mm)	Flexibility (Deflection Load N)	Torqability		Bio-compatibility
			CW°	CCW°	
ACTONE® Original	1.3	7.62	160	180	Yes
ACTONE® (Grounded)	1.3	6.32	150	190	Yes
CREGANNA	1.3	1.37	Failed	Failed	Yes
Spiral Cut	1.3	0.98	Failed	Failed	Yes

5.4.6. GUIDE TUBE FINAL DESIGN

After performing the tests on the commercially available hypotubes, it was realized that they could not be used in this research work. This is in part due to the fact that this work required a hypotube, which could transfer a one-to-one torque in both directions; must have a deflection force of less than 8.5 N and sustain a 70 N compressive force without any kink. It was also observed during hysteroscopy that friction exists between the guide tube and the instrument channel of the hysteroscope because of their metallic surfaces. Therefore, trackability was an additional requirement from the guide tube.

Considering all the testing results and observations, the optimum guide tube design was required to have a balance of all the following performance characteristics: column strength, flexibility, torqueability, kink resistance and trackability. However, the best performance in one characteristic was directly affecting the other characteristics.

Therefore, an innovative design was required that could cope with these conflicting desirables.

A. DESIGN AND CALCULATIONS

To achieve the best possible design, all the design requirements for a guide tube applicable for this study were listed:

1. Pushability can be achieved by:
    a) Maximizing cross-sectional area of guide tube.
    b) Using a stiffer material having higher modulus of elasticity.
    c) Using material of higher tensile strength.
2. Torqability can be improved by:
    a) Maximizing polar moment of inertia of the guide tube.
    b) Using a stiffer material having higher shear modulus.
3. Kink resistance can be increased by:
    a) Maximizing wall thickness of the tube.
    b) Using material of higher ductility.
4. Trackability can be enhanced by:
    a) Reducing friction in between guide tube and hysteroscope.

In order to achieve maximum of all cross-sectional area, polar moment of inertia and wall thickness of the guide tube, the OD was kept at the maximum possible value and the ID at a minimum. Therefore, 1.3 mm as OD and 0.125 mm as thickness were decided for the guide tube. It was decided to use SS-316LVM hardened tube to achieve higher modulus of elasticity, tensile strength and shear modulus. In order to reduce friction between guide tube and hysteroscope, heat shrink tubing was recovered on the guide tube.

The flexibility at the distal end of the guide tube was achieved by the addition of segmented (inter-segment gap of 0.32mm) chains of “dove tail” shaped helical slots with a pitch of 0.87 mm as shown in Fig. 5.18. These laser-cut slots shape were designed to provide the required flexibility and torqability. The helical profile of the slots provided the required flexibility to the shaft. While the addition of dovetail shape provided stability during torque application.

In order to deal with the curvatures of the cervix and fallopian tube without perforation, the guide system needed to be flexible. On the other hand, stiffness was required to transfer one-to-one torque to the implant. It was observed during hysteroscopy as detailed earlier that only a small portion of the guide tube emerges out of the hysteroscope and the rest remains inside the instrument channel. Therefore, a transitional flexibility was introduced onto the guide tube and only the emerged portion of the guide tube was made flexible. Hence, the laser cut patterns for flexibility were added at the 60 mm length distal portion of the guide tube. The rest of the guide tube was kept stiff for better pushability and torque transmission. Thus, to acquire maximum torqability from the guiding system, a combination of flexibility and stiffness was designed into the guide tube.

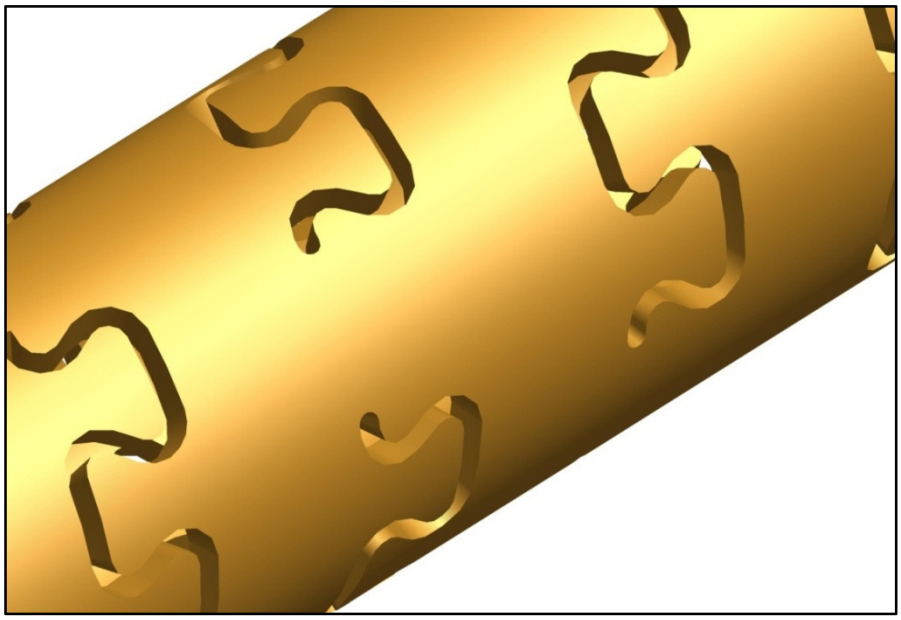

FIGURE 5.18: LASER CUT PATTERN ON GUIDE TUBE

To couple the guide tube with the implant, straight splines were designed on a SS-316LVM hardened tube, with OD 1.535 mm, length 3.5 mm and thickness 0.11 mm. The matching straight splines of this coupling crown were used to couple the guide tube with the implant. Four holes were introduced onto the coupling crown to laser weld it onto the distal end of the guide tube as shown in Fig. 5.19.

B. CAD MODEL

The 3D parametric models of the guide tube, coupling crown and the assembly were generated using Pro/E as shown in Fig. 5.19. These 3D models were further used for FEA simulation and generating CNC programs for the laser-cutting machine.

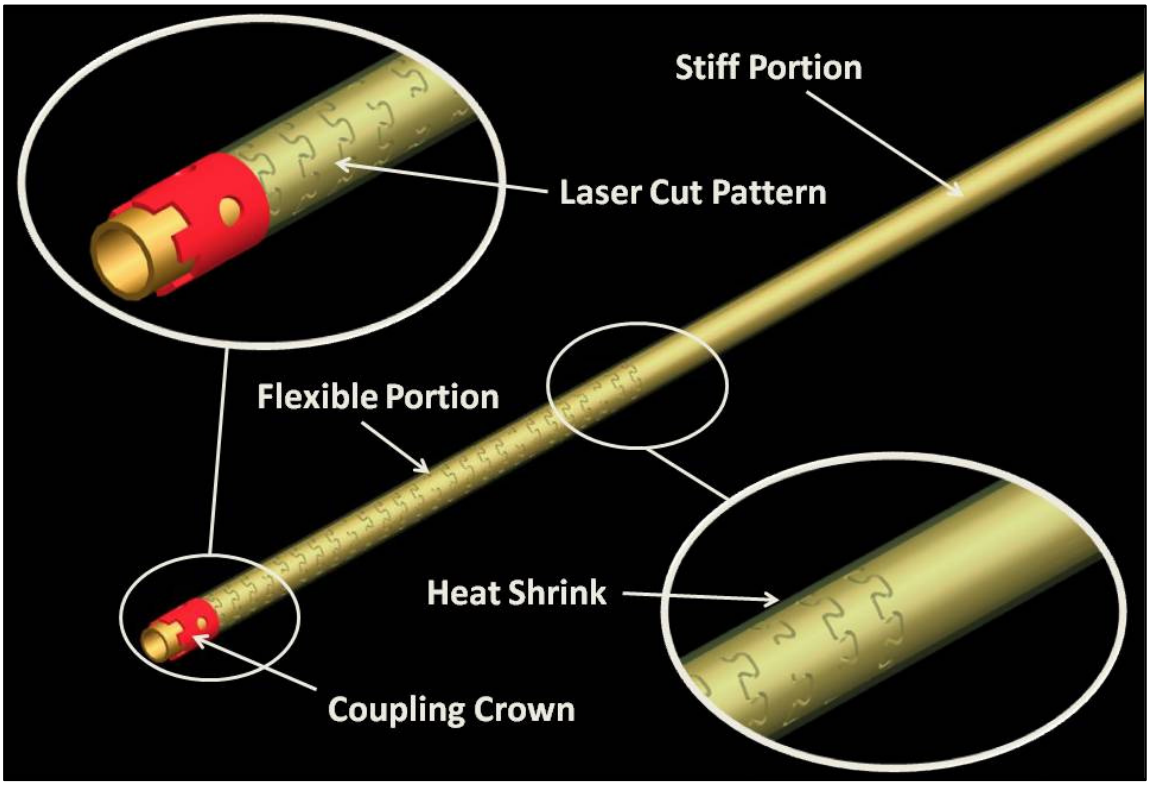

FIGURE 5.19: 3D MODEL OF GUIDE TUBE

C. FEA SIMULATIONS

The parametric model of the guide tube generated in Pro/E was integrated with ANSYS WB for FEA simulations. During operation of the device, the guide tube experiences the deployment and release forces, among which the maximum are a 16 N-mm torque and a compression of 70 N. The guide tube was therefore designed to withstand these forces during operation. The intermittent slot chains on the guide tube have helical periodicity. These chains have repeatability after 315° with an intermittent gap of 36°. Therefore, only two chains were considered in the simulations to reduce computation time.

Non-linear analysis was performed to investigate the mechanical behaviour of the guide tube. To simulate guide tube functionality, a bilinear isotropic hardening rule was adapted to describe the mechanical properties of the material. Material properties of hardened SS-316LVM were assigned in the ANSYS WB environment. Boundary conditions were applied to simulate the actual conditions in which fixed displacement was applied at the distal end of the model geometry. The load was applied in five load steps at the proximal end:

1. Clockwise moment of 16 N-mm
2. Compressive force 30 N
3. Counter-clockwise moment of 16 N-mm
4. Compressive force 25 N
5. Compressive force 70 N

Mesh dependency was tested and both tetrahedron and hexahedron elements were tried for meshing. The default mesh was refined by defining the element size. The volume of the guide tube was finally meshed with hexahedron elements and there were 63859 nodes and 24050 elements in the model as shown in Fig. 5.20. The von-Mises stress distribution at the conclusion of final load step is shown in Fig. 5.21. The contours and graphical representation of total deformation at the end of final step are shown respectively in Fig. 5.22 and Fig. 5.23.

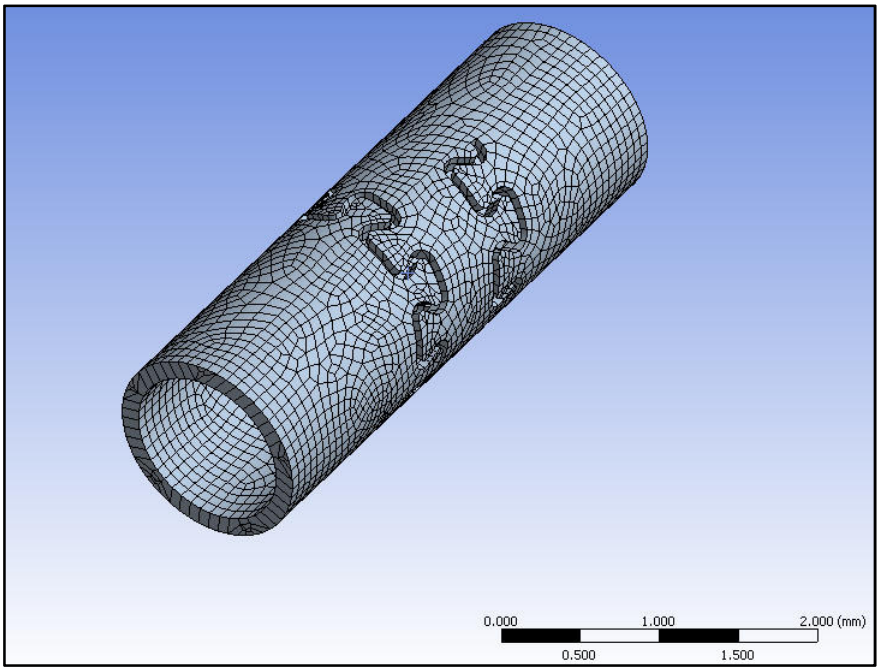

FIGURE 5.20: FE MESH OF GUIDE TUBE

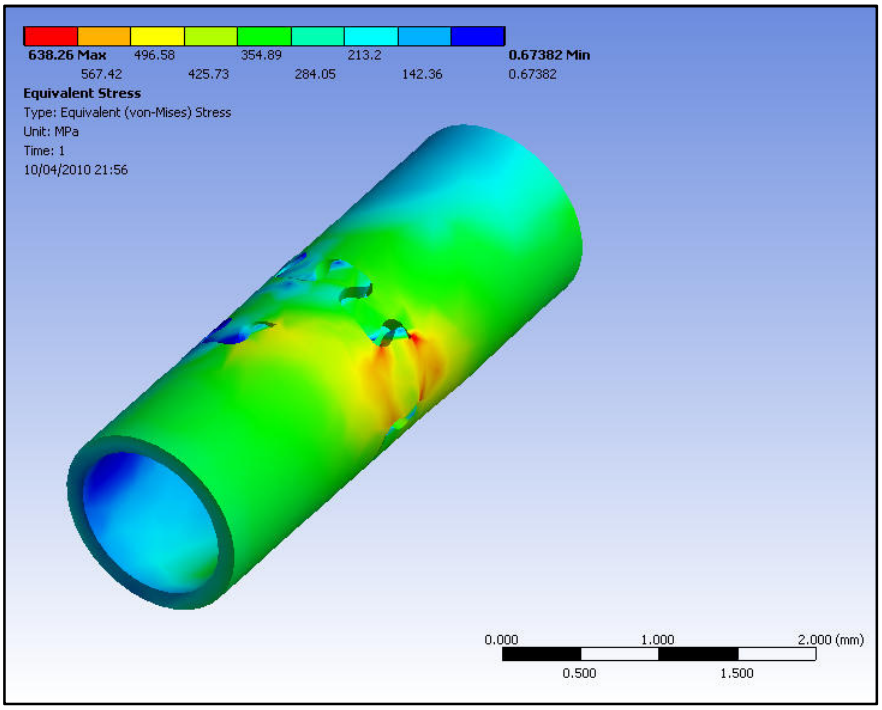

FIGURE 5.21: VON-MISES STRESS DISTRIBUTION IN GUIDE TUBE

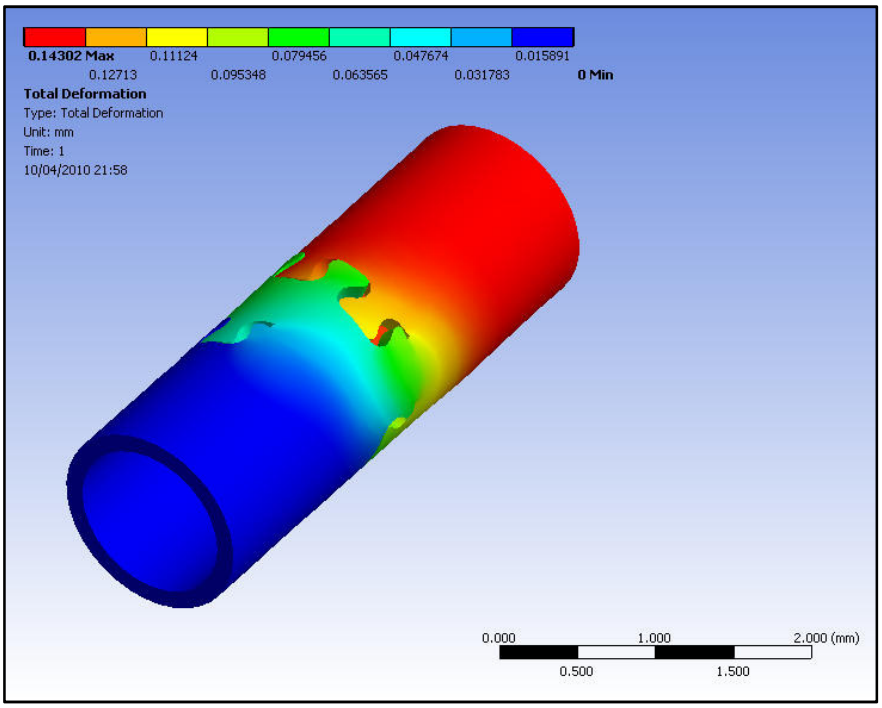

FIGURE 5.22: TOTAL DEFORMATION IN GUIDE TUBE

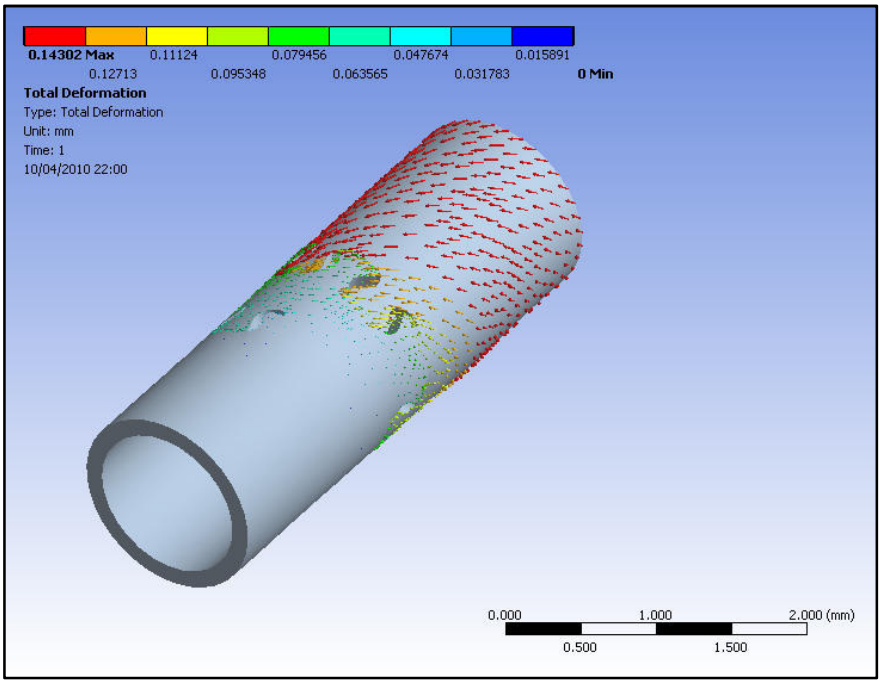

FIGURE 5.23: DIRECTIONAL REPRESENTATION OF TOTAL DEFORMATION

D. DEVELOPMENT AND TESTING

The guide tube and coupling crown was fabricated on the LPL stent cutter as described in Chapter 3. The guide tube was fabricated from hardened SS316LVM tubing, with OD 1.3 mm, thickness 0.125 mm and length 350 mm. The coupling crown was fabricated from hardened SS316LVM tubing, with OD 1.535 mm, thickness 0.11 mm and length 3.5 mm. Fig. 5.24 illustrates the fabricated guide tube from the laser-cutting machine. Fig. 5.25 shows the laser cut crown welded at the distal end of the guide tube.

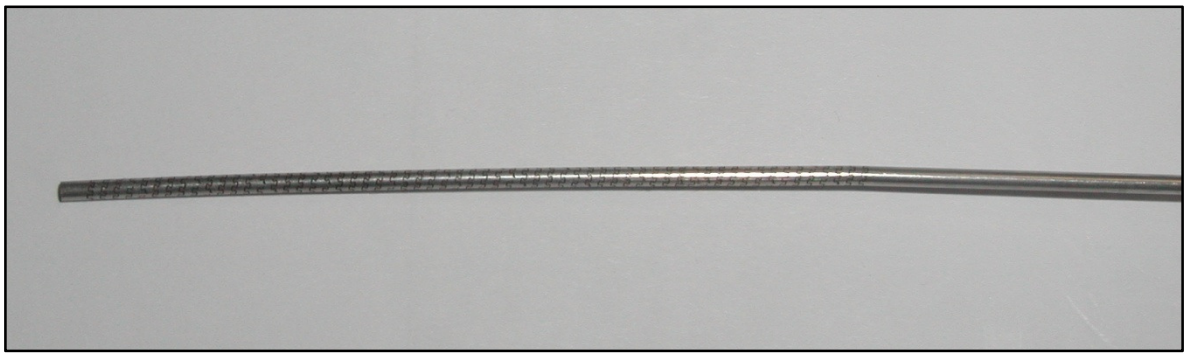

FIGURE 5.24: LASER CUT GUIDE TUBE

FIGURE 5.25: CROWN WELDED ON GUIDE TUBE

The sub-lite wall polytetrafluoroethylene (PTFE) heat shrink was used to improve trackability of the guide tube. PTFE is very lubricous, has a broad working temperature and the lowest coefficient of friction of any polymer material [167]. The frictional coefficient between PTFE and stainless steel is very low. The PTFE heat shrink, with expanded ID 1.524 mm (AWG 20), recovered ID 0.991 mm and wall thickness 0.051 mm was obtained from Zeus, USA [167] and is shown in Fig. 5.26. The PTFE heat shrink requires 340°C ± 5°C to recover. The Gallenkamp laboratory oven mentioned in Section 3.6.4 was used to recover the PTFE heat shrink on the guide tube. Fig. 5.27 shows the recovered heat shrink on the guide tube.

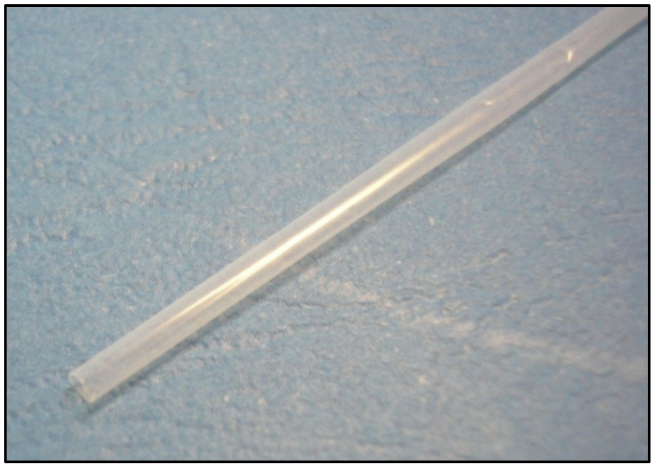

FIGURE 5.26: PTFE HEAT SHRINK

FIGURE 5.27: GUIDE TUBE WITH ASSEMBLED CROWN AND HEAT SHRINK

The final design of the guide tube was tested for flexibility and torqablility. The same setups as described sections in 5.4.5.1 and 5.4.5.2 were used again for flexibility and torqability testing respectively. The flexibility test performed on the tensile testing machine to measure the deflection force is shown in Fig. 5.28 and Fig. 5.29. During these testing, a deflection force of 0.76 N was measured.

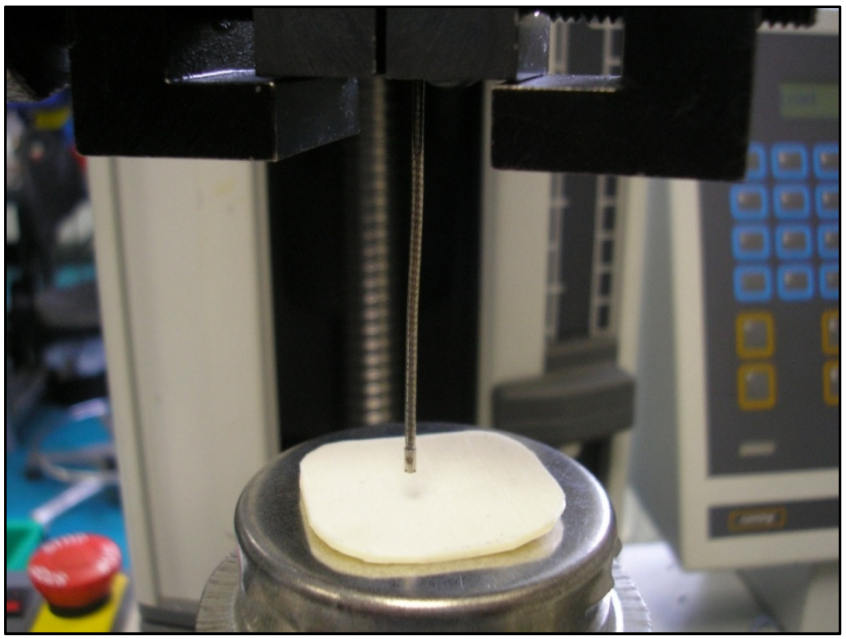

FIGURE 5.28: FLEXIBLITY TESTING OF GUIDE TUBE ON UNIVERSAL TESTING MACHINE

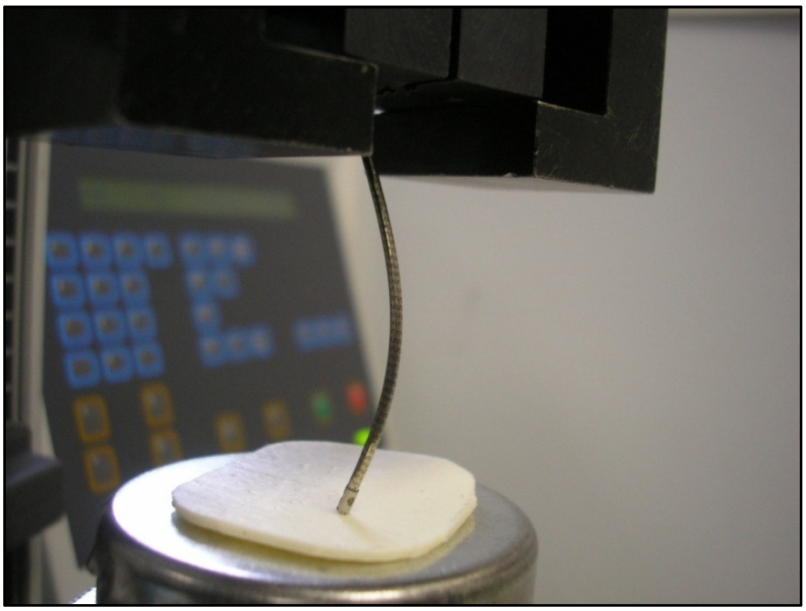

FIGURE 5.29: DEFLECTED GUIDE TUBE IN FLEXIBILITY TEST

A bend radius test was also performed to validate the flexibility of the guide tube. This test was performed under a video inspection probe, Deltronics to measure the bending radius of the guide tube. The setup of this test is shown in Fig. 5.30. It was measured in the test that the guide tube was able to bend around a 40 mm diameter.

FIGURE 5.30: BENDING RADIUS FLEXIBILITY TESTING

5.5. DESIGN, DEVELOPMENT AND VALIDATION OF GUIDE WIRE

Guide wire technology has improved markedly and a number of companies are now designing wires specifically for the human anatomy and for particular tubal variations of calibre and tortuosity. The companies producing these guide wires claim that they possess all the properties of an ideal guide wire. In this study, properties of following four different types of guide wires were investigated:

1) A nitinol guide wire.
2) A stainless steel wire.
3) A multi-filament stainless steel cable.
4) A coiled stainless steel cable.

5.5.1. NITINOL WIRE

Nitinol is a series of metal alloys of nickel and titanium and was first produced by the Naval Ordnance Laboratory in 1965 [168]. They are also called shape memory alloy because they remember their shape if deformed. Superelastic nitinol is now a common and well-known engineering material in the medical industry. While the greater flexibility of the alloy drives many of the applications, there are actually a large number of lesser-known advantages of nitinol in medical devices. Different diameters and types of nitinol wire were ordered and tested for their mechanical behaviour.

Shape memory nitinol alloy B and M in two different diameters were obtained from Memory Metalle GmbH, Am Kesselhaus, Germany. These alloys have body transformation (35° C) and intermediate transformation temperatures (65° C). These straight annealed wires with light oxide surface were obtained in Ø 0.7 mm and Ø 1.0 mm as shown in Fig. 5.31.

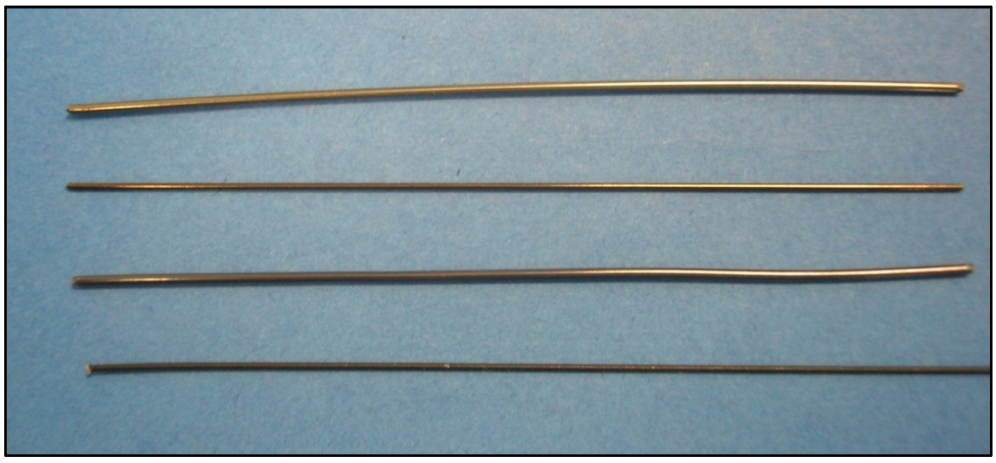

FIGURE 5.31: MARTENSITIC ALLOY NITINOL WIRES

5.5.2. STAINLESS STEEL WIRE

The SS-316LVM round wires drawn to diameter 0.7 mm and 1.0 mm were purchased from Fort Wayne Metals, Ireland seen here in Fig. 5.32. This austenitic stainless steel is initially electric-arc melted. Then, further refinement for the purity and homogeneity of the metal, it is vacuum arc re-melted. The chemical composition of the obtained SS-316LVM wire is detailed in Table 5.2.

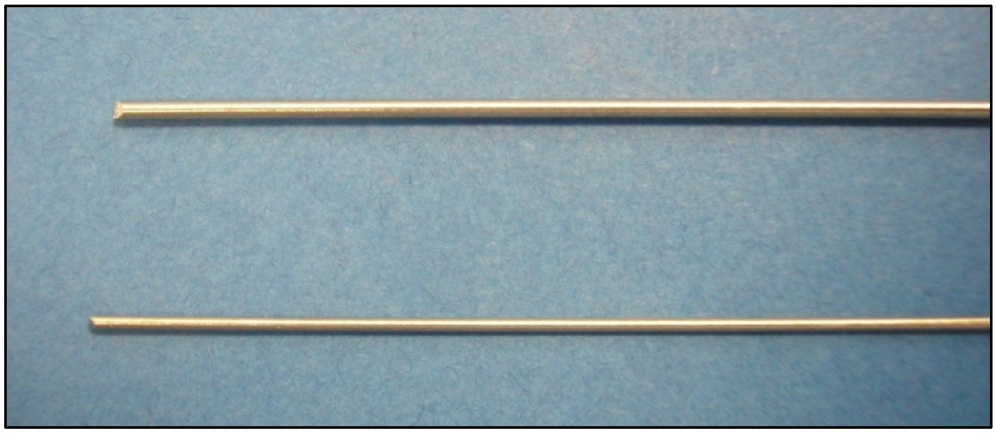

FIGURE 5.32: SS-316 WIRES

TABLE 5.2: CHEMICAL COMPOSITION OF SS-316LVM WIRE

Element	**Percentage**
Carbon	0.023-0.017
Manganese	1.84-1.72
Silicon	0.37-0.43
Phosphorus	0.014-0.016
Sulphur	0.001- 0.001
Chromium	17.57-17.45
Nickel	14.68-14.52
Molybdenum	2.79-2.66
Copper	0.03-0.8
Nitrogen	0.03-0.3
Iron	Balance

5.5.3. STAINLESS STEEL MULTI-FILAMENT CABLE

Multi-filament cable is made of two or more wires twisted together [169]. It has greater strength and flexibility than a single wire filament. As shown in Fig. 5.33, three different types of SS-316LVM multi-filament cables, with diameter 0.7 mm were obtained from Fort Wayne Metals, Mayo, Ireland. The construction of these cables was 1 x 3, 1 x 7 and 1 x 19 where 1 x 7 was the stiffest and 1 x 19 was most-flexible.

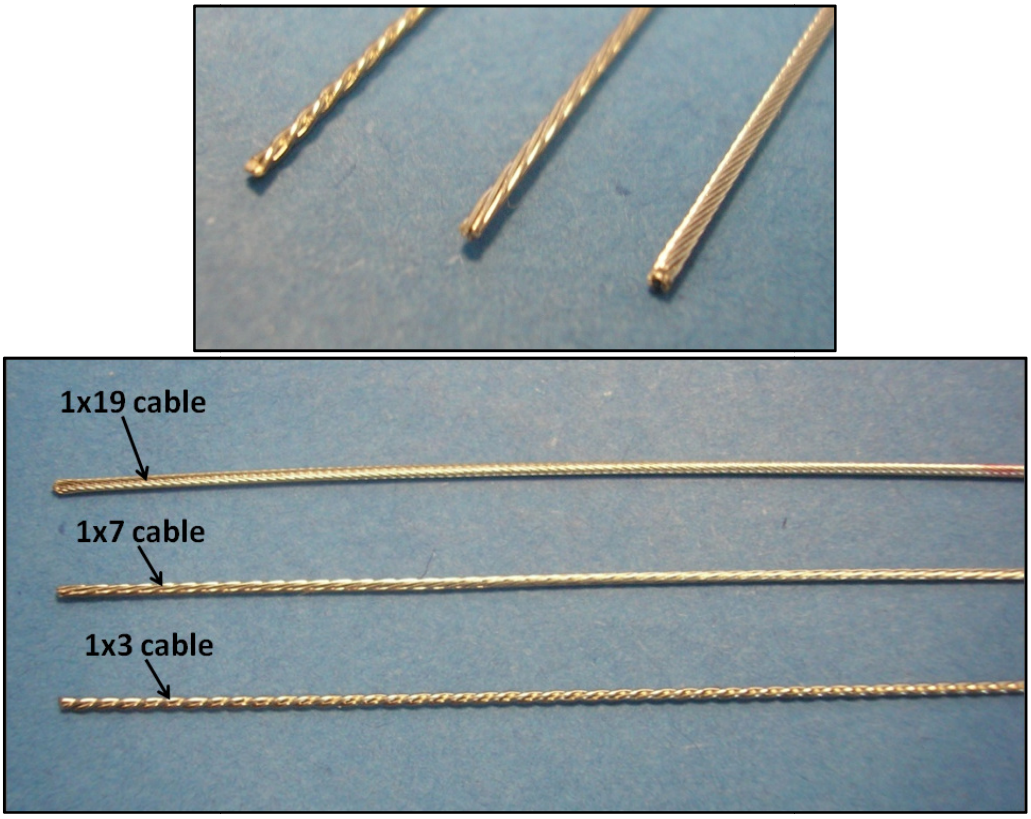

FIGURE 5.33: MULTI-FILAMENT CABLES

5.5.4. STAINLESS STEEL COILED WIRE

Flexible coiled stainless steel wire is constructed by winding a wire around a full-length centre core wire. The centre core provides added strength to the wire. The coiled wire, with diameter 1.0 mm was obtained from Lake Region Manufacturing Co. Ltd., Co. Wexford, Ireland. The SS-316 coiled wire is shown in Fig. 5.34.

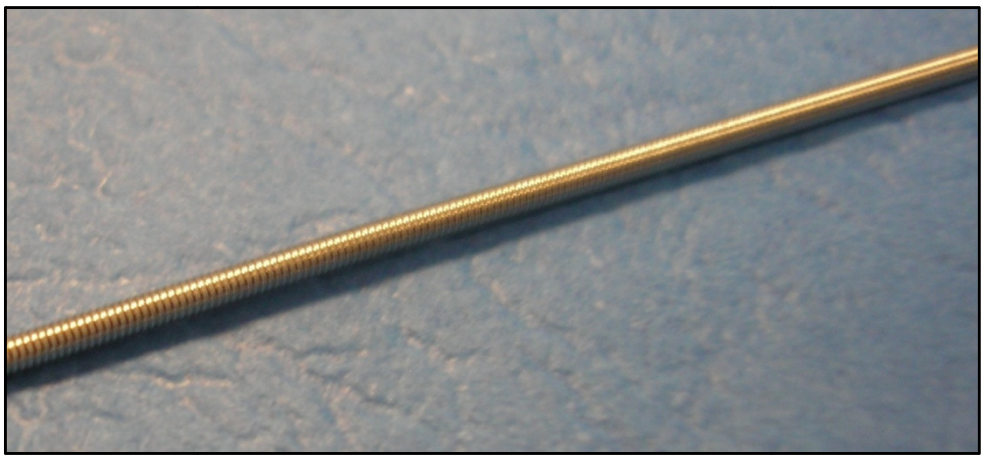

FIGURE 5.34: COILED SS-316 WIRE

5.5.5. COMPARATIVE ANALYSIS OF GUIDE WIRES

All types of guide wires discussed earlier were investigated for their mechanical properties desired for the required guide tube. The investigation includes biocompatibility, flexibility, torqability and tensile testing.

A. BIOCOMPATIBILITY

The comparison of common biocompatible materials is shown in Fig. 5.35. The comparison shows that the nitinol is more resistant to chemical breakdown than SS316-LVM, but less than titanium. Therefore, titanium has the most suitable biocompatibility, followed by nitinol and SS316-LVM, in descending order.

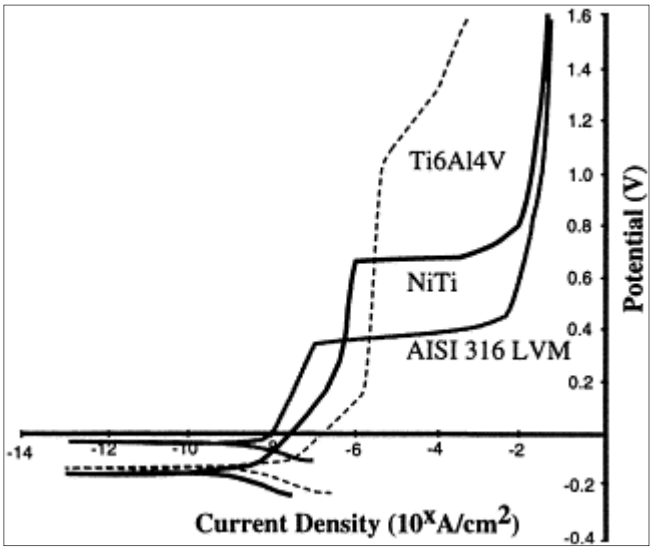

FIGURE 5.35: COMPARISON OF BIO-COMPATIBLE MATERIALS [170]

B. FLEXIBILITY

The flexibility test of all the available guide wires was performed using Lloyd machine. These tests were performed to measure the deflection forces of the wire. The setup used for flexibility test of the guide tube was also used in this case. The sample wires were griped in the upper chuck of the machine as shown in Fig. 5.36. The same amount of 5 mm displacement was applied and the deflection force was measured. The measured deflection forces are listed in Table 5.3. The deflected wire during testing is show in Fig. 5.37.

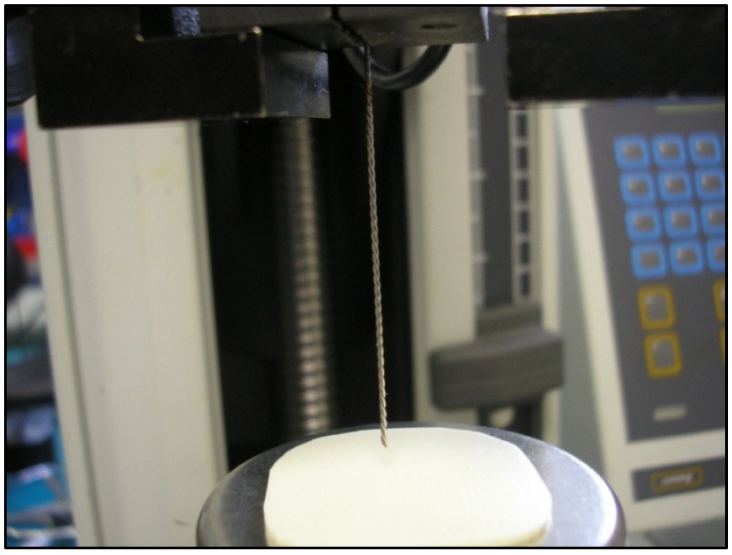

FIGURE 5.36: GUIDE WIRE GRIPPED FOR FLEXIBLITY TESTING

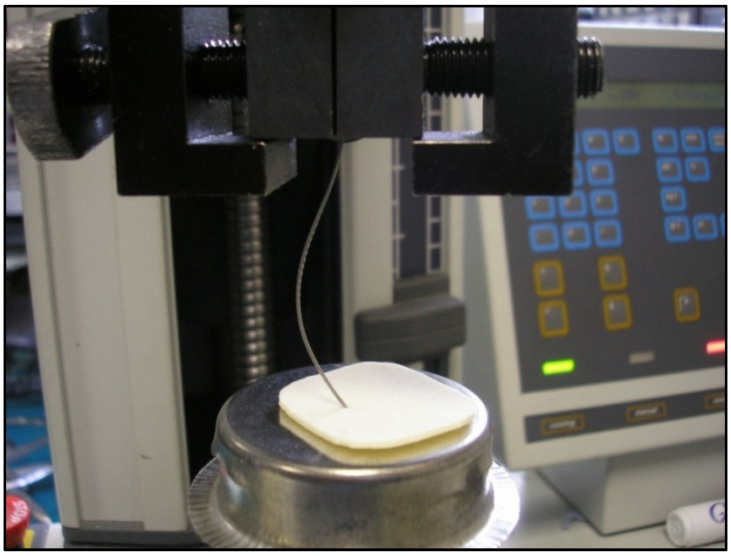

FIGURE 5.37: DEFLECTED GUIDE WIRE IN FLEXIBILITY TEST

C. TENSILE STRETCHING (ELONGATION)

As the guide wire is also used to apply tensile force to the release mechanism, elongation of the wires was investigated. The tensile stretch of the wires was evaluated using Lloyd universal testing machine. Samples of length 380 mm were prepared from all type of wires. The wires were clamped in the grips of the machine and a tensile force of 70 N was applied on the wires as shown in Fig. 5.38. This value of the tensile force is the maximum amount of release force that guide wire had to apply during release operation. The elongations in all tested wires are listed in Table 5.3.

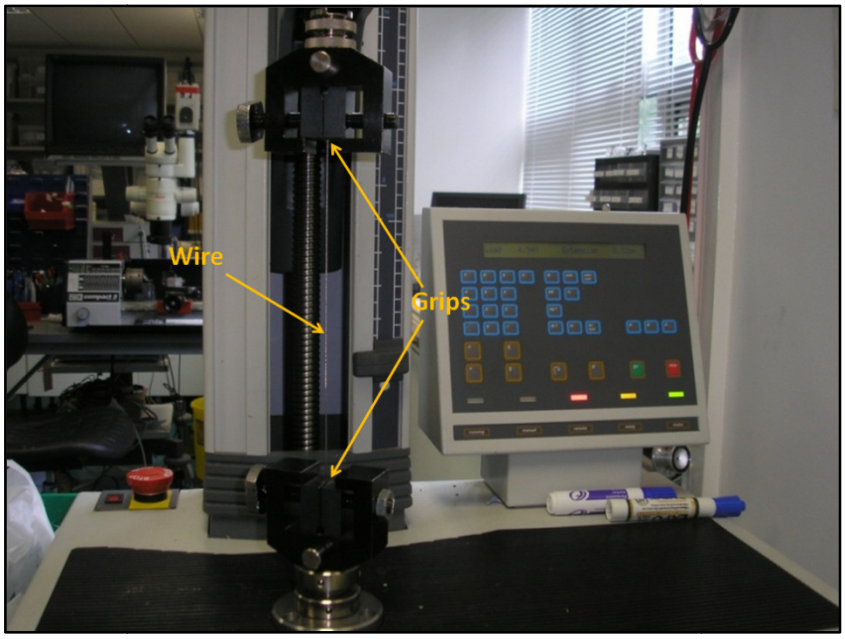

FIGURE 5.38: TENSILE STRETCH OF GUIDE WIRES

Comparative tensile behaviour of the stainless steel and nitinol by Stöckel et. Al. is shown in Fig. 5.39 [168].

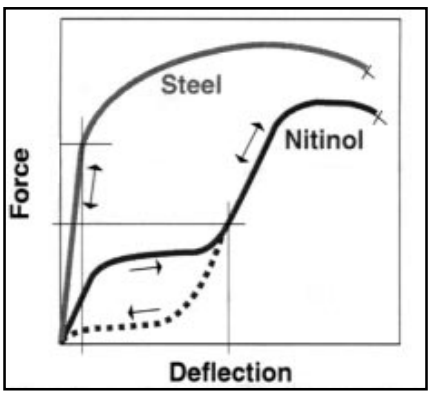

FIGURE 5.39: TENSILE BEHAVIOUR OF STAINLESS STEEL AND NITINOL [168]

D. TORQABILITY TESTING

The torqability testing of the wires were performed on the torque testing equipment. In this setup, the guide wires were gripped in the chuck of the torque meter. The other end of the guide wire was gripped inside the fabricated torque application handle. A torque of 16 N-mm was applied to the guide wire in both clockwise and counter-clockwise direction. The rotational displacement in applying this torque was recorded for both directions. The measured values are tabulated in Table 5.3. The torque measuring setup is shown in Fig. 5.40.

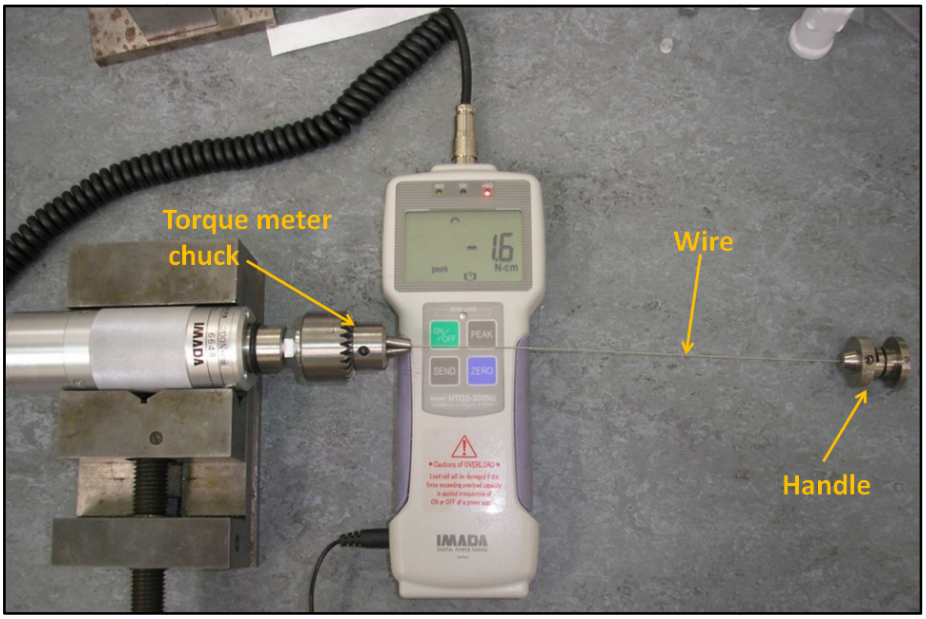

FIGURE 5.40: TORQUE TESTING OF GUIDE WIRE

It was found that the SS-316 coil wire and SS-316 (1x19) cable were unable to transmit the required torque. It was also observed that when a torque was applied against the wound direction of the SS-316 (1x19) cable, it unraveled at a torque value of 8 N-mm as shown in Fig. 5.41. This shortcoming made this cable unsuitable for this work.

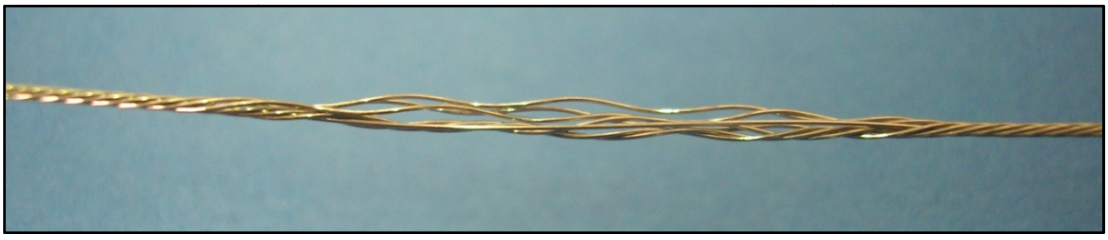

FIGURE 5.41: UNRAVELLING OF CABLE (1X7)

The complete depiction of all testings on various commercially available guide wires are detailed in Table 5.3. It was obvious from the uterus perforation test that the deflection force of the guide wire should be less than 8.5 N. However, the comparative analysis of all wires demonstrated that the SS-316 wire cannot be used as a guide wire because of its stiffness and is more likely to perforate the uterus. It was obvious from the comparative analysis that the SS-316 (1x19) cable and SS-316 coiled wire were unable to transmit the required torque. Also, the tensile testing of the wires demonstrated that the elongation and flexibility of nitinol is comparatively higher as compared to the SS-316 cables. So, these options were also eliminated from the prospective list. Finally, the apparent choices were the SS-316 (1x7) and (1x3) cables.

TABLE 5.3: COMPARATIVE ANALYSIS OF GUIDE WIRES

Wire	**Diameter (mm)**	**Flexibility / Deflection (N)**	**Torqability (Angle° / 16 N-mm)**	**Wire Elongation (mm)**	**Bio-compatibility**
Nitinol Alloy M	1.0	4.98	360	2.27	Yes
	0.7	3.16	490	1.51	Yes
Nitinol Alloy B	1.0	6.2	345	2.83	Yes
	0.7	3.98	480	1.79	Yes
SS-316	1.0	16.87	45	0.49	Yes
	0.7	10.08	60	0.56	Yes
SS-316 Cable (1x3)	0.7	2.72	860	0.58	Yes
SS-316 Cable (1x7)	0.7	1.47	1080	0.44	Yes
SS-316 Cable (1x19)	0.7	0.78	Failed	0.38	Yes
SS-316 Coiled	1.0	1.68	Failed	Failed	Yes

5.5.6. GUIDE WIRE FINAL DESIGN

In order to achieve all the required properties from the guide wire, it was decided to design the required guide wire. Therefore, to acquire maximum torqability from the guide wire, a transition was introduced into the guide wire. It was envisaged to take benefit of SS-316 wire stifness and SS-316 cable (1x7) flexibility. The SS-316 wire was quiet stiff but it inherited almost one-to-one torque transfer capability. On the other hand the SS-316 cable had required flexibility but meagre torque transmission property.

Finally, a combination wire and cable was designed, which comprised of stiff SS-316 wire and flexible SS-316 (1x7) cable. The configuration of this guide wire is shown in Fig. 5.42. The interface of these Ø 0.7 mm wire and cable was designed using a coupling tube, with OD 1.0 mm, thickness 0.1 mm and length 7 mm. This coupling tube is made of SS-316LVM hardened tube. In this configuration, the coupling tube is laser welded with both the multi-filament SS-316LVM cable (1x7), with a length of 65 mm and the stiff SS-316LVM wire, with a length of 315mm. The developed combination guide wire is shown in Fig. 5.43.

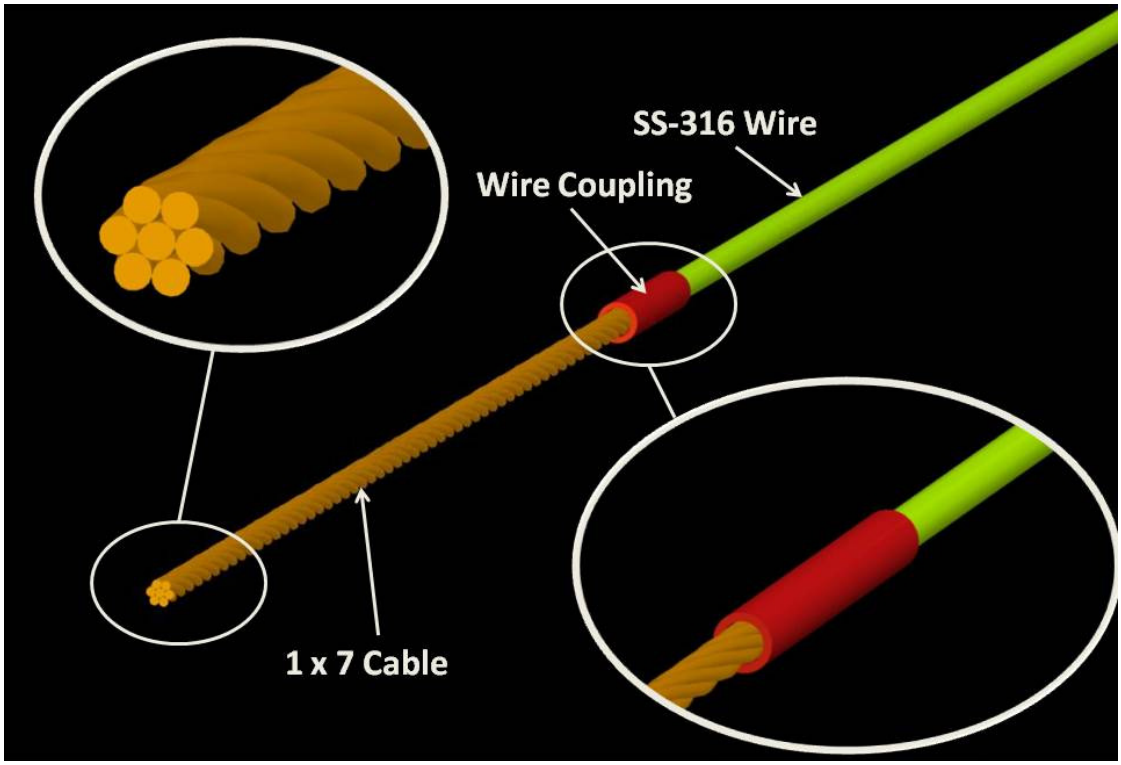

FIGURE 5.42: 3D MODEL OF THE GUIDE WIRE

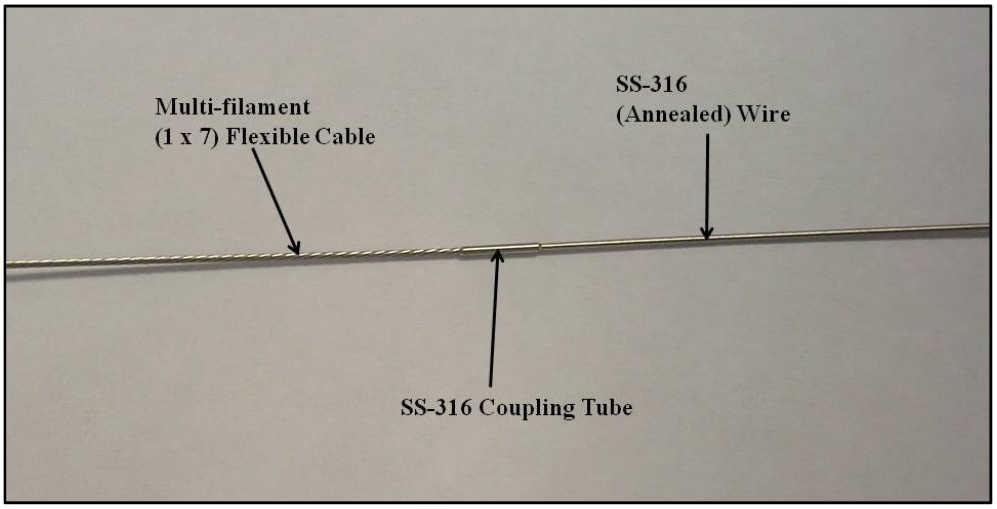

FIGURE 5.43: FINAL DESIGN OF GUIDE WIRE

CHAPTER 6

DESIGN, DEVELOPMENT AND VALIDATION OF ACTUATOR

6.1. INTRODUCTION

The majority of the non-surgical medical devices are delivered in a low profile form into human body and subsequently require specialized operations for their deployment and release. Therefore, an actuator handle is required for deployment in most of these devices. The device presented in this thesis required the design of an ergonomic actuator as the deployment and release mechanism. The following chapter discusses all the development phases of this actuator, starting from initial design followed by improved and finalized design. Development and validation of each phase is also detailed.

6.2. DESIGN EVALUATION OF ACTUATOR

To comprehend the actuator design, an appreciation of the functionality of the implant is required. As mentioned in Chapter 4, the implant is designed to be deployed and released in a five steps sequence:

Step 1: A counter-clockwise (CCW) torque of 15.4 N-mm, which generates an out-of-plane displacement in the implant's distal slots.

Step 2: An axial compression of 25 N that plastically deforms the displaced slots into the shape of the first set of six distal wings.

Step 3: A clockwise (CW) torque of 16 N-mm, which generates an out-of-plane displacement in the implant's proximal slots

Step 4: An axial compression of 25 N that plastically deforms the displaced slots into the shape of second set of six proximal wings.

Step 5: A tensile force of 70 N on the release tube breaks the link of the implant to the actuator.

It has also been discussed in Chapter 5 that the implant is inserted hysteroscpically in a low profile form, by means of a flexible guide tube and inner guide wire. As the

implant requires torque and compression for deployment, both the guide tube and wire serves the purpose of torque transmission and compression to the implant. Because of the flexibility, the guide tube and guide wire lacks one-to-one force transfer property. Therefore, to transfer the above-mentioned forces to the implant, large rotational and translational displacements were required from the actuator. The challenging task was to design an actuator that could provide controlled rotations of more than 360°.

6.3. INITIAL ACTUATOR DESIGN

The main objective of the initial design of the actuator was to investigate the mechanical behavior of the implant. The design evaluation of the implant required a lot of functionality testing by bench top in-air deployments. These deployments were not possible without an actuator. However, the design finalization of the actuator was not possible before the finalization of the implant and guiding system, Therefore, a manual actuator was designed that could be used for implant deployment, determination of rotational and longitudinal displacements and for testing of the guiding system.

6.3.1. DESIGNING AND MODELING

The actuator included a fore-body to attach with the guide tube, a handle-body to hold the actuator, a rear-body to grip the guide wire, rotate and apply torque and a release-wheel to release the implant and to apply compression. The 3D model of this actuator is shown in Fig. 6.1.

In this simple design, the fore-body was slidably connected to the handle-body. The rotation was locked through a pin-in-slot mechanism. The guide tube was attached to the fore-body using a grub screw. The handle-body was rotatably connected to the rear-body through a “socket set screw-rolling ball tip”. The handle-body included threads on the outer surface of the distal portion. These threads were used to engage the release-wheel as the release wheel was sandwiched in between the handle-body and the fore-body. Therefore, the rotation of the release-wheel provided the required longitudinal displacement to the implant as shown in Fig. 6.2.

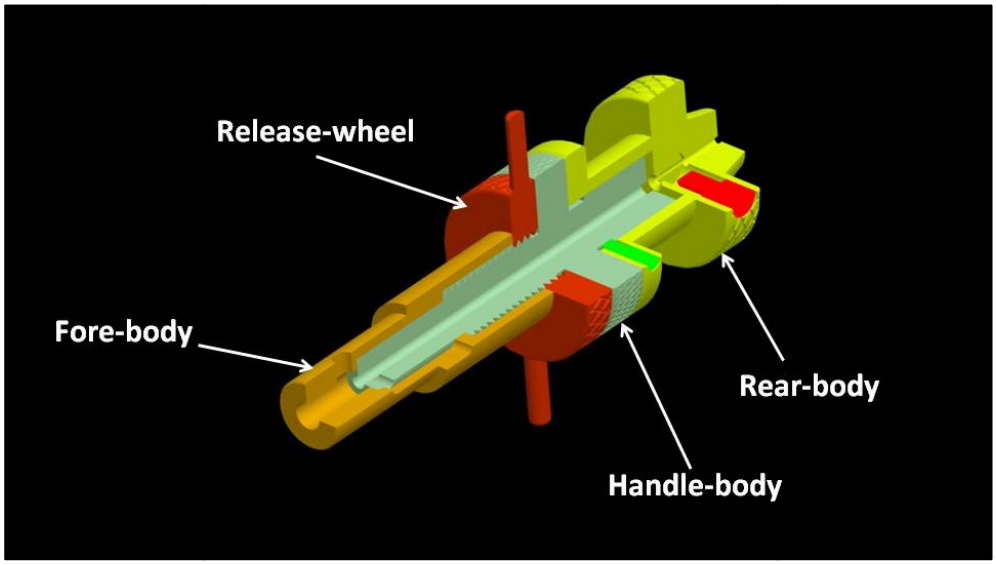

FIGURE 6.1: 3D MODEL OF INITIAL DESIGN

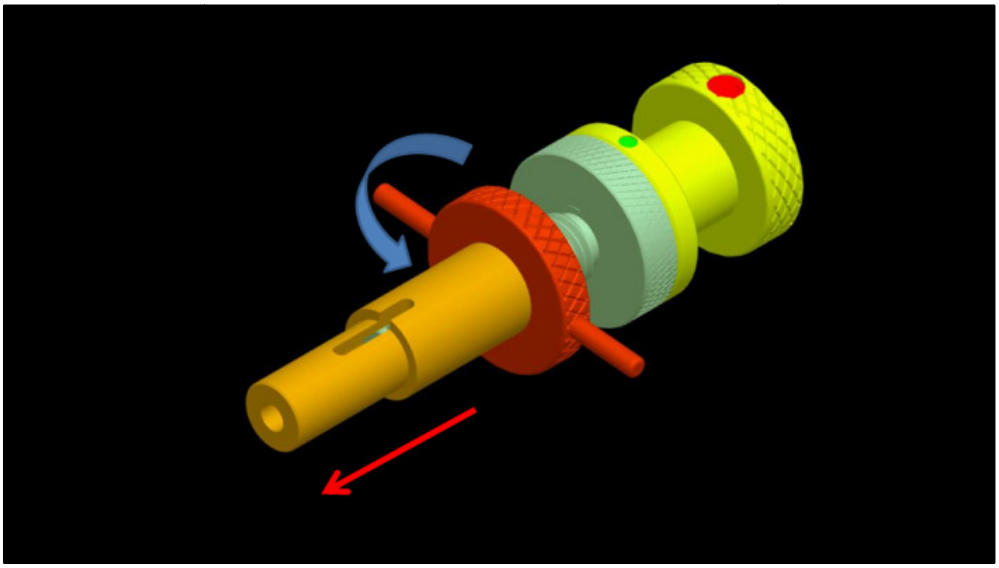

FIGURE 6.2: FUNCTIONALITY OF MANUAL ACTUATOR

6.3.2. DEVELOPMENT AND TESTING

The actuator was fabricated from SS-316 using a Schaublin 140-CNC lathe. All the actuator components were manufactured and inspected before assembly. Knurling was performed on the outer surfaces of the hand held components to provide a better handgrip. The fabricated actuator components are shown in Fig. 6.3. The actuator after assembly is shown in Fig. 6.4.

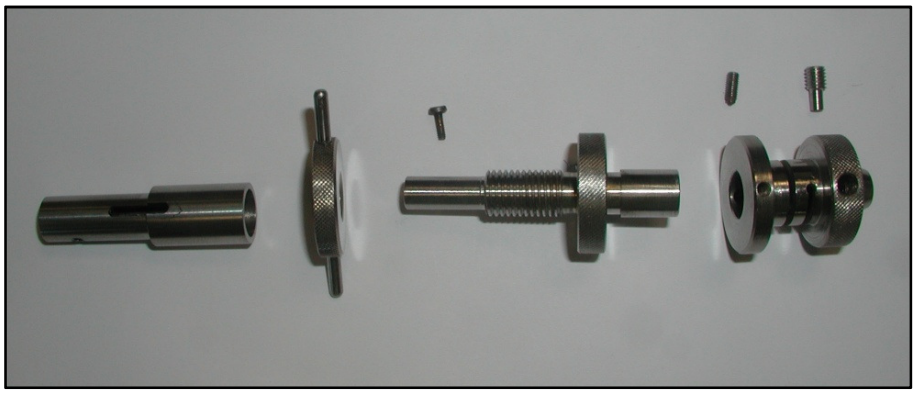

FIGURE 6.3: FABRICATED ACTUATOR COMPONENTS

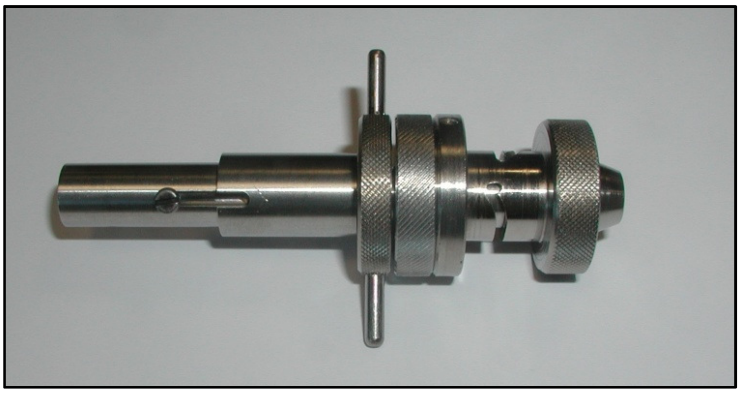

FIGURE 6.4: ASSEMBLED INITIAL ACTUATOR

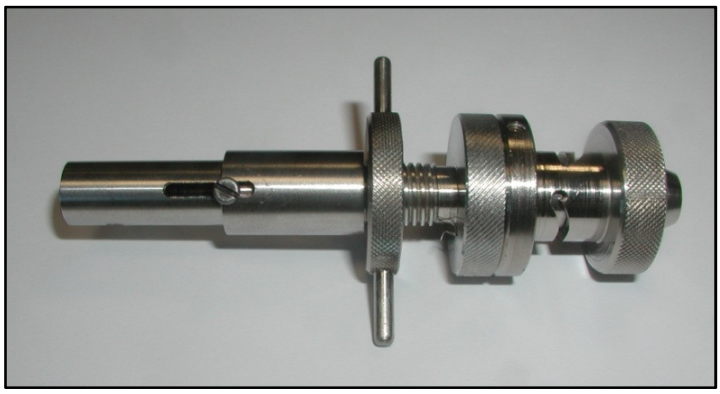

FIGURE 6.5: ACTUATOR APPLYING LONGITUDNAL DISPALCEMENT

The main purpose of this initial actuator was for the design evaluation of mechanical behaviour of the implant. The rotations required to deploy the implant were evaluated by measuring the rotational angles in between the handle-body and rear-body. The longitudinal displacements (gap between the release wheel and the handle-body) as seen in Fig. 6.5 were measured by measuring the gap in between the release knob and the handle-body. Thus, this actuator was a very convenient and efficient tool in design finalization of the implant and guiding system. In addition, this actuator was used in the first explant study in which deployment and release of implant was performed blindly

by actually counting the rotations in between the handle body and both the fore-body and rear-body. The complete device with this initial actuator is shown in Fig. 6.6.

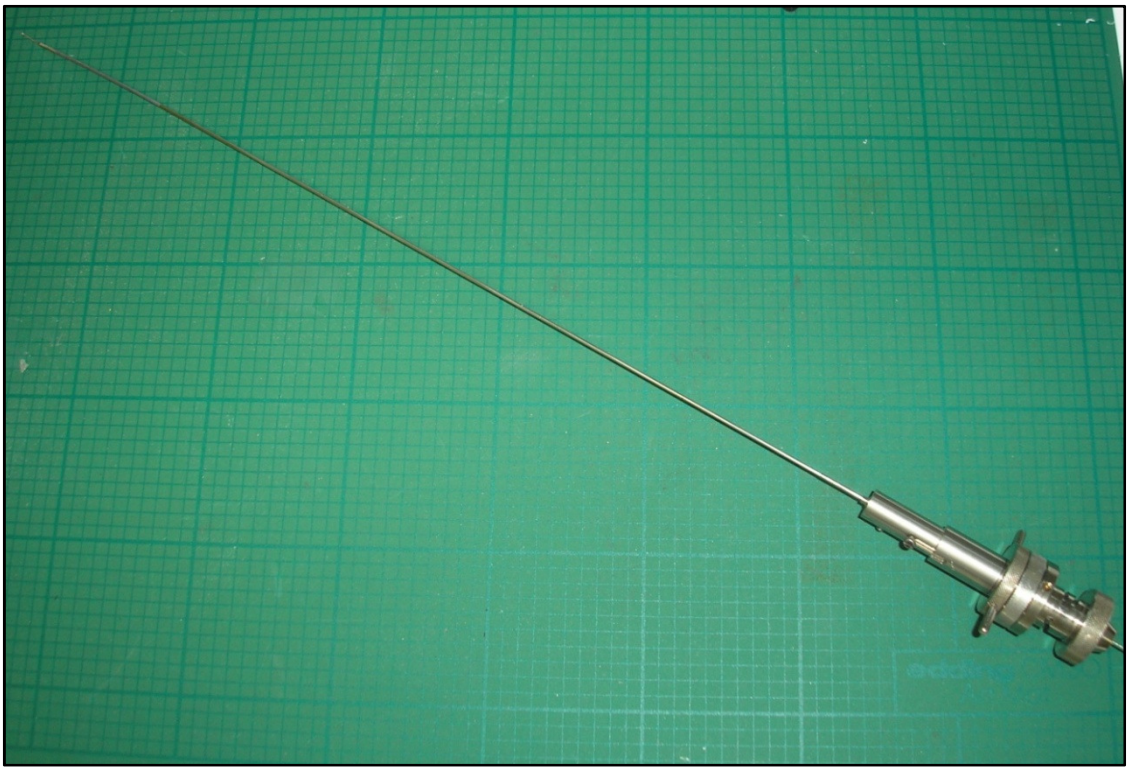

FIGURE 6.6: COMPLETE DEVICE WITH PRELIMINARY ACTUATOR

6.4. DESIGN IMPROVEMENT

After arriving at an effective design of the implant and guiding system, a working design of the actuator was presented. by providing the required deployment forces, this actuator was capable of blindly deploying the implant into the tubal ostium.

6.4.1. DESIGNING AND MODELING

An improved actuator shown here in Fig. 6.7 was designed to provide the required deployment and release displacements precisely in a specified sequence. This design included a handle-body to hold the actuator, a fore-body to apply both torque and compression to the implant and a lever to release the implant from the delivery system. As evaluated in the previous Chapter, to apply a CCW torque of 15.4 N-mm to the implant through the guide wire and guide tube, a rotation of 410° was required. Similarly to transmit a CW torque of 16 N-mm a rotation of 970° was required. To achieve these rotational angles in the actuator, an innovative design using three

telescopic cylinders in sequence were used as shown in Fig. 6.8. These cylinders were slidably and rotatably connected to each other through a pin-in-slot mechanism. A combination of slots and engagement of the pins in the cylinders provided the required rotations. The axial displacements were achieved through the helical shape of the slot ends. As a result, the actuator was capable of providing the required displacements to the implant for deployment.

A lever mechanism was used in the release mechanism of the actuator. This mechanism included a release lever, two connecting links and a release shaft. The force on the release lever was converted into the axial force on the release shaft and consequently transferred to the implant. This mechanism was finalized using Pro/Mechanica Motion. The mechanism was simulated in Pro/Mechanica Motion before finalization to remove any discrepancies in design. A design for manufacturing concept was followed during the designing of the actuator. Therefore, the components were miniature but easy to manufacture at the workshop.

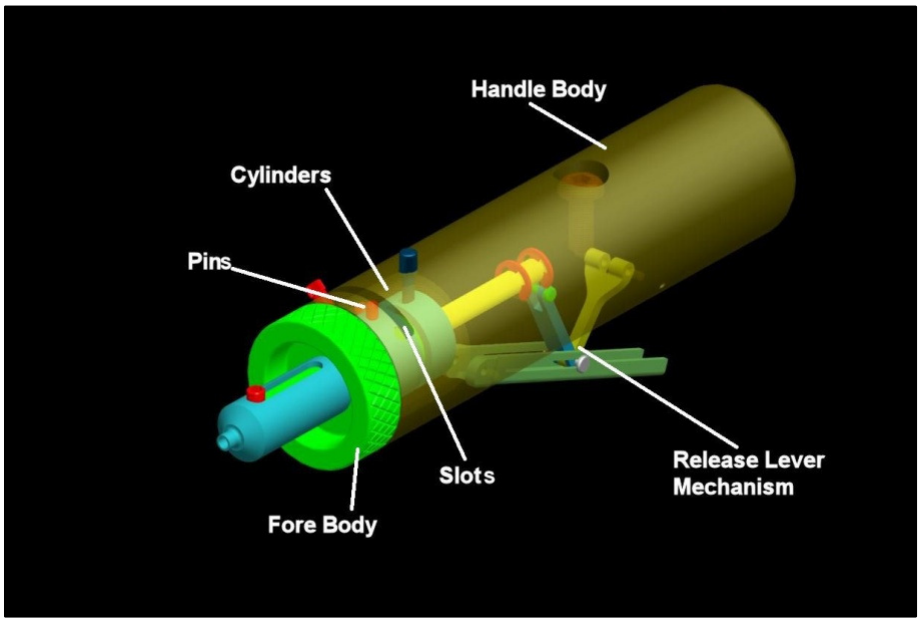

FIGURE 6.7: IMPROVED ACTUATOR DESIGN

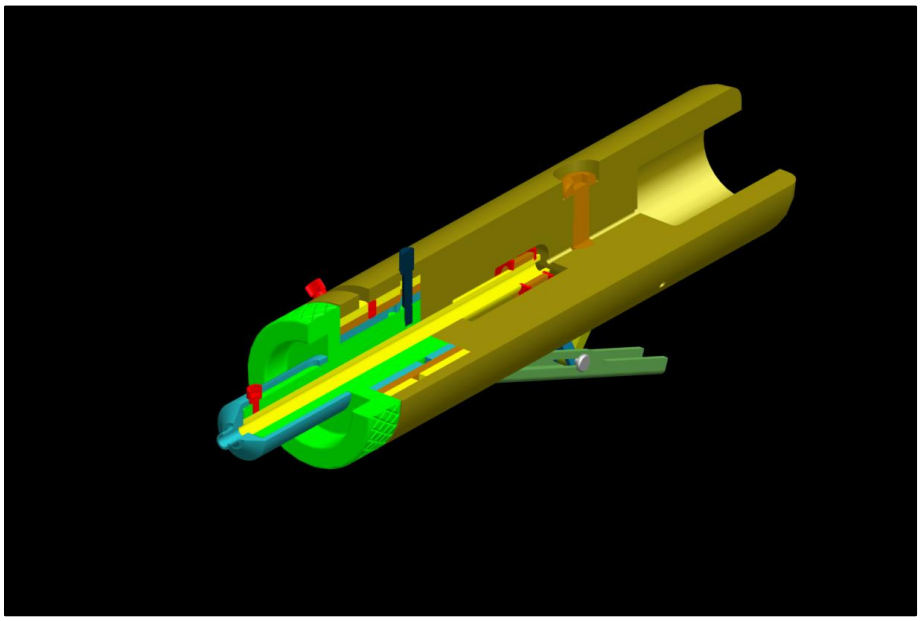

FIGURE 6.8: THREE QUARTER SECTION OF THE ACTUATOR

6.4.2. DEVELOPMENT AND TESTING

In order to achieve the µm level accurate displacements required from the actuator, a high precision manufacturing method was required. The Pro/E models were used for the generation of CNC codes. The actuator was manufactured on a high precision CNC at the school workshop. The machined components of the actuator are shown in Fig. 6.9. The operation to cut slots in the cylinders was performed on the *ONA PRIMA E250* wire EDM machine. The slotted cylinders are shown in Fig. 6.10. These slots control the deployment of the implant by providing required rotations and longitudinal displacements. The miniature release mechanism components are shown in Fig. 6.11. The blind cavities in the handle-body were machined on an "*ard Pulse P50* sinker EDM". The standard circlips used to clamp the release shaft and the lever bracket were obtained from RS Components Ltd., Northants, UK. The assembly drawing of this design is detailed in the appendices. Ease of manufacturing and assembly was considered during the design of the actuator. The assembled actuator is shown in Fig. 6.12.

FIGURE 6.9: ACTUATOR MACHINED COMPONENTS

FIGURE 6.10: SLOTTED CYLINDERS

FIGURE 6.11: RELEASE MECHANISM COMPONENTS

FIGURE 6.12: ASSEMBLED ACTUATOR

6.4.3. LIMITATIONS OF DESIGN

Successful deployments of the implant during bench-top testing validated the operational concepts. During these tests and deployments, the following limitations were observed in the actuator design.

1. The actuator was designed to provide the required rotational and linear displacements and therefore could only be used with the specific guide wire for which it was designed.

2. A mechanism to prevent any inadvertent reverse rotations and to avoid backlash (opposing torque) from the implant, guide wire and guide tube was required.
3. The actuator release lever interfered with the hysteroscope during placement of the implant.

All the above-mentioned limitations lead to the necessity of a further improved actuator design presented in next section.

6.5. ACTUATOR FINALIZED DESIGN

The ergonomically designed actuator presented in this section automatically controls the deployment and release of the implant at the target location by applying the required forces in a specified sequence. The designing and 3D modeling of the actuator was performed using Pro/E is shown in Fig. 6.13.

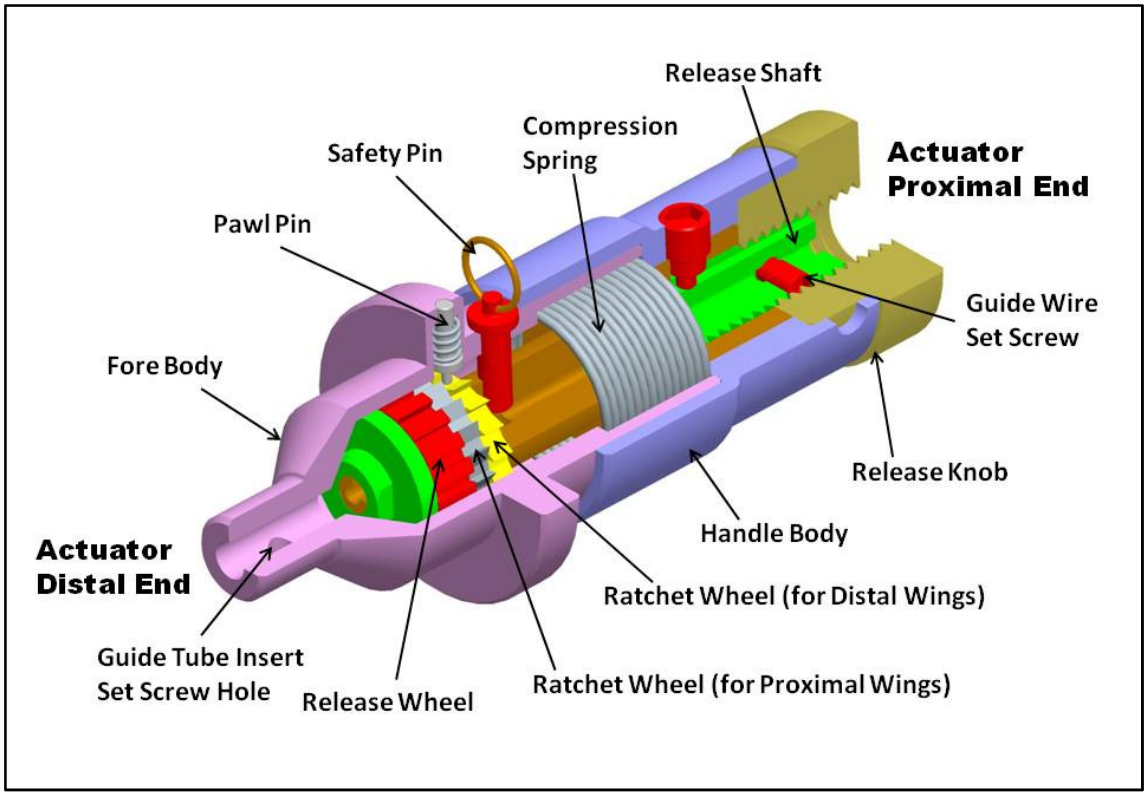

FIGURE 6.13: SCHEMATIC DIAGRAM OF THE ACTUATOR

6.5.1. BASIC CONFIGURATION

The actuator comprises a handle-body, with a diameter of 25 mm, which is adapted to hold the actuator. At the distal end, a fore-body, with maximum Ø 32 mm is slidably and rotatably connected to the handle-body. These optimal diameters of the handle-body and fore-body were adapted from the previous work of Kong et. al. [171,172]. The addition of a compression spring in between the fore-body and the handle-body automates the compression steps of the implant deployment sequence. This reduces the deployment and release sequence from five steps as mentioned earlier to three steps. In order to acquire a 25 N compressive force to deploy both the wing, a compression spring with a spring rate of 1.67 N/mm was used. At the initial stage, this spring is deflected 18 mm thereby applying a force of 30 N, which reduces to 25 N for the proximal wings.

This actuator topology was based on a ratchet wheel and pawl pin configuration. The fore-body is therefore operatively connected to handle-body through a ratchet mechanism in which the handle-body incorporates ratchet wheels and the fore handle includes a pawl pin as shown in Fig. 6.13. The ratchets were incorporated into the actuator to control the precise CW and CCW rotations by way of restricting any inadvertent reverse rotations. In addition, they prevent backlash from the implant and guide system during torque application. The precision of the latching was dependent on the number of teeth in the ratchet wheel. The design of the size of the ratchet wheel, number of teeth and size of pawl pin was based on the preferred size of actuator, the minimum feature size of machining, strength of the teeth and positive locking of teeth and pawl pin. The actuator also features a safety pin, which locks the actuator, preventing accidental deployment during handling or transportation. This safety pin needs to be removed prior to the deployment sequence.

The proximal end of the handle-body includes a release mechanism, which controls the release of the implant. This release mechanism includes an externally threaded release shaft and an internally threaded release knob. The release shaft is slidably connected to the handle-body and the release knob is rotatably connected to the handle-body. The power screw mechanism in between the release knob and release shaft converts the rotary motion of the release knob into axial linear motion of the release shaft. A tensile force of 70 N is required to release the implant. The power screw mechanism provides this force by converting the torque applied on the release knob.

The actuator was designed to limit this release torque to 520 N-mm i.e. that a human hand can apply with an index finger on a cylinder of Ø 25 mm [172]. ISO (International Organization for Standards) basic threads were selected for this mechanism because of the available machining resources. However, in this mechanism the release torque can be reduced by using square threads. Considering the size of the actuator, M10 coarse threads (pitch 1.5 mm) were preferred. A standard ISO M10 thread profile with basic dimensions is shown in Fig. 6.14 [173]. The torque required to apply the force of 70 N was calculated using a force balance diagram of a standard ISO threads with a single start as shown in Fig. 6.15.

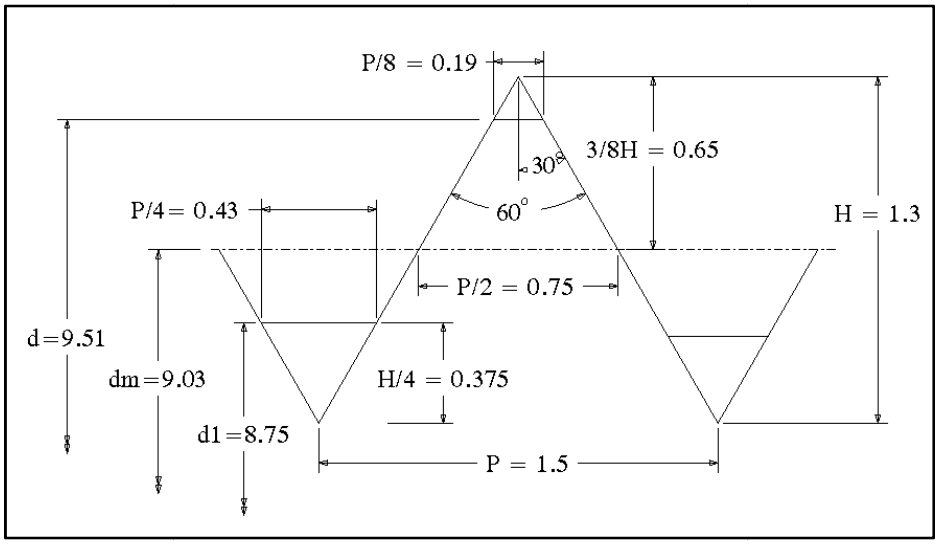

FIGURE 6.14: ISO M10 THREAD PROFILE WITH BASIC DIMENSIONS

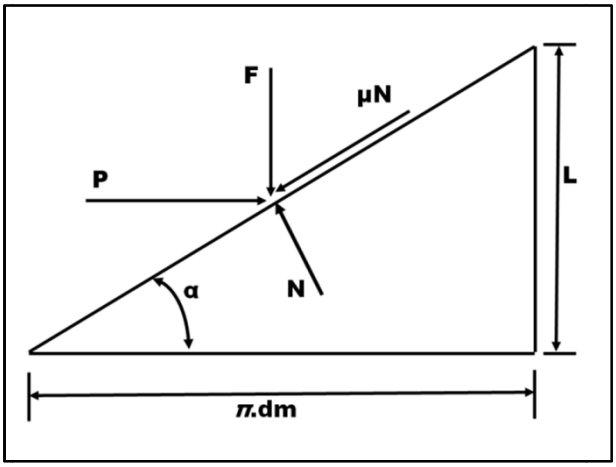

FIGURE 6.15: FORCE BALANCE DIAGRAM OF A STANDARD ISO THREAD

Where Nominal diameter = d

Thread pitch = P

Height of fundamental triangle = $H=0.86603P$

Pitch diameter $dm = d-0.75H$

Minor diameter (bolt) = $d3=d-1.22687P$

Minor diameter (nut) = $D1=d-1.08253P$

Thread depth (bolt) = $h3= (d-d3)/2$

Thread depth (nut) = $H1= (D-D1)/2$

From Fig. 6.15, L = np for a multi start drive, n being the number of start threads. Here L is the half pitch, N is the normal reaction and μN is the frictional force.

For equilibrium

$$P - \mu N cos \propto - N sin\alpha = 0 \quad \text{EQ. 6.1}$$

$$F + \mu N sin\alpha - N cos\alpha = 0 \quad \text{EQ. 6.2}$$

This gives

$$N = \frac{F}{(cos\propto - \mu sin\alpha)} \quad \text{EQ. 6.3}$$

$$P = \frac{F(\mu cos\propto + sin\alpha)}{(cos\propto - \mu sin\alpha)} \quad \text{EQ. 6.4}$$

Torque transmitted to apply load is given by

$$T_R = P\frac{dm}{2} \quad \text{EQ. 6.5}$$

Rearrangement of Eq. 6.1 results in

$$T_R = F\frac{dm(\mu cos\propto + sin\alpha)}{2(cos\propto - \mu sin\alpha)} \quad \text{EQ. 6.6}$$

Since,

$$tan\alpha = \frac{L}{\pi dm} \quad \text{EQ. 6.7}$$

$$T_R = F\frac{dm(\mu\pi dm + L)}{2(\pi dm - \mu L)} \quad \text{EQ. 6.8}$$

Were $\alpha = 30°$, $dm = 9.026$, $L = 0.75$, $F = 70$ N and $\mu = 0.74$ for steel on steel

$$T_R = 70\frac{14.026(0.7*3.14*14.026 + 0.75)}{2(3.14*14.026 - 0.7*0.75)} \quad \text{EQ. 6.9}$$

This analysis suggests that a torque of 242.13 N-mm is required on the release knob to attain a tensile force of 70 N from the release mechanism resulting in release of the implant from the actuator.

6.5.2. MODE OF OPERATION

The three step operational sequence of the actuator shown in Fig. 6.16 (a-d) is detailed below:

a) During the preliminary stage, the safety pin is engaged and the actuator is fully locked, preventing the implant from accidental deployment, handling loads and spring compressive force. The pawl pin is in the first (distal) ratchet. The compression spring is 18 mm deflected and exerting a 30 N force absorbed by safety pin.

b) In the first step, the safety pin is removed, shifting the 30 N of compressive force from the safety pin to the implant. The fore-body can now be rotated CCW and the pawl pin latches into the ratchet wheel (for distal wings). This operation applies torque to the implant, allowing the distal slots to displace outwards. When the compressive force overcomes the internal resistance of the implant slots, the distal wings are formed by the compression of the slots. During this process, the pawl pin is pushed into the proximal ratchet locking the CCW rotation. At the end of this step, the spring deflection is reduced from 18 mm to 15.5 mm thereby reducing the spring force to 25 N.

c) In the second step, the fore-body can only be rotated CW and the pawl pin latches in the ratchet wheel (for proximal wings). The compression spring is 15.5 mm deflected and exerting a force of 25 N to the implant. During the process of wings formation, the pawl pin is driven into the release wheel by the compression spring. At the end of this step, the pawl pin is settled in the release wheel, which locks all rotations and backward translation of the fore-body. Spring deflection is further reduced from 15.5 mm to 13 mm, thus reducing the spring force to 21 N.

d) In the final step, the only possible operation is the rotation of the release knob. The release knob can be rotated CW to effect the release shaft which moves axially backward. This axial movement of the release shaft away from the implant exerts a tensile force on the implant's release mechanism. At a release torque of 242.13 N-mm, the corresponding tensile force reaches a value of 70 N, causing the release mechanism to break, thus releasing the implant from the delivery actuator.

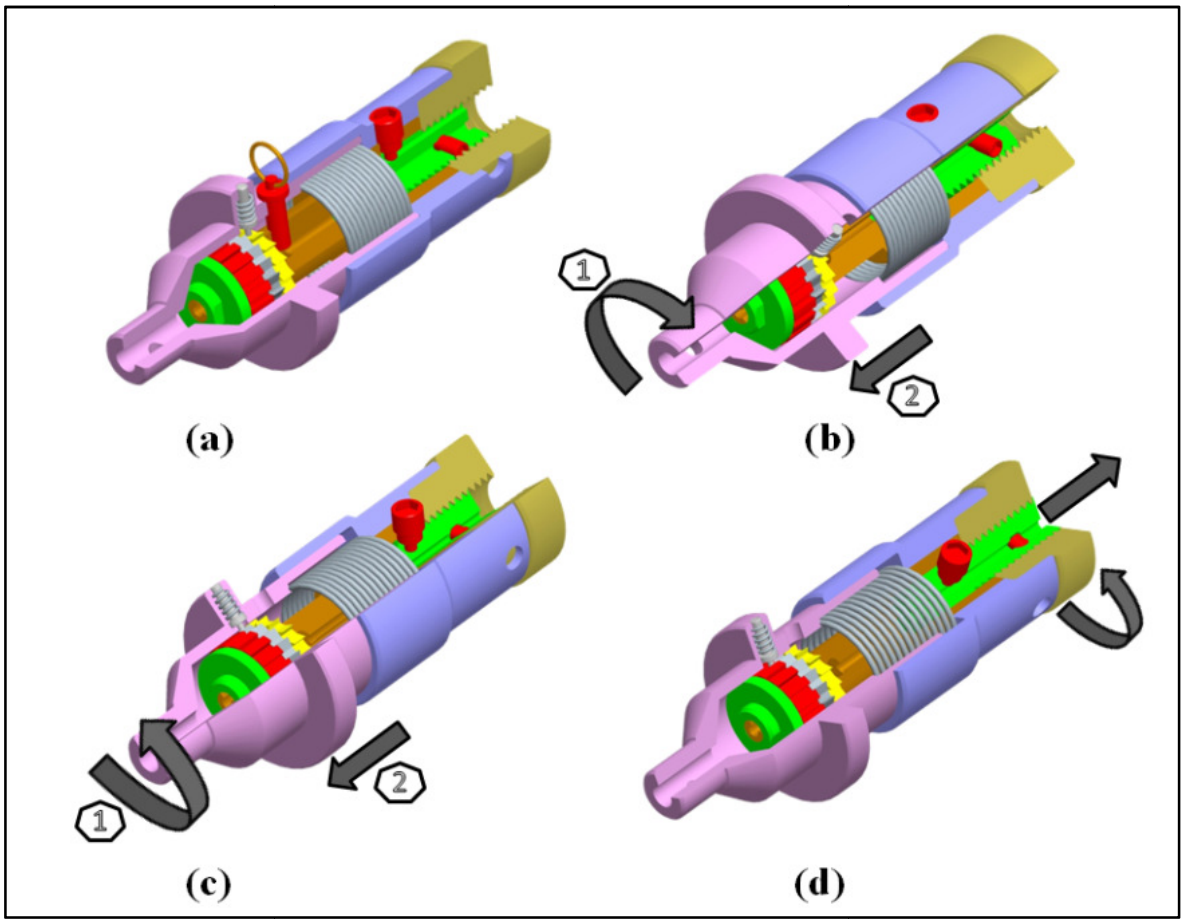

Figure 6.16: Operational Sequence of Actuator (a) Initial Condition (b) Counter-Clockwise Rotation followed by Spring Compression (c) Clockwise Rotation followed by Spring Compression (d) Clockwise Rotation of Release Knob

TABLE 6.1: ACTUATOR HANDLING AND OPERATIONAL LOADS

Components		Deployment and Release		Handling Loads	
		Compression / Tension (N)	Torque (N-mm)	Grip Force (N)	Torque (N-mm)
Handle-body		70	15.4, 16	826	520
Fore-body		25, 30, 70	15.4, 16	0	520
Ratchet Mechanism	Ratchet Wheel	0	0	0	520
	Pawl Pin	0	0	0	520
Release Mechanism	Release Knob	70	320	826	0
	Release Shaft	70	15.4, 16	0	0

6.5.3. FEA AND OPTIMISATION

Finite Element Analysis using ANSYS WB was performed to simulate functionality and to investigate the mechanical behaviour of the actuator under deployment, release and handling forces as mentioned in Table 6.1. Design optimisation of the actuator was performed using Design Xplorer, a module of ANSYS WB. The objective of these optimisation studies was to investigate the mechanical behavior of the actuator and to minimize its mass. All the actuator components were analyzed and optimized individually in this process. FEA analysis was defined according to the actual scenario in the simulation module of ANSYS WB. A biocompatible grade of stainless steel SS-316, a nickel-chromium-molybdenum alloy steel, was chosen for the actuator. The Material properties of SS-316 were assigned in the ANSYS WB environment. Young's modulus E used for this material was 193 GPa, Poisson ratio υ was 0.3, yield strength σy was 690 MPa and the ultimate tensile strength σu was 860 MPa. The upper and lower limiting values of design variables were assigned to parameters leading to the generation of Automatic Design Points (ADP). Based on the ADP, the response of maximum von-Mises stress with respect to design variables was plotted and reviewed to the best feasible design point. Goal driven optimisation was performed based on ADP study and a candidate design based on current goals was generated with the best candidate design being selected and inserted as a soft design. The best candidate design was used to generate the hard reference design by performing FEA analysis in ANSYS WB environment. Finally, the reference design point was rated and the current (optimum) parameter values for the best design were automatically updated from the DesignXplorer into the parameter manager consequently updating Pro/E model. A final analysis was performed in the WB environment to verify the results obtained from the design optimisation.

The actuator was designed and optimized to withstand the deployment and release forces. The mechanical loads were evaluated with the worst-case scenarios of the dominant handling loads. All the actuator components were optimized against their respective loadings as mentioned in Table 6.1. The objective of these optimisation studies was to minimize the mass of the actuator components. Therefore, the minimum volume was defined as objective variable (goal), the maximum von-Mises stress with the limiting values of 680±10 MPa was defined as the state variable (constraint). The design optimisation studies of individual components are discussed below:

A. FORE-BODY

The fore-body was optimized against the deployment and release loads. The fore-body is physically attached to the guide tube by a socket set screw. Thus, torque and compression is transmitted to the guide tube through the socket set screw hole. In order to simulate the fore-body separately, the fixed displacement boundary condition was applied on the screw hole. Fig. 6.17 (a) shows all the applied boundary conditions for the optimisation study. The proximal end of the fore-body is constrained radially in the handle-body. Therefore, the cylindrical boundary condition was applied on this end. A moment of 16 N-mm was applied on the grip surface having a maximum diameter and a compressive force of 70 N was applied on the rear surface. In the optimisation study, the design parameters *insrt_end_thk, cone_thk, rear_cyl_thk* and *mid_srf_wdth* were defined for the fore-body thicknesses of the insert end, conical end, rear cylinder and the middle surface. The volume of the fore-body was meshed with hexahedron elements as shown in Fig. 6.17 (b). An optimisation study was performed to achieve an optimum volume while satisfying the constraints on the maximum von-Mises stress. The final analysis was performed on the optimum geometry to verify the optimisation results. The von-mises stress distribution and the total deformation in the optimized model are shown in Fig. 6.17 (c) and 6.17 (d) respectively.

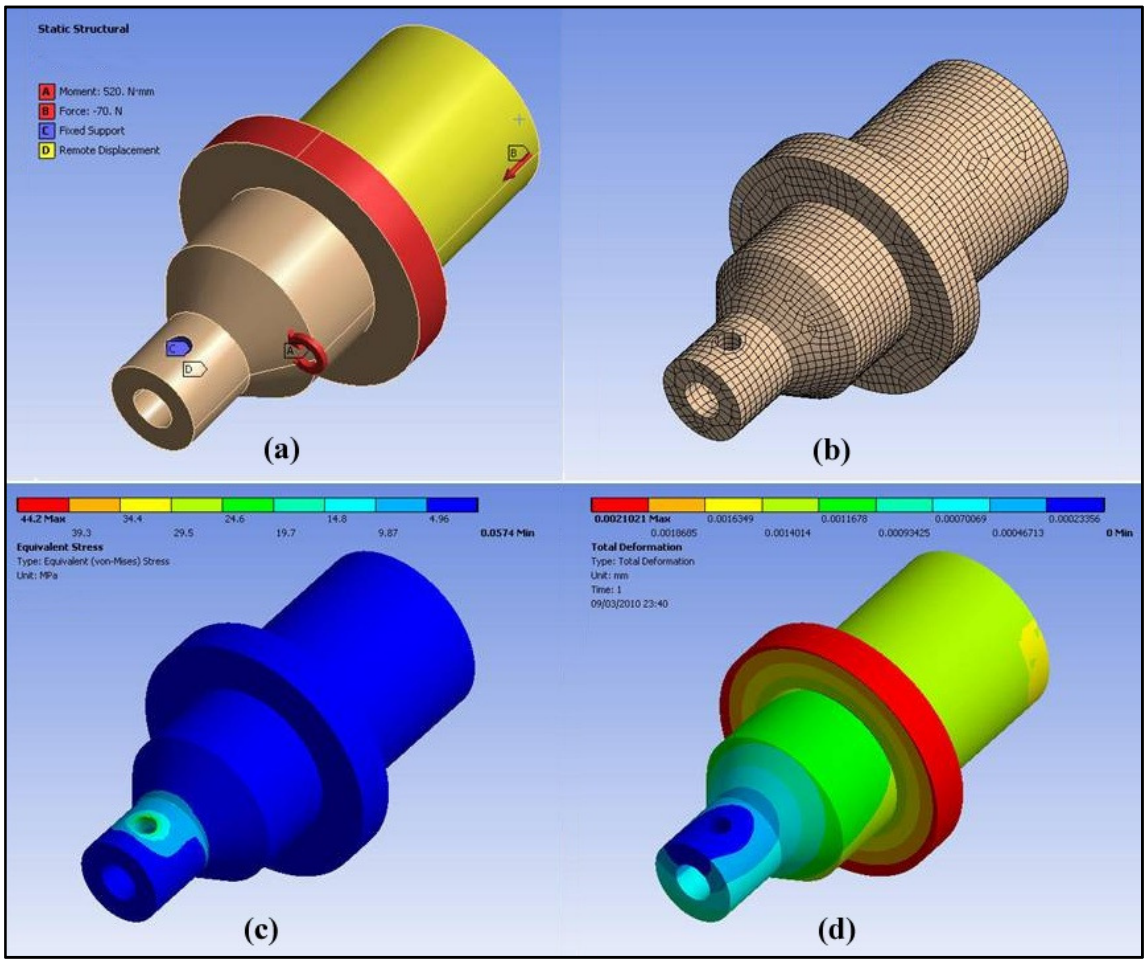

FIGURE 6.17: OPTIMISATION OF FORE-BODY (a) APPLIED BOUNDARY CONDITIONS (b) FE MESH (c) VON-MISES STRESS DISTRIBUTION (d) TOTAL DEFORMATION

B. HANDLE-BODY

The handle-body is designed to be gripped by the hand during usage of the actuator. Therefore, it was analyzed against both the maximum grip force of a human hand and the forces required for implant deployment and release as detailed in Table 6.1. The handle-body retains the fore-body inside the distal portion, the ratchet shaft at the mid portion and the release knob at the proximal end. The boundary conditions were applied to represent this whole scenario as shown in Fig. 6.18 (a). A human hand wearing a latex glove can apply a grip force of 826 N on a Ø 25 mm cylindrical body [174]. Hence, a force of 826 N in the form of pressure was applied on the outer surface of the handle-body. The release knob exerts a 70 N axial force during implant release, which was applied at the proximal end of the handle-body. The objective and state function of the optimisation study were the same as detailed earlier. The design parameters

frnt_cyl_thk and *rear_cyl_thk* were defined for the front and rear segment thicknesses of the handle-body. The parametric model was meshed with hexahedron elements as shown in Fig. 6.18 (b). Optimisation was performed on the initial design and the final analysis was performed on the optimum geometry to verify the optimisation results. Fig. 6.18 (c) and 6.18 (d) shows the von-Mises stress distribution and total deformation in the final validation analysis.

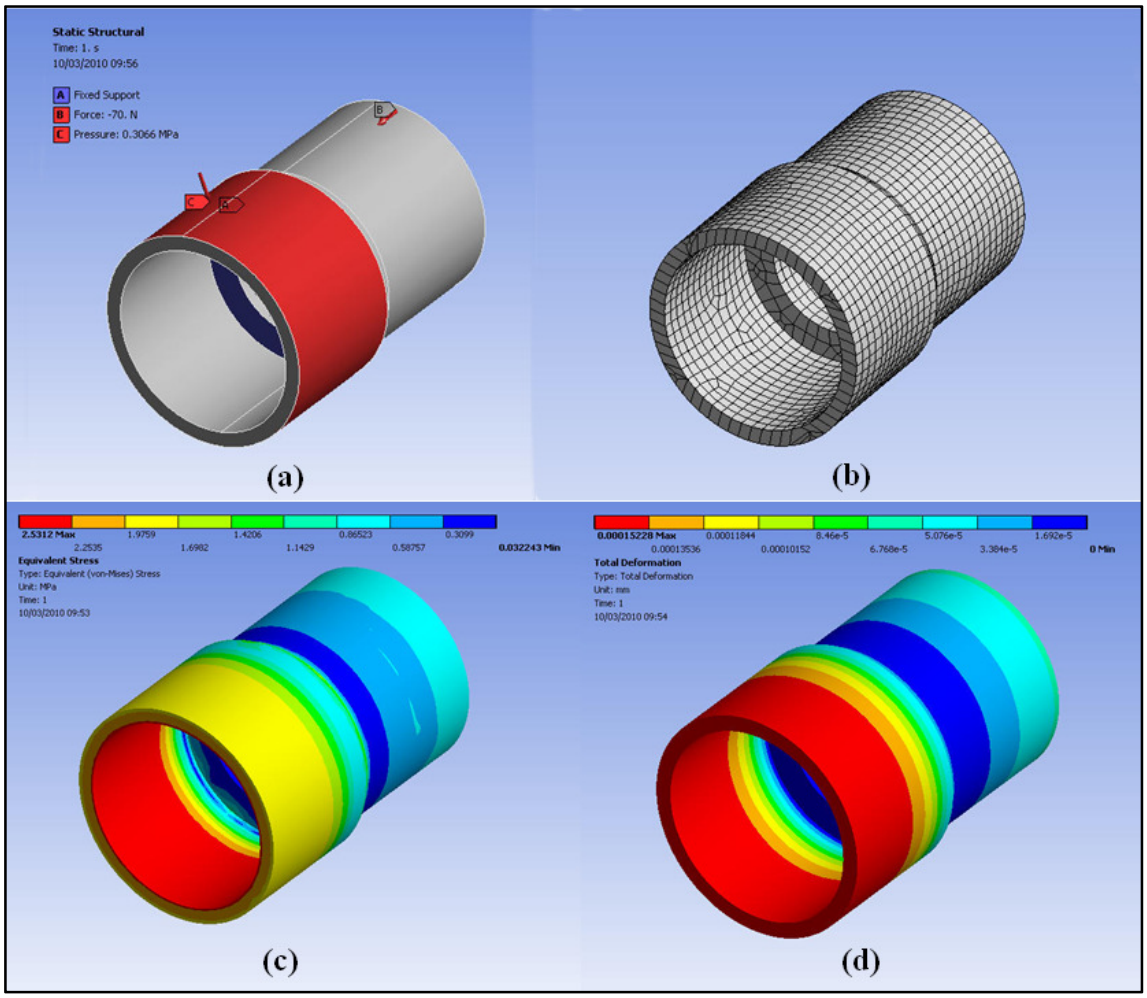

FIGURE 6.18: OPTIMISATION OF HANDLE-BODY (a) APPLIED BOUNDARY CONDITIONS (b) FE MESH (c) VON-MISES STRESS DISTRIBUTION (d) TOTAL DEFORMATION

C. RATCHET MECHANISM

During deployment, the only force experienced by the ratchet mechanism is the frictional force between the pawl pin and the ratchet wheel. The worst-case scenario for the ratchet mechanism would be an inadvertent reverse torque produced by mishandling of the actuator. The torque a human hand can apply on a Ø 25 mm cylindrical body with an index finger and thumb is 520 N-mm [171]. This value was also experimentally validated by testing the actuator using a torque meter. The ratchet mechanism was analyzed against this torque value. Boundary conditions were applied to simulate the actual conditions as shown in Fig. 6.19 (a) in which fixed displacement were applied on the surfaces of the pawl pin, in contact with the fore-body. A moment of 520 N-mm was applied on the inner cylindrical surface ratchet wheel. Surface-to-surface frictional contact was defined between the pawl pin and ratchet wheel with a frictional coefficient of 0.74. Fig. 6.19 (b) shows the model meshed with hexahedron elements. The design parameters were defined for both the ratchet wheel and the pawl pin. The parameters *teeth_ang, teeth_width, pin_up_dia* and *pin_lwr_dia* were defined for the teeth angle, teeth width, pin upper diameter and pin lower diameter. An optimisation study was performed after defining the objective and state function. Fig. 6.19 (c) and 6.19 (d) shows the von-Mises stress distribution and the total deformation in the ratchet wheel and pawl pin.

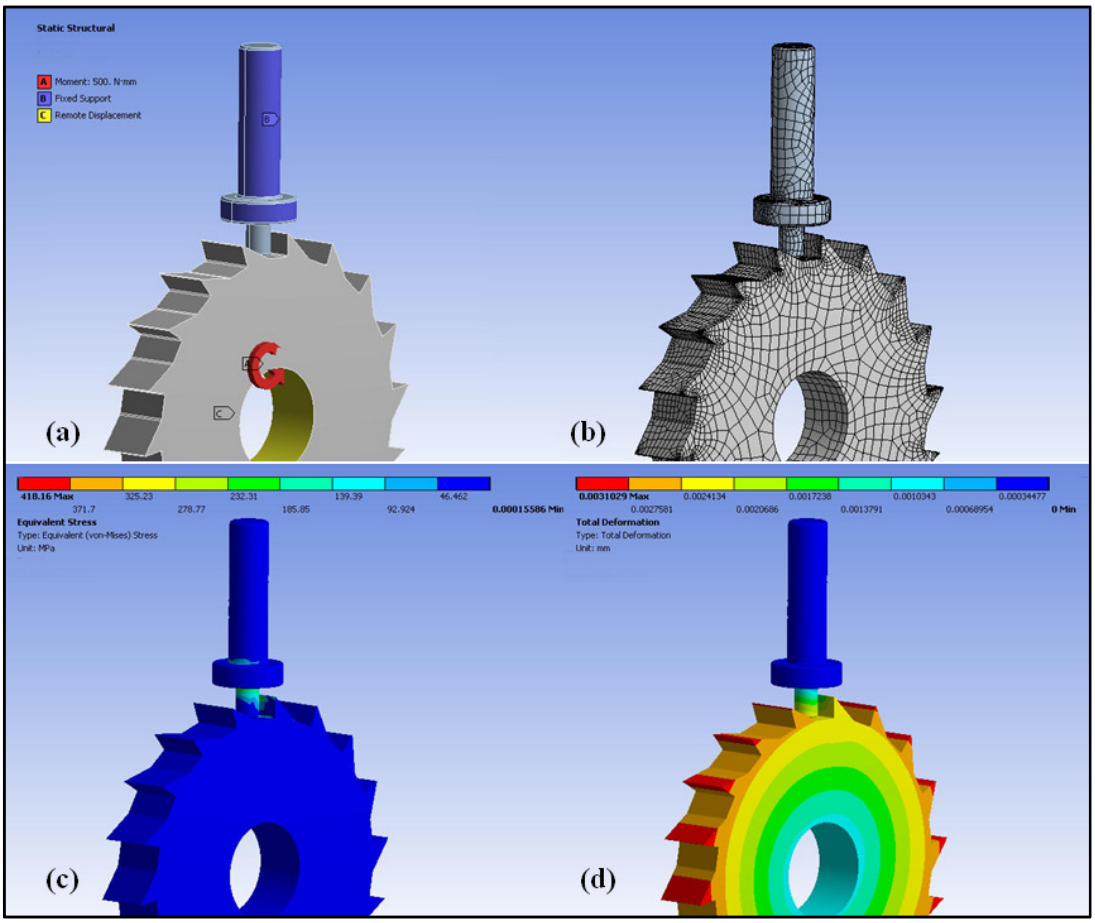

FIGURE 6.19: OPTIMISATION OF RATCHET MECHANISM (a) APPLIED BOUNDARY CONDITIONS (b) FE MESH (c) VON-MISES STRESS DISTRIBUTION (d) TOTAL DEFORMATION

D. RELEASE MECHANISM

Release forces were applied on both the release knob and the shaft to investigate their mechanical behaviour. In order to analyse the release mechanism, surface-to-surface frictional contact was defined in between the release knob and release shaft. To simulate the actual conditions those surfaces of the release knob, which remains in contact with the handle-body were constrained along the longitudinal axis. Fig. 6.20 (a) details the boundary conditions applied on the assembly model. The mathematically calculated release torque of 242 N-mm was applied on the outer surface of the release knob. A tensile force of 70 N was applied on the release shaft along the longitudinal axis. As Fig. 6.20 (b) shows the model was meshed with tetrahedron elements and static, analysis was performed to evaluate the stresses. The total deformation and the von-Mises stress distribution in the release knob and the release shaft are shown in Fig. 6.20 (c) and 6.20 (d) respectively. It can be observed that the maximum value of von-Mises stress is below the yield strength of the material.

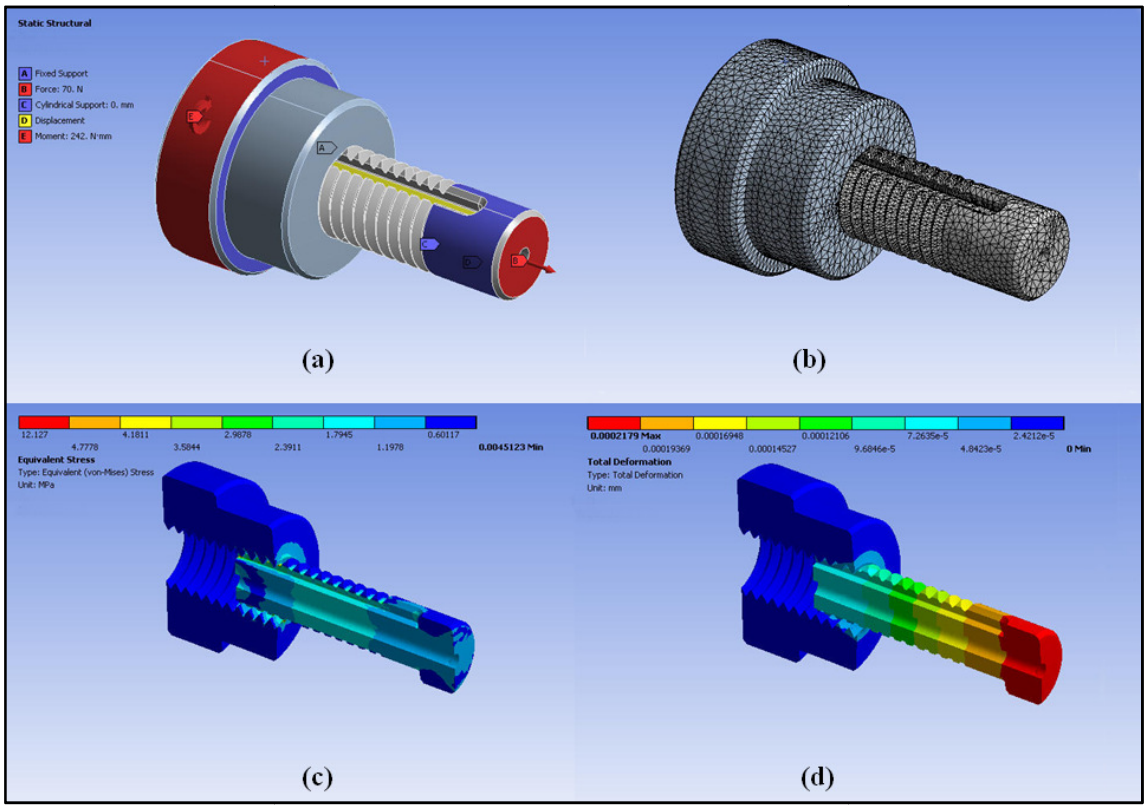

FIGURE 6.20: RELEASE MECHANISM (a) APPLIED BOUNDARY CONDITIONS (b) FE MESH (c) VON-MISES STRESS DISTRIBUTION (d) TOTAL DEFORMATION

The FEA simulations were performed to investigate the mechanical behaviour and functionality of the actuator against deployment, release and handling loads. Optimisation was performed to achieve the minimum mass of the actuator. During the actuator components optimisation studies, it was observed that the machining constraint became the limiting factor on design variables. Because even at thicknesses comparable to the implant thickness, the von-Mises stresses among the components were well below the maximum limiting value (yield strength of the SS-316). Therefore, the optimum design of the actuator components was maintained at those material thicknesses, which were possible to machine.

E. MESH CONVERGENCE

Mesh convergence was performed on all the FE models of the actuator components. The effect of mesh density on the model accuracy was investigated using six different FE meshes detailed in Table 6.2. In Table 6.2, type A is the coarsest and type F is the finest mesh. The FE meshes were varied by varying the element size and the mesh relevance. To estimate the mesh convergence, the von-Mises stresses in each model were compared for each mesh refinement by keeping same the rest of the variables. Fig. 6.21 (a-d) shows the convergence tests on the actuator components to assess the necessary level of mesh refinement.

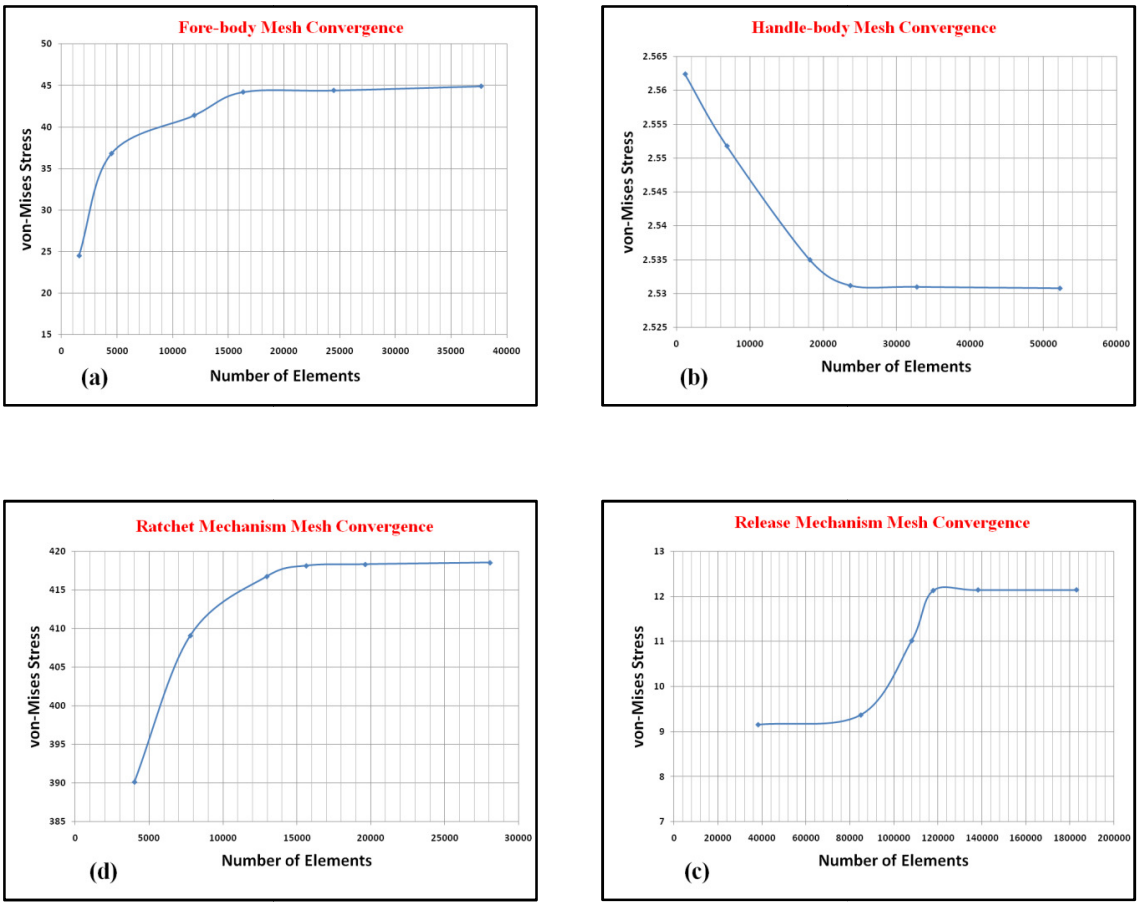

FIGURE 6.21: MESH CONVERGENCE (a) FORE-BODY (b) HANDLE-BODY (c) RATCHET MECHANISM (d) RELEASE MECHANISM

TABLE 6.2: MESH CONVERGENCE DATA FOR ACTUATOR COMPONENTS

Model	Mesh	Number of Nodes	Number of Elements	Von-Mises Stress (MPa)
Fore-body	A	5115	1580	24.5
	B	16309	4483	36.8
	C	40979	11925	41.4
	D	58663	16313	44.2
	E	85139	24457	44.4
	F	127873	37711	44.9
Handle-body	A	4986	1148	2.5624
	B	25267	6846	2.5518
	C	62781	18164	2.535
	D	89549	23673	2.5312
	E	120083	32745	2.531
	F	180356	52277	2.5308
Ratchet Mechanism	A	13187	4007	390.1
	B	32113	7792	409.1
	C	55574	12968	416.77
	D	59988	15637	418.16
	E	82921	19633	418.34
	F	116639	28083	418.56
Release Mechanism	A	67111	38178	9.157
	B	141680	84883	9.3707
	C	177190	108033	11.016
	D	191492	117792	12.127
	E	223101	138168	12.141
	F	291262	182953	12.143

6.5.4. DEVELOPMENT AND TESTING

A. PROTOTYPING

A stainless steel prototype was fabricated using a 140-CNC lathe for high accuracy requirement. The intricate ratchet wheels were fabricated using ONA PRIMA E250 wire EDM machine Fig. 6.22 shows the machined ratchet wheels. All engineering drawings were developed using Pro/E software and CNC programs were directly generated using Pro/NC a module of Pro/E. All machined critical dimensions were inspected using Video Inspection Probe, Deltronic Inc. and were found within a tolerance ± 0.05 mm. Fig. 6.23 details the fabricated actuator components. The fabricated prototype shown in Fig. 6.24 was used for various mechanical testing and validation of the actuator mechanisms. In addition, it was used for functionality test by deploying and releasing the implant on the test-bench.

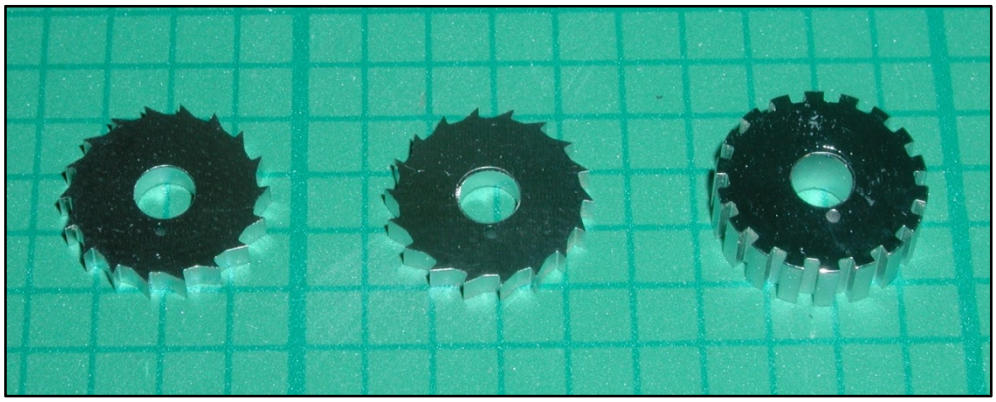

FIGURE 6.22: FABRICATED RATCHET AND RELEASE WHEELS

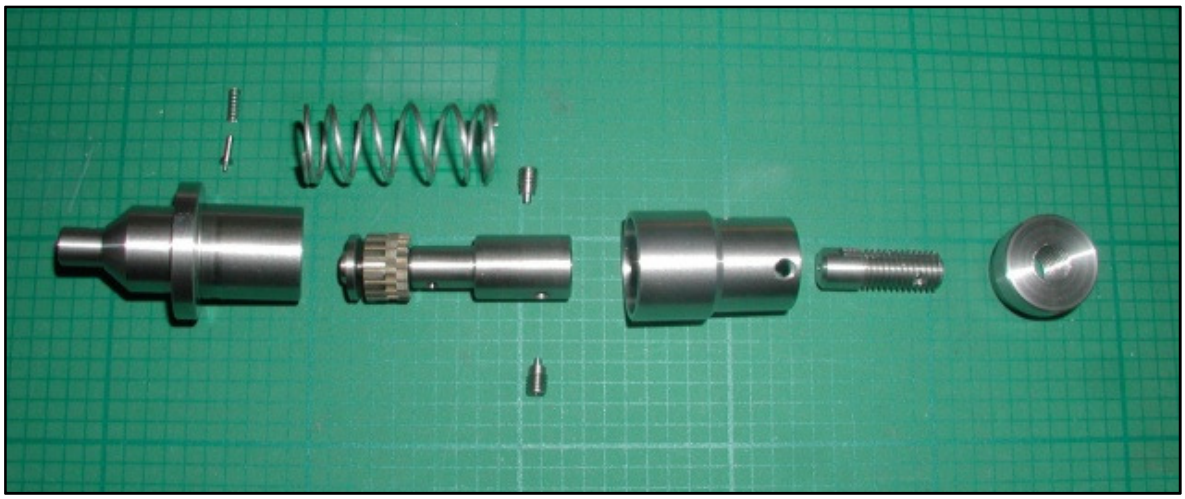

FIGURE 6.23: FABRICATED STAINLESS STEEL ACTUATOR (EXPLODED)

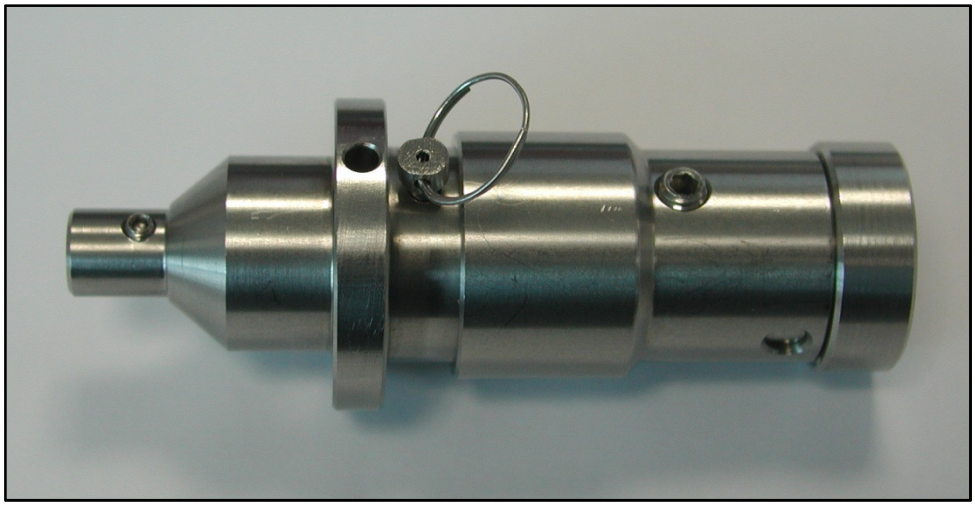

FIGURE 6.24: FABRICATED STAINLESS STEEL ACTUATOR

B. TORQUE TESTING ON HANDLE-BODY

The torque a human hand can apply on a Ø 25 mm cylindrical body with an index finger and thumb is 520 N-mm [171]. This value used in FEA simulations was experimentally validated by measuring torque on the actuator using torque-measuring equipment. The torque measuring setup is shown in Fig. 6.25 (a) in which torque is being applied on the handle-body. The torque meter was held in a vise. Due to the limitation of torque meter's chuck Ø, a solid shaft was used to interface the actuator with the torque meter. One end of this shaft was griped in the torque meter and the opposite insert shaped end into the fore-body. Once the task was setup, the torque meter was reset and the recording mode was set to peak torque value. The handle-body was held with an index finger and thumb as per in normal operation mode. The torque was applied on the handle-body in both CW and CCW directions and peak torque values were documented. This recorded torque was compared with the available values from the previous studies [171,172].

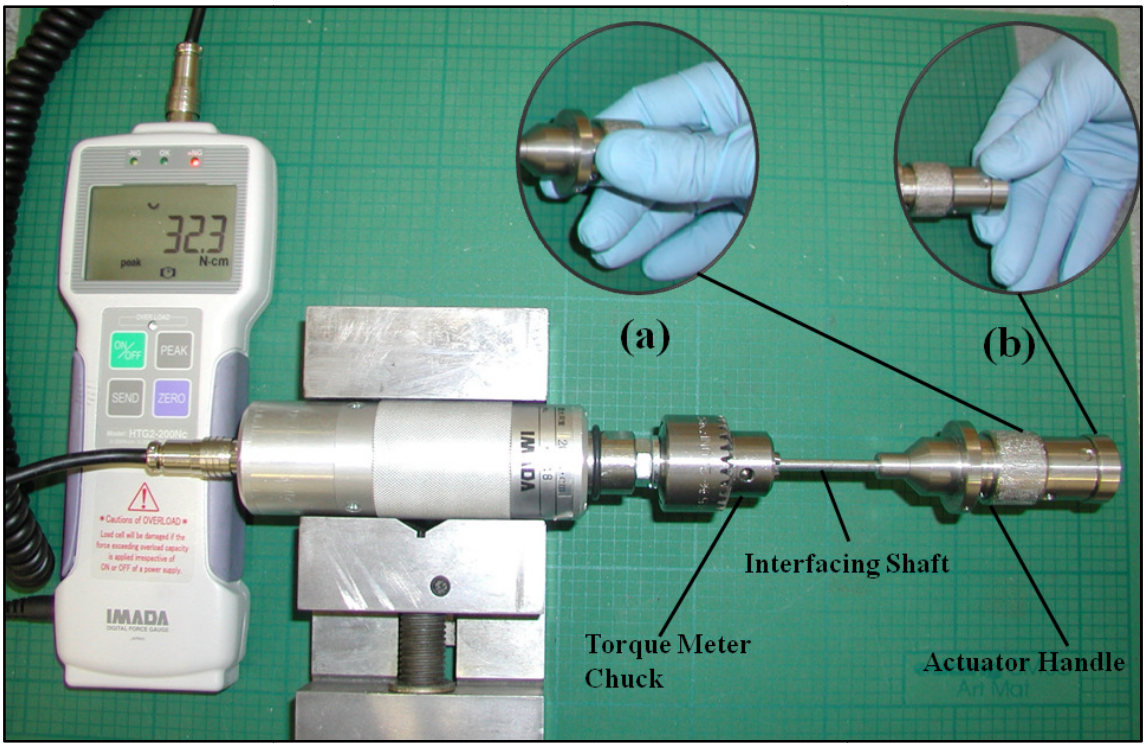

FIGURE 6.25: TORQUE MEASURING SETUP FOR TORQUE MEASUREMENT ON (a) HANDLE-BODY (b) RELEASE-KNOB

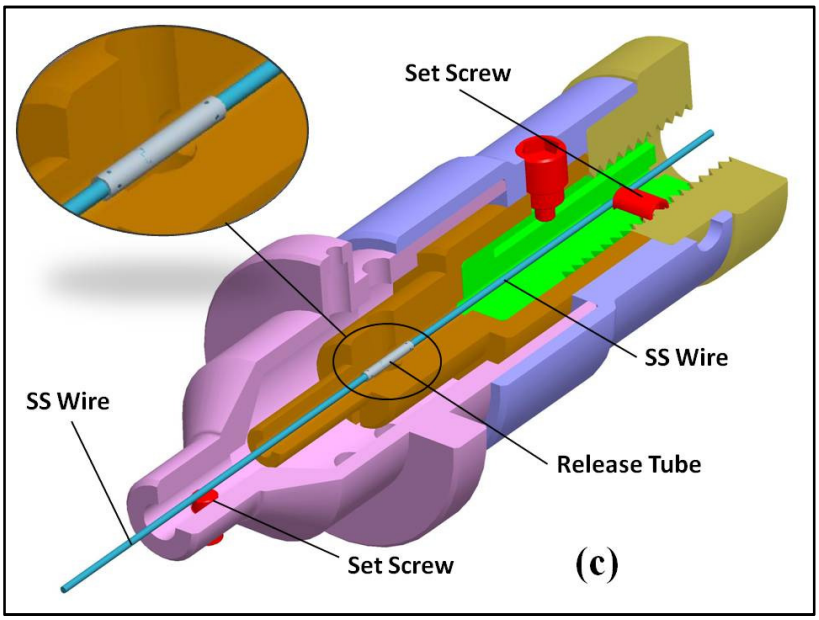

FIGURE 6.26: RELEASE TUBE GRIPPED INSIDE ACTUATOR

C. TORQUE TESTING ON RELEASE KNOB

The torque on the release knob was measured by breaking the release tube inside the actuator. The setup to measure the torque to release the implant by breaking the release tube was quite specific. The release tube, with a length of 7 mm, an outer Ø of 1 mm and a thickness of 0.125 mm is made of hardened SS-316LVM tube and includes a pair of slots. This symmetric pair of laser cut slots forms an arc shape at both ends and a rectangular pattern in between. The gap in between this pair of slots forms a neck region, which is designed to break at a specified load. In order to hold the release tube inside the actuator, two lengths of SS-316 wires were laser welded at both ends of release tube. The release tube was positioned at the centre of the actuator and the end wires were clamped as shown in Fig. 6.26. One end of the wire was griped at the distal end of the fore-body using “guide tube insert set screw (Fig. 6.13)” and other end in the release shaft using “guide wire lock screw (Fig. 6.13)”. On completion of setup, the torque measuring equipment was set to peak mode and torque was applied on the release knob as shown in Fig. 6.25 (b). Because of the power screw mechanism the applied torque on the release knob acted as a tensile force on the release tube. This torque was applied until breakage of the release tube. The measured torque of 264.4 N-mm was compared with the theoretically calculated torque value.

D. COMPRESSION TESTING

The compression force applied by the actuator during the deployment sequence was validated using a tensile testing machine. Here the handle-body was clamped in the upper jaw of the tensile testing machine and the fore-body was constrained axially in the lower jaw as shown in Fig. 6.27. The machine was programmed from the console to simulate the sequence of compression forces applied by the actuator. The three step sequence includes, firstly the compression force exerted by the actuator on the implant at initial stage; secondly, the compression force at the end of distal wings deployment; thirdly, the compression force at the end of proximal wings deployment. This sequence was executed and the compression forces at the end of each step were compared with the designed values. The characteristic curve obtained from tensile testing machine for the actuator compressive forces is shown in Fig. 6.28

The compression forces during the formation of the wings were also measured. For this measurement, the same setup mentioned above was used except an implant was loaded on the actuator using a smaller guide tube. The implant was deployed in this setup and the compression forces were measured through the load cell of the machine. The compression force achieved during this study was compared with the values of simulated values.

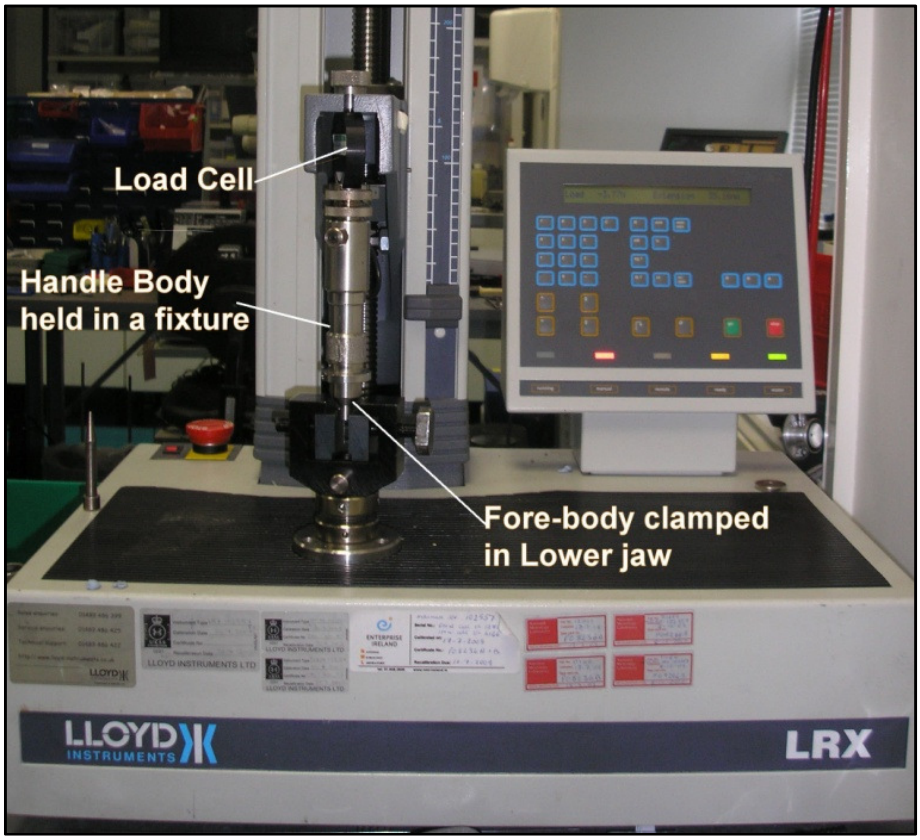

FIGURE 6.27: TESTING SETUP FOR COMPRESSION LOAD MEASUREMENTS

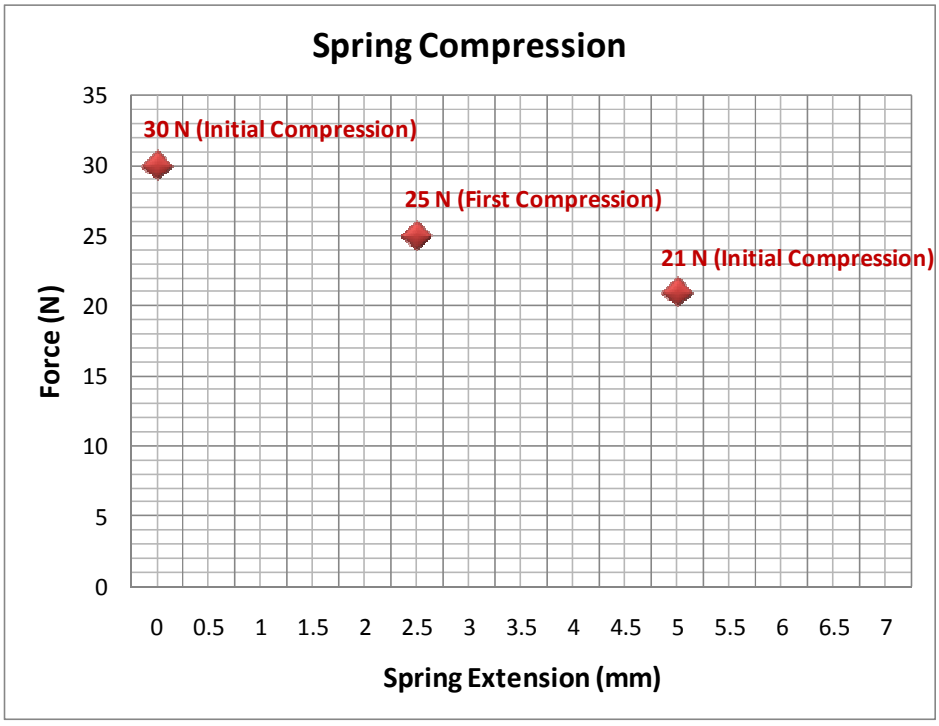

FIGURE 6.28: ACTUATOR COMPRESSIVE FORCE CHARACTERISTIC CURVE

CHAPTER 7

STERILIZATION DEVICE RESULTS AND DISCUSSION

7.1. INTRODUCTION

This research work presents the design, development and verification of a novel mechanical occlusion device that achieves permanent female sterilization via the transcervical approach. This chapter presents the summary of the complete device, its in-vitro validation in a hysteroscpic diagnostic model and explanted uterus. Finally, the validation results of the device are presented and discussed.

7.2. DEVICE SUMMARY

The device is designed to deploy an implant under hysteroscopic visualization into the intramural segment of the fallopian tube to provide an instant mechanical occlusion, as shown in Fig. 7.1.

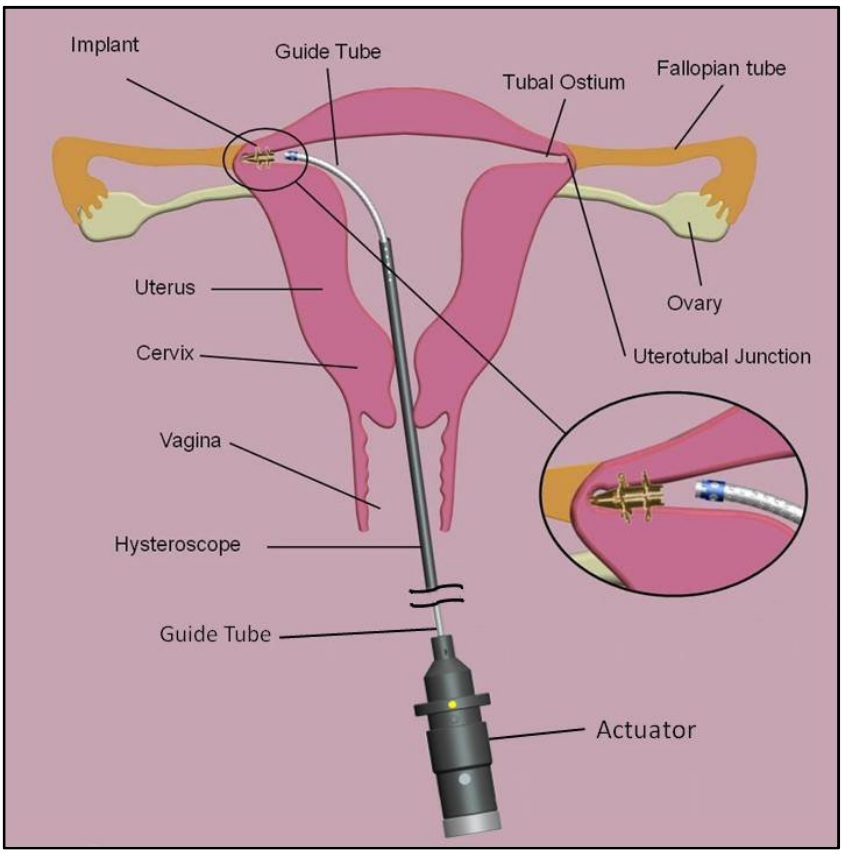

FIGURE 7.1: DEVICE DEPLOYMENT AT THE LEFT FALLOPIAN TUBE

As discussed in chapters 4, 5 and 6, the device consists of three major systems, an implant for occlusion of the fallopian tube, a guide tube and wire combination for guidance of the implant through the cervix and an actuator handle to control the deployment and release of the implant, as shown in Fig. 7.2. The implant is attached at the flexible distal end of the guiding system. The proximal end of the guiding system is attached with the actuator handle. The occlusion system can be advanced through a 5-French (F) (1.67mm internal diameter) operating channel of a standard hysteroscope. During insertion, the implant forms a low profile cylindrical shape and is advanced through the use of a guiding system. After arriving at the target location within the human uterus, the required forces for the deployment and release of the implant are applied through the actuator in a specified sequence.

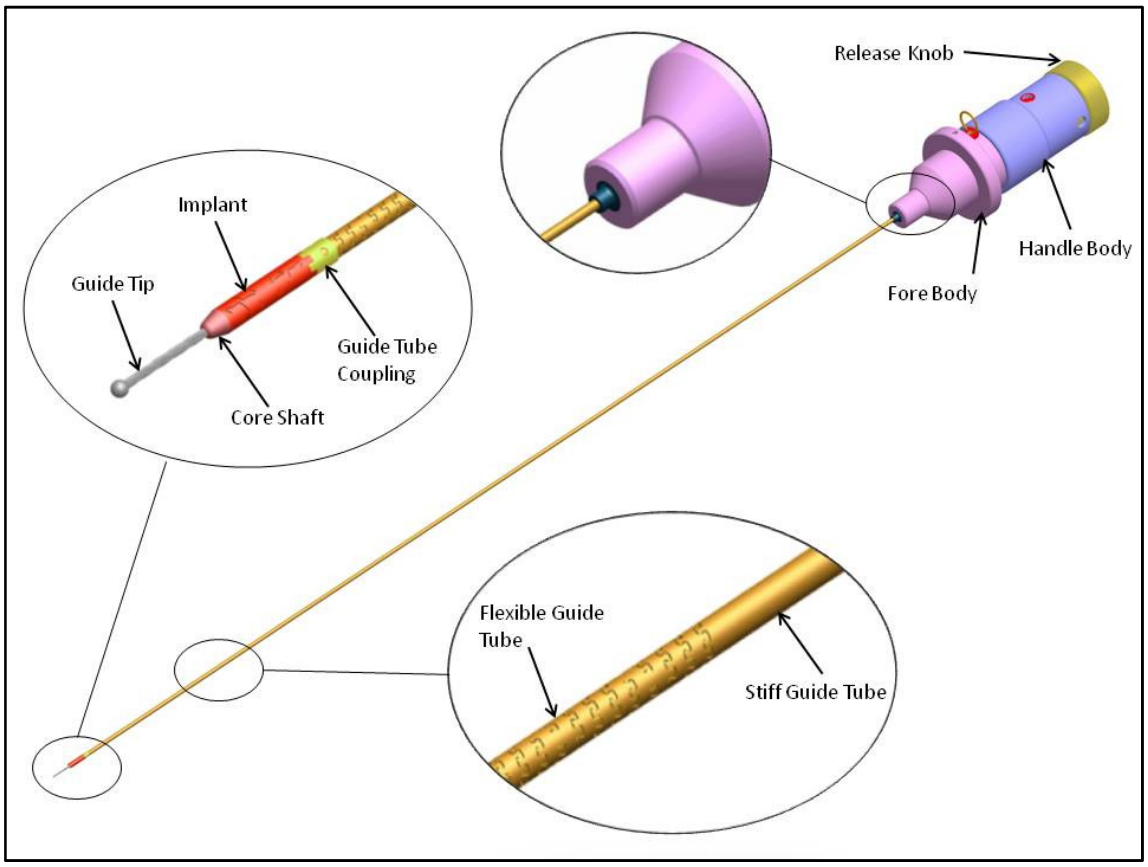

FIGURE 7.2: COMPLETE DEVICE CONFIGURATION

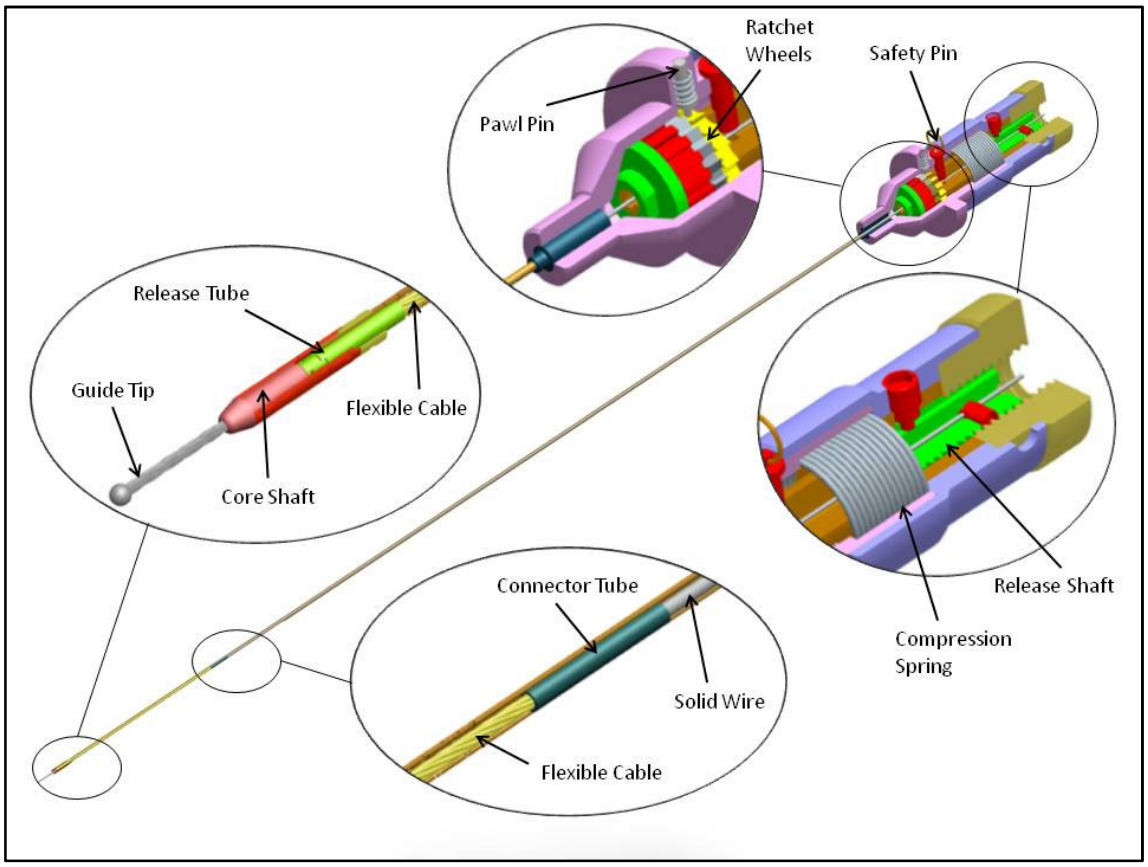

FIGURE 7.3: THREE QUARTER SECTION OF THE COMPLETE DEVICE

7.2.1. THE IMPLANT

The implant consists of a flexible guide tip at the distal end and a main cylindrical body housing an inner release system comprising of a core shaft and release tube as shown in Fig. 7.3. The implant main cylindrical body, with a length of 6.5 mm, an OD of 1.535 mm and a thickness of 0.1 mm, is made of annealed SS-316LVM. It features two sets of six slots at the distal and proximal segments. Post deployment, these slots determine the implant final shape by formation of two sets of six wings. These wings serve to anchor the implant by protruding into the tubal ostium and entrapping the tissue of the intramural section to instantaneously occlude the fallopian tubes. The proximal end of the implant includes straight splines used to couple with the guide tube. Fig. 7.4 depicts the comparison of the un-deployed and deployed implant. The guide tip is a Ø 0.5 mm, multi-filament (7x7x7) cable with a spherical ball shape of Ø 1 mm at the distal end. The guide tip is designed to guide the implant through the uterus into the fallopian tube. Hence, a fine balance between column strength (for push-ability and forward progression) and flexibility (to negotiate the curvatures of the uterus and fallopian tube)

is required. The core shaft at the distal end of implant is a hardened SS-316LVM solid shaft, whose one end is conical and laser welded to the distal end of the implant and other end of the release tube. The release tube, with a length of 7 mm, an outer Ø of 1 mm and a thickness of 0.125 mm is made of hardened SS-316LVM tube and includes a pair of slots. This symmetric pair of laser cut slots forms an arc shape at both ends and a rectangular pattern in between. The gap in between this pair of slots forms a neck region, which is designed to break at a specified load. Once the implant is deployed into the intramural segment of the fallopian tube, the weak link designed on the release tube is broken, releasing the implant from the guide system and consequently from delivery actuator.

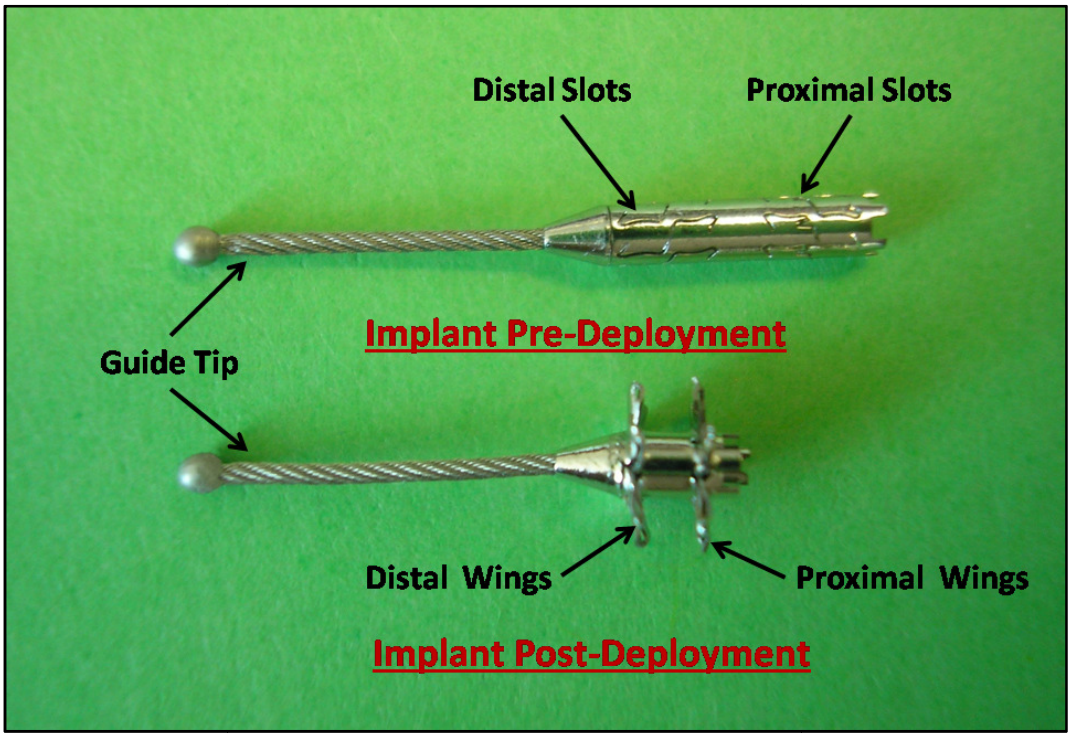

FIGURE 7.4: IMPLANT PRE-DEPLOYMENT AND POST-DEPLOYMENT

7.2.2. GUIDE SYSTEM

The implant is delivered into the tubal ostium by the guiding system, which includes an outer guide tube and an inner guide wire. The guide tube includes straight splines at the distal end, which are matched exactly with the implant splines. These matching straight splines are used to couple the guide tube with the implant as shown in Fig. 7.2. The inner guide wire is attached to the implant's release tube as shown in Fig. 7.3. In order to deal with the curvatures of the uterus and fallopian tube, the guide system needs to be flexible. On the other hand, stiffness is required to transfer one-to-one torque to the implant. In order to acquire maximum torqability from the guiding system, a combination of flexibility and stiffness is designed into the guide system. As the device is delivered through the rigid channel of the hysteroscope and only a small distal portion of guide system emerge out of the hysteroscope and the rest remains inside the instrument channel. Therefore, only the emerged distal portions of the guide tube and wire were designed flexible. The guide tube, with a Ø 1.3 mm and a thickness of 0.125 mm is made of SS-316LVM hardened tube. The flexibility at the distal end of the guide tube was achieved by the addition of a segmented (inter-segment gap of 0.32 mm) chain of "dove tail" shaped helical slots with a pitch of 0.87 mm as shown in Fig. 7.2. These laser-cut slots shape was designed to provide the required flexibility and torqability. In order to obtain flexibility at the distal end of the guide wire, a multi-filament cable was laser welded with a single rigid wire as shown in Fig. 7.3. Thus, the 360 mm long guide wire, comprises of a Ø 0.7 mm multi-filament (1x7) SS-316LVM cable with a length of 65 mm and a Ø 0.7 mm annealed SS-316LVM wire.

7.2.3. ACTUATOR HANDLE

The proximal end of the guiding system is attached to the actuator handle. The material used for the components of the actuator is SS-316LVM. The actuator handle comprises a handle body of Ø 25 mm adapted to hold the actuator. At the distal end, a fore body is slidably and rotatably connected to the handle body. The fore body is also operatively connected to handle body through a ratchet mechanism in which the handle body incorporates a pair of ratchet wheels and the fore body includes a pawl pin as shown in Fig. 7.3. These ratchets are used to control the precise clockwise and counter-clockwise movements by restricting any inadvertent reverse rotations. A compression spring is used in between the handle body and fore body to assist the movements in axial directions. The actuator also features a safety pin, which locks the actuator,

preventing accidental deployment during handling or transportation. This safety pin needs to be removed prior to deployment. The proximal end of the handle body includes a release mechanism to control the release of the implant as shown in Fig. 7.2 and Fig. 7.3. This release mechanism includes a threaded release shaft slidably connected to the handle body and a release knob rotatably connected to the handle body. The power screw mechanism in between the release knob and release shaft converts the applied torque through the release knob into a tensile force on the release shaft. The release torque was limited to a value that a human hand can apply with an index finger on a cylinder of Ø 25 mm. The guide tube connected to the fore body experiences compression and the guide wire connected to the release shaft experiences tension during clockwise rotation of the release knob. This results in breaking of the release tube from the specified location, releasing the implant.

7.3. DEVICE OPERATION

The initial form of the implant is shown in Fig. 7.5. The device is designed to deploy and release in a five steps sequence, which can also be visualized by figures on page 26, Appendix C.

Step 1: The CCW rotation of the fore body applies a 15.4 N-mm clockwise torque to the implant, which generates an out-of-plane displacement in the distal slots as shown in Fig. 7.6.

Step 2: The compression spring applies a 30 N of axial compression force on the implant that plastically deforms the displaced slots into shape of the six distal wings as shown in Fig. 7.7.

Step 3: The CW rotation of the fore body applies a 16 N-mm counter-clockwise torque to the implant, which generates an out-of-plane displacement in the proximal slots as shown in Fig. 7.8.

Step 4: The compression spring applies a 25N of axial compression force on the implant that plastically deforms the displaced proximal slots into shape of the six proximal wings as shown in Fig. 7.9.

Step 5: The CW rotation of release knob applies a 70N of tensile force on the release tube allowing it to break at the designed location resulting in the release of the implant from actuator handle as shown in Fig. 7.10.

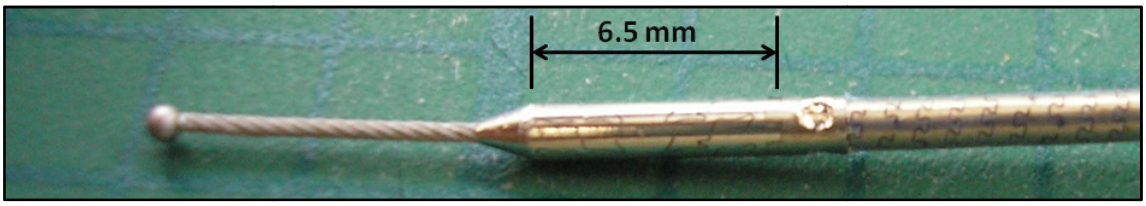

FIGURE 7.5: INITIAL STAGE

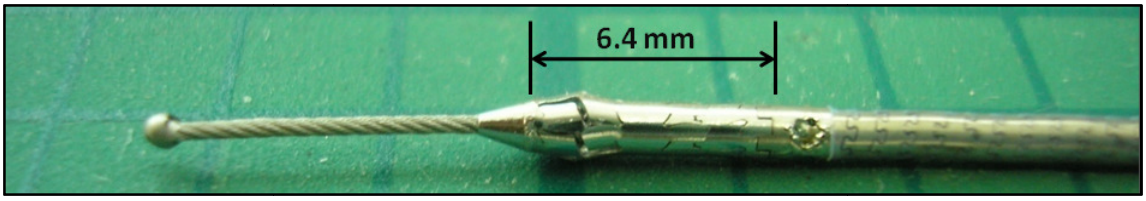

FIGURE 7.6: SEQUENCE STEP 1

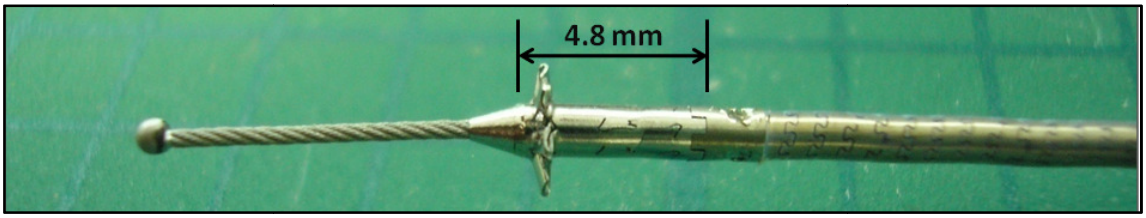

FIGURE 7.7: SEQUENCE STEP 2

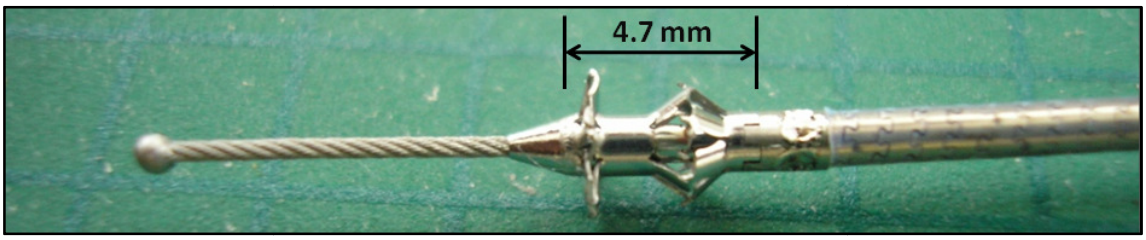

FIGURE 7.8: SEQUENCE STEP 3

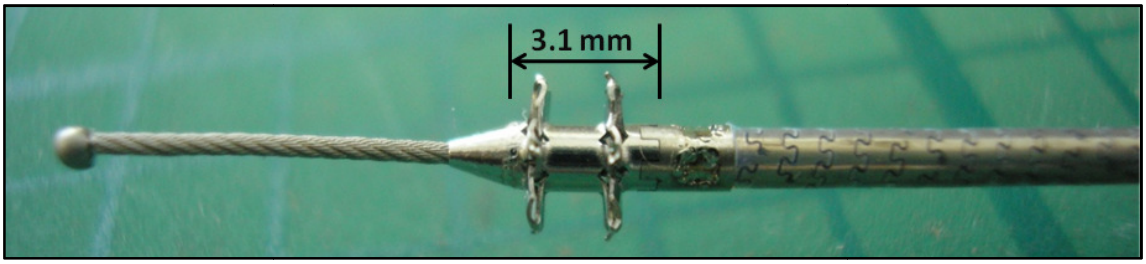

FIGURE 7.9: SEQUENCE STEP 4

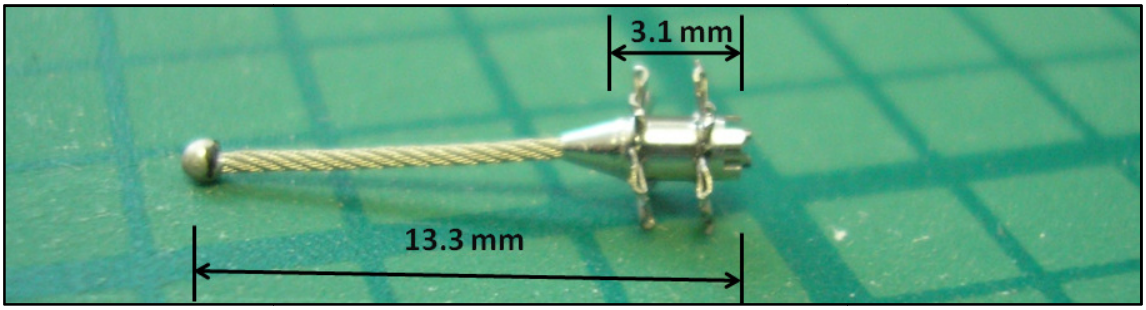

FIGURE 7.10: SEQUENCE STEP 5 (DEPLOYED IMPLANT)

7.4. DEVICE VALIDATION AND RESULTS

Validation of the device has been performed following a number of successful bench-top deployments *in-air*, *in-hysteroscopic* diagnostic model and *in-vitro* on animal tissue and explanted human uteri.

7.4.1. BENCH TESTING

The device was evaluated a number of times (n>80) in the laboratory. The evaluations include bench-top deployments of the implant *in-air*, *in-hysteroscopic* diagnostic model and *in-vitro*. The bench-top in-air and in-vitro testing were performed to assess efficacy of the device and validate the individual components including the implant, the delivery system and the actuator handle. In the *in-vitro* study, the device was implanted in porcine tissue, arteries and fallopian tubes. Bench-top deployments involved the deployments of the device *in-air* to validate the results of the FEA simulations and evaluate the functionality and mechanical behaviour of the device. Figs. 7.11 and 7.12 show a device introduced into a 5-F hysteroscope pre-deployment and post-deployment, respectively.

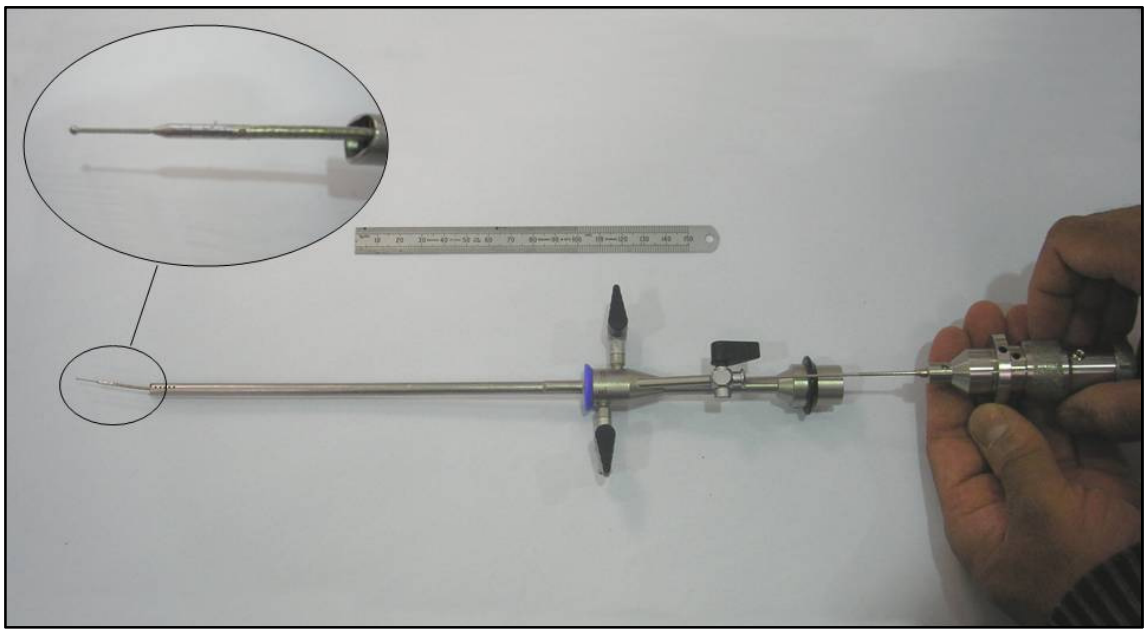

FIGURE 7.11: BENCH-TOP PRE-DEPLOYED DEVICE

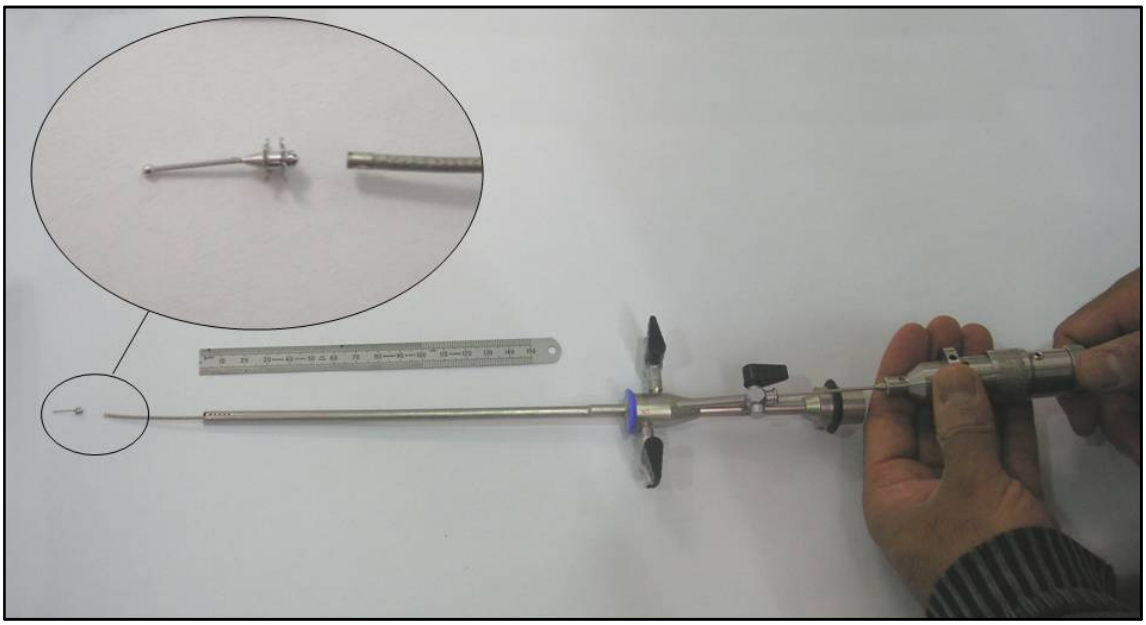

FIGURE 7.12: BENCH-TOP POST-DEPLOYED DEVICE

The device was also validated using a hysteroscopic diagnostic model obtained from Limbs and Things, Bristol, UK. This is a comprehensive intra-uterine examination training system with a variety of uteri to test instrument handling. This model includes a universal base, a uterus clamp and three diagnostics uteri. These uteri covers all the conditions of the uterus including, normal anatomy, polyps and fibroids. Therefore, device was investigated in all three types of uterus conditions for its functionality and deliverability. In the testing, the diagnostic model was attached with a saline bottle to simulate an actual scenario. The hysteroscope was introduced to visualize the uterus anatomy as shown in Fig. 7.13. The device was then introduced into the uterus through the hysteroscope. During this testing, it was observed that the simulator provided the realistic simulation of device manoeuvres and the device was successfully delivered and deployed at the target location.

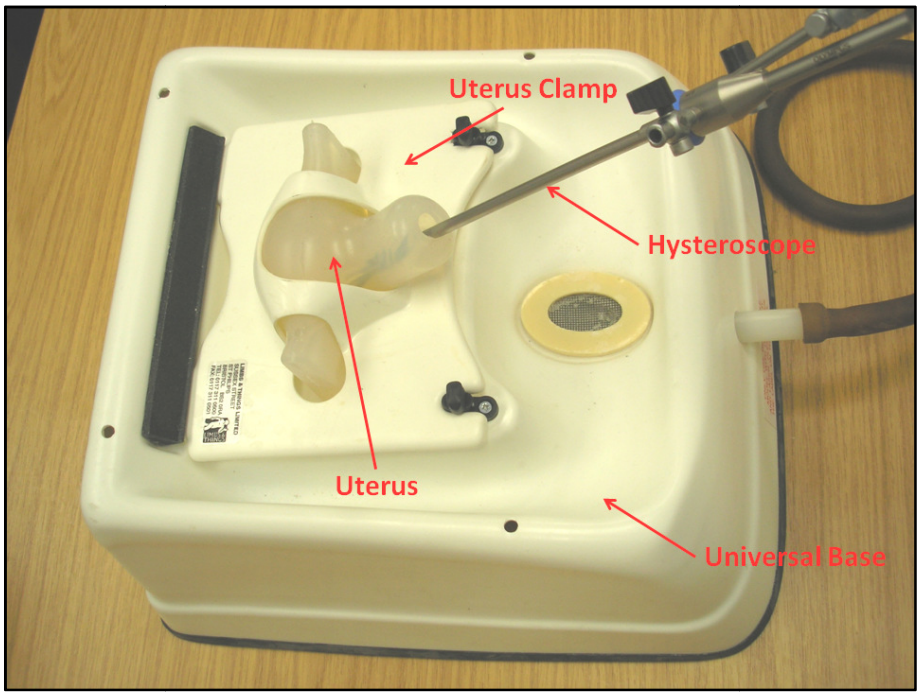

FIGURE 7.13: DEVICE TESTING IN HYSTEROSCOPIC DIAGNOSTIC MODEL

In-vitro bench testing (n = 30) was carried out on both porcine and bovine heart tissue. These tests were performed to validate the deployment inside tissues against the loading exerted by the tissue on the implant. In this testing the tissues were gripped in clamps using sand paper to prevent slippage of tissues. The device was then inserted into the tissue and firmly placed. Then the implant was deployed using the delivery actuator. After implant deployment, the tissues were dissected to examine the deployed implant. Fig. 7.14 shows the deployed implant in the porcine tissue. It was observed that the implant wings had completely entrapped the tissue in between.

The implant deployed in the bovine tissue can be seen in Fig. 7.15. The implant was extracted from the tissue by dissection under microscope as shown in Fig. 7.16. The deployed implant was inspected and was found that the implant deployed successfully with all six wings perfectly formed and entrapped tissue in between. The incisors were fully anchored into the tissue.

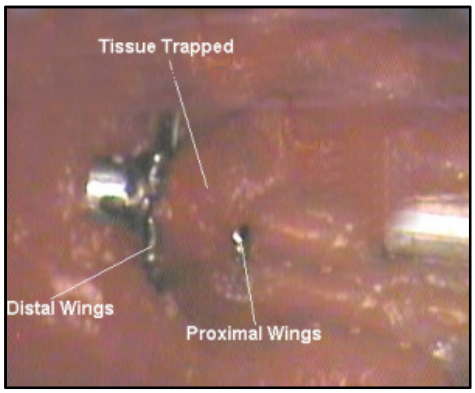

FIGURE 7.14: IMPLANT DEPLOYED IN PORCINE TISSUE

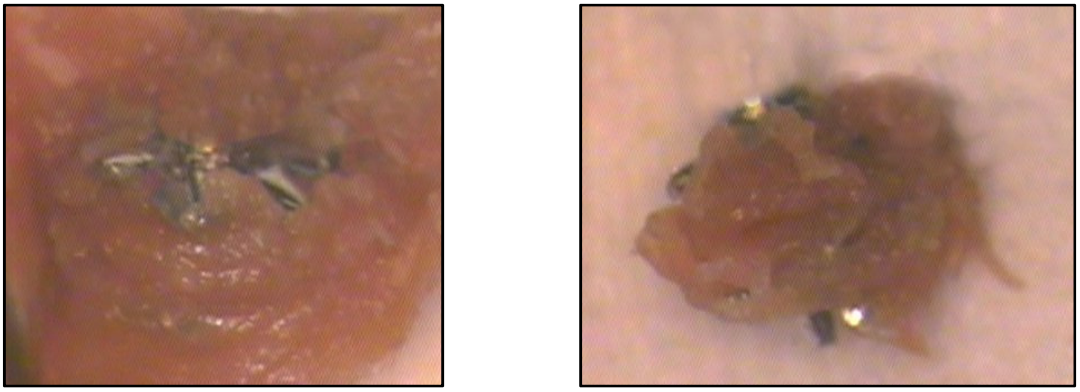

FIGURE 7.15: IMPLANT ENTRAPPED IN BOVINE TISSUE

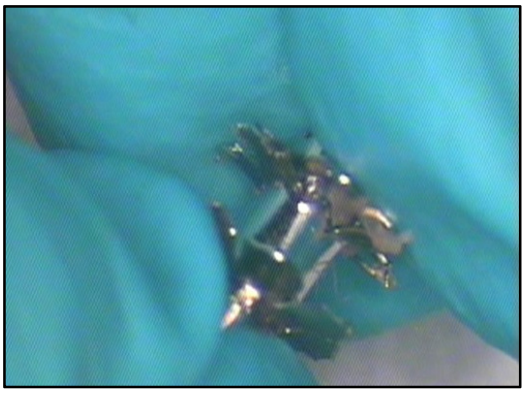

FIGURE 7.16: IMPLANT EXTRACTED AFTER DISECTING BOVINE TISSUE

7.4.2. EXPLANT STUDIES

To validate the performance of the device in conditions very similar to *in-vivo* implementation, *in-vitro* experiments were conducted using explanted uteri. These uteri were removed at hysterectomy for various benign indications at the Midland Regional Hospital, Mullingar, Ireland. Explanted uteri were chosen as the test model as this is most representative model of the *in-vivo* situation. These studies (n = 11) were

performed to validate the functionality, deliverability and effectiveness of the device for instant closure of human fallopian tubes. The device was delivered and deployed bilaterally into the tubal Ostia. A small calibre hysteroscope with a 5-F operating channel was used to deliver the implant into the ostium tissue. The hysteroscope was attached to a light source and camera to enable video recordings to be captured. The inflow channel of the hysteroscope was connected to the saline bag. The uterus was distended with this saline solution. The hysteroscope was introduced under direct vision into the uterus and both tubal opening were observed as shown in Fig. 7.17(a). After positioning, the device was guided through the hysteroscope as shown in Fig. 7.17(b). On approaching the tubal ostium, the implant was positioned in the intramural segment of the fallopian tube until the straight splines at the implant distal end became invisible as shown in Fig. 7.17(c). After placement, the implant was deployed and released from the delivery actuator as shown in Fig. 7.17(d). The deployment of the implant using the delivery actuator is shown in Fig. 7.19. The delivery system was withdrawn and the procedure was repeated on the contra-lateral tube. After successful deployment of implants in both tubes, a hydraulic pressure test of the uterus was performed to verify occlusion of the fallopian tubes. The pressure was applied by placement of the saline bag in the pressure cuff, which was set to a pressure of 300 mmHg. Methylene blue was added in the saline solution to observe any leakage. Finally, the ostium and tubes were dissected to examine the placement and deployment of the implant in the intramural section of the ostium. The implant along with some tissue was extracted to further examine the wing shape, deployed implant and tissue entrapped as shown in Fig. 7.18.

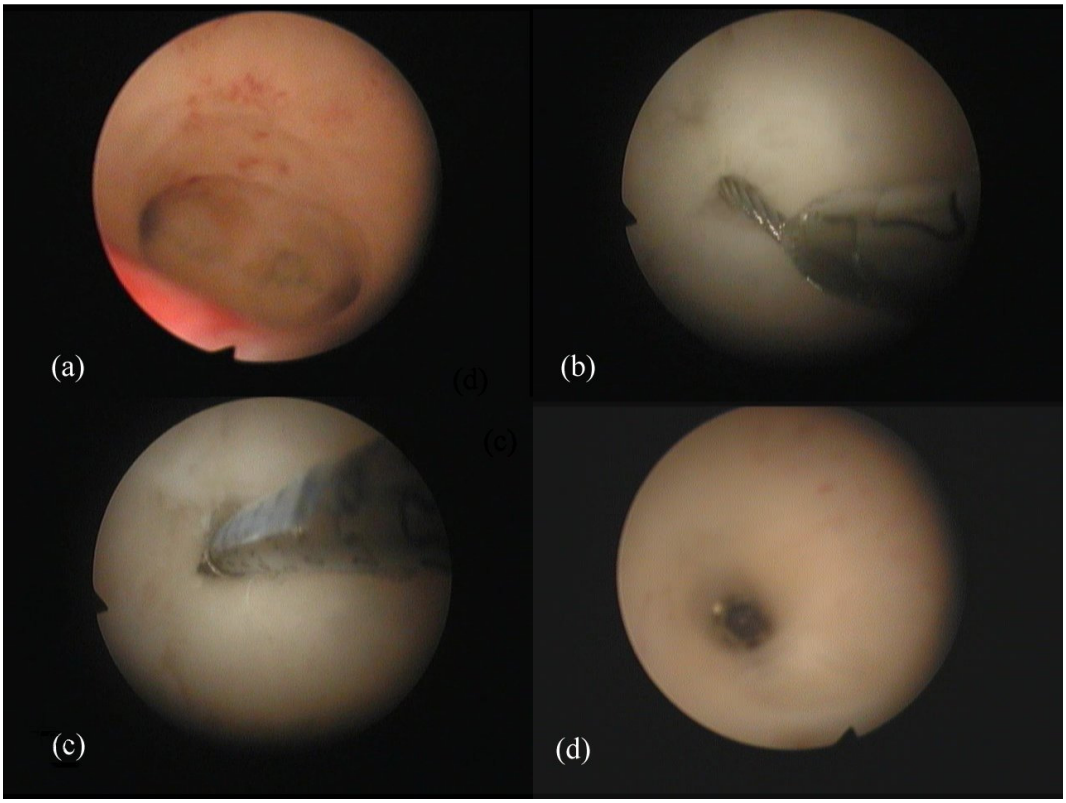

FIGURE 7.17: HYSTEROSCOPIC VIEWS OF EXPLANT STUDIES (a) TUBAL OSTIA (b) IMPLANT GUIDE TIP INGOING LEFT TUBAL OPENING (c) IMPLANT OPTIMALLY PLACED AT LEFT TUBAL OSTIUM (d) DEPLOYED IMPLANT AT LEFT TUBAL OSTIUM

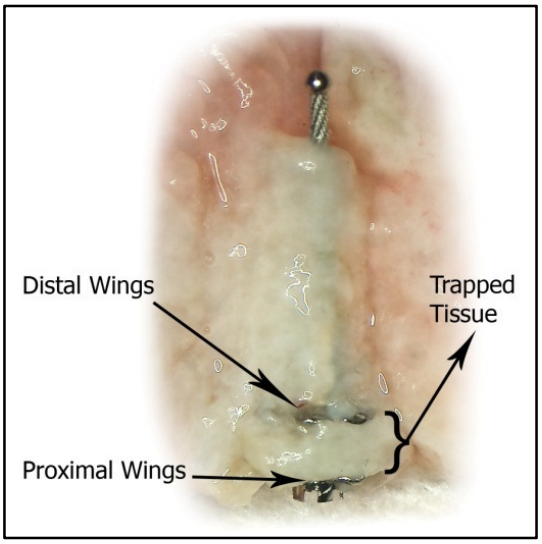

FIGURE 7.18: IMPLANT ENTRAPPED IN UTERUS TISSUE

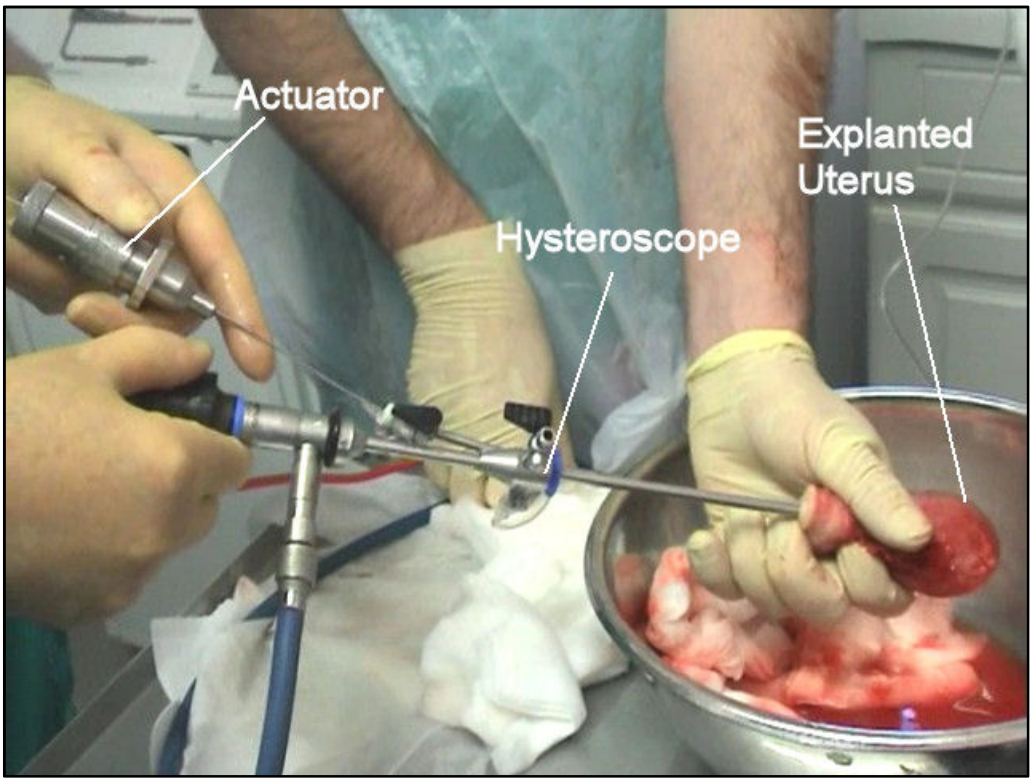

FIGURE 7.19: *In-vitro* DEVICE TESTING IN EXPLANTED UTERUS

These studies showed that the implant deployed successful in the entire 11 explanted human uteri. Un-obstruction of the fallopian tubes before deployment was confirmed from the spurt of saline emerging from the excised fallopian tubes ends as shown in Fig. 7.20(a). The occluded fallopian tube after implant deployment is shown in Fig. 7.20(b). As expected, the device had successfully occluded the fallopian tubes in all uteri. Immediately after the bilateral deployment of device in the uteri, the hydraulic pressure tests were performed. In these tests, saline solution and methylene blue were introduced into the uterus at a pressure of 300 mmHg. The pressure was held for 5 minutes to ensure the blockage of the fallopian tubes. It is apparent from Fig. 7.20(c) that there was no leakage during these hydraulic pressure testing. These uteri were dissected after hydraulic pressure testing and the implant along with some tissue was examined under microscope to further investigate the implant wings shape, deployed implant and tissue trapped as shown in Fig. 7.20(d). The blue colour of tissue indicates the presence of methylene blue. It was observed in dissection that there was no indication of methylene blue ahead of the implant distal wings as shown in Fig. 7.21. This demonstrates the capability of the device to achieve instant occlusion of the fallopian tubes even at a pressure of 300 mmHg.

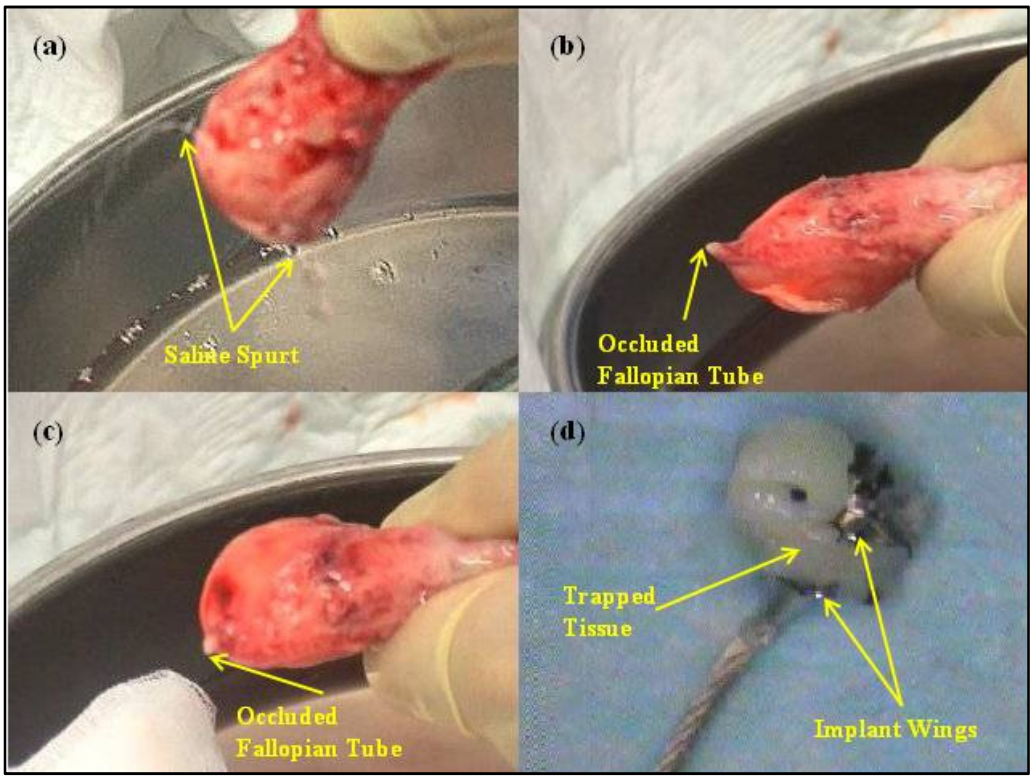

FIGURE 7.20: UTERUS IN EXPLANT STUDIES (a) UN-OBSTRUCTED FALLOPIAN TUBES PRE-DEPLYMENT (b) OCCLUDED FALLOPIAN TUBE POST-DEPLOYMENT (c) HYDRAULIC PRESSURE TESTING POST-DEPLOYMENT (d) DEPLOYED IMPLANT ENTRAPPING DISSECTED TISSUE

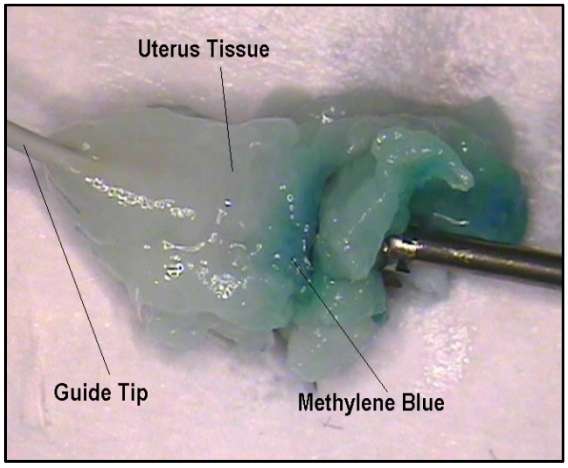

FIGURE 7.21: OCCLUSION DEMONSTRATION USING METHYLENE BLUE

7.4.3. DISCUSSION

The device for transcervical female sterilization presented in this research work has various advantages over tubal sterilization such as avoiding general anaesthesia, no incision in the body, a clinical procedure and decreased cost. Its main advantage over other transcervical procedures is the instant mechanical occlusion to effect female sterilization. The design of the device, 3D modelling, FEA simulations and optimisation were performed using CAD and FEA software. In addition to FEA, optimisation was also performed by experimentation and testing. The implant was fabricated using a laser cutting machine (LPL Stent Cutter). The fabricated implant was deployed under microscope and its mechanical behaviour was studied. The wing profile of the deployed implants was measured using video inspection probe and its profile was reconstructed using Pro/E. This experimentally measured profile of the wings was superimposed on the profile obtained from FEA simulations and compared. The standard error of mean of the difference of experimental and simulated profile was 0.003543 and the maximum percent error was 3.129%.

The forces required to deploy device were validated experimentally on the test bench. On application of 16.0 N-mm moment in ANSYS WB simulations, a 0.353 mm out-of-plane displacement in implant slots was obtained. A comparable 15.4 N-mm was measured experimentally using torque measuring equipment, when same amount of radial expansion (from Ø1.535 mm to Ø2.241 mm) in implant slots was achieved. In order to plastically deform the expanded implant slots, a force of 25.38 N and 25.32 N was measured using a tensile testing machine for proximal and distal wings respectively. These forces are comparable to a force of 25 N obtained from the FEA simulations. In-house *in-vitro* and mechanical bench testing validated the mechanical behaviour and functional aspects of the implant.

FEA simulations were performed to investigate the mechanical behaviour and functionality of the actuator against deployment, release and handling loads. Optimisation was performed to achieve the minimum mass of the actuator. During the actuator components optimisation studies, it was observed that the machining constraint was a limiting factor on design variables. It was observed that, even at thicknesses comparable to the implant, the von-Mises stresses among the components were well below the maximum limiting values. Therefore, the optimum design was maintained based on the machining constraints.

The actuator in this study was fabricated using CNC lathe, milling machine, wire EDM and sinker EDM. The CNC programs for the CNC machines were generated using Pro/NC and data generated from Pro/E was used to write code for the wire EDM. The fabricated actuator was inspected on both coordinates measuring machine (CMM) and video inspection probe and critical dimensions were found within an accuracy of 50 µm. The actuator was experimentally validated under deployment and handling loads using both a torque meter and a tensile testing machine. Using video inspection probe, the functionality of the actuator and accurate measures of the involved displacements were recorded. These measurements proved that the actuator followed the specified sequence with a maximum displacement error of 90 µm. It was also demonstrated that the ratchet mechanisms worked perfectly, preventing the backlash torque both from the implant and guide system. In addition, it provides actuator locking at the end of each sequence. Complete locking of the actuator was proved at the final release stage, thereby preventing the implant from any further deformation post deployment and during release.

It was verified by torque testing that the actuator can withstand an inadvertent force of 520 N-mm in either a CW or CCW direction. The compressive force applied by the actuator on the implant was validated using tensile testing machine and it was observed that the actuator provides the designed compressive force of 30 N and 25 N for the deployment of distal and proximal wings respectively. Release torque was experimentally evaluated using torque measuring equipment. The measured 246.4 N-mm release torque was comparable to the theoretically calculated value 242.13 N-mm with an accuracy of 1.76%.

The testing and validation of the guiding system in hysteroscopic diagnostic model and explanted uteri proved that the guiding system is capable to negotiate the anatomy of the uterus tortuous paths. The flexibility and deflection force measurement testing of the guiding system demonstrated that both the deflection forces 0.76 N of guide tube and 1.47 N of guide wire are far less than the uterus perforation force 8.5 N. All these testing validated the safety and effectiveness of the guiding system against the curvatures of the cervix and the fallopian tube. In addition, the successful deployments of the implant using the designed guiding system proved that the guiding system is able to transfer the required forces from the actuator to the implant. Thus, it was demonstrated that the optimally designed guiding system easily navigates the device

through the hysteroscope, into the uterus and deploy successfully at the target location.

In-vitro deployments (n=11) of the implant into explanted human uteri were performed. As expected, the device had successfully occluded the fallopian tubes in all uteri. Various state-of-the-art commercially available techniques evaluate tubal occlusion by applying dye under pressure of 100 – 150 mmHg for 4 minutes to the explanted tubes [12], [13]. In this research, instant occlusion of the fallopian tubes was demonstrated at much higher pressure for longer duration. Saline water and methylene blue was used for this purpose and the capability of the device to achieve instant occlusion of the fallopian tubes was proved at 300 mmHg pressure for 5 minutes.

The statistical methods used to analyse and report the results of explants studies were the statistical summaries of results and tabulation of the data. Occlusion of each fallopian tube was treated as an individual event representing 0 or 1 for “no” or “yes” occlusion respectively. Bilateral deployments of the implant were attempted in 11 explant studies. Successful instant occlusion was achieved in 22 out of 22 (100%) fallopian tubes. Since there were zero failures among 11 explanted uteri, statistical significance was not established because of zero numerator problems. However, these effective in-vitro tests are important in the development of the device as they provide a clear indication of the device’s capabilities and weaknesses prior to commencing in-vivo verification and validation activities. Data generated from investigations in explanted uteri verified the efficacy of the implant without the risk to patients participating in *in-vivo* clinical studies.

CHAPTER 8

CONCLUSIONS AND FUTURE RECOMMENDATIONS

8.1. INTRODUCTION

This study involved the design, development and validation of a novel mechanical occlusion device for transcervical female sterilization that uses a natural body passage and obviates any surgical incision. The conclusions drawn from this thesis and future recommendations for continuation of this work are summarized in this chapter.

8.2. CONCLUSIONS

This device is minimally invasive, safe, effective, easy to use, consistent, reproducible and feasible for the hysteroscopic occlusion of fallopian tubes.

1. This novel device is a new prospect for transcervical sterilization, which uses inherent body channel and provides an immediate occlusion of the fallopian tubes.
2. The occlusion implant's size and low profiled shape, allows its transcervical deployment into the tubal ostia using a small calibre 5 F hysteroscope that allows the device usage in the clinical setup or GP surgery.
3. This device is going into *in-vivo* clinical trials and, if these are successful, it will be mass-produced and introduced into the market.

8.3. FUTURE RECOMENDATIONS

The device presented in this thesis has successfully validated the instant and effective occlusion of fallopian tubes for permanent female sterilization. The following future work is recommended:

1. In order to launch this device onto the market, the device needs to be disposable, cost effective and lightweight. The only mass carrying component of the device is the delivery actuator. Therefore, the actuator needs to be designed from plastic material. Finite element analysis is recommended for the designing of plastic actuator. FEA of the plastics is highly dependent upon the accuracy of the material models used in the analysis. Further material data would be required for the accurate FEA study of plastic actuator and its components.

2. About 180 million couples per annum are relying on female sterilization to avoid further pregnancies [8]. However, the sterilization procedures of permanent nature have discouraged some couples from choosing these methods [6,175,176,177]. Therefore, much work is still required to make this device an effective method of reversible hysteroscopic female sterilization. To achieve this goal, the following areas need to be investigated:
    - The collapsible wings on the implant that can be collapsed before retrieval to withdraw the implant (device reversibility).
    - A retrieval mechanism design in the current actuator or a complete design separate retrieval actuator.
    - A coupling system in between the implant and delivery system that could be used to engage the implant for retrieval process.
3. The concept and design of the complete device could be used for other medical applications.
4. The actuator concept could be implemented in various medical and aerospace applications, where rotational and translations displacements are required.

WORKS CITED

[1] S Brechin and A Bigrigg, "Male and female sterilization," *Current Obstetrics & Gynaecology*, vol. 13, pp. 38-44, 2003.

[2] H McSwain and F B Mark, "Fallopian Tube Occlusion, An Alternative to Tubal Ligation," *Tech. Vasc. Interventional Rad*, vol. 5, pp. 24-29, 2006.

[3] J T Jensena, M I Rodriguezb, and S Zalanyi, "Transcervical polidocanol as a nonsurgical method of female sterilization: a pilot study," *Contraception*, vol. 70, pp. 111–115, 2004.

[4] A L Thurkow, "Hysteroscopic sterilization: away with the laparoscope?," *International Congress Series*, vol. 1279, pp. 184-188, 2005.

[5] E W Wilson, "The evolution of methods for female sterilization," *Int. J. Gynaecol. Obstet.*, vol. 51, pp. 3-13, 1995.

[6] A Magos and L Chapman, "Hysteroscopic tubal sterilization," *Obstet. Gynecol. Clin.*, vol. 31, pp. 31705-31719, 2004.

[7] C Westhoff and A Davis, "Tubal sterilization: focus on the U.S. experience," *Fertility and Sterility*, vol. 73, no. 5, 2000.

[8] J Abbott, "Transcervical sterilization," *Best Practice & Research Clinical Obstetrics & Gynaecology*, vol. 15, no. 5, pp. 743-756, 2005.

[9] A S Sonmez, I Aruh, R C Dunn, and R H Kaufman, "Sterilization with fibrin sealant in a rabbit uterine horn model," *American Journal of Obstetrics and Gynecology*, vol. 177, no. 3, pp. 573-578, 1997.

[10] J R Brumsted, G Shirk, M J Soderling M. J, and T Reed, "Attempted transcervical occlusion of the fallopian tube with the Nd:YAG laser," *Obstet Gynecol*, vol. 77, no. 2, 1991.

[11] J Donnez, V Malvaux, M Nisolle, and F Casañas, "Hysteroscopic sterilization with the Nd:YAG laser," *J Gynecol Surg.*, vol. 6, pp. 149-153, 1990.

[12] V E Carr-Brendel, D R Stewart, D C Harrington, J G Leal, and T Vancaillie, "A new transcervical sterilization procedure: results of a pilot implant study in humans," *Obstetrics & Gynecology*, vol. 97, no. 4, p. 8, 2001.

[13] V E Carr-Brendel, D R Stewart, D C Harrington, P M Breining, and T Vancaillie, "A new transcervical sterilization procedure—6-month preclinical results," *Obstetrics & Gynecology*, vol. 97, no. 4, pp. 15-16, 2001.

[14] A Ubeda, R Labastida, and S Dexeus, "Essure®: a new device for hysteroscopic tubal sterilization in an outpatient setting," *Fertility and Sterility*, vol. 82, no. 1, pp. 196-199, 2004.

[15] J M Cooper, C S Carignan, D Cher, and J F Kerin, "Microinsert nonincisional hysteroscopic sterilization," *Obstetrics & Gynecology*, vol. 102, no. 1, pp. 59-67, 2003.

[16] J. F. Thompson. (2010, August) Austin Peay State University. [Online]. http://www.apsu.edu/thompsonj/Anatomy

[17] Frederic H. Martini, *Fundamental of Anatomy & Phisiology*, Fifth Edition ed. New Jersey: Prentice Hall, 2001, ch. The Reproductive System, Chapter 28, pp. 1040-1045.

[18] AYK Wong and SM Walker, "Falloposcopy-a prerequisite to the proper assessment of tubal infertility," *HKMJ*, vol. 5, pp. 76-81, 1999.

[19] J F Kerin, "New methods for transcervical cannulation of the fallopian tube," *Int J Gynaecol Obstet*, vol. 51, pp. 29-39, 1995.

[20] J F Kerin, L Daykhovsky, and J Segalowitz, "Falloposcopy: a microendoscopic technique for visual exploration of the human fallopian tube from the uterotubal ostium to the fimbria using a transvaginal approach," *Fertil Steril*, vol. 54, p. 390, 1990.

[21] J F Kerin, E Surrey, L Daykhovsky, and W S Grundfest, "Development and application of falloscopy for transvaginal endoscopy of the fallopian tube," *J Laparoendosc Surg*, vol. 1, no. 1, pp. 47-56, 1990.

[22] J F Kerin, D B Williams, A C Pearlstone, W S Grundfest, and E S Surrey, "Falloposcopic classification and treatment of fallopian tube lumen disease," *Fertil Steril*, vol. 57, no. 4, pp. 731-741, 1992.

[23] J F Kerin, E S Surrey, D B Williams, L Daykhovsky, and W S Grundfest, "Falloposcopic observations of endotubal isthmic plugs as a cause of reversible obstruction and their histological characterization.," *J Laparoendosc Surg*, vol. 1, no. 2, pp. 103-110, 1991.

[24] A H DeCherney, "Anything you can do I can do better.or differently!," *Fertil Steril*, vol. 48, p. 374, 1987.

[25] Sweeny J. William, "The Interstitial Portion of the Uterine Tube-Its Gross Anatomy," *Obstetrics and Gynecology*, vol. 19, pp. 3-8, 1962.

[26] E, Glob. Sokol, "Glob. libr. women's med., (ISSN: 1756-2228) 2008; DOI 10.3843/GLOWM.10001," 2008.

[27] M Potts and M Campbell, "Glob. libr. women's med., (ISSN: 1756-2228); DOI 10.3843/GLOWM.10376," 2008.

[28] C A Quarini, "History of contraception," *Women's Health Medicine,The Medicine Publishing Company Ltd*, vol. 2, no. 5, pp. 28-30, 2005.

[29] P Lopes, E Gibon, T Linet, and H J Philippe, "Hysteroscopic tubal sterilization with Essure intratubal devices: A case-control prospective with inert local anesthesia or without anesthesia," *European Journal of Obstetrics & Gynecology and Reproductive Biology*, vol. 138, no. 2, pp. 199-203, 2008.

[30] A O Famuyide, M R Hopkins, S A El-nashar, and D J Creedo, "Hysteroscopic Sterilization in Women With Severe Cardiac Disease: Experience at a Tertiary Center," *Mayo Clin Proc*, vol. 83, no. 4, pp. 431-438, 2008.

[31] E W Wilson, "The development of new technologies for female sterilization: conclusions

and recommendations for research," *Int. J. Gynaecol. Obstet.*, vol. 51, pp. 71-74, 1995.

[32] C Melville and A Bigrigg, "Male and female sterilization," *Obstetrics, Gynaecology and Reproductive Medicine*, pp. 330-334, 2008.

[33] F W Jansen, K Kapiteijn, J Hermans, and Trimbos-Kempe, "A survey on (operative) laparoscopy in The Netherlands in 1992"," *European Journal of Obstetrics & Gynecology and Reproductive Biology*, vol. 64, no. 1, pp. 105-109, 1996.

[34] E W Wilson, "Sterilization," *Bailliere's Clinical Obstetrics and Gynaecology*, vol. 10, pp. 103-112, 1996.

[35] Itriage. [Online]. http://www.itriagehealth.com/procedure/laparotomy--(surgically-open-the-abdomen)

[36] A W Huber, Ml D Mueller, F Ghezzi, A Cromi, and E Dreher, "Tubal sterilization: Complications of laparoscopy and minilaparotomy," *European Journal of Obstetrics & Gynecology and Reproductive Biology*, vol. 134, pp. 105–109, 2007.

[37] J Melnikow and K Jones. (2008) Mini-laparotomy. [Online]. https://hvelink.saintlukeshealthsystem.org/library/healthguide/en-us/support/topic.asp?hwid=zm2659

[38] Dorland. Technique Pomeroy. [Online]. http://img.tfd.com/dorland/thumbs/technique_Pomeroy.jpg

[39] A M Kaunitz, G Harkins, and J S Sanfilippo. (April 2008) OBG Management. [Online]. http://www.obgmanagement.com/supplement.asp?aid=6132

[40] D Eisenberg and J Sciarra, "Glob. libr. women's med.," *(ISSN: 1756-2228); DOI 10.3843/GLOWM.10400*, 2008.

[41] G S Berger. (2002) Tubal Ligation and Resection. [Online]. http://www.tubal-reversal.net/tubal_ligation_resection.htm

[42] H Uchida, "Uchida tubal sterilization," *Am J Obstet Gyneco*, vol. 121, p. 153, 1975.

[43] G S Berger. (2002) Tubal Reversal. [Online]. http://www.tubal-reversal.net/

[44] R Garry, "Laparoscopic surgery," *Best Practice & Research Clinical Obstetrics & Gynaecology*, vol. 89-104, no. 20, 2006.

[45] S Watson. Laparoscopy. [Online]. http://www.lapsurgery.com.au/laparoscope.html

[46] B Sanders, "Glob. libr. women's med," *(ISSN: 1756-2228) DOI 10.3843/GLOWM.10404*, 2008.

[47] G Goynumer, F Kayabasoglu, S Aydogdu, and L Wetherilt, "The effect of tubal sterilization through electrocoagulation on the ovarian reserve," *Contraception*, vol. 80, no. 1, pp. 90-94, 2099.

[48] R M Soderstrom, "Reconsider unipolar methods for female sterilization," *Am J Obstet Gynecol*, vol. 175, no. 4, pp. Part 1 Letters 1083-1084.

[49] C S Curry, J R Darby, and B R Janssen, "Evaluation of pain following electrocautery tubal ligation and effect of intraoperative fentanyl," *Journal of clinical anesthesia*, vol. 8, no. 3, pp. 216-219, 1996.

[50] G S Berger. (2002) laparoscopic surgery. [Online]. http://www.tubal-reversal.net/blog/tag/laparoscopic-surgery

[51] Y Yildirim, M Polat, and C E Taner, "Laparoscopic tubal bipolar coagulation and corpus luteum function," *International Journal of Gynecology and Obstetrics*, vol. 92, p. 139—140, 2006.

[52] Hulka Clip. (2007) Museum für Verhütung und Schwangerschaftsabbruch. [Online]. http://www.verhuetungsmuseum.at/verhuetung/sterilisation/object.php?id=1039

[53] R Dominik, D Gates, D Sokal, M Cordero, and J Lasso de la Vega, "Two randomized controlled trials comparing the Hulka and Filshie Clips for tubal sterilization," *Contraception*, vol. 62, no. 4, pp. 169-175, 2000.

[54] S Sumiala, J Tuominen, K Irjala, P Klemi, and J Mäenpää, ", J. 2000, "Luteal function declines after laparoscopic sterilization by Hulka or Filshie clips," *Contraception*, vol. 62, no. 4, pp. 177-180, 2000.

[55] A J Penfield, "The Filshie clip for female sterilization: A review of world experience," *American Journal of Obstetrics and Gynecology*, vol. 182, no. 3, pp. 485-489, 2000.

[56] R E Clegg, "Filshie clip closure: Determination of closure through the analysis of X-rays," *Journal of Forensic and Legal Medicine*, vol. 15, no. 8, pp. 510-515, 2008.

[57] U Ezeh, J Martin, N Taub, and A Breeson, "Local anaesthetic on Filshie clips," *The Lancet*, vol. 346, no. 8981, pp. 1032-1034, 1995.

[58] A Graf, A Staudach, H Steiner, D Spitzer, and A Martin, "An evaluation of the Filshie clip for postpartum sterilization in Austria," *Contraception*, vol. 54, no. 5, pp. 309-311, 1996.

[59] W J van Wijngaarden and G M Filshie, "Laparoscopic Supracervical Hysterectomy with Filshie Clips," *The Journal of the American Association of Gynecologic Laparoscopists*, vol. 8, no. 1, pp. 137-142, 2001.

[60] Bernardo Froes. (2008) Coisas de menina. [Online]. http://www.coisasdemenina.com/filshie-clip-novo-metodo-de-laquadura.html

[61] John Storment. (2009) Tubal Ligation Reversal. [Online]. tubalreversalla.com/Ligation/tubal_ring.html

[62] H C Pymar and M D Creinin, "Prospective randomized, controlled study of postoperative pain after titanium silicone rubber clip or Silastic ring tubal occlusion," *Contraception*, vol. 69, no. 2, pp. 145-150, 2004.

[63] J H Meyer Jr, "A five year experience with Laparoscopic Falope Ring sterilization," *International Journal of Gynecology & Obstetrics*, vol. 20, no. 3, pp. 183-187, 1982.

[64] V Sepilian, D Finck, and D Williams, "Improving postoperative pain management after

falope ring laparoscopic tubal sterilization," *The Journal of the American Association of Gynecologic Laparoscopists*, vol. 9, no. 3, pp. 50-50, 2002.

[65] H B Peterson, Z Xia, L S Wilcox, L R Tylor, and J Trussell, "Pregnancy after tubal sterilization with silicone rubber band and spring clip application," *Obstetrics & Gynecology*, vol. 97, no. 2, pp. 205-210, 2001.

[66] H C Pymar, M D Creinin, and M C Vallejo, "Prospective randomized controlled study of postoperative pain after Filshie clip or Falope ring," *Obstetrics & Gynecology*, vol. 99, no. 4, pp. 25-26, 2002.

[67] G Benagiano and L Mencaglia, "Diagnostic hysteroscopy," *Practical Training and Research in Gynecologic Endoscopy*.

[68] J N Prigg. (2009) New Horizons Center for Women Health. [Online]. http://drprigg.com/Hysteroscopy.html

[69] G A Vilos and B Abu-Rafea, "New developments in ambulatory hysteroscopic surgery," *Best Practice & Research Clinical Obstetrics & Gynaecology*, vol. 19, no. 5, pp. 727-742, 2005.

[70] G Thierry, C A Vancaillie, and E Leonard, "A new method of transcervical female sterilization preliminary results in rabbits," *Fertility and Sterility*, vol. 51, pp. 335-338, 1989.

[71] D Stewart, T Vancaillie, and J Garza Leal, "Fallopian tube tissue response, a new transcervical sterilization procedure," *The Journal of the American Association of Gynecologic Laparoscopists*, vol. 8, no. 3, pp. 67-67, 2001.

[72] H C Rivoire, D J Fagundes, S Bigolin, and A T N Fagundes, "Hysteroscopy and the butyl-cyanoacrylate on experimental sterilization of rabbit uterine tubes," *Acta Cirúrgica Brasileira*, vol. 22, no. 5, 2007.

[73] D F Kraemer, P, P Yen, and M Nichols, "An economic comparison of female sterilization of hysteroscopic tubal occlusion with laparoscopic bilateral tubal ligation," *Contraception*, vol. 80, no. 3, pp. 254-260, 2009.

[74] J F Kerin et al., "Hysteroscopic sterilization using a micro-insert device: results of a multicentre Phase II study," *Human Reproduction*, vol. 18, no. 6, pp. 1223-1230, 2003.

[75] S Ploteau and P Lopes, "Pregnancy after hysteroscopic tubal sterilization despite two hysterosalpingograms showing bilateral occlusion," *European Journal of Obstetrics & Gynecology and Reproductive Biology*, vol. 147, no. 2, pp. 238-239, 2009.

[76] S Papaioannou, "A hypothesis for the pathogenesis and natural history of proximal tubal Blockage," *Human Reproduction*, vol. 19, no. 3, pp. 481-485, 2004.

[77] A L Thurkow, "Study of the siloxane intratubal device (itd) application method, Hysteroscopic sterilization," pp. 7-12, 1997.

[78] G Van der Leij, "Hysteroscopic Sterilization: Study of the siloxane intratubal device (itd) application method.," Universiteit van Amsterdam, Netherlands, 1997.

[79] W Droegemueller, B E Greer, J R Davis, E L Makowski, and A Pollard, "Cryocoagulation of the endometrium at the uterine cornua," *Am J Obstet Gynecol*, vol. 131, no. 1, pp. 1-9, May 1978.

[80] L M Kukreja, "In vitro occlusion of human fallopian tubes with Nd:YAG laser," *Natl Med J India*, vol. 11, no. 3, pp. 122-124, 1998.

[81] G Benagiano, "Non-surgical female sterilization with quinacrine: an update," *Contraception*, vol. 63, pp. 239–45, 2001.

[82] J Zipper and E Kessel, "Quinacrine sterilization: a retrospective," *International Journal of Gynecology & Obstetrics*, vol. 83, no. 2, pp. 7-11, 1998.

[83] S R Neuwirth, "Update on transcervical sterilization," *International Journal of Gynecology & Obstetrics*, vol. 51, no. Suppl. I, pp. 23-28, 1995.

[84] D C Sokal, J Zipper, and T King, "Transcervical quinacrine sterilization: clinical experience," *International Journal of Gynecology & Obstetrics*, vol. 51, no. 1, pp. 57-69, 1995.

[85] J Zipper and V Trujillo, "25 years of quinacrine sterilization experience in Chile: review of 2,592 cases," *International Journal of Gynecology & Obstetrics*, vol. 83, no. 2, pp. 23-29, 1998.

[86] A P Krishnaja and P S Chauhan, "Quinacrine dihydrochloride, the non-surgical female sterilant induces dicentrics, rings, and marker chromosomes in human peripheral blood lymphocytes treated in vitro: a preliminary report," *Mutation Research/Genetic Toxicology and Environmental Mutagenesis*, vol. 466, no. 1, pp. 43-50, 2000.

[87] T J Vancaillie, C A Eddy, and L Laufe, "A new method of transcervical female sterilization preliminary results in rabbits," *Fertil. Steril.*, vol. 51, pp. 335-338, 1989.

[88] R A Erb, R H Davis, and G A Kyriazis, "System and technique for blocking the fallopian tubes," *Journal of Reproductive Medicine*, vol. 14, no. 2, pp. 42- 61, 1975.

[89] B. Rakshit, "Intratubal Blocking device for sterilization without laparotomy," *Calcutta Med. J.*, vol. 65, no. 3, pp. 90-95, 1968.

[90] R F Valle and T Read, *Hysteroscopic sterilization: Diagnostic and Operative Hysteroscopy: A Text and Atlas*, 2nd ed., Baggish M S, J Barbot, and R F Valle, Eds. Boston, MA, Mosby, 1999.

[91] R F Valle, "Glob. libr. women's med.," *(ISSN: 1756-2228); DOI 10.3843/GLOWM.10401*, 2008.

[92] P Litta et al., "Hysteroscopic permanent tubal sterilization using a nitinol-dacron intratubal device without anaesthesia in the outpatient setting: procedure feasibility and effectiveness," *Human Reproduction*, vol. 20, no. 13, pp. 3419–3422, 2005.

[93] Van der Leij and F B Lammes, "Office Hysteroscopic Tubal Occlusion with Siloxane Intratubal Devices (The Ovabloc® method)," *International Journal of Gynecology & Obstetrics*, vol. 53, pp. 253-260, 1996.

[94] Ovabloc. [Online]. http://www.ovabloc.nl/ovabloc/

[95] Adiana. (2007) MedGadget Internet Journal of Emerging Medical Technologies. [Online]. http://www.medgadget.com/archives/2007/12/adiana_transcervical_sterilization_system_occludes_tubes_gets_fda_nod.html

[96] B S Bowman, V E Carr-Brendel, and V K Dhaka, "New transcervical sterilization procedure: optimal epithelial ablation," *Obstetrics & Gynecology*, vol. 97, no. 4, p. 16, 2001.

[97] V E Carr-Brendel et al., "A new transcervical sterilization procedure: results of a pilot implant study in humans," *Obstetrics & Gynecology*, vol. 97, no. 4, p. 8, 2001.

[98] (2009) Hologic, Women's Health Company. [Online]. http://www.adiana.com/info/what_is_adiana/adiana-permanent-contraception-works.html

[99] C Sutton, "Hysteroscopic surgery," *Best Practice & Research Clinical Obstetrics & Gynaecology*, vol. 20, no. 1, pp. 105-137, 2006.

[100] R F Valle, J M Cooper, and John F Kerin, "Hysteroscopic tubal sterilization with the essure nonincisional permanent contraception system," *Obstetrics & Gynecology*, vol. 99, no. 4, pp. 11-11, 2002.

[101] T M Price and J E Nichols, "Long-term patient satisfaction with the Essure nonincisional permanent contraceptive method," *Obstetrics & Gynecology*, vol. 101, no. 4, pp. 15-15, 2003.

[102] M H Wittmer, D L Brown, R P Hartman, A O Famuyide, and B F King, "Sonography, CT, and MRI Appearance of the Essure Microinsert Permanent Birth Control Device," *AJR*, vol. 187, pp. 959-964, 2006.

[103] R D Smith, "Contemporary hysteroscopic methods for female sterilization," *International Journal of Gynecology & Obstetrics*, vol. 108, no. 1, pp. 79-84, 2010.

[104] R F Valle, C S Carignan, and T C Wright, "Tissue response to the STOP microcoil transcervical permanent contraceptive device: results from a prehysterectomy study," *Fertility and Sterility*, vol. 76, no. 5, 2001.

[105] A C Donnadieu, X Deffieux, A Gervaise, R Frydman, and H Fernandez, "Essure® sterilization associated with endometrial ablation," *International Journal of Gynecology & Obstetrics*, vol. 97, no. 2, pp. 139-142, 2007.

[106] R Lynne, H Heather, and D Sean, "UK experience using the ESSURE micro-insert for hysteroscopic sterilization," *Reviews in Gynaecological Practice*, vol. 3, pp. 1-4, 2003.

[107] J M Cooper, V Herendael, J F Kerin, and T Price, "A new approach to transcervical tubal sterilization with the STOP device," *International Journal of Gynecology & Obstetrics*, vol. 70, no. 1, p. A56, 2000.

[108] J F Kerin, C S Carignan, and D Cher, "The safety and effectiveness of a new hysteroscopic method for permanent birth control: results of the first Essure; clinical study," *Obstet Gynaecol*, vol. 41, no. 4, p. 364, 2001.

[109] R Roy, S Hinduja, and R Teti, "Recent advances in engineering design optimisation: Challenges and future trends," *CIRP Annals - Manufacturing Technology*, vol. 57, pp. 697–715, 2008.

[110] O Zirn, S Weikert, and F Rehsteiner, "Design and Optimization of Fast Axis Feed Drives Using Nonlinear Stability Analysis," *CIRP Annals-Manufacturing Technology*, vol. 45, no. 1, pp. 363–366, 1996.

[111] K Mori and K Osakada, "Net Shape Approach for Sintering Process of Graded Laminated Powder Materials Using Finite Element Simulation," *CIRP Annals Manufacturing Technology* , vol. 48, no. 1, pp. 239–242, 1999.

[112] F Krause, M Ciesla, C Stiel, and A Ulbrich, "Enhanced Rapid Prototyping for Faster Product Development Processes," *CIRP Annals-Manufacturing Technology*, vol. 46, no. 1, pp. 93–96, 1997.

[113] Sihn W, Warnecke H Janz D, "Product Redesign Using Value-Oriented Life Cycle Costing," *CIRP Annals-Manufacturing Technology*, vol. 54, no. 1, pp. 9–12, 2005.

[114] D T Pham and Pham P T N, "Artificial Intelligence in Engineering," *International Journal of Machine Tools & Manufacture*, vol. 39, no. 6, pp. 937–949, 1999.

[115] D Y Yang, J H Kim, M S Chun, C H Lee, and C H Park, "Development of Integrated and Intelligent Design and Analysis System for Forging Processes," *CIRP Annals-Manufacturing Technology*, vol. 49, no. 1, pp. 177–180.

[116] ANSYS Workbench, *Release 11.0 Documentation for ANSYS Workbench*., 2007.

[117] J S Arora, *Introduction to Optimum Design*, 2nd ed. London: Elsevier Academic Press, 2004.

[118] D Spath, W Neithardt, and C Bangert, "Integration of Topology and Shape Optimization in the Design Process," *FE-DESIGN GmbH*, 2001.

[119] B Nima, A Peter, S Jürgen, M Ottmar, and P Martin, "A New Approach for Sizing, Shape and Topology Optimization," in *SAE International Congress and Exposition*, Detroit, Michigan USA, 1996.

[120] S D Rajan, D T Nguyen, A Vaidya, S Yang, and J St. Ville, "Multiphysics CAD-Based Design Optimization," *Mechanics Based Design of Structures and Machines*, vol. 34, pp. 157-180, 2006.

[121] S D Rajan, A D Belegundu, and A Damle, "Finite Element Analysis & Design Optimization in a Distributed Computing Environment," *American Institute of Aeronautics and Astronautics*, pp. 1-11.

[122] G Foucault, J C Cuilliere, V Francois, J C Leon, and R Maranzana, "Adaptation of CAD model topology for finite element analysis.," *CAD Computer Aided Design*, vol. 40, pp. 176–196, 2008.

[123] I Kosaka, C Charpentier, and B C Watson, "An Interface between SDRC I-DEAS and the GENESIS Structural Analysis and Optimization Code," in *8th Symposium on Multidisciplinary Analysis and Optimization*, Long Beach, CA, 2000, pp. AIAA-2000-

4933.

[124] N Cristello and Y Kim, "Design Optimization of an Automotive Universal Joint Considering Manufacturing Cost," in *17th IASTED International Conference Modeling and Simulation*, Montreal, Canada, 2006.

[125] W Liu and Y Yang, "Multiobjective optimization of an auto panel drawing die face design by mesh morphing.," *CAD Computer Aided Design*, vol. 39, pp. 863–869, 2007.

[126] J Bayandor, M L Scott, and R S Thomson, "Parametric optimisation of composite shell structures for an aircraft Krueger flap," *Composite Structures*, vol. 57, pp. 415–423, 2002.

[127] Q Liu, W Liu, F Ruan, and H Qiu, "Parameters' automated optimization in sheet metal forming process," *Journal of Materials Processing Technology*, vol. 187–188, pp. 159–163, 2007.

[128] Vanderplaats. (2007) Vanderplaats Research and Development, Inc. [Online]. http://www.vrand.com/education.html

[129] R Ansola, J Canales, J A Tarrago, and J Rasmussen, "An integrated approach for shape and topology optimization of shell structures," *Computers and Structures*, vol. 80, pp. 449–458, 2002.

[130] X Huang and Y M Xie, "Convergent and mesh-independent solutions for the bi-directional evolutionary structural optimization method," *Finite Elements in Analysis and Design*, vol. 43, pp. 1039 – 1049, 2007.

[131] H Sippel, Ed Stanton, and Greg Crose, "The Usage of Numerical Optimization Techniques in the Development Process," in *XXV. FEM-Congress*, Baden-Baden Germany, 1998.

[132] O Müller, P Häußler, R Lux, B Ilzhöfer, and A Albers, "Automated Coupling of MDI/ADAMS and MSC.CONSTRUCT for the Topology and Shape Optimization of Flexible Mechanical Systems," in *International ADAMS User Conference*, Berlin, 17-19 Nov. 1999.

[133] W Annicchiarico and M Cerrolaza, "An Evolutionary Approach for the Shape Optimization of General Boundary Elements Models," *Electronic Journal of Finite Elements in Analysis and Design 1998*, vol. 2, pp. 251-266, BETEQ 2001.

[134] R J Yang, D L Dewhirst, J E Allison, and A Lee, "Shape Optimization of Connecting rod pin end Using a Generic Model," *Finite element in Analysis and Design*, vol. 11, pp. 257-264, 1992.

[135] K H Chang and K K Choi, "A Geometry-Based Parameterization Method for Shape Design of Elastic Solids," *Mechanics of Structures and Machines*, vol. 20, no. 22, pp. 215-252, 1992.

[136] A D Belegundu and S D Rajan, "A Shape Optimization Approach based on Natural design Variables and Shape Functions," *Computer Methods in Applied Mechanics and Engineering*, vol. 66, no. 1, pp. 87-106, 1998.

[137] S Kodiyalam, V Kumar, and P M Finnigan, "Constructive Solid Geometry Approach to Three dimensional structural Shape optimization," *AIAA Journal*, vol. 30, pp. 1408-1415, 1992.

[138] D A Tortorelli, "A Geometric representation Scheme Suitable for Shape Optimization," *Mechanics of Structures and Machines*, vol. 21, pp. 95-121, 1993.

[139] A Petchsasithon and P Gosling, "Integrated thickness and shape optimization of linear shells," in *13th ACME Conference: University of Sheffield*, Sheffield, March 2005, pp. 21-22.

[140] N E Igor, V K Gennadiy, and A L Igor, "How to Execute Robust Design Optimization," in *9th AIAA/ISSMO Symposium on Multidisciplinary Analysis and Optimization*, Atlanta, Georgia, 4-6 Sep. 2002.

[141] M Rehan and A G Olabi, "Automated CAD System Based Design Optimization Methodology," in *25th International Manufacturing Conference*, Dublin, 2008, pp. 377-385.

[142] Pro/Mechanica Simulation Advisor, *Pro/E Documentation*., 2007.

[143] ANSYS, *Release 11.0 Documentation for ANSYS*., 2007.

[144] G Poole, W C LIU, and J Mandel, "Advancing analysis capabilities in ANSYS through solver technology," *ANSYS, Inc.*, October 2001.

[145] S F Millward, P Claman, A Leader, and J E H Spence, "Technical Report: Fallopian Tube Recanalization- A Simplified Technique," *Clinical Radiology*, vol. 49, pp. 496-497, 1994.

[146] M Guiahi, K N Goldman, M M McElhinney, and C G Olson, "Improving hysterosalpingogram confirmatory test follow-up after Essure hysteroscopic sterilization," *Contraception*, vol. 81, no. 6, pp. 520-524 , June 2010.

[147] M Hastings-Tolsma, P Nodine, and S B Teal, "Essure: Hysteroscopic Sterilization," *Journal of midwifery & women's health*, vol. 51, no. 6, pp. 510-514, 2006.

[148] S D Hillis, Polly A Marchbanks, Lisa Ratliff Tylor, and H B Peterson, "Tubal Sterilization and Long-Term Risk of Hysterectomy: Findings from the United States Collaborative Review of Sterilization," *Obstetrics & Gynecology*, vol. 89, no. 4, pp. 609-614, 1997.

[149] M Rehan and A G Olabi, "Novel Implant for Transcervical Sterilization," *Journal of Bioscience and BioEngineering*, vol. 110, no. 2, pp. 242-249 , August 2010.

[150] J E Coleman and C Cummins, "Anastomosis Devices and Method," US Patent 20090105733A1, 2009.

[151] F C Bardi and S Kyriakides, "Plastic buckling of circular tubes under axial compression—part I: Experiments," *International Journal of Mechanical Sciences*, vol. 48, pp. 830–841, 2006.

[152] L J Hart-Smith, "Buckling of thin cylindrical shells under uniform axial compression,"

Int.J.Mech.Sci., vol. 12, no. 4, pp. 299-313, 1970.

[153] M A Renjie and G Lu, "Plastic buckling of circular cylindrical shells under combined in-plane loads," *International Journal of Solids and Structures*, vol. 38, pp. 741-757, 2001.

[154] M Kumosa and D Hull, "Finite element analysis of a circumferentially cracked cylindrical shell under uniform tensile loading," *Eng.Fract.Mech.*, vol. 31, no. 5, pp. 817-826, 1988.

[155] Xu A Xinsheng, Maa Jianqing Maa, C W Lim b, and Ge Zhang, "Dynamic torsional buckling of cylindrical shells," *Computers and Structures*, vol. 88, pp. 322–330, 2010.

[156] M A Renjie and G Lu, "A study of elastic-plastic buckling of cylindrical shells under torsion," *Thin-Walled Structures*, vol. 40, pp. 1051–1071, 2002.

[157] M A Renjie and G Lu, "A study of elastic-plastic buckling of cylindrical shells under torsion," *Thin-Walled Structures*, vol. 40, no. 12, pp. 1051-1071, 2002.

[158] X Xu, "Dynamic torsional buckling of cylindrical shells," *Comput.Struct.*, vol. 88, no. 5-6, pp. 322-330, 2010.

[159] M Kumosa and D Hull, "Finite element analysis of a circumferentially cracked cylindrical shell loaded in torsion," *Eng.Fract.Mech.*, vol. 32, no. 1, pp. 123-136, 1989.

[160] *ASM Handbook, Volume 1, Properties and Selection: Irons,Steels, and High Performance Alloys*., 2005.

[161] M Rehan and A G Olabi, "Integration of CAD Model Topology for Parametric Design Optimization," *Advance Software Engineering*, 2010.

[162] Olabi A G Rehan M, "Parametric Design Optimization By Integrating CAD Systems And Optimization Tools," *American Institute of Physics*, vol. 6, no. CP1, pp. 681-692, 2009.

[163] S G Igor, Z M Evgenii, and A R Alexandre, *CRC Handbook of Physical Quantities, Friction, Chapter 6*. Boca Raton, F. L.: CRC Press, 1997.

[164] A Agostini et al., "Risk of Uterine Perforation during Hysteroscopic Surgery," *The Journal of the American Association of Gynecologic Laparoscopists*, vol. 9, no. 3, pp. 264-267, 2002.

[165] N D Goldstuck, "Insertion forces with intrauterine devices: implications for uterine perforation," *European Journal of Obstetrics & Gynecology and Reproductive Biology*, vol. 25, no. 4, pp. 315-323, 1987.

[166] (2007, April) Asahi Intecc. [Online]. http://www.asahi-intecc.com/industrial/product/cabletube.html

[167] "ZEUS, Orangeburg, SC 29118 United States,".

[168] Dieter Stöckel, "NITINOL MEDICAL DEVICES AND IMPLANTS," in *SMST-2000*, 2001, pp. 531-541.

[169] "Fort Wayne Metals, Mayo, Ireland,".

[170] T Duerig, A Pelton, and D Stöckel, "An overview of nitinol medical applications," *Materials Science and Engineering A*, vol. 273-275, pp. 149-160, 1999.

[171] Y K Kong and B D Lowe, "Optimal cylindrical handle diameter for grip force tasks," *International Journal of Industrial Ergonomics*, vol. 35, pp. 495-507, 2005.

[172] Y K Kong and B D Lowe, "Evaluation of handle diameters and orientations in a maximum torque task," *International Journal of Industrial Ergonomics*, vol. 35, pp. 1073–1084, 2005.

[173] K O Kverneland, *Screw Threads, Chapter 8, Metric Standards for Worldwide Manufacturing*. New York: ASME Press, 1996.

[174] B Wimer, R G Dong, D E Welcome, C Warren, and T W McDowell, "Development of a new dynamometer for measuring grip strength applied on a cylindrical handle," *Medical Engineering & Physics*, vol. 31, pp. 695–704, 2009.

[175] N Burden, "Transcervical Tubal Sterilization in the Ambulatory Surgery Setting," *Journal of PeriAnesthesia Nursing*, vol. 20, no. 3, pp. 209-210, 2005.

[176] W L Ledger, "Implications of an irreversible procedure," *Fertility and sterility*, vol. 82, no. 5, pp. 1473-1473, 2004.

[177] A J Baxter, "New developments Advances in hysteroscopic sterilization," *The Obstetrician & Gynaecologist*, vol. 8, pp. 103–106, 2006.

[178] Primary Information Service, *CNG Cylinder Design, Technology, Standard, and Policy*. Chennai, India, 2008.

APPENDICES

APPENDIX A: INTEGRATED FEA AND OPTIMIZATION

A.1. APPLIED EXAMPLES

Based on the two IFPO methodologies explained earlier, two examples were solved to demonstrate the significance and capabilities of IFPO. In the following examples, integrated design optimisation was performed using the methodologies explained earlier using ANSYS WB and Pro/Mechanica in integrated mode with Pro/E. The results obtained from these methodologies were validated against the optimisation achieved using ANSYS optimiser and by manual iterations on ANSYS.

A.1.1. CASE STUDY: CNG CYLINDER DESIGN OPTIMISATION

This case study looked at the problem of design optimisation of a Compressed Natural Gas (CNG) cylinder. CNG is a substitute for gasoline or diesel fuel [178]. The growing use of natural gas as a fuel for vehicles is due in part to economic and environmental reasons. On an energy-equivalent basis, CNG is lower in price and is considered environmentally "clean" as compared to other fuels. CNG cylinders have been designed to satisfy a variety of requirements; they must be capable of storing gas at high pressures in order to reach a high specific energy content of the fuel, the weight must be kept to a minimum, demonstratively safe over the required life and the cost must not be more than a small fraction of the overall cost of the vehicle. There are four types of cylinders in use for CNG and among them steel cylinders are currently the most widely used (over 90%) [178] thus used for this study. Such cylinders normally store CNG at a working pressure of 200 bars and are fitted with a safety shut-off valve.

A.1.1.1. MODEL GEOMETRY

The typical geometry of a CNG cylinder is cylindrical with hemispherical domes. Due to the space constraints in automobiles, the size of the CNG cylinder is kept to a minimum by using an elliptical profile in the domes or at least in the rear dome. The most common size CNG cylinder was selected to model the geometry having an internal

diameter of 232 mm and length of 1039 mm. The design parameters *front_dome_thk, rear_dome_thk, cylinder_thk* and *ellipse_offset* were defined for the "thickness of front dome", "thickness of rear dome", "thickness of cylinder" and "offset between ellipse centres" respectively. The inner profile of the rear dome was 2:1 ellipse as mentioned in Eq. A.1.

$$\frac{x^2}{58^2} + \frac{y^2}{116^2} = 1 \qquad \text{EQ. A.1}$$

Where 116 is the major axis representing the radius of cylinder and 58 is the minor axis of the elliptical profile. In such geometries, the maximum stresses are at the interface of ellipse and cylinder. In order to limit these stresses, an offset was introduced in between the centres of outer and inner elliptical profiles to increase the material thickness at this interface. The advantage of this offset was to reduce stresses by adding minimum material. The front dome was hemi-spherical with an opening of 25.4 mm for standard 14 TPI shutoff valve. In order to reduce the computation time, symmetry conditions were used and only one quarter of the cylinder was modelled, as shown in Fig. A.1.

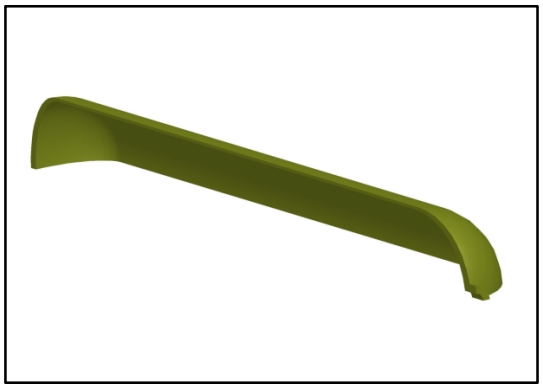

FIGURE A.1: 3D MODEL OF CNG CYLINDER

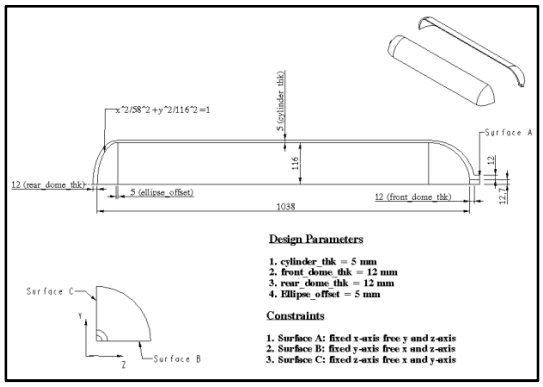

FIGURE A.2: SKETCH OF INITIAL MODEL AND BOUNDARY CONDITIONS

A.1.1.2. MATERIAL PROPERTIES

Steel cylinders are usually manufactured from AISI 4135 alloy steel containing Chromium and Molybdenum. The higher the strength of this steel the thinner the wall, the lighter the cylinder. The mechanical properties used were as follows: Young Modulus E = 205 GPa, Poisson Ratio ν = 0.29, Density ρ = 7850 kg/m^3 and Yield Strength σ_y = 690 MPa.

A.1.1.3. BOUNDARY CONDITIONS

As the geometry of the CNG cylinder was symmetrical, only one quarter of the cylinder was modelled. Ideal boundary conditions were applied to constrain the model as shown in Figure A.2. The surface along xy plane was fixed in the z-direction and free in the x and y directions, the surface along yz plane was fixed in x-direction and free in y and z directions and the surface along xz plane was fixed in y-direction and free in x and z directions. Symmetry boundary conditions were applied on the symmetric planes. The proof pressure of 250 bars was calculated and applied on the inner surface of the cylinder.

A.1.1.4. INTEGRATED FEA AND OPTIMISATION METHODOLOGIES

Both IFPO methodologies were implemented for the optimisation of CNG cylinder. In both methodologies, parametric modelling was performed in Pro/E. As the outer profiles of front and rear dome had to be changed during optimisation, parametric equations were written for them. The design parameters were included and the equation for the outer profile of rear dome was developed using Eq. A.2.

$$\frac{x^2}{\left(rear\_dome\_thk\text{-}csy\_thk+58\right)^2}+\frac{y^2}{(cylinder\_thk+116)^2}=1 \qquad \text{EQ. A.2}$$

Therefore, during the optimisation process all the geometry could be varied by varying design parameters and consequently the equation of profiles. Shape animate was performed on the model to verify the effect of the design parameters on the topology of the model. The design variables were varied from their lower to upper limit. The first methodology defined in Chapter 3 was implemented; the design variables were defined in Pro/E and successfully transferred to the parameter manager of the ANSYS WB environment. Material properties of Steel AISI 4135 and the boundary conditions were defined in the ANSYS WB environment. Mesh density was tested and the default mesh size was refined by defining the element size. The model was meshed and initial analysis was performed as can be seen in Fig. A.3. Upper and lower limiting values of the three design variables were imposed and the response of maximum von-Mises stress with respect to design variables was plotted as shown in Fig. A.4 and A.5. After achieving the optimum geometry through the IFPO procedure, the parameters were simultaneously updated in the Pro/E environment hence updating the 3D model. All the associated deliverables were also updated during this process. A final analysis can be performed on the optimum geometry to verify the results as shown in Fig. A.6.

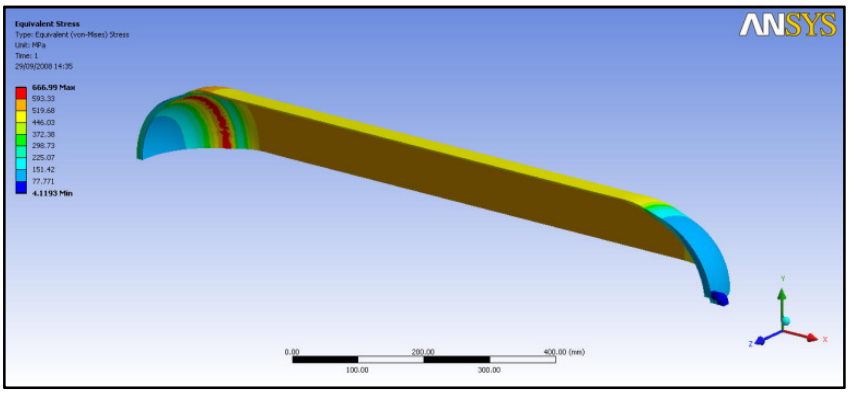

FIGURE A.3: INITIAL MODEL VON-MISES STRESSES

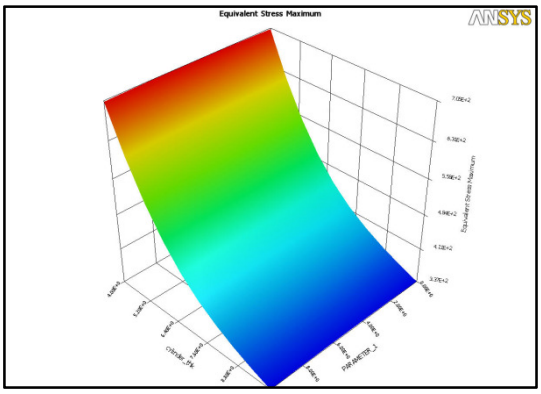

FIGURE A.4: *cylinder_thk*

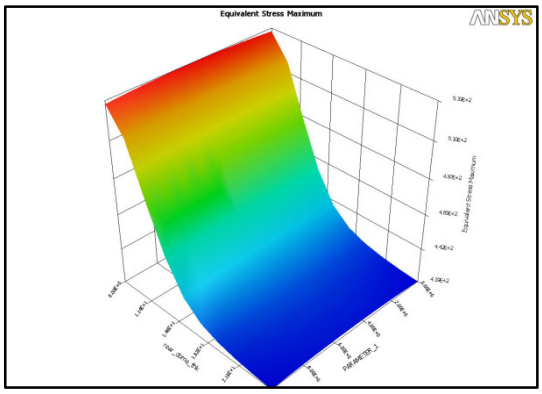

FIGURE A.5: *rear_dome_thk*

DESIGN VARIABLES VARIATIONS DURING ITERATIONS

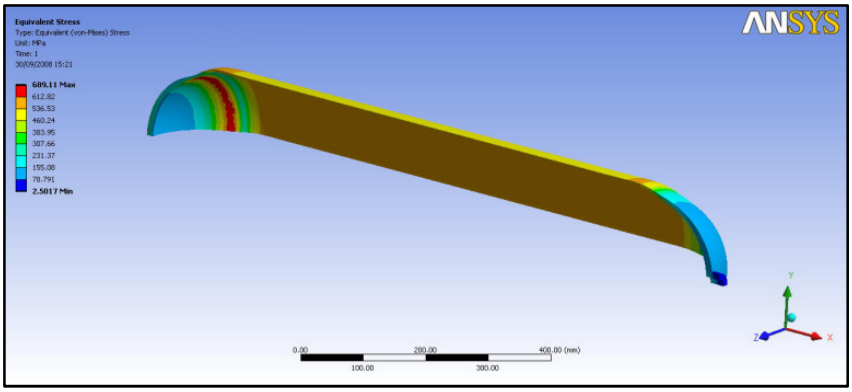

FIGURE A.6: OPTIMISED MODEL VON-MISES STRESSES

After achieving the optimisation through first IFPO methodology, the second methodology explained in Chapter 3 was implemented to achieve an optimal solution. The parametric model was generated in Pro/E as defined earlier. The material properties of AISI 4135 alloy steel were assigned and boundary conditions were applied in Pro/Mechanica. In order to define the optimisation and sensitivity study, the base line analysis was performed as shown in Fig. A.7. A global sensitivity study was performed by plotting the design variables variation versus von-Mises stress revealing the response of variables during optimisation process as shown in Fig. A.8, A.9 and A.10. Finally,

the optimisation study was defined to achieve the objective function; to minimize the mass of the CNG cylinder while keeping the stress within required boundaries. Optimisation study was defined by imposing limits on the von-Mises stress and defining initial values and boundaries of design parameters. Optimisation was launched and the optimisation run was completed after 12 iterations. A final analysis of optimised geometry was performed and results were reviewed as shown in Fig. A.11.

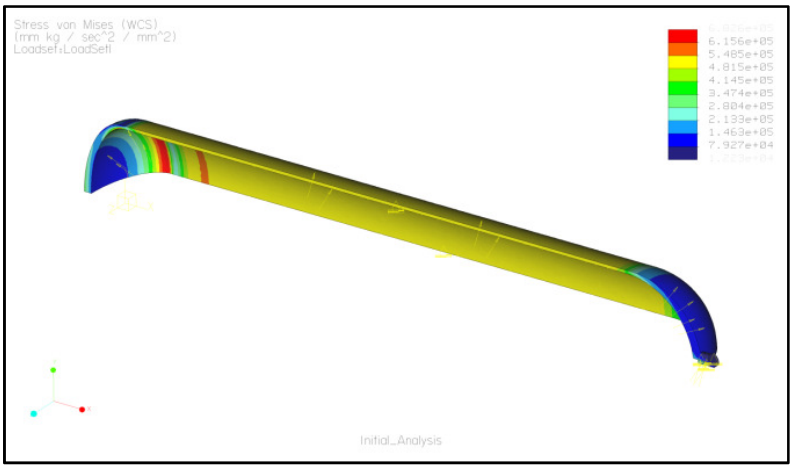

FIGURE A.7: INITIAL MODEL VON-MISES STRESSES

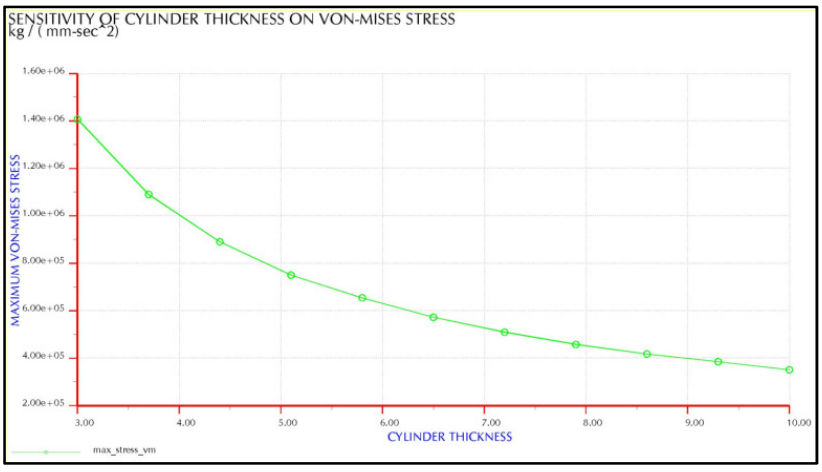

FIGURE A.8: VON MISES STRESS SENSITIVITY VS. DESIGN VARIABLE: *cylinder_thk*

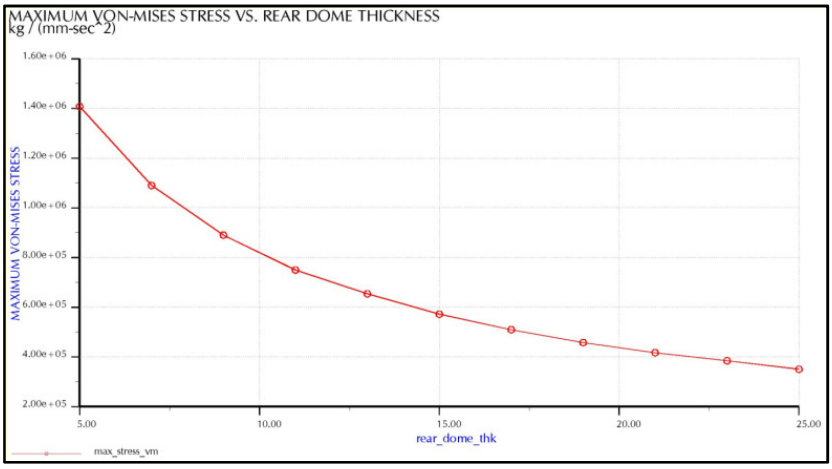

FIGURE A.9: VON MISES STRESS SENSITIVITY VS. DESIGN VARIABLE: *rear_dome_thk*

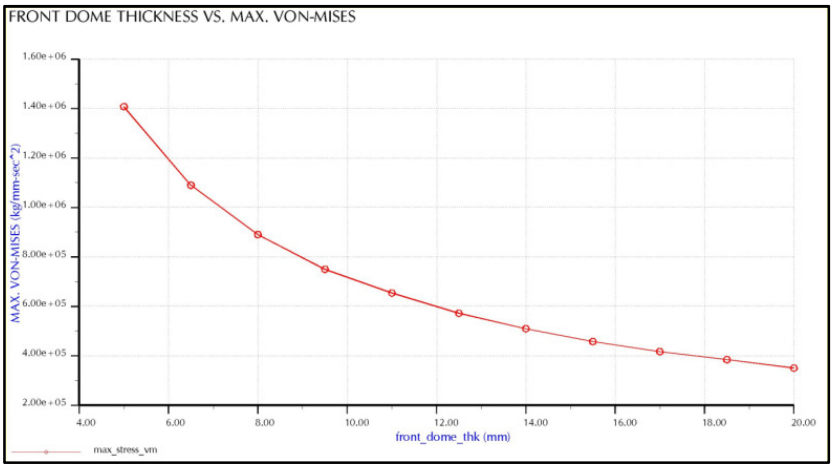

FIGURE A.10: VON MISES STRESS SENSITIVITY VS. DESIGN VARIABLE: *front_dome_thk*

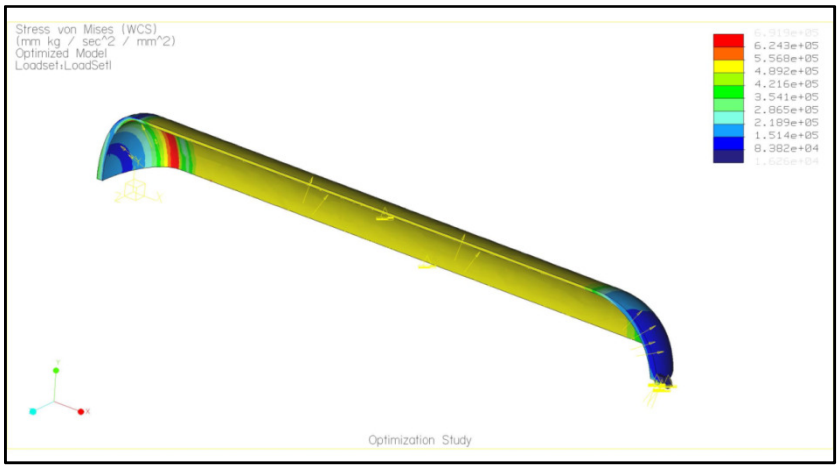

FIGURE A.11: OPTIMISED MODEL VON MISES STRESSES

A.1.1.5. VALIDATION METHODOLOGIES

In order to validate the results of the IFPO, two validation methodologies were implemented. As explained earlier, the standard ANSYS optimisation procedure was used as first validation methodology for optimisation of the CNG cylinder. Parameters were defined for cylinder thickness, rear dome thickness and front dome thickness for parametric modelling. The elliptical coordinate system was used to model the rear dome. For the inner profile of rear dome, a value of 2 was assigned for parameter *par1* (ratio of ellipse y-axis radius to x-axis radius). For outer profile of rear dome *par1* was calculated as in Eq. A.3.

$$par1 = \frac{116+cylinder\_thk}{(58+rear\_dome\_thk-csy\_thk-cylinder\_thk)} \quad \text{EQ. A.3}$$

Eq. A.3 of *par1* elliptical coordinate systems was incorporated for the parametric modelling of the outer profile of the rear dome. During the optimisation iterations, an updated value of *par1* was required therefore; a variable elliptical coordinate system was used to model the outer profile of the rear dome. The cylindrical coordinate system was used to model the front dome. To generate the outer profile of the front dome the centre of the circle was parameterize to maintain tangency between the varying dome and the cylinder. In order to calculate the centre of profile, the equation of circle was used Eq. A.4

$$(x-a)^2+(y-b)^2=r^2 \quad \text{EQ. A.4}$$

Where *a* and *b* are the x and y coordinates of centre of circle

As centre lies on axis of CNG cylinder therefore *b=0* and *a* was calculated as in Eq. A.5

$$a = (980 + front\_dome\_thk) - \sqrt{(116 + cylinder\_thk)^2 + (12.7 + front\_dome\_thk)^2} \quad \text{EQ. A.5}$$

Eq. A.5 was incorporated in the parametric modelling of the outer profile of the front dome. After building the parametric model in ANSYS, the scalar parameters (design variables) *cylinder_thk, rear_dome_thk* and *front_dome_thk* were defined. Von-Mises stress was the controlling factor of optimisation so it was defined as a state variable with its limiting values. The geometric volume of the CNG cylinder was defined as the objective function, which was minimized. The CNG cylinder was constrained as defined earlier. The system was solved for original geometry and von-Mises stress distribution is shown in Fig. A.12. An optimisation input file was created for the ANSYS optimiser and optimisation was performed using optimisation variables. The

variations in each design variable was plotted against their corresponding iteration as shown in Fig A.13, A.14 and A.15. The optimisation was achieved by ANSYS optimiser after 7 iterations as represented in Fig. A.16.

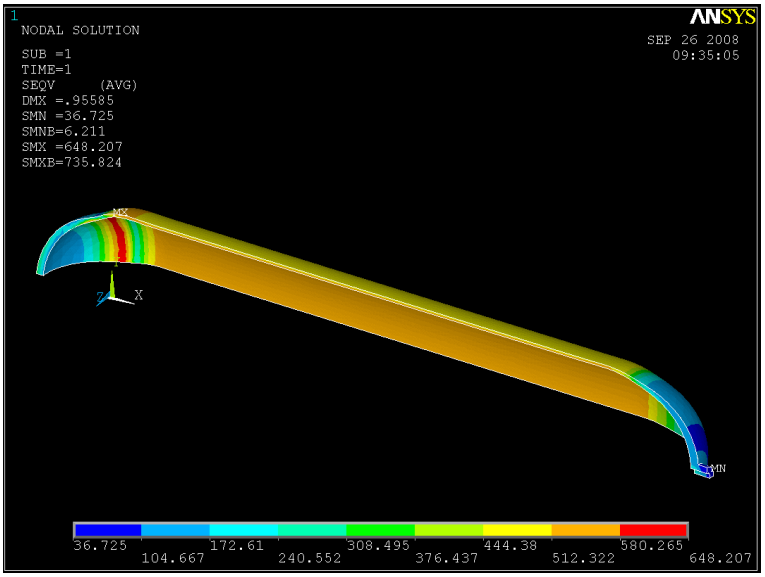

FIGURE A.12: INITIAL MODEL VON-MISES STRESS

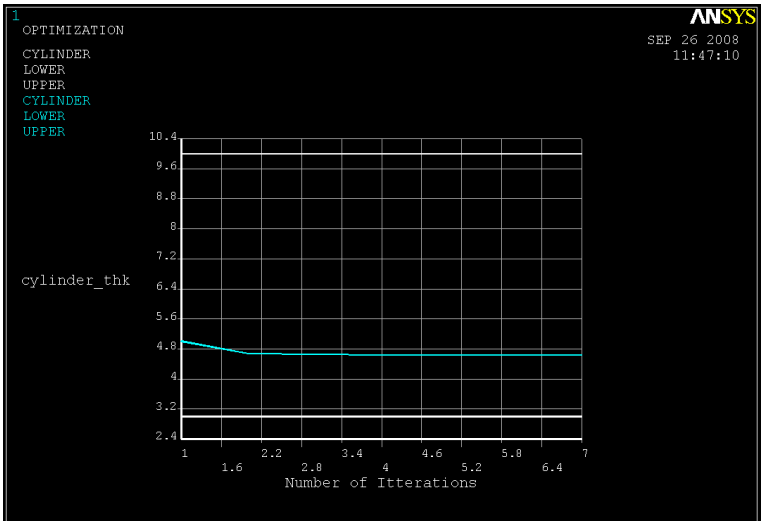

FIGURE A.13: DESIGN VARIABLE SENSITIVITY DURING ITERATIONS: *cylinder_thk*

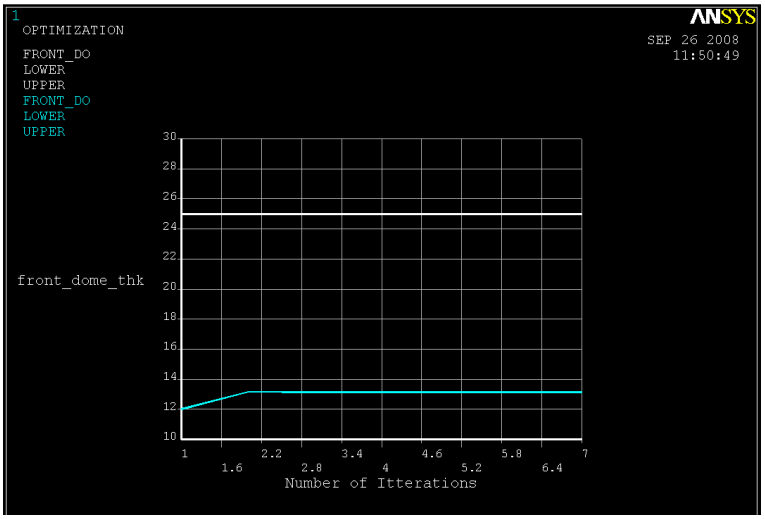

FIGURE A.14: DESIGN VARIABLES SENSITIVITY DURING ITERATIONS: *front_dome_thk*

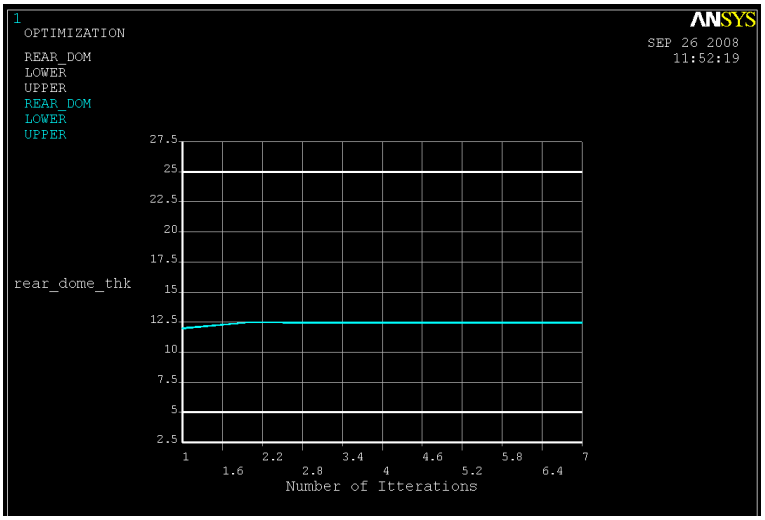

FIGURE A.15: DESIGN VARIABLES SENSITIVITY DURING ITERATIONS: *rear_dome_thk*

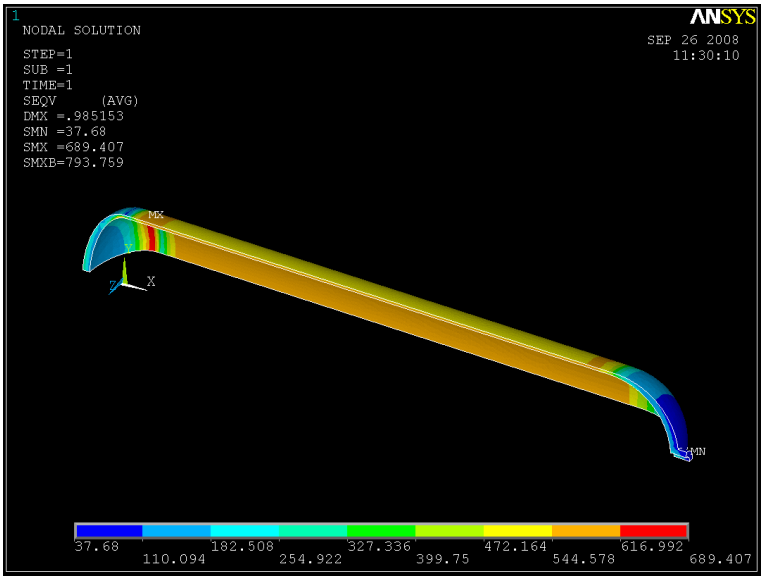

FIGURE A.16: OPTIMISED MODEL VON MISES STRESS

In the second methodology for validation of integrated optimisation, manual iterations were performed using ANSYS. Parametric model of CNG cylinder was generated in ANSYS using bottom up modelling technique. The model was meshed using solid elements (SOLID95). Boundary conditions were applied on the model and solved for initial geometry. As ANSYS solver was used in both first and second validations methodologies therefore the results of initial analysis were identical in both cases. All the three design variables *cylinder_thk*, *rear_dome_thk* and *front_dome_thk* were varied manually by a time consuming step by step approach to identify the optimum design as shown in Fig. A.17.

Considering the obtained results from IFPO and validation methodologies, it can be seen that the results of the IFPO are comparable to standard optimisation procedures.

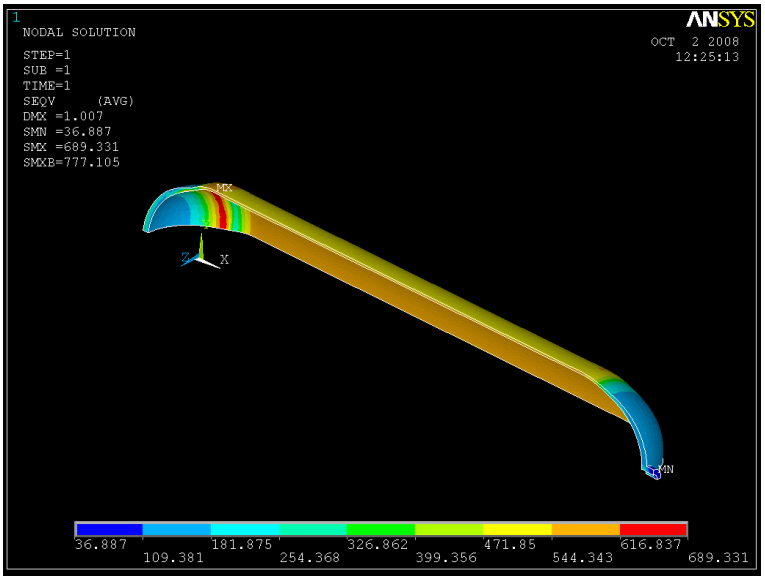

FIGURE A.17: OPTIMISED MODEL VON MISES STRESS

A.1.2. CASE STUDY: LIFTING HOOK DESIGN OPTIMISATION

In this case study, the two IFPO methodologies were implemented on a lifting hook. This lifting hook is a central part of a lifting beam and the first component in the load path. The objective of this case was to optimise the design of the lift hook having minimum mass or volume starting from a rough model. Fig. A.18 shows a sketch and 3D model that was the starting point of the design optimisation problem. A vertical load of 10 tons (10,000 kg.) was applied at the ends of the hook. The bottom face of the lifting surface was totally constrained. The mechanical properties used were as follows:

E = 200 GPa, v = 0.3, ρ = 7850 kg/m^3 and Yield Strength of 200 MPa. The design parameters were the thickness, base width, and shear height. An over estimated value of 50 mm was taken as an initial thickness in order to demonstrate the optimisation process. Half of the base of the lift hook was taken as base width and the height of region above lift location was taken as shear height. The state variable (constraint) was maximum von-Mises stress having limiting value of 200 MPa and the objective variable (goal) was minimum volume. All the optimisation variables and boundary conditions are shown in Fig. A.18.

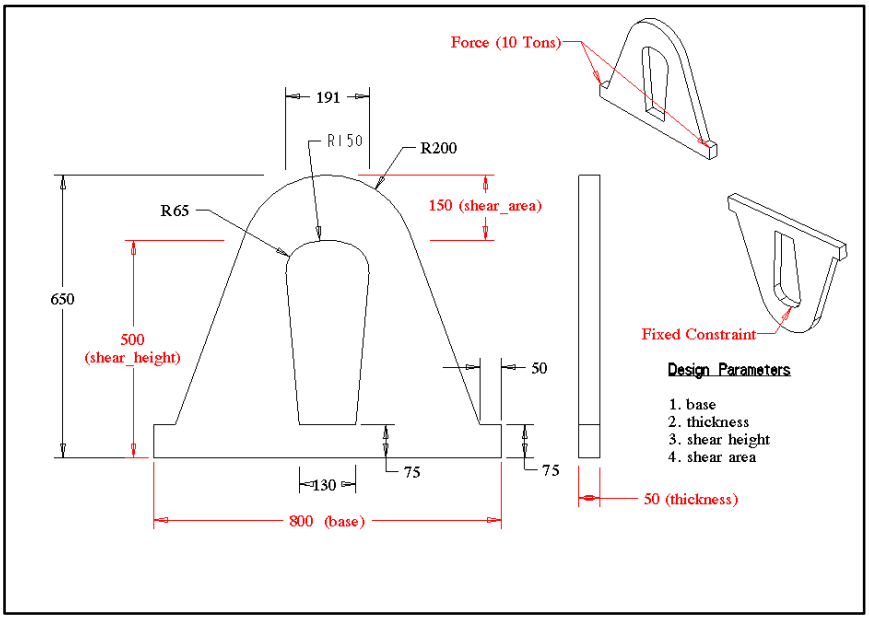

FIGURE A.18: SKETCH OF INITIAL MODEL AND BOUNDARY CONDITIONS

In both integrated and non-integrated methodologies, the model was constrained from the central lifting position and force was applied in form of pressure. As seen in Eq. A.7, the pressure was applied as a variable quantity in order to keep the value of force constant throughout the optimisation process.

$$A = W \times thickness \quad \text{(area on which pressure was applied)} \qquad \text{EQ. A.6}$$

Where $W = (50+50)$ mm (Width of faces)

$$P = F / A \qquad \text{EQ. A.7}$$

$$= 100{,}000 \text{ N} / (100 \times thickness) \text{ mm}^2$$

$$= 1000 / thickness \text{ MPa}$$

A.1.2.1. INTEGRATED FEA AND OPTIMISATION METHODOLOGIES

The procedure for IFPO using Pro/E and ANSYS WB was followed in the first methodology. Fig. A.19 shows the analysis of the initial geometry presenting the stress distribution in lifting hook. The value of maximum von-Mises stress before optimisation was 90.7 MPa. Fig. A.20 shows the response of von-Mises stress versus design variables. After optimisation study, the volume was reduced from 1.33×10^7 mm^3 to 4.18×10^6 mm^3. The design variables were successfully transferred in between Pro/E and ANSYS WB. The final analysis showing maximum von-Mises stress in optimum geometry is presented in Fig. A.21. The Pro/E model was automatically updated after optimisation as shown in Fig. A.22.

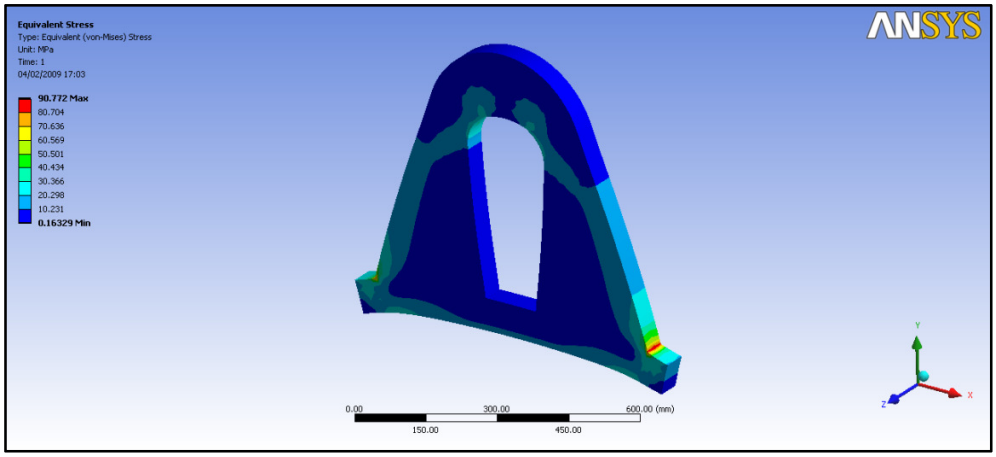

FIGURE A.19: INITIAL MODEL VON-MISES STRESSES

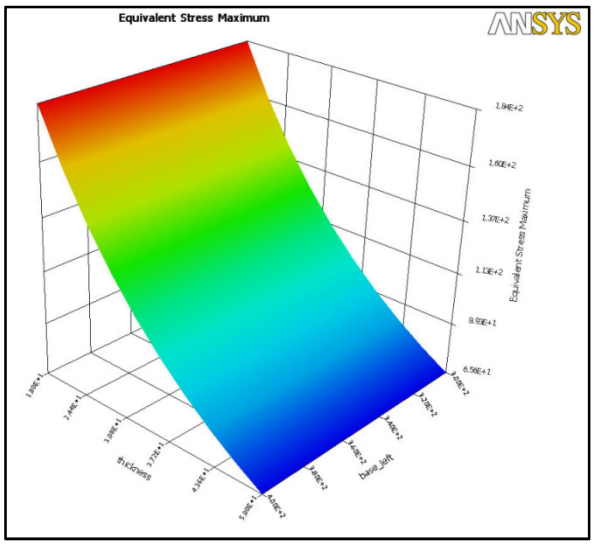

FIGURE A.20: RESPONSE OF VON-MISES STRESSES VS. THICKNESS AND BASE_WIDTH

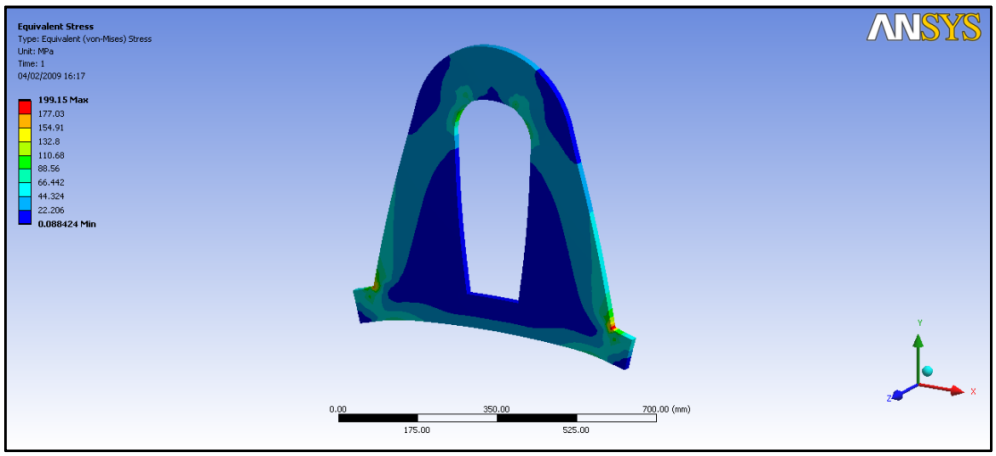

FIGURE A.21: OPTIMIZED MODEL VON-MISES STRESSES

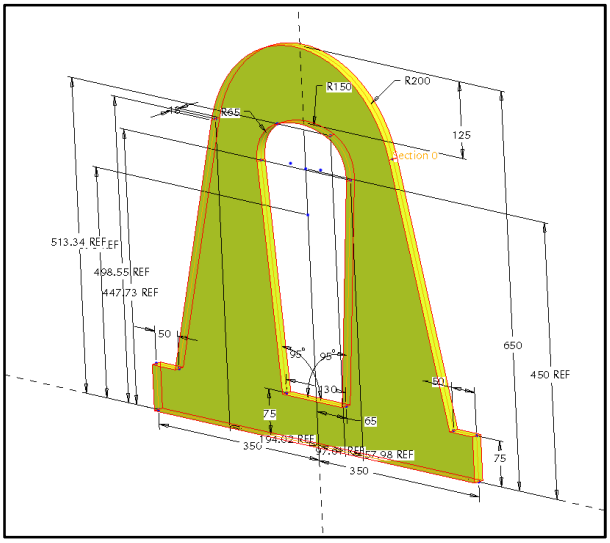

FIGURE A.22: AUTOMATICALLY UPDATED PRO/E MODEL

Next, the second methodology for parametric optimisation using Pro/Mechanica in integrated mode with Pro/E was repeated for this study. Baseline analysis on the initial geometry was performed and its results are shown in Fig. A.23. The sensitivity of design variables on the topology of model is shown in Fig. A.24, Fig. A.25 and Fig. A.26. The stress distribution in optimum geometry is shown in Fig. A.27 and it shows that the von-Mises stress after optimisation were within desired limit. The final volume was reduced to 4.29 x10^6 mm^3 after 11 design iterations. Finally, optimal configuration was automatically incorporated in the Pro/E model resulting in optimised 3D model.

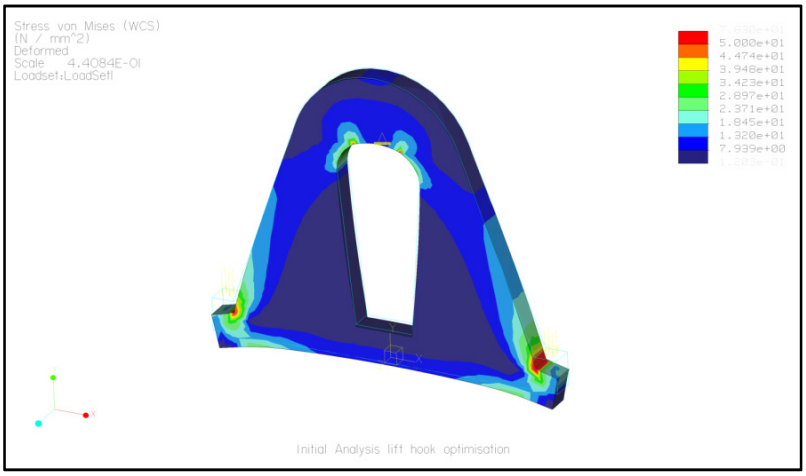

FIGURE A.23: INITIAL MODEL VON MISES STRESSES

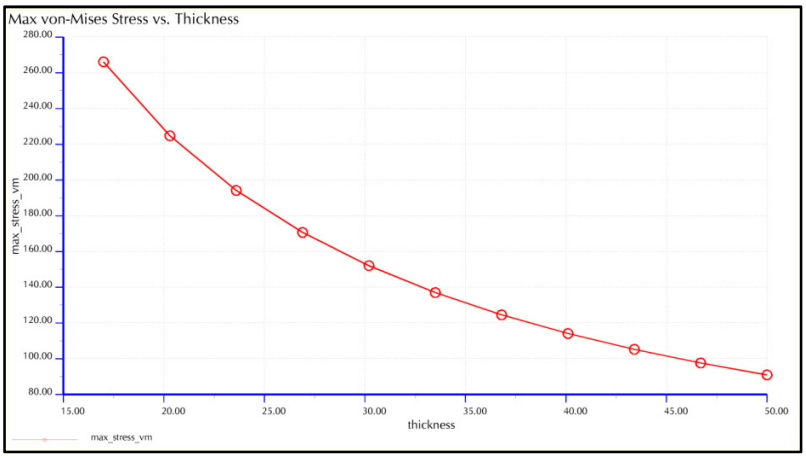

FIGURE A.24: *thickness* VS. VON MISES STRESSES

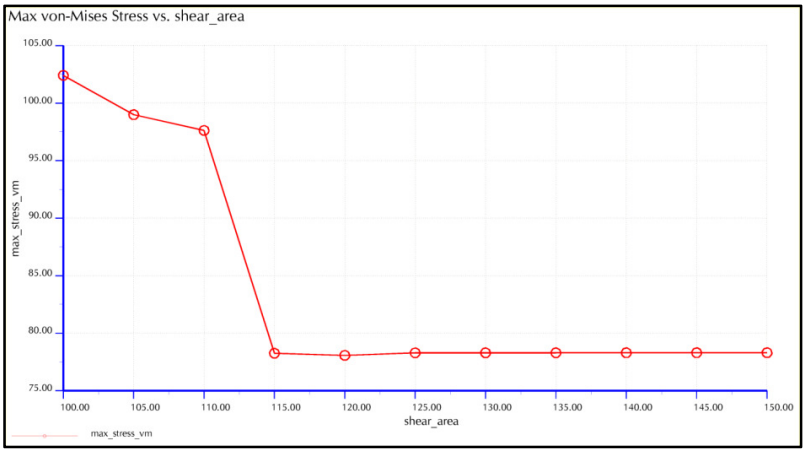

FIGURE A.25: *shear_area* VS. VON-MISES STRESSES

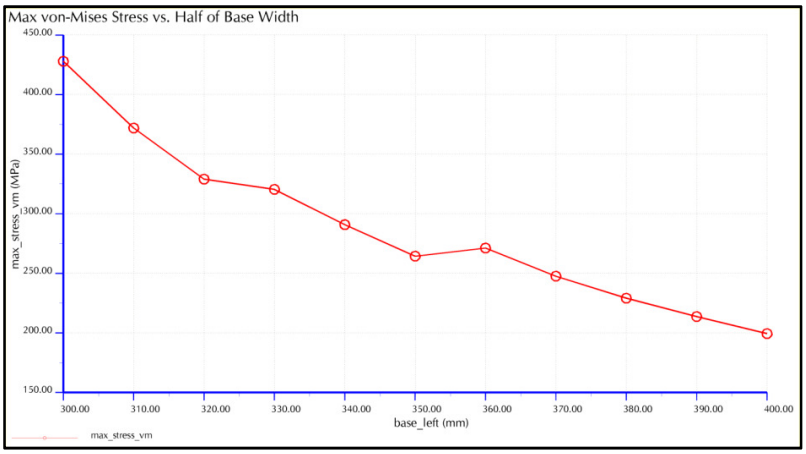

FIGURE A.26: *base_width* VS. VON MISES STRESSES

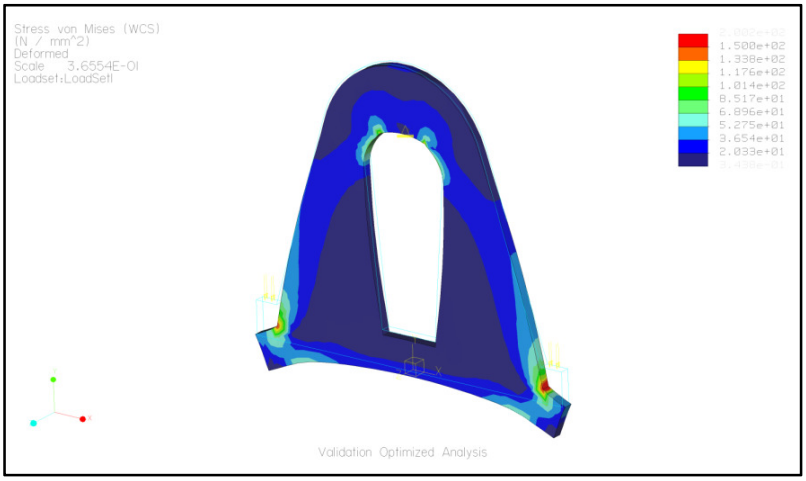

FIGURE A.27: OPTIMIZED MODEL VON MISES STRESSES

A.1.2.2. VALIDATION METHODOLOGIES

As described in the earlier case study, the ANSYS optimiser was used for validation of integrated parametric optimisation. The *thickness*, *shear_height* and *base_width* of the lift hook were defined as scalar parameters. A parametric model was generated in ANSYS using these design variables. Limits were imposed on maximum stress and the objective (minimum volume) of the study was defined. Stress distribution in the initial geometry is shown in Fig. A.28. Optimisation was performed using an input file and optimisation variables. Fig A.29, A.30, and A.31 show the variation of design variables during iterations. After 12 iterations, the initial geometry was optimised and the stress distribution after optimisation is shown in Fig. A.32.

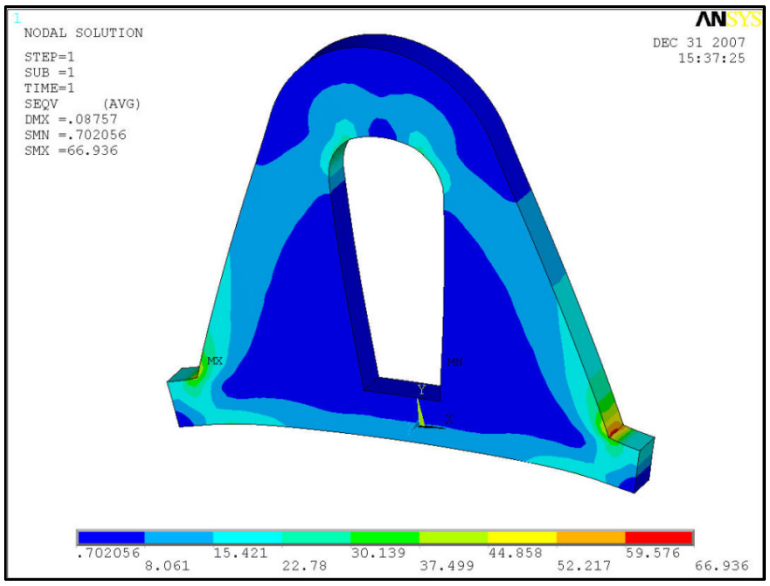

FIGURE A.28: INITIAL MODEL VON-MISES STRESSES

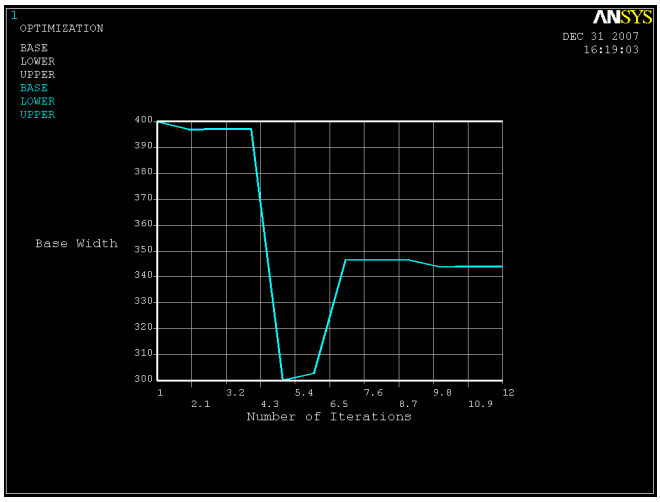

FIGURE A.29: DESIGN VARIABLES SENSITIVITY DURING ITTERATIONS: *base_width*

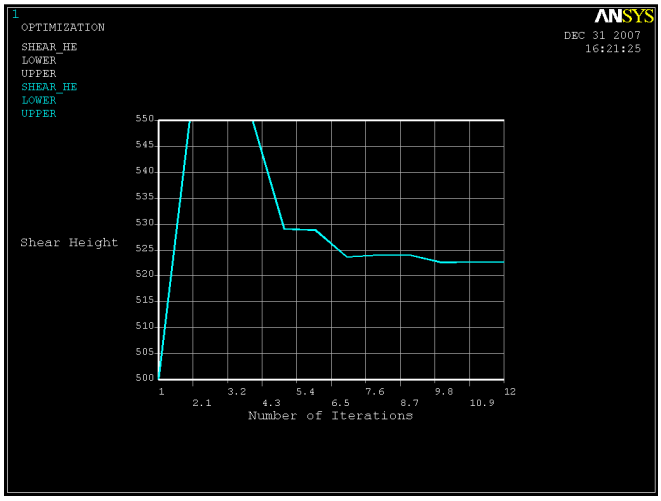

FIGURE A.30: DESIGN VARIABLES SENSITIVITY DURING ITEERATIONS: *shear_height*

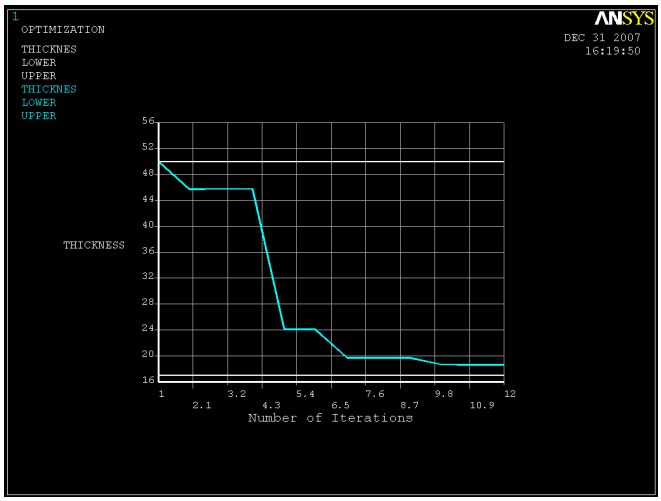

FIGURE A.31: DESIGN VARIABLES SENSITIVITY DURING ITTERATIONS: *thickness*

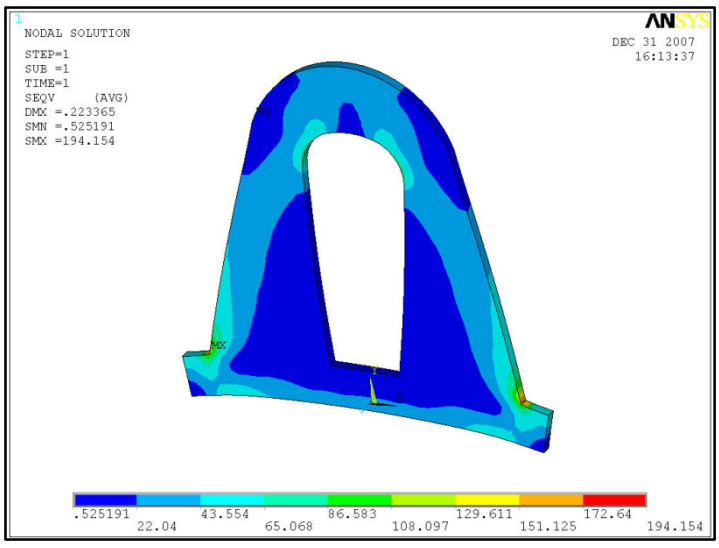

FIGURE A.32: OPTIMISED MODEL VON-MISES STRESSES

In the second validation methodology, manual iterations were performed using ANSYS v11.0 to achieve optimisation as described in first case study. A parametric model was generated using APDL and a log file was used to vary the design variables and topology of the model. Optimisation was performed using the limiting values of maximum von-Mises stress. The volume was reduced to 4.15×10^6 mm^3 by varying the three design variables thickness, shear area and base width one by one. The stress distribution of optimum design is shown in Fig. A.33.

Again as expected, the results of parametric optimisation are comparable with pre-established optimisation methodologies.

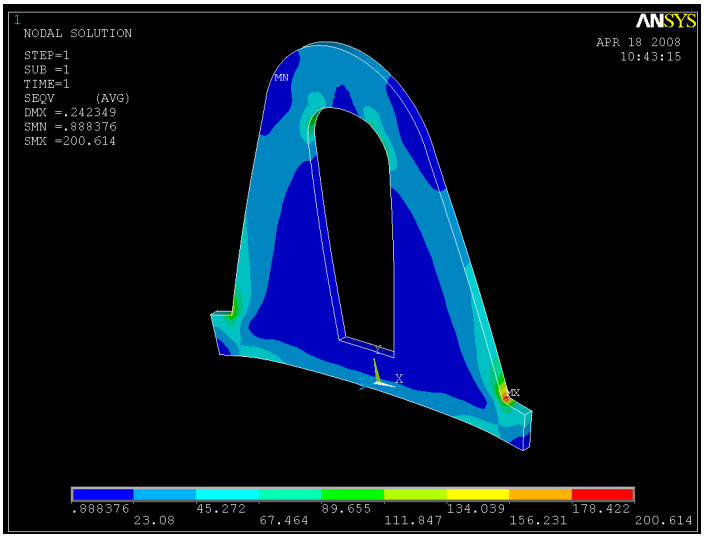

FIGURE A.33: OPTIMIZED MODEL VON MISES STRESSES

A.1.3. COMPARATIVE ANALYSIS OF FEA AND OPTIMISATION METHODOLOGIES

IFPO was demonstrated and validated using two different geometries in two case studies. Table A.1 represents the comparison of design variables and the yielded results in the CNG cylinder before and after optimisation. All the design variables were varied during optimisation iterations to achieve the objective function (mass of the CNG cylinder) while satisfying the design constraint (max von-Mises stresses). In both the IFPO methodologies using ANSYS WB and Pro/Mechanica as optimisation tools, a mass reduction of 5.88% and 3.72% was achieved respectively. The values of the design variables after parametric optimisation are comparable to the values obtained from the non-integrated validation methodologies using ANSYS optimiser and manual iterations. Table A.2 shows the complete picture of the parametric optimisation of a lifting hook and its comparison with standard techniques. In this case study, grossly overestimated

values of design variables were selected to demonstrate the capabilities of parametric optimisation. The thickness of the lift hook was one of the most influencing parameter of optimisation. Therefore, a substantial reduction in mass was observed in this case study. The design optimisation of the lifting hook was achieved successfully leading to a weight saving in between 60% to 68% among the different optimisation methodologies. In both case studies, the design variables were integrated successfully in between Pro/E, Pro/Mechanica and ANSYS WB. Consequently, CAD models were updated automatically after optimisation thus reducing the design cycle time. Both case studies demonstrated that the results of parametric optimisation using Pro/Mechanica and ANSYS WB were in close match with ANSYS optimiser and manual iterations. It was observed that the maximum value of von-Mises stresses in Pro/Mechanica was relatively at higher side even in initial geometry. Therefore, the optimisation trends of the objective function indicate that reduction in Pro/Mechanica was lesser as compared to other techniques.

TABLE A.1: CNG CYLINDER: COMPARISON OF FEA AND OPTIMISATION METHODOLOGIES

Parameters	**Initial Model**			**ANSYS Workbench**	**Pro / Mechanica**	**ANSYS Optimiser**	**Manual Iterations**
cylinder_thk (mm)	5			4.69	4.989	4.638	4.7
rear_dome_thk (mm)	12			12.6	10.274	12.453	11.9
front_dome_thk (mm)	12			10.975	10	10.733	10
Volume (mm^3)	$1.167x10^6$			$1.098\ x10^6$	$1.124\ x10^6$	$1.084\ x10^6$	$1.081\ x10^6$
Mass (kg)	9.104			8.567	8.764	8.455	8.434
Max. von-Mises Stress (MPa)	Workbench	ANSYS	Pro/Mechanica	689.1	691.9	689.4	689.3
	666.99	648.2	682.6				
Mass Reduction (%age)	0			5.88	3.72	7.11	7.37

TABLE A.2: LIFTING HOOK: COMPARISON OF FEA AND OPTIMISATION METHODOLOGIES

Parameters	**Initial Model**			**ANSYS Workbench**	**Pro / Mechanica**	**ANSYS Optimiser**	**Manual Iterations**
thickness (mm)	50			18	21.07	18.63	17.98
base_width (mm)	400			350	376.13	344	350
shear_height (mm)	150			125	144.44	127.35	120
Volume (mm^3)	$1.33x10^7$			$4.18\ x10^6$	$5.29\ x10^6$	$4.27\ x10^6$	$4.15\ x10^6$
Mass (kg)	104.6			32.86	41.58	33.54	32.64
Max. von-Mises Stress (MPa)	Workbench	ANSYS	Pro/Mechanica	199	200	194	200
	90.7	66.9	78.3				
Mass Reduction %age	0			68.58	60.24	67.93	68.8

APPENDIX B: DETAILED DRAWINGS

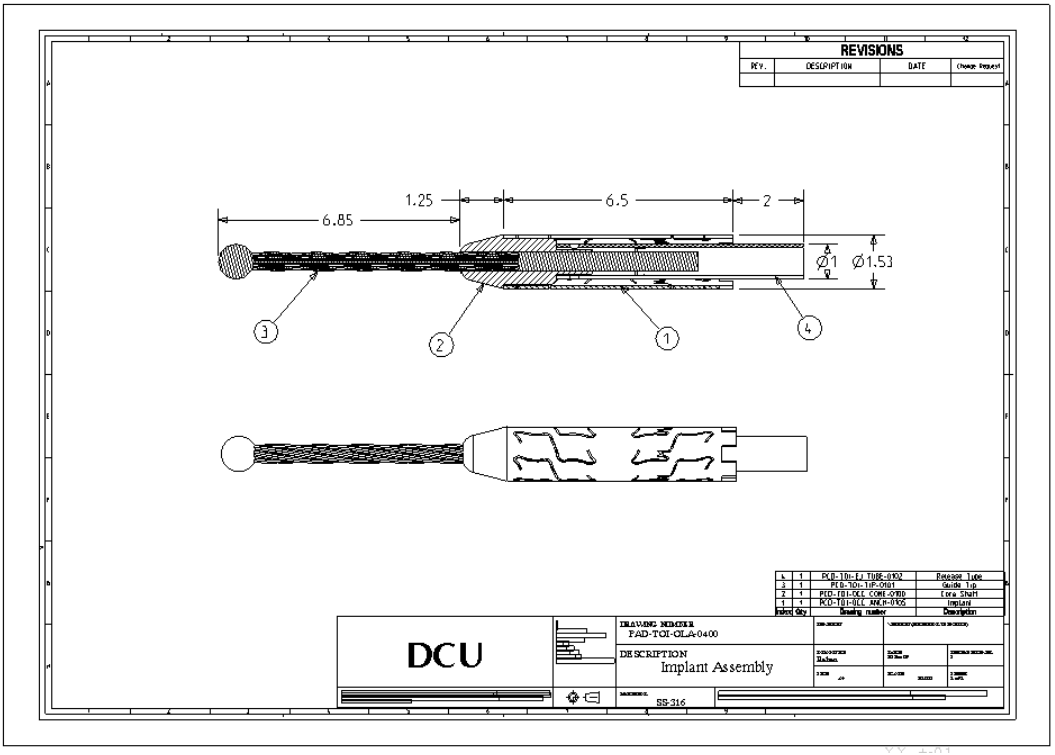

FIGURE B.1: IMPLANT ASSEMBLY

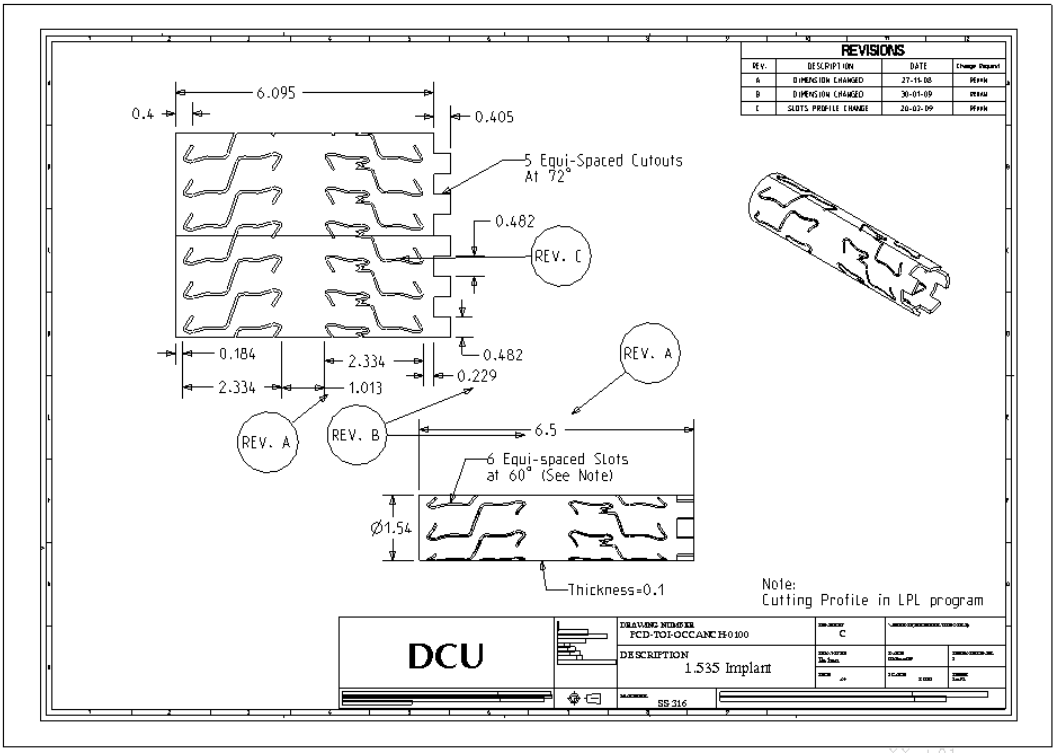

FIGURE B.2: IMPLANT

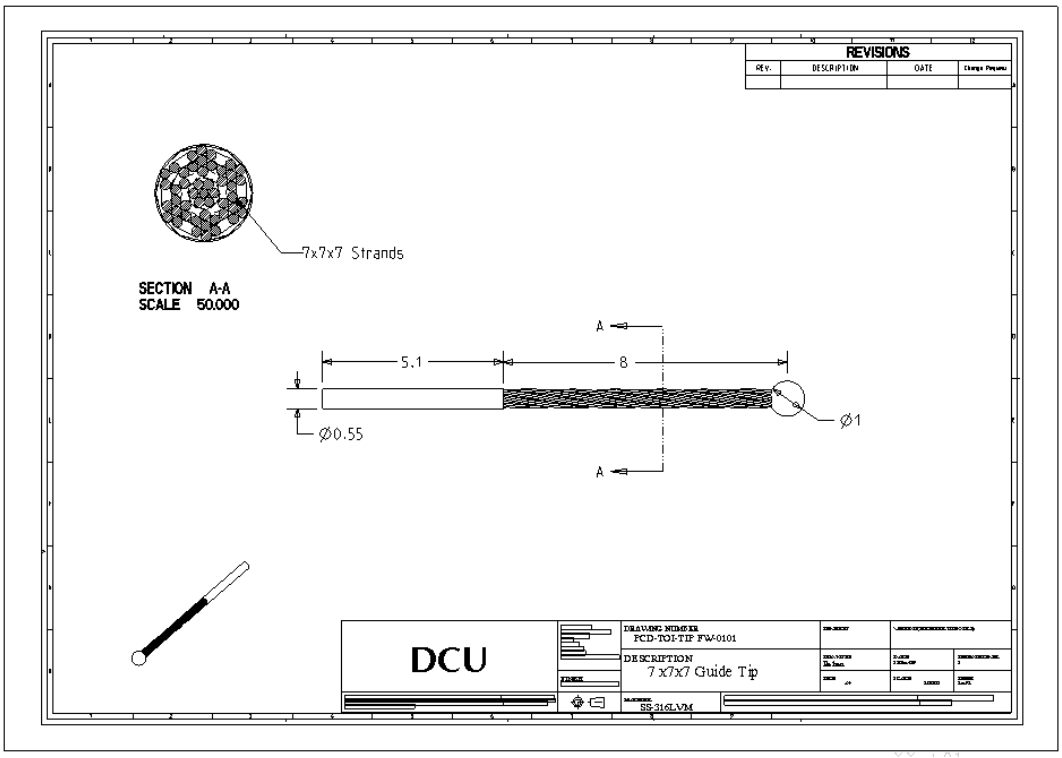

FIGURE B.3: GUIDE TIP

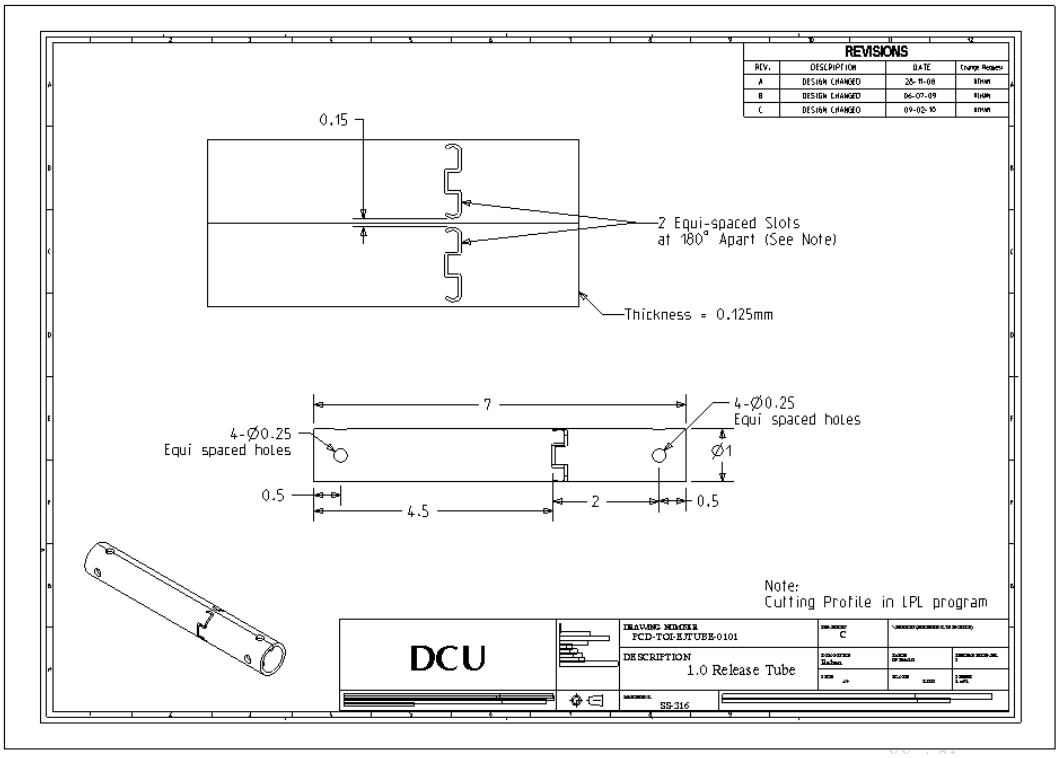

FIGURE B.4: RELEASE TUBE

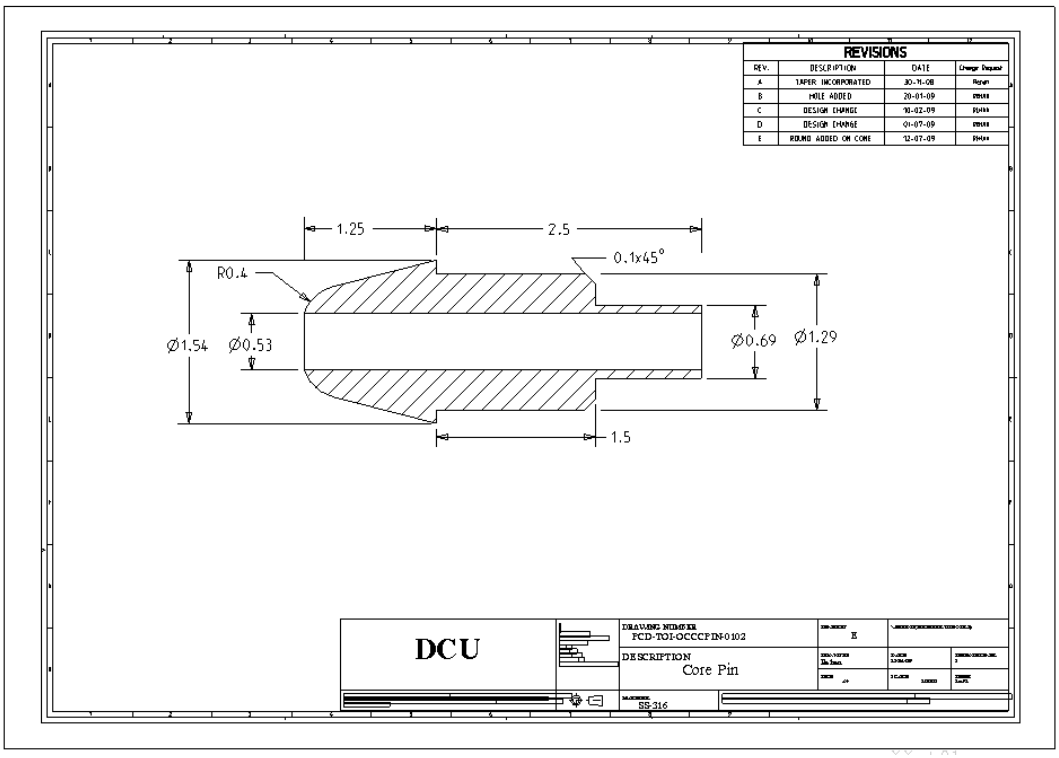

FIGURE B.5: CORE SHAFT

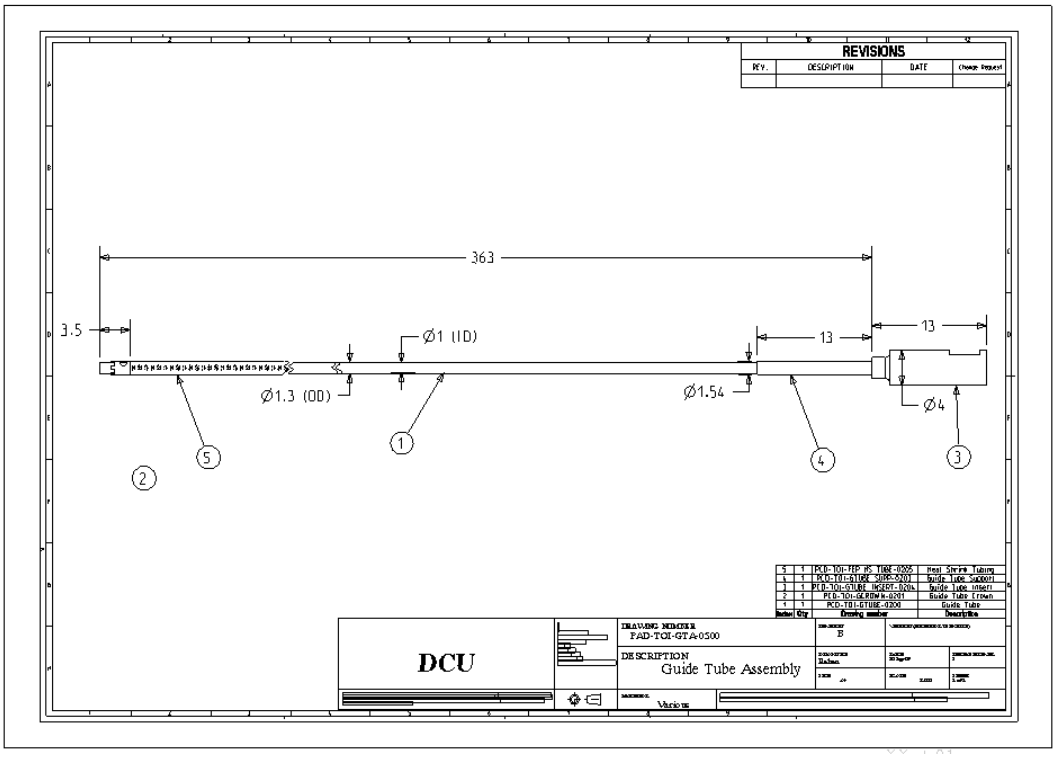

FIGURE B.6: GUIDE TUBE ASSEMBLY

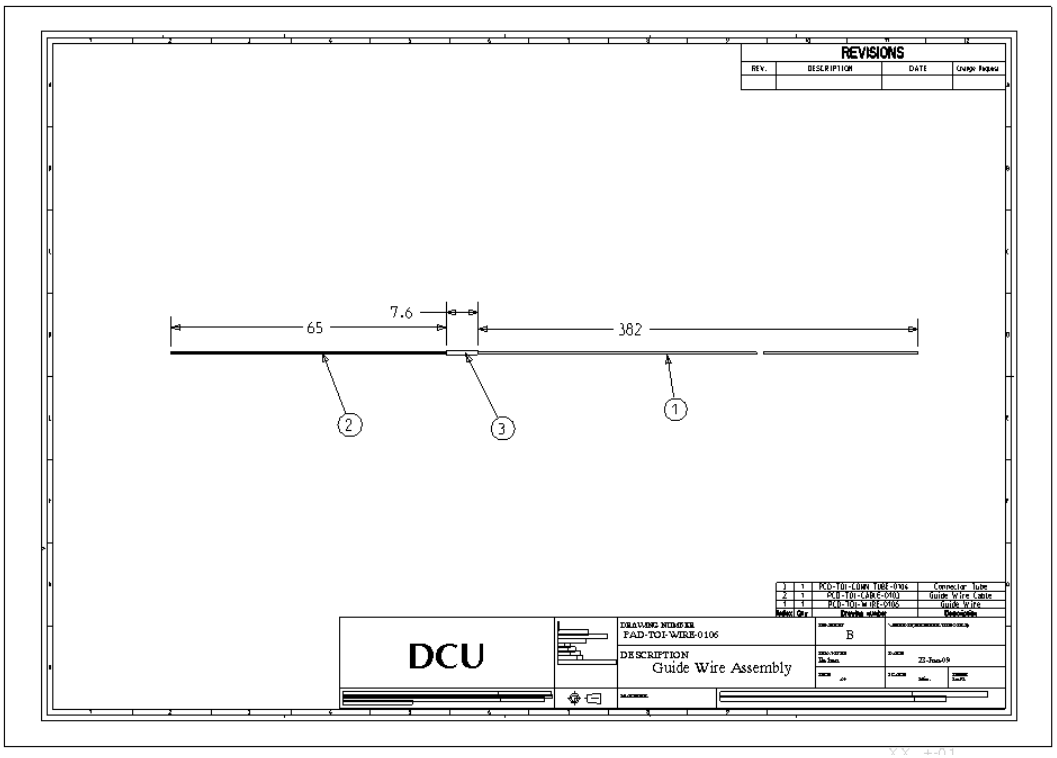

FIGURE B.7: GUIDE WIRE ASSEMBLY

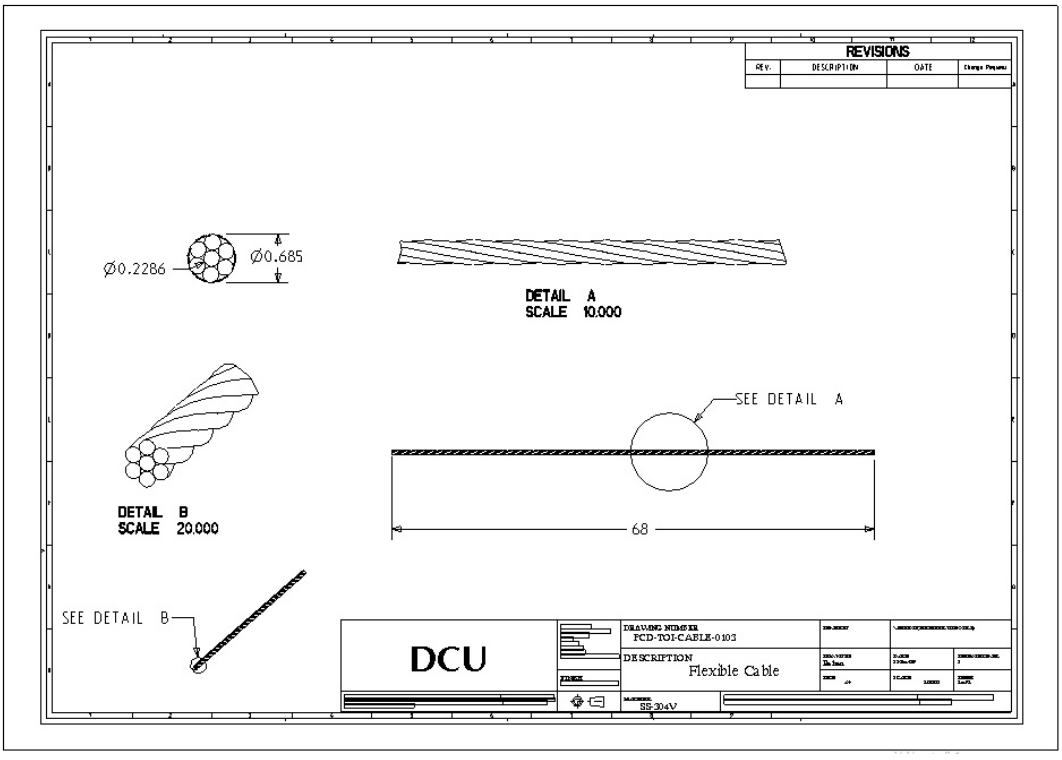

FIGURE B.8: GUIDE WIRE

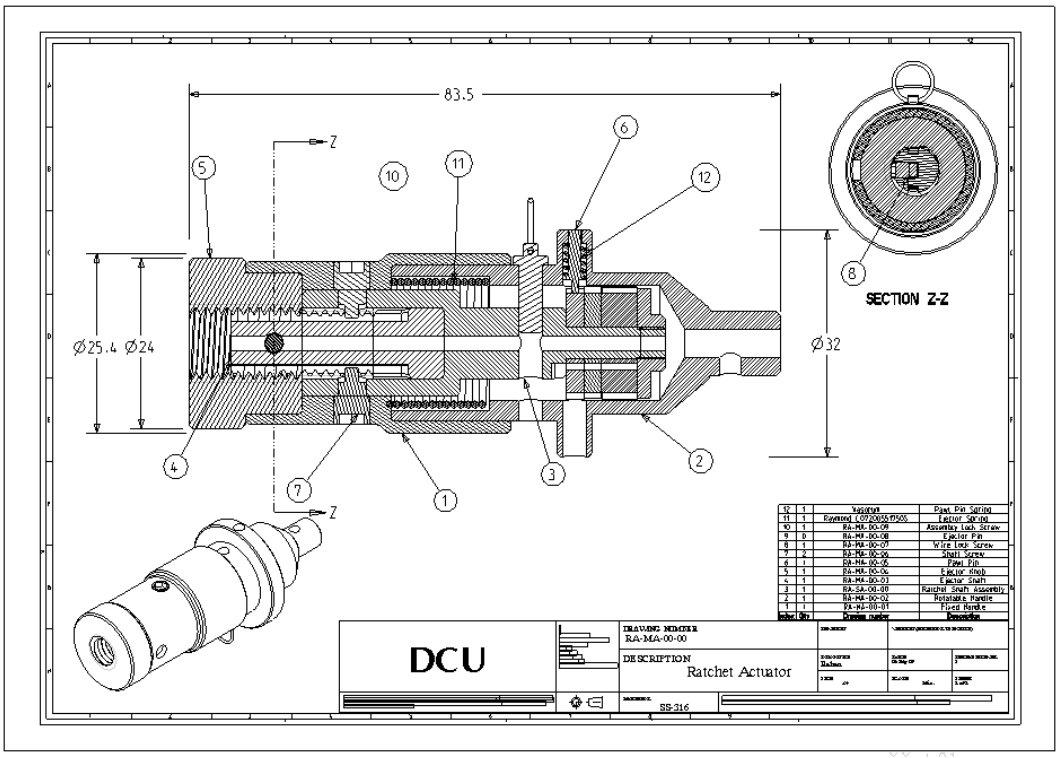

FIGURE B.9: FINAL ACTUATOR ASSEMBLY

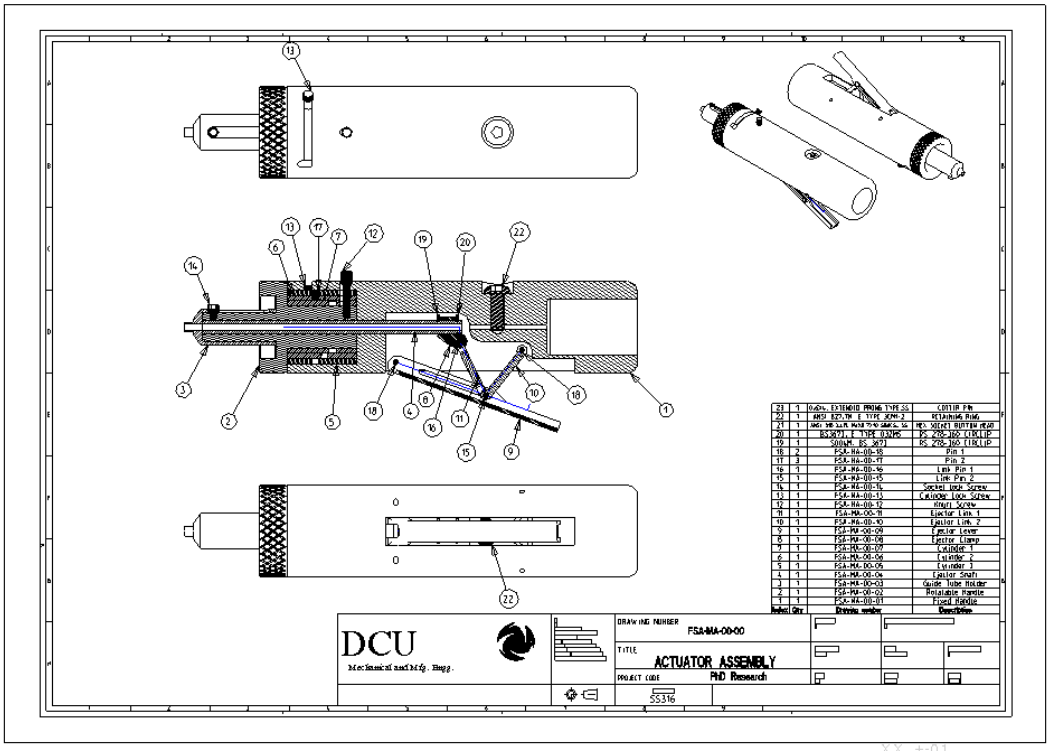

FIGURE B.10: IMPROVED ACTUATOR ASSEMBLY

APPENDIX C: DEPLOYMENT SEQUENCE

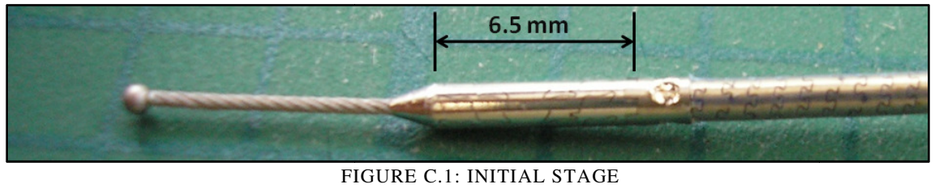

FIGURE C.1: INITIAL STAGE

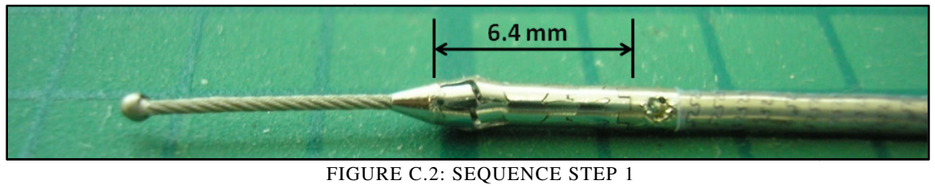

FIGURE C.2: SEQUENCE STEP 1

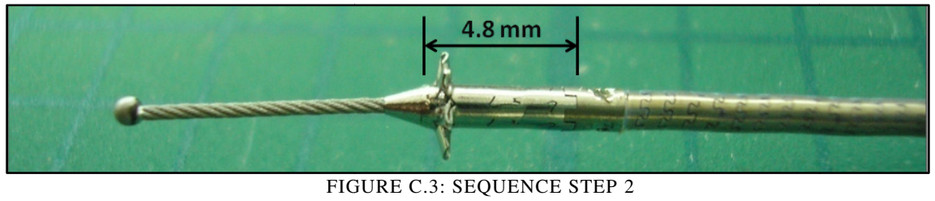

FIGURE C.3: SEQUENCE STEP 2

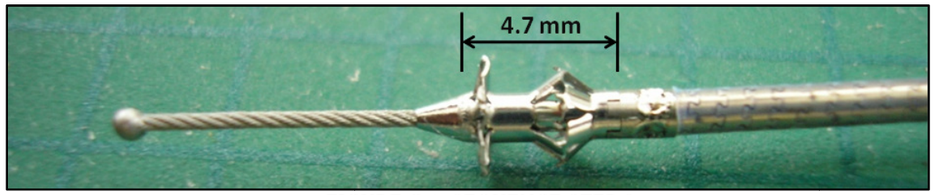

FIGURE C.4: SEQUENCE STEP 3

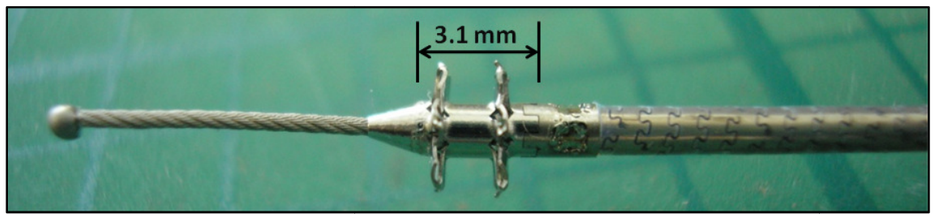

FIGURE C.5: SEQUENCE STEP 4

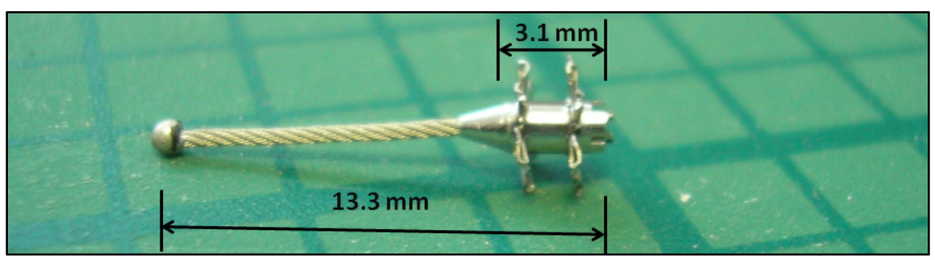

FIGURE C.6: SEQUENCE STEP 5 (DEPLOYED IMPLANT)